UNIVERSIDAD COMPLUTENSE DE MADRID
FACULTAD DE CIENCIAS FÍSICAS

TESIS DOCTORAL

Tin and titanium oxide nanostructures and their PEDOT:PSS-based composites: applications in solar cells, thermoelectrics and gas sensors

Nanoestructuras de óxidos de estaño y titanio y sus composites basados en PEDOT:PSS: aplicaciones en células solares, termoeléctricos y sensores de gases

MEMORIA PARA OPTAR AL GRADO DE DOCTOR

PRESENTADA POR

Antonio Vázquez López

Directores

David Maestre Varea
Ana Isabel Cremades Rodríguez

Madrid

UNIVERSIDAD COMPLUTENSE DE MADRID
FACULTAD DE CIENCIAS FÍSICAS

TESIS DOCTORAL

Tin and titanium oxide nanostructures and their PEDOT:PSS-based composites: applications in solar cells, thermoelectrics and gas sensors

Nanoestructuras de óxidos de estaño y titanio y sus composites basados en PEDOT:PSS: aplicaciones en células solares, termoeléctricos y sensores de gases

MEMORIA PARA OPTAR AL GRADO DE DOCTOR

PRESENTADA POR

Antonio Vázquez López

DIRECTOR

David Maestre Varea & Ana Isabel Cremades Rodríguez

Tin and titanium oxide nanostructures and their PEDOT:PSS-based composites: applications in solar cells, thermoelectrics and gas sensors

Nanoestructuras de óxidos de estaño y titanio y sus composites basados en PEDOT:PSS: aplicaciones en células solares, termoeléctricos y sensores de gases

by

Antonio Vázquez López

Under the supervision of

David Maestre Varea

&

Ana Isabel Cremades Rodríguez

Departamento de Física de Materiales

Fac CC. Físicas

Universidad Complutense de Madrid

A thesis submitted for the degree of

Doctor of Philosophy

Madrid, 2021

A mi familia
A Jimena

Acknowledgments/ Agradecimientos/ Agradecementos

Reservo este espacio para agradecer a todas las personas que han colaborado en que la realización de esta tesis doctoral haya sido posible. En primer lugar, quiero agradecer enormemente a mis directores de tesis David Maestre y Ana Cremades por haberme ofrecido la oportunidad de realizar este trabajo de investigación, por su ayuda y apoyo desde el minuto 0. He aprendido muchísimo de vosotros. No tengo palabras para mostrar mi agradecimiento. David, muchas gracias por la ayuda tanto técnica, científica como personal, quiero decir que eres un gran tutor y mentor. Ana, muchas gracias por el apoyo durante la tesis y por la confianza que has depositado en mí, te deseo lo mejor en tus nuevos proyectos.
Quisiera agradecer también al resto de los miembros del grupo de investigación FINEGROUP por su ayuda y positivismo (Pedro Hidalgo, Emilio Nogales, Bianchi Méndez, Ruth Martínez-Casado, Paloma Fernández, Carlos Díaz-Guerra y Ana Urbieta) y por haberme hecho sentir parte del grupo de nanomateriales electrónicos desde el comienzo. No puedo olvidar agradecer a los técnicos de laboratorio: Esther y Carlos Romero. A Esther, gracias por la ayuda durante los laboratorios de FES-I y II, haciendo que las clases hayan sido más sencillas y amenas. A Carlos Romero, gracias por tu pasión científica, tus ganas de *cacharrear* y tus conocimientos en electrónica, transmites la pasión por la ciencia mejor que nadie, gracias a ti ha nacido en mi un gran interés en la electrónica.

Gracias a los *post-doc* (Belén Sotillo y Javier Bartolomé). Sois el pilar fundamental que mantiene la investigación viva, el puente *pre-doc/senior researcher*. Sin vuestros conocimientos, espíritu científico y voluntad por ayudar, no hubiese adquirido los conocimientos que tengo. Tampoco me puedo olvidar de los doctorandos que ya se han marchado de los que tanto he aprendido (Marta, Francisco Carreño y Paloma Almodóvar) y de los jóvenes que quedan (Yuriko, Jesús, Bea y Javi G.). A María, que me ha acompañado desde el TFM, gracias por siempre estar dispuesta a echar una mano y por tu ayuda en mis comienzos en la Fac. CC. Químicas. A Jaime *Billy* por ser un compañero de batallas, de DFT, pádel y bares. A Marina, con la que he compartido no sólo la misma situación de hacer una tesis en *sub*-3 años sino también por nuestra estancia en Noruega, en la que nos caímos mil veces en la nieve. A Mica y Rocío, os deseo lo mejor y os animo, no queda nada.

Me gustaría agradecer a los distintos colaboradores que han permitido que esta tesis haya podido ser llevada a cabo. Quiero expresar mi gratitud hacia el Dr. J. Ramírez-Castellanos por permitirme utilizar las instalaciones en el Dpt. de Química Inorgánica, Fac. CC Químicas en la UCM, que ha sido un pilar en esta tesis. También quiero agradecer mucho su simpatía, ayuda y el positivismo que transmite. Igualmente quiero agradecer a la Dr. R. Martínez-Casado por su colaboración mediante los cálculos de DFT, que han brindado una perspectiva nueva al manuscrito. Muchas gracias.

During this PhD, I was fortunate to spend some time abroad at different institutions. I would like to thank the various members of ENWAIR Corp. (İTÜ, Istanbul, Turkey) especially N. Yuca for the great scientific collaboration regarding Li-ion batteries, as well as for her hospitality during our short visit to Istanbul. I cannot forget to thank the members of the BACH line from Elettra sincrotronne, in Trieste, Italy I. Píš and S. Nappini. During my brief stay in 2018 they offered great help with XPS and XAS measurements, as well as being very responsive in offering help with analysis. I am very grateful for the fruitful collaboration we have established and for your kindness. Thank you. And of course, I would like to personally thank to Smagul Karazhanov for hosting me during my 3-month internship at the SOL department at the *Institutt for energiteknikk* (IFE) in Kjeller, Oslo, Norway. From the first day I felt very welcomed by the group, where I was able to learn a lot about work organization as well as acquiring a lot of experience by using their great facilities. I cannot express enough my gratitude for their hospitality. I would also like to thank the various members of the group for their technical help and friendliness (C.C. You, B. Thomassen, H. Haug and E. S. Marstein).

Debo agradecer a todas aquellas personas que me han apoyado durante estos años.

- A mis dos grandes amigos y ex-compañeros físicos de la USC, Jaime y Marco Antonio, que aunque la distancia nos separe espero que sigamos teniendo una amistad duradera. Sois dos amigos de verdad.
- Na que é e sempre será a miña casa, Sarria (Lugo), agradecer a todos e cada un dos amigos de sempre, os do caseto, nomeariavos a todos pero somos unha ducia. Sempre que vou facédesme sentir como que nunca marchei de Sarria, pese a que cada un de nós está nunha parte distinta do mundo, e desexo siga dese xeito por moito tempo. Grazas, sodes únicos. Non podo esquecer agradecer ao meu amigo Alberto Lebón polos ánimos constantes e por estar aí. Moitas grazas, chegarás moi lonxe.
- En Madrid, agradecer enormemente a mis compañeros de piso almerienses durante estos años (Fernando, Joaquín y Chacón), habéis sido un gran apoyo y envidio, no sólo vuestra evidente buena vida, sino vuestra visión y perspectiva de la misma. Siempre me sacáis una sonrisa con vuestros planes. He aprendido mucho de vosotros. Igualmente quiero agradecer a Héctor, ex-compañero de laboratorio de Física, por nuestro reencuentro en Madrid, muchas gracias por

re-aparecer y por el tiempo que hemos pasado por Madrid.

Por supuesto, no puedo expresar mi gratitud suficientemente a todas las mujeres de mi familia, sobre todo a mi madre, mi hermana, mi tía Cristina, y a mis dos abuelas. Sin vosotras no hubiese llegado a donde estoy hoy, a vosotras os debo todo. A mi abuelo José, del cual espero algún día heredar su ética de trabajo. Eres y serás por siempre un ejemplo a seguir. Esta tesis también está dedicada a mi padre Jorge y a mi abuelo Antonio.

A Jimena, gracias por aguantarme durante todo este tiempo conmigo al pie del cañón, sinceramente, sin ti esto no hubiese sido posible. Gracias por tu apoyo cada día durante esta etapa, en la que me has apoyado cuando las cosas se ponían más cuesta arriba, me has ayudado mucho. Eres, y vas a ser, una gran investigadora.

Finalmente agradezco el apoyo económico proporcionado por MINECO/FEDER RTI2018-097195-B-I00 y M-ERA.NET PCIN-2017-106 por su apoyo financiero.

Quiero disculparme ya que probablemente han sido tantas, que alguna pueda haberse quedado en el tintero. Pero su impronta está aquí presente.

Let me tell you the secret
that has led me to my goal;
My strength lies solely in my
tenacity.

LOUIS PASTEUR

Contents

Resumen

Nanoestructuras de óxidos de estaño y titanio y sus composites basados en PEDOT:PSS: aplicaciones en células solares, termoelétricos y sensores de gases

Los semiconductores de *band gap* ancho basados en materiales inorgánicos como el SnO, el SnO_2 o el TiO_2 presentan excelentes propiedades físicas y químicas que los hacen adecuados para diferentes aplicaciones relacionadas con la energía, como las baterías de ion de litio, la detección de gases o las células solares. Su empleo en estas aplicaciones podría verse mejorado con métodos de fabricación controlados así como mediante la introducción de dopantes de manera controlada para modificar su morfología, tamaño o propiedades optoelectrónicas. Además, los materiales orgánicos han suscitado un interés creciente debido a sus excepcionales propiedades, como la flexibilidad, la maleabilidad o el bajo coste. El PEDOT:PSS es un polímero orgánico que posee no sólo conductividad de tipo p, sino también transparencia a la luz visible, propiedades valiosas para las aplicaciones energéticas. La combinación de ambos compuestos inorgánicos/orgánicos que conforman los denominados *composites* híbridos están adquiriendo una atención creciente debido a sus mejoradas propiedades derivadas de la sinergia entre las partes que lo componen, orgánicas e inorgánicas. En esta tesis se muestran y discuten los resultados obtenidos a partir de diversas técnicas de microscopía y espectroscopía en las que se sintetizan tres tipos de óxido semiconductoras diferentes, en forma de nanopartículas y otras estructuras, cada una de las cuales posee propiedades únicas: SnO, SnO_2 y TiO_2, este último en fase anatasa. Cada óxido semiconductor ha sido sintetizado tanto sin dopar como dopado con un elemento ligero, el Li o un dopante de metal de transición, el Ni. En segundo lugar, se obtienen y caracterizan capas delgadas de PEDOT:PSS, así como compuestos que combinan PEDOT:PSS y las nanopartículas, obtenidos mediante la mezcla de dichos elementos y depositados sobre sustratos de silicio tipo n o de vidrio mediante la técnica de *spin coating*. Por último, se analiza la posible aplicación de estos materiales como termoeléctricos, sensores de gas y células solares híbridas de silicio. En particular, los capítulos que componen esta tesis se pueden dividir en:

Capítulo 1: En este capítulo inicial se presenta una breve introducción de los materiales y aplicaciones, así como de los objetivos que se pretenden alcanzar en esta tesis.

Capítulo 2: Se explican brevemente los diferentes métodos de síntesis empleados para la obtención de las nanoparticulas y otras nanoesctructuras además del método para obtener las láminas delgadas, así como la gran variedad de técnicas de caracterización, analizando desde el origen físico hasta el equipamiento específico empleado en este trabajo.

Capítulo 3: Este capítulo se centra en la síntesis y caracterización de nanopartículas de SnO_2, tanto sin dopar como dopadas con Li o Ni mediante hidrólisis. Los efectos debidos a la incorporación de los dopantes se analizan mediante diversas técnicas descritas en el capítulo 2. Finalmente, se ha probado su posible implementación como ánodos en baterías de ion-litio y se ha analizado el efecto del estado de carga del Sn en su rendimiento.

Capítulo 4: Se analizan las nanopartículas de TiO_2 en fase anatasa sin dopar y dopadas con Li o Ni, sintetizadas mediante hidrólisis, en dos concentraciones distintas. El análisis microestructural confirma la alta cristalinidad de las nanopartículas dopadas, así como su reducido tamaño y la presencia del dopante. Se ha profundizado en los efectos del bajo dopado de Li y Ni mediante espectroscopia de fotoelectrones y cálculos de primeros principios basados en Density Functional Theory (DFT). También se ha analizado su aplicación como ánodos en baterías de ion-litio. Por último, se han observado cambios en la transición anatasa-rutilo (ART) inducida térmicamente en las muestras dopadas, que conducen a una ART más rápida. También se ha inducido mediante irradiación con un láser UV.

Capítulo 5: Se estudiaran nanoestructuras y plaquetas de óxido de estaño (II) (SnO), tanto sin dopar como dopadas con Li o Ni, sintetizadas mediante un procedimiento de hidrólisis. Siguiendo este procedimiento, se obtuvieron nanoestructuras de SnO poco oxidadas, entendiéndose esto como una baja presencia de SnO_2 en las mismas. Se ha realizado un estudio sobre la estabilidad de estas estructuras bajo temperatura, tiempo de almacenamiento e irradiación UV. Se han observado diferentes mecanismos de oxidación mediante la irradiación láser, el control de las condiciones de irradiación puede conducir a la creación de distintas regiones oxidadas de manera controlada, conformadas principalmente por SnO_2. Por último, se ha conseguido la creación de un patrón de SnO/SnO_2 a medida, con potencial aplicabilidad en dispositivos optoelectrónicos y de sensado.

Capítulo 6: Se ha analizado el uso de poli(3,4-etilendioxitiofeno)-poli(estireno sulfonato) (PEDOT:PSS) como capa pasivadora de obleas de silicio, con o sin la adición de nanopartículas formando compuestos híbridos, como posible candidato en las células solares híbridas de silicio, creadas mediante *spin coating*. En primer lugar, se analizó el método de deposición de PEDOT:PSS y la estabilidad bajo diferentes condiciones. Se prestó especial atención al estudio de la estabilidad del polímero bajo iluminación láser UV, empleando diversas fuentes láser y filtros, capaces de controlar la energía de irradiación. La capacidad pasivadora de las estructuras ha sido analizado mediante la medida de los tiempos de vida de los portadores de carga sobre la muestra.

Capítulo 7: Se han obtenido láminas delgadas de PEDOT:PSS y sus compuestos a base de etilenglicol, así como las nanopartículas sintetizadas en los capítulos anteriores (SnO, SnO_2 y TiO_2) obtenidas mediante la técnica de *spin coating* sobre sustratos de vidrio. Se han estudiado otras dos aplicaciones: Por un lado su pos-

ible uso como sensores de gases mediante el empleo de distintos gases como analito (etanol, vapor de agua), distintos gases de arrastre y diferentes condiciones de temperatura. Asimismo, se prueban sus propiedades termoeléctricas. Para ello, se diseña y prueba un montaje para medir el coeficiente Seebeck. Para ambas aplicaciones, se encontró que los composites basados en nanopartículas de SnO muestran un mejor comportamiento.

Capítulo 8: En este último capítulo se presentan las principales conclusiones obtenidas durante los capítulos anteriores.

Abstract

Tin and titanium oxide nanostructures and their PEDOT:PSS-based composites: applications in solar cells, thermoelectrics and gas sensors

Wide band gap semiconductors based on inorganic materials such SnO, SnO_2 or TiO_2 present excellent chemical properties which make them suitable for different energy-related application such as Li-ion batteries, gas sensing or solar cells. Their involvement in such applications could be improved with controlled fabrication methods as well as by controlled doping to modify their morphology, size or optoelectronic properties. Besides, organic materials have attracted growing interest due their outstanding unique properties as flexibility, malleability or low cost. PEDOT:PSS is an organic polymer which possesses not only p-type conductivity but also transparency to visible light, valuable properties for energy applications. The combination of both inorganic/organic compounds conforming hybrid composites are dragging attention due to the superior properties derived from the synergy between inorganic/organic counterparts. In this thesis, obtained results based on diverse microscopy and spectroscopy techniques are shown and discussed in which three different semiconductor oxide nanoparticles are synthesized, each of which possesses unique properties: SnO, SnO_2 and anatase TiO_2 both undoped and doped with a light element, Li or a transition metal dopant, Ni. Secondly, PEDOT:PSS thin layers are assembled and characterized as well as composites combining PEDOT:PSS and the nanoparticles, assembled by mixing the aforementioned elements and deposited over either n-type silicon or glass substrates, using the technique of spin coating. Finally, the possible application of these materials as thermoelectric, gas sensors and hybrid silicon solar cells are analyzed.

Chapter 1: A brief introduction of the materials and applications as well of the objectives to be achieved in this thesis are presented in this initial chapter.

Chapter 2: The different synthesis methods employed in this thesis as well as the wide variety of characterization techniques are briefly explained, from the undergoing physical origin to the specific equipment employed in this work.

Chapter 3: This chapter is focused on the synthesis and characterization of SnO_2 nanoparticles, both undoped and Li or Ni doped via hydrolysis. Effects due to the incorporation of the dopants are analyzed by means of electron microscopy, X-Ray diffraction, photoluminescence, Raman spectroscopy and some other techniques described in chapter 2. X-Ray photoelectron spectroscopy techniques have been also used in the analysis of the samples. Finally, their possible implementation as anodes in Li-ion batteries has been tested and the effect on the Sn charge state on their performance has been analyzed.

Chapter 4: Anatase TiO_2 nanoparticles undoped or doped either with Li or Ni synthesized via hydrolysis, in two different concentrations are analyzed by means of the techniques aforementioned described. X-ray absorption spectroscopy shows subtle changes which are attributed to the dopant presence. Their implementation as anodes in Li-ion batteries has been also analyzed. Finally, changes in the thermally induced anatase-to-rutile transition (ART) have been also observed in the doped samples, leading to a dopant-promoted faster ART which occurs at lower temperature. The same transition has been triggered induced by UV-laser irradiation.

Chapter 5: Tin(II) oxide (SnO) nanostructures and platelets both undoped and Li or Ni doped, synthesized via an hydrolysis procedure, are characterized. Following this procedure, low oxidized SnO nanostructures have been obtained, as low presence of SnO_2 is observed, even after months of the synthesis procedure. A study on the stability of this structures under temperature, storage time and UV irradiation has been realized. Different oxidation mechanism have been observed via laser irradiation, as the control on the irradiation conditions led to different-controlled oxidized regions, mostly conformed by SnO_2. Finally, a tailored spatial SnO/SnO_2 micropatterning has been achieved by controlled laser irradiation with potential applicability in optoelectronics and sensing devices.

Chapter 6: Poly(3,4-ethylenedioxythiophene)-poly(styrenesulfonate) (PEDOT:PSS) has been used as a passivation layer of silicon, with or without the addition of nanoparticles forming hybrid composites, has been analyzed as a possible candidate in hybrid silicon solar cells. The thin layers have been assembled via spin coating, by spreading the composite mixture over glass or n-type silicon substrates. Firstly, PEDOT:PSS deposition method, performance and stability under different substrate pre- or post-treatments has been analyzed. Special attention has been given to the study of the stability of the polymer under laser illumination, for which different laser sources and neutral filters have been employed.

Chapter 7: PEDOT:PSS and its based composites based on ethylene glycol as well as the nanoparticles synthesized on the previous chapters (SnO, SnO_2 and TiO_2) have been assembled by spin coating over glass substrates. Two other applications have been studied for these materials and are discussed in this chapter: On one hand its possible use as gas sensors are tested with variable gas analyte (ethanol, water vapor) as well as different conditions of temperature. On the other hand, the thermoelectric properties of PEDOT:PSS based composites are tested. To achieve this goal, a setup to measure Seebeck coefficient has been designed and tested. For both applications, it has been observed that composites based on SnO nanoparticles show improved behavior.

Chapter 8: In this last chapter, the main conclusions obtained during the previous chapters are presented.

List of Figures

List of Tables

Acronyms

AFM Atomic Force Microscopy. 40
ART Anatase to Rutile phase Transition. 6, 107, 114, 126, 239

BF Bright Field. 30
BFP Back-Focal Plane. 31
BSE BackScattered Electrons. 26

CaB Carbon Black. 67
CB Conduction Band. 29
CCD Charge-Coupled Device. 31, 56
CIE Commission Internationale de l'Eclairage. 148
CIS Constant Initial State. 123
CL Cathodoluminescence. 29
CTM Charge Transfer Multiplet. 76
CVD Chemical Vapor Deposition. 69, 114, 191

DEC DiEthyl Carbonate. 67, 113
DEG DiEthylene Glycol. 191
DF Dark Field. 30
DFT Density Functional Theory. II
DMSO Dimethyl Sulfoxide. 9, 11, 20, 165, 169, 191
DOS Density Of States. 75, 239
DP Diffraction Patterns. 31
DS Doublet Separation. 74, 119
DSSC Dye-sensitized Solar Cell. 1

EC Ethylene Carbonate. 67, 113
EDS Energy Dispersive X-Ray Spectroscopy. 28
E-T Everhart-Thornley. 27
EG Ethylene Glycol. 9, 11, 20, 165, 169, 191

FEC FluoroEthylene Carbonate. 67, 113
FFT Fast Fourier Transform. 136
FoM Figure of Merit. 198, 242
FWHM Full Width at Half Maximum. 26, 71, 134

GIWAXS Grazing Incidence Wide-Angle X-ray Scattering. 224
G-L Gauss-Lorentz. 121
GO Graphene Oxide. 11, 195, 234
GQDs Graphene Quantum Dot(s). 234

HTL Hole Transport Layer. 8, 190

ICP-OES Induced Coupled Plasma-Optical Emission Spectroscopy. 32
ICSD Inorganic Crystal Structure Database (file). 49
IDT Interdigital Trasducer. 230, 244
IPA IsoPropyl Alcohol (2-propanol). 31
IR Infrared. 29
ITC Intelligent Temperature Control. 34
ITO Indium-Tin-Oxide. 1, 8

LiBs Lithium-ion Batteries. 4, 69, 80, 151

MFC Mass Flow Controller. 210

MOs Metal Oxide semiconductors. 158, 223

NIR Near-InfraRed. 42
NW NanoWire. 233

PAA Poly(Acrylic Acid). 67, 113
PECVD Plasma-Enhanced Chemical Vapor Deposition. 190
PES PolyEtherSulfone. 166
PeSC Perovskite Solar Cells. 8, 114, 190
PF Power Factor. 217, 220, 222, 244
PL Photoluminescence. 32
PLD Pulsed Laser Deposition. 114
PL-QSSPC Photoluminescence based on Quasi-Steady State Photoconductance. 36
PLE Photoluminescence Excitation. 33
PMT PhotoMulTiplier. 27, 34
ppm parts-per million. 209, 244
PSC Polymer Solar Cells. 8, 190
PVD Plasma Vapor Deposition. 191

rGO reduced-Graphene Oxide. 11, 195, 234
rms root-mean-square. 41
RPES Resonant PhotoEmission Spectroscopy. 66
RT Room Temperature. 30, 56, 58, 72

SAED Selected Area (Electron) Diffraction. 31, 32
SE Secondary Electrons. 26
SEI Solid Electrolyte Interphase. 77
SEM Scanning Electron Microscope. 26
SRH Shockley–Read–Hall. 189
SRV Surface recombination Velocity. 189
STE Self-Trapped Excitons. 92
STH Self-Trapped Holes. 57
SWNT Single-Walled Carbon Nanotubes. 234

TCO Transparent Conducting Oxides. 1
TE Thermoelectric (material). 2, 22, 222, 223
TEM Transmission Electron Microscope. 30
TEY Total Electron Yield. 39, 40, 64

UHV Ultra-High Vacuum. 38
UV Ultraviolet. 29

VB Valence Band. 29, 74
VIS Visible. 35

WBS Wide Band(gap) Semiconductors. 1, 2, 7

XAS X-Ray Absorption Spectroscopy. 39
XPS X-Ray Photoelectron Spectroscopy. 37
XRD X-Ray Diffraction. 25

ZT Figure of Merit (thermoelectric). 9, 222

List of Publications

Publications Related to This Thesis

A. Journal Articles

1. **Unraveling the role of Lithium and Nickel doping on the defect structure and phase transition of anatase TiO_2 nanoparticles**
   A. Vázquez-López, D. Maestre, R. Martínez-Casado, J. Ramírez-Castellanos, I. Píš, S. Nappini and A. Cremades, *Submitted*.

2. **Hybrid materials and nanoparticles for hybrid silicon solar cells and Li-ion batteries**
   A. Vázquez-López, M. García-Carrión, E. Hall, A. Yaseen, I. Kalafat, M. Taeño, J. Zhu, X. Zhang, E. Arici, O. Suat Taskin, D. Maestre, E. Nogales, P. Hidalgo, J. Ramírez-Castellanos, B. Méndez, N. Yuca, S. Karazhanov, E. S. Marstein and A. Cremades, *Journal of Energy and Power Technology*, **2021**, 3, 2; doi:10.21926/jept.2102020.

3. **In situ local oxidation of SnO induced by laser irradiation: A stability study**
   A. Vázquez-López, D. Maestre, J. Ramírez-Castellanos, A. Cremades, *Nanomaterials*, **2021**, 11, 4, 976; doi:10.3390/nano11040976.

4. **Influence of doping and controlled Sn charge state on the structural stability and performance of SnO_2 nanoparticles as anodes in Li-ion batteries**
   A. Vázquez-López, D. Maestre, J. Ramírez-Castellanos, J. M. González-Calbet, I. Píš, S. Nappini, N. Yuca, A. Cremades, *J. Phys. Chem. C*, **2020**, 124, 34, 18490–18501; doi:10.1021/acs.jpcc.0c06318.

5. **Improved Silicon surface passivation by hybrid composites formed by PEDOT:PSS with anatase TiO_2 nanoparticles**
   A. Vázquez-López, A. Yaseen, D. Maestre, J. Ramírez-Castellanos, S. Zh. Karazhanov, E. S. Marstein and A. Cremades, *Materials Letters*, **2020**, 271, 127802; doi:10.1016/j.matlet.2020.127802.

6. **Synergetic Improvement of Stability and Conductivity of Hybrid Composites formed by PEDOT:PSS and SnO Nanoparticles**

A. Vázquez-López, A. Yaseen, D. Maestre, J. Ramírez-Castellanos, E. S. Marstein, S. Zh. Karazhanov, and A. Cremades, *Molecules*, **2020**, 25, 695; doi:10.3390/molecules25030695.

B. Book Chapter(s)

1. **Low-Dimensional Structures of In_2O_3, SnO_2 and TiO_2 with Applications of Technological Interest**
   J. Bartolomé, M. Taeño, A. Vázquez-López, F. del Prado, M. García-Tecedor, G C. Vásquez, J. Ramírez-Castellanos, A. Cremades, D. Maestre, *Oxide-Based Materials and Structures*, CRC Press, **2020**, 99-136; ISBN:9780429286728.

C. Congress Proceedings

1. **Synthesis of low dimensional oxide based complex materials by a vapor-solid method**
   J. García-Alonso, D. Maestre, J. Bartolomé, M. García-Tecedor, A. Vázquez-López, M. Taeño, F. del Prado, E. Nogales, A. Cremades, *Proceedings Volume 11687, Oxide-based Materials and Devices XII*, **2021**, 116871X; doi:10.1117/12.2591251.

Chapter 1. Introduction

During the last decades, semiconductor oxides have been attracting increasing interest as novel nanomaterials on both the scientific literature and on the technological field of research. Among the wide variety of materials considered as semiconductor oxides, we could highlight the group known as Wide Band(gap) Semiconductors (WBS) such as TiO_2, SnO_2, Ga_2O_3, ZnO or In_2O_3, which found application in fields as electronic,[1] optoelectronic (in photovoltaics and LEDs), photocatalysis,[2] electrochromism,[3] batteries[4] or gas sensing devices[5]. These oxides possess certain advantages exhibiting exotic optoelectronic properties with high optical transparency and electrical conductivity, stability and low toxicity which arise interest for their study by the scientific community. Although they inherently possess a wide band gap, the combination of native defects, in many cases oxygen vacancies and oxygen-related defects, creates donor levels near the conduction band contributing with a high electron concentration, which is the reason attributed to their intrinsic n-type behavior. This n-type behavior is presented for mostly of them, such as SnO_2 or TiO_2 while a few others, such as SnO, presents p-type behavior.

On one hand, and since the discovery of the photototalytic splitting of water under UV light, TiO_2 has been established as the main photocatalytic material[6,7]. As well, with the discovery by Gräztel et al. of the Dye-sensitized Solar Cell (DSSC), which generated photocurrent via the injection from the excited dye molecules into the WBS metal oxide,[8] its implementation on photovoltaic applications have been growing non-stop. In addition, TiO_2 is commonly employed in a variety of other fields such as hydrogen storage,[9] Li-ion batteries[10,11] and supercapacitors[12] to many other non-energy related applications ranging from pigments to sunscreen[8]. Regarding currently environmental concerns, TiO_2 has been considered as a non-toxic sustainable material[13]. On the other hand, SnO_2 is one of the most common Transparent Conducting Oxides (TCO) which, due to its high electrical conductivity and transparency to visible light, became a fundamental material in optoelectronic applications nowadays being part of solar cells or displays. Among the materials used as TCO, currently Indium-Tin-Oxide (ITO) composed by Indium and Tin is the most widely used as it is non-toxic as compared with the

previous technologies involving CdO. The application of SnO_2 covers also a wide range from Li-ion batteries to gas sensors[14–16].

Unlike to SnO_2 or TiO_2, SnO has not been as well-studied mainly due to its metastability as SnO tends to oxidize to the most stable SnO_2 rutile-like structure. SnO is one of the few p-type semicondutor oxides, group that shares with a few oxides such as NiO or CuO[17,18]. In the last lustrum, increasing attention has been focused on this material as it demonstrates potential applicability as anode for Li- or Na-ion batteries[19,20].

To pursuit certain applications, it would be useful to be able to modify certain properties of a WBS. This is possible by modifying its morphology, controlling its size[8] which increases the surface-volume ratio, its crystalline phase or even adding dopants[12]. Among these materials, it is fair to say that TiO_2 and SnO_2 have been the most investigated materials in the area of energy and environmental applications. Nevertheless, there is still room for improvement in that field of research. Besides, some challenging issues are yet to overcome in order to improve and broaden the range of applications of these versatile oxide materials. In this thesis it has been studied the effect of doping by introducing two different elements: a light metal (Li) and a transition metal (Ni). The effects of the size of the nanoparticles on several applications has been studied as well.

In the recent years, research has been also focused on nanostructured materials composed by organic materials or bio-inspired materials. It can not be omitted that the scientific world has observed the potential of organic materials which are present in different materials fields and allows to develop light and flexible devices as well as reducing cost offering an eco-friendly approach. The actual state of art of photovoltaics is dominated by organic materials research[21]. In this novel generation, the combination inorganic-organic are currently showing notable advances[22]. Hybrid composites combining organic and inorganic materials have recently become of great interest in fields such as sensors[23] or microelectronic devices, based on the synergy between their counterparts which can lead to the development of flexible, low-cost, and scalable devices with good stability and tunable electrical and optical properties. Due to their outstanding properties, in these hybrid composites, the organic material is often a conductive polymer, as in this thesis.

In particular, poly(3,4-ethylene-dioxythiophene) -poly(styrenesulfonate) (PEDOT:PSS) is one of the most successful conducting polymers due to the simplicity to obtain films as well as its optical transparency and tuneable electronic properties. PEDOT:PSS has been used in photovoltaic applications,[24] energy conversion and storage[25] and most notably as Thermoelectric (material) (TE)[26]. However, limiting factors such as low electrical conductivity in its pristine form and stability of the pristine material remain unsolved for achieving long-lasting devices. The addition of dopants such as organic solvents, metallic nanoparticles or even addition of other inorganic materials allows to obtain new functionalities and improves the performance[27] in technologies such as hybrid silicon solar cells[28].

In the following section, the most relevant properties of SnO, SnO_2 or TiO_2

as well as PEDOT:PSS will be described. The interest of their study from the standpoint of their applications will be highlighted. To conclude this chapter, the objectives and the thesis structure will be presented and discussed.

1.1. Tin dioxide, SnO_2, rutile

Tin dioxide, (tin(IV) oxide, stannic oxide) SnO_2, is a wide-band gap n-type semiconductor, with a band gap value of $E_{GAP} \sim 3.6$ eV at room temperature. In nature, it is often found as a mineral called *cassiterite* which crystallographic structure is known as *rutile* (space group $P4_2/mnm$). Rutile possesses tetragonal symmetry with lattice parameters of $a = b = 4.738$ Å, $c = 3.186$ Å , with a center Sn atom surrounded by an O octahedron with the oxygen atoms at the corners. These octahedron are slightly distorted. The space group D_{4h} possesses a 6 atoms unit cell with two Sn ions are placed at positions $(0, 0, 0)$ and $\left(\frac{1}{2}, \frac{1}{2}, \frac{1}{2}\right)$ while four O ions are placed at $\pm\,(u, u, 0)$ and $\pm\left(\frac{1}{2} + u, \frac{1}{2} - u, \frac{1}{2}\right)$. Consequently, there are $3N = 18$ vibrational lattice modes at the Γ point of the Brillouin Zone[29]. In Fig.1.1(a)-(b) both the unit cell of SnO_2 and the previously mentioned octahedron are shown.

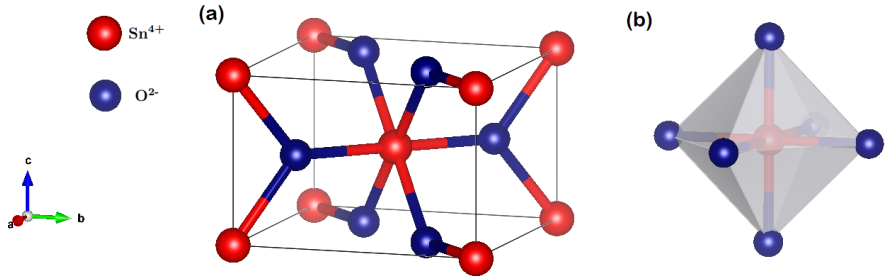

Fig. 1.1: (a) Rutile SnO_2 unit cell (b) SnO_6 octahedron.*

* images represented with VESTA(Visualization for Electronic and Structural Analysis, v.3.4.7) software.

Among SnO_2 properties, some of the most notable ones are shown in Table 1.1. By general means, SnO_2 is considered to possess high transparency in the visible range as well as great electronic conductivity. These properties, in addition to its good chemical stability are the main reasons behind its success on a wide variety of applications. Highlighted applications are described below:

- **Gas sensor:** The action of a different gas atmosphere over the SnO_2 surface affects the charge transfer processes. These changes can be observed by measuring the resistance on the sample under variable atmospheres. SnO_2 has been generally used as gas sensor to detect the presence of different gases such as NO_x, CO or NH_3[14].

Table 1.1: Some properties of Romarchite SnO and Cassiterite SnO_2. Information extracted from different sources[18,30,31].

	SnO	**SnO_2**
	Tin(II) oxide	Tin(IV) oxide
Mineral name	**Romarchite**	**Cassiterite**
Crystal system	Tetragonal	Tetragonal
Schöenflies notation	D_{4h}^{7}	D_{4h}^{14}
Space group	$P4/nmm$	$P4_2/mnm$
Group number	129	136
Density, ρ, ($g \cdot cm^{-3}$)	5.94-6.45	6.61-6.99
Melting point, ($^{\circ}C$)	1080	1650
E_{GAP} **(300 K), (eV)**	Direct: ∼2.5-3.4 Indirect: ∼0.7	Direct, ∼3.6
Refractive index, n	1.9-2.4	1.9-2.18
Electron mobility, μ_e, ($cm^2V^{-1}s^{-1}$)	2.4-18.71	6.26
Dielectric constant, ϵ	7.25-7.8	2.5-3.9
Bulk modulus, K(GPa)	44	176
Semiconductor type	p-type	n-type

- **Li-ion batteries:** SnO_2 possesses a high theoretical specific capacity (∼ 790 $mAhg^{-1}$), much higher than graphite (∼ 370 $mAhg^{-1}$), the most common anode material in current Lithium-ion Batteries (LiBs). However this would produce a large volume expansion with its subsequent huge internal stress which could limit the use of SnO_2 in this technology[15,16]. Hence, challenges should be faced to improve the performance of SnO_2 based LiBs.

1.2. Tin oxide, SnO, romarchite

On the other hand, tin monoxide, (tin(II) oxide , stannous oxide) (SnO, Sn^{2+}) romarchite, possesses p-type conductivity and often exhibits a layered structure with tetragonal space group $P4/nmm$ and with lattice parameters $a = b = 3.803$ Å and $c = 4.838$ Å . It exhibits a litharge-like structure with a variable optical bandgap, with a direct transition ranging between $\sim 2.5 - 3.4$ eV at room temperature, and an indirect transition at ~ 0.7 eV[32]. Therefore, this material with its layered structure offers a good host matrix for ion intercalation. Fig.1.2(a)-(b) shows both the unit cell of SnO and its layered structure. Some of the most notable properties of SnO have been summarized in Table 1.1.

SnO phase is rather metastable as it is easily oxidized to SnO_2 which has resulted in fewer works dealing with SnO as compared with SnO_2. Most of the works deal with SnO thin layers or non-stoichiometric SnO_x layers[18] due to the difficulty to unambiguously attribute one oxidation state to SnO, thus very limited knowledge about this material is present on the scientific literature, despite its promising use in diverse applications. Due to this natural oxidation transition, applications based on SnO/SnO_2 structures are commonly followed rather than pure SnO, which is particularly useful as each oxide possesses different conductivity behavior (n-type

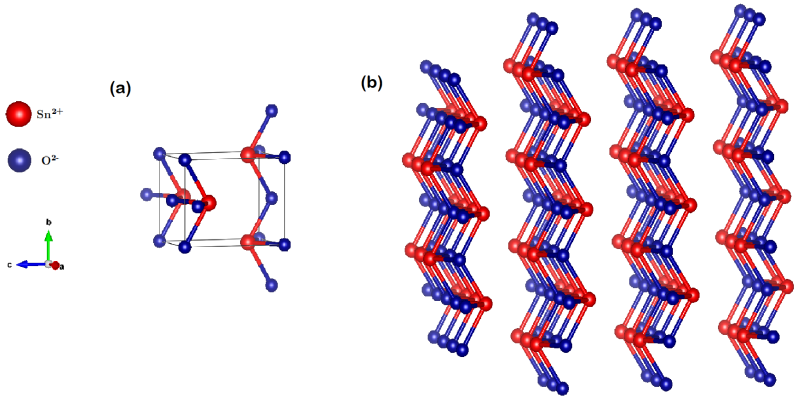

Fig. 1.2: (a) Romarchite SnO unit cell and (b) its layered structure represented by a 3x3x3 supercell.

for SnO_2 or p-type for SnO).

- **Gas sensor:** The interaction between different gas atmosphere particles over the SnO surface can affect the charge transfer processes. These changes can be observed as the resistance measured on the sample changes under the presence of different gas analytes. SnO has been used as gas sensor to detect the presence of different gases such as NO_2, H_2 or acetone[33–35].

- **Thermoelectric material:** It has been reported that SnO might be a potential candidate as thermoelectric due its band structure. Moreover, it would be an attractive thermoelectric material with the added value of its low toxicity[31].

- **Li- or Na-ion batteries:** Due to its different morphology depending on the synthesis condition and its layered structure it could accommodate without major volumetric expansion Na^+ or Li^+ ions. In this regard, it has been proposed as a possible anode for batteries, competing with SnO_2[36].

1.3. Titanium dioxide, TiO_2, anatase

TiO_2 (titanium dioxide, titania), is an n-type wide band gap semiconductor. It is known to crystallize in three main different structures, one stable *rutile* (tetragonal, $D_{4h}^{14} - P4_2/mnm$), and two metastable *anatase* (tetragonal, $D_{4h}^{19} - I4_1/amd$) and *brookite* (orthorhombic, *Pbca*)[33]. TiO_2 undergoes phase transitions with increasing temperature, which are irreversible. The main studied phases are anatase and rutile, as anatase is present until reaching temperatures 700°C, where rutile becomes dominant. Dopant inclusion can modify the temperatures ranges

in order to obtain rutile from anatase following a well-known transition, the as-called Anatase to Rutile phase Transition (ART). In this thesis, only the anatase phase will be studied. Anatase phase possesses one Ti atom surrounded by 6 Oxygen atoms conforming TiO_6 octahedron slightly distorted with two apical bond lengths $D_0 = 1.979 - 1.966$ Å greater than the other four basal bond lengths $d_0 = 1.932 - 1.937$ Å [9,37]. The space group $I4_1/amd$ possesses 12 atoms unit cell with Ti atoms located at $\left(0, \frac{1}{4}, \frac{3}{8}\right)$ and $\left(0, \frac{3}{4}, \frac{5}{8}\right)$ and O atoms located at $\left(0, \frac{1}{4}, z\right)$, $\left(0, \frac{1}{4}, 1-z\right)$, $\left(0, \frac{1}{4}, \frac{1}{4}-z\right)$ and $\left(0, \frac{1}{4}, z-\frac{1}{4}\right)$ for internal coordinate z[38]. Anatase structure as well as the TiO_6 octahedron are shown in Fig.1.3.

Anatase n-type behavior is mostly due to the presence of defects and impurities as well as high concentration of oxygen vacancies which is similar for rutile, where there is a high presence of Ti^{3+}. However, there are differences between anatase an rutile mostly due to their different band and electronic structure. Physical properties of the different TiO_2 phases are summarized on Table 1.2. Anatase band gap is slightly higher than rutile at 300K, and this phase shows lower refraction index while its superior electron mobility is interesting for optoelectronic properties. A few of its applications are described below:

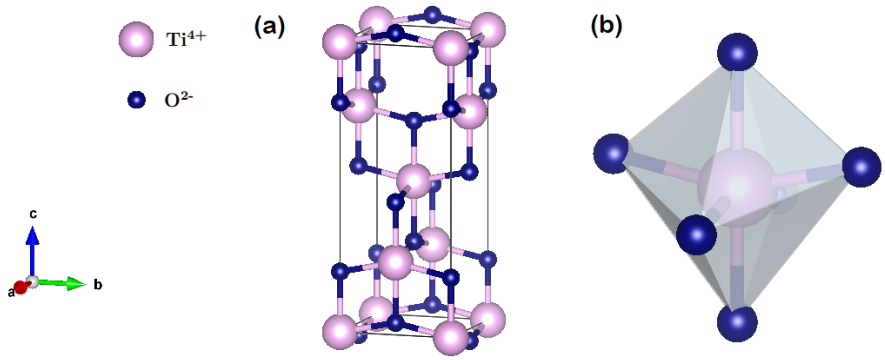

Fig. 1.3: (a) Anatase TiO_2 unit cell (b) TiO_6 octahedron.

- **Li-ion batteries:** Despite its low specific capacity and electrical conductivity, TiO_2 based anodes presents outstanding stability over time[10] which together with its structural stability, low cost and low toxicity, places TiO_2 as a potential candidate regarding long-lasting LiBs.

- **Photocatalyst:** Over the last 40 years TiO_2 has been established as the most well-known and prime of choice photocatalyst due to its absorption edge which can be excited with UV light[40]. Via its photocatalitic activity, TiO_2 applications are vast. As a few examples TiO_2 could be used to decompose harmful organic compounds or to reduce CO_2[41].

Table 1.2: Some properties of Brookite, Anatase and Rutile TiO_2. Information extracted from different sources[33,39]

TiO_2			
Titanium(IV) oxide			
Mineral name	**Brookite**	**Anatase**	**Rutile**
Crystal system	Orthorhombic	Tetragonal	Tetragonal
Schöenflies notation	D_{2h}^{15}	D_{4h}^{19}	D_{4h}^{14}
Group number	61	141	136
Space group	Pbca	$I4_1/amd$	$P4_2/mnm$
Density, ρ, $(g \cdot cm^{-3})$	4.11	3.89	4.25
Melting point, $(^{\circ}C)$	-	-	1840
E_{GAP} **(300 K), (eV)**	$\sim 3.0 - 3.6$ eV	Indirect; ~ 3.2 eV	Direct; ~ 3.05 eV
Refractive index, n	2.61-2.63	2.52-2.53	2.8-2.9
Electron mobility, μ_e, $(cm^2V^{-1}s^{-1})$		4-20	0.1-1
Dielectric constant, ϵ	14 - 110	10-30	9-89.8
Bulk modulus, K**(GPa)**	191	188	206
Solubility in HF	-	Soluble	Insoluble
Semiconductor type	n-type	n-type	n-type
a(Å)	5.456	3.784	4.580
b(Å)	9.182	3.784	4.580
c(Å)	5.143	9.515	2.950

1.4. Doped TiO_2, SnO_2 and SnO

One of the main objectives over the last decade with the use of WBS in optoelectronics has been the absorption edge shifting and band engineering aiming for a higher response on the visible spectra. The introduction of certain defects or controlled impurities, such as dopants, has been one of the main methods, as the presence of those defects could create mid-gap states as well as reduce the band gap. Similarly, the charge carrier separation as well as conductivity could be enhanced[39].

SnO_2 and TiO_2 have been doped with a variety of elements over the last years. SnO_2 has been doped with rare earths[42,43] or transition metal dopants (Fe,[15] or Co[44]) showing differences on their optical properties. A particular attention has been focused on the study of Sb-doped SnO_2[43,45,46] which exhibits different electrochemical properties due to enhanced charge carrier concentration. Among binary oxides, TiO_2 has been probably the one doped with the biggest elements variety. To name a few, it has been doped with transition metals (Cr,[47] Co[48] or Fe[49]) and with light metals (B, Na[39]) which often shifted its absorption edge and modified its optoelectronic properties.

In this thesis we have selected two different dopants, a light metal (Li) and a transition metal (Ni). Both dopants have not been as widely studied so far and some aspects regarding the doping-mediated variation of the structure of defects and the resulting optoelectronic properties still should be addressed. Authors such as Srivastava et al.[50] have shown interest on the use of Li-doped SnO_2 as gas sensor in form of thin films, while other authors have studied the effect of Li-doping on micro tubular tin oxide structures[51]. Simulations have shown interest on the use

or Li and the different positions that it can occupy in the oxide lattice, as interstitial or substitutional[52]. Ni has been used as a co-dopant with other transition metals such as Fe,[53] while bare Ni doping has shown a band gap narrowing[53,54]. Likewise, Li- and Ni- TiO_2 have been less investigated, particularly for the anatase TiO_2 phase. Nonetheless, recent reports show that Li or Ni-doped TiO_2 exhibits superior photocatalitc activity under visible light[40,55] as well as being regarded as phase transformation promoters to rutile from anatase[39]. Doped SnO is understudied in comparison with its doped allotrope, SnO_2. On top of SnO metastability, the creation of such doped structures is difficult, mainly because the use of high temperatures, oxidation atmospheres or other synthesis proceedings which could enhance SnO_2 formation. Reports on doped SnO had been focusing on the study mostly of its possible magnetic properties via Fe[56] or Mn doping[57].

1.5. PEDOT:PSS

In 1977, H. Shirakawa, A.G. MacDiarmid and A.J. Heeger discovered that oxidation with chlorine, bromine or iodine vapour made polyacetylene (PA) films 10^9 times more conductive than they were originally[58], which is regarded as the first organic conductive polymer. For this discovery, in the year 2000 they were awarded the Nobel Prize in Chemistry. Since then, the development and discovery of different conductive polymers, which easily found use on electronic devices, has grown exponentially due to their exploitable properties: mechanical flexibility, easy-processability and light-weight. Organic polymers properties are potentially modifiable as being composed by polymer chains which under doping conditions can change its chemical properties and structure. A promising finding in this area was the discovery of poly(3,4-ethylene-dioxythiophene) (PEDOT) which conductivity could reach 600 $S{\cdot}cm^{-1}$ with high transparency to visible light. Its main drawback was its insolubility in water which hinders any manufacturing process. This was overcome by polymerizing it with another water soluble polyelectrolyte, poly(styrenesulfonate) (PSS). The short insoluble PEDOT chain is adhered to the water-soluble PSS long chain by coulombic interaction which dispersed the polymer in water. The combination of Poly(3,4-ethylene-dioxythiophene) doped with poly(styrenesulfonate) is referred as PEDOT:PSS, which structure is shown on Fig.1.4(a).

PEDOT:PSS has been extensively used in organic electro-optical devices mainly due to its transparency in the visible range ($\sim$ 90% between 400-700 nm) and good p-type electrical conductivity, superior carrier mobility and large work function (5-5.2 eV)[59]. In photovoltaics it is employed as different counterparts, traditionally it has been used as a hole injection and transport layer in organic light-emitting diodes or organic solar cells. It is in fact still a popular choice as Hole Transport Layer (HTL) in Perovskite Solar Cells (PeSC)[60]. It has been also employed as a transparent conductive oxide, replacing traditional ITO as both top or bottom electrode in a variety of Polymer Solar Cells (PSC)[24]. Since 2012,[61] PEDOT:PSS has been also used as front contact for silicon heterojuntion solar cells. From that moment

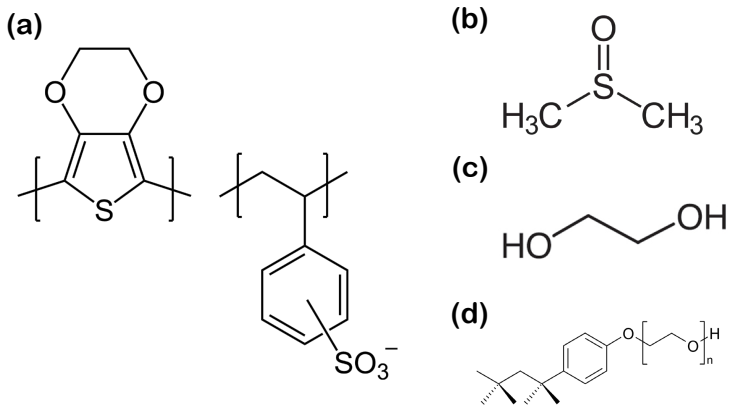

Fig. 1.4: Chemical structures of the different organic compounds used in this thesis (a) PEDOT:PSS, (b) DMSO (c) EG and (d) Triton X-100.

on, many different approaches have been suggested for improving its performance either implementing an inorganic interlayer or adding different compounds[62]. PEDOT:PSS is also a promising organic thermoelectric material due to its advantages of good thermoelectric properties (Figure of Merit (thermoelectric) (ZT) as high as ~ 0.42), low thermal conductivity, flexibility and non-toxicity compared with the traditional inorganic thermoelectric materials[63,64]. Other remarkable applications of PEDOT:PSS range from Li-ion batteries[65] or organic electrochemical transistors[66].

However, PEDOT:PSS shows a relatively low conductivity in its pristine form diluted in water, typically in the range of 0.1-1 $S{\cdot}cm^{-1}$ attributed to the water soluble/insulator PSS chains. Electrical conductivity could be enhanced with the addition of different elements which is referred as *secondary doping*[i] such as sorbitol, glycerol, or polar solvents including Dimethyl Sulfoxide (DMSO),[68] Ethylene Glycol (EG) (their chemical structures are shown in Fig.1.4(b)-(c)), and dimethylformamide (DMF), among others[26]. Such additives can improve the PEDOT:PSS conductivity up to three orders of magnitude, mainly due to changes on the PEDOT:PSS chain structure configuration. This secondary doping approach has been the most common method to enhance electrical response since the 2000s[63]. However, this is not the unique approach, other methods such post-treatment via immersion on the same polar solvents, the use of surfactants or the use of acids have shown improvement on either the surface structure or the electrical conductivity, which eventually led to optimized sheet resistance[26]. Among the different surfactants, Triton X-100, which is a non-ionic surfactant polymer of polyethylene glycol

[i]The acceptation of *secondary doping* is given as *primarily doping* is referred to doping on the previous step i.e. when PEDOT was prepared, commonlyvia oxidative or electrochemical polymerization of EDOT-based monomers[67]. Also note that the term *doping* is used in the same context sense that in semiconductor physics and this acceptation is widely accepted in polymer science.

and p-t-octylophenol with chemical formula t-Oct-C_6H_4-$(OCH_2CH_2)_xOH$ where x= 9-10, has also been utilized to increase PEDOT:PSS films conductivity by stabilizing PEDOT nanosized particles[69]. Triton X-100 chemical structure is shown in Fig.1.4(d).
In summary, PEDOT:PSS can be easily spin coated onto surfaces creating very thin layers of this material which not only are transparent to visible light, but they also show relative high conductivity necessary for high performance energy devices.

Unfortunately, one major issue that organic polymers faces is degradation. Organic polymers are sensitive to many factors which they may undergo during their usage time. For instance, as part of a solar cell device it would face adverse atmosphere conditions such high gas concentrations, humidity, reaching intense temperatures ($> 70°C$ on the cell device) and continuous UV-C irradiation. All these factors will affect its performance as well as decrease its total lifetime expectancy. Scientific literature has not focused extensively on this issue rather than searching for record efficiency values, which we would discuss on the following chapters. Some works indeed have been tested the viability of using these organic compounds over long irradiation times[70] or high temperatures as well as variable atmospheres[71] showing the importance of this topic.

PEDOT:PSS aqueous dispersion is commercially available and preferred over synthesized PEDOT:PSS, as the commercially-available PEDOT:PSS has some quality standards which assure electrochemical homogeneity on the obtained product. It was firstly commercialized under the trade name of Baytron® by Bayer AG, then by H. C. Starck, and currently by Heraeus under the trade name of Clevios™[25]. Depending on the PEDOT:PSS ratio among other factors, PEDOT:PSS could be less conductive such as the Sigma-Aldrich-739324 or Clevios M121 AI 4083 which is useful for hole transport layers while higher conductive grades, including Clevios PH500 or PH1000, are fundamental to create highly conductive electrodes[60]. Two different purchased PEDOT:PSS have been used in this thesis and its main characteristics are summarized in Table 1.3. It should be highlighted again that both PEDOT:PSS possess some different properties, mostly related to high or low pristine conductivity, respectively, for Ossila (Clevios) or Sigma-Aldrich.

- In chapter 6, the Ossila (Clevios) PEDOT:PSS (labeled as M122 by the manufacturer), was used to produce the results concerning a 3-month internship at the Institute for Energy Technology (*Institutt for Energiteknikk*, IFE) in Kjeller (Norway). In this chapter, PEDOT:PSS with high conductivity grade will be used as silicon passivation layer in hybrid silicon solar cells.

- In chapter 7, PEDOT:PSS purchased from Sigma-Aldrich (which conductivity was measured and the obtained value was close to $\sigma \sim 0.1$ S·cm^{-1}) will be used and tested as thermoelectric material and chemoresistive gas sensor. For both applications, high conductivity may be counterproductive to observe resistance changes due to a gas analyte or it could decrease Seebeck coefficient, downgrading its thermoelectric performance.

Table 1.3: PEDOT:PSS properties obtained from the data sheets provided by the respective manufacturers . (*) With use of 5% DMSO by volume as a morphology enhancer.

PEDOT:PSS	Poly(3,4-ethylenedioxythiophene)-poly(styrenesulfonate)	
Company	Ossila/Herraeus	Sigma-Aldrich
Product Code	M122 (PH 1000)	739324
pH	1.5 – 2.5 at 25 °C	5-7
Melting/freezing point	0 °C	-
Boiling point/range	100 °C	-
Relative density	1 g·cm^{-3} at 23°C	0.982 g·mL^{-1} at 25 °C
Resistivity	< 0.0012 Ω·cm*	labeled as high-conductivity grade
Sheet Resistance	-	$< 100\Omega/\square$
Solid content	1.0 - 1.3 wt.% (in water)	1.1% in H_2O
Viscosity	< 50 mPa·s	< 100 mPa·s (at 22 °C)
PEDOT:PSS ratio	1:2.5	-
Particle Size Distribution	D_{50} = 30nm	-
Work Function	4.8 - 5.0 eV	-
Refractive index, n	-	n20/D 1.335

Regarding secondary dopants, in this thesis the effect of both DMSO or EG have been studied. Triton X-100 has been also evaluated as a surfactant/dopant for PEDOT:PSS. Table 1.4 summarizes the main properties of these compounds.

Table 1.4: Data sheet of the different secondary dopants used in this thesis .

Reactant	DMSO	EG	Triton X-100
Linear Formula	$(CH_3)_2SO$	$HOCH_2CH_2OH$	$C_8H_{17}C_6H_4(OCH_2CH_2)_nOH$
Molecular weight $g \cdot mol^{-1}$	78.13	62.07	-
pH	-	-	5.0–8.0 at 20 °C
Density, ρ, $(g \cdot mL^{-1})$	1.10	1.113 at 25°C	1.07 at 20°C
Boiling point	189°C	195-198°C	>200°C
Refractive index, n	n20/D 1.479	n20/D 1.431	-
Solubility in H_2O	Miscible	Miscible	Miscible
Company	Sigma-Aldrich	Sigma-Aldrich	Sigma-Aldrich
Assay	99.7%	99.8%	-

1.6. Composites based on PEDOT:PSS

In the previous sections, we have discussed that the use of SnO_2 and other oxides as anodes in Li-ion batteries could presents some drawbacks concerning the volumetric expansion due to the Li intercalation within the atomic planes of SnO_2. These effects could be avoided with the use of hybrid composites. Oxide nanoparticles have been commonly mixed with graphene,[72] Graphene Oxide (GO) or reduced-Graphene Oxide (rGO)[73]. Deng et al.[73] summarized the advantages of using SnO_2/graphene nanocomposites: prevention of SnO_2 agglomeration, buffering the volume change on the charge/discharge process and improved electronic response

of the electrode.
Not only carbonaceous materials can offer a host matrix for MOs nanoparticles also polymeric materials can be used for this purpose. Polymer composites consist of a polymer with embedded nanoparticles or nanofillers dispersed on the polymer matrix. From this time on we will refer to simply as *composites*. PEDOT:PSS-based composites originate a novel field of research which is attracting increased attention in recent years. Initially, searching for enhanced organic solar cell performance, plasmonic active nanoparticles (Au, Ag) were used[74], which have shown enhanced electronic behavior due to the positive charge nature of the nanoparticles which interact with the oppositely charged PEDOT and PSS. However, this field is under explored and fewer research could be found with the use of metal oxide nanoparticles as fillers, neither the study of the conformation of these composites nor their morphological modification and corresponding optoelectronic behavior.

The combination of PEDOT:PSS with MOs such as TiO_2 can lead to improved performance and tunable optoelectronic properties[75], enhanced passivation of silicon surfaces[27] or to an increase of the quantum efficiency in PSC electrodes[76]. These properties motivates the study presented on this thesis.

1.7. Thesis objectives and organization

Herein, the synthesis, characterization and applications of the different materials has been performed. Firstly, undoped SnO, SnO_2 or anatase TiO_2 nanoparticles as well as doped with Li or Ni, have been synthesized via a wet chemical route based on hydrolysis. Secondly, composites based on PEDOT:PSS and the synthesized nanoparticles have been deposited over glass or silicon substrates. Finally, those composites have been tested as possible candidates for chemosensors, hybrid silicon solar cells and thermoelectrics.

After the nanoparticles (and other hierarchical structures) synthesis, an in-depth characterization of their physical and chemical properties has been performed under a variety of techniques. The structural characterization has been performed using X-Ray diffraction (XRD) and Raman spectroscopy in a confocal microscope. Morphology has been analyzed via scanning electron microscopy (SEM) as well as (high resolution) transmission electron microscopy ((HR)TEM) also employing selected area electron diffraction (SAED). Compositional properties of the samples have been analyzed via energy dispersive X-Ray spectroscopy (EDS) inside a SEM chamber as well as employing inductively coupled plasma-optical emission spectrometry (ICP-OES) to detect light elements such as Li. Electronic characterization has been studied in a synchrotron facility via X-ray photoelectron spectroscopy (XPS) both out and on resonance for certain core levels as well as via X-ray absorption spectroscopy (XAS). Optical properties have been studied via photoluminescence (PL) in a confocal microscope using an UV laser or in a photoluminescence spectrometer, using a Xe-lamp on a variety of wavelengths, as well as allowing studying photoluminescence excitation (PLE). Cathodoluminescence has

been measured on a SEM chamber. Electric characterization has been studied with help of Hall effect measuring system. The assembled thin layers have been obtained using a spin-coating technique and the subsequent samples, both with and without the nanoparticles addition, have been also analyzed. In this case, the morphology, topography and structure have been analyzed using an optical microscope, with atomic force microscopy (AFM) in contact mode and with Raman spectroscopy. The composition properties have been also tested with EDS. Optical properties have been measured using with UV-VIS spectroscopy. Electronic properties have been obtained once again by means of x-ray photoelectron spectroscopy (XPS). Electric properties have been analyzed using Hall effect.

The possible use of these thin layers have been also analyzed with different equipments: In order to test their possible use a gas sensors, the films have been tested using a chemiresistive setup with a flow of different test gases (ethanol, water vapor) which also allows to increase the temperature of the device, as thermoelectrics on a home-made setup to measure Seebeck coefficient based on the use of a Keithley 2000 multimeter to measure voltage and a temperature acquisition data card while increasing temperature with two Peltier modules and, finally, as hybrid silicon solar cells testing passivation properties with photoluminescence based on quasi-steady-state photoconductance (PL-QSSPc) and I-V measurements.

The first objective of this thesis has been the procurement of an appropriate method to synthesize the oxide nanoparticles both doped and undoped, with a set of requirements: simplicity, effective dopant addition, small size and possibility to obtain large material quantity, as well as analyzing synthesized powders physical-chemical properties. Li and Ni have been selected as possible dopant candidates based on the scientific literature and the increasing interest on these dopants for energy related applications. Two different dopant concentrations have been used to discern the effects attributed to the variable quantity of dopant. Moreover, the study of Li- or Ni- doped SnO_2 or TiO_2 is less significant in volume of publications than other dopants and, most precisely, in the case of SnO is practically nonexistent, to our knowledge. SnO has been also studied due to its outstanding properties which make this material a candidate for energy related applications. However, its metastability has hindered its study on the scientific literature. This section of the dissertation has been realized under the supervision of Dr. Julio Ramírez-Castellanos, at the Dpt. of Inorganic Chemistry, Faculty of Chemistry, at the Complutense University of Madrid.

The second objective, intimately related to the first one, has been to obtain an exhaustive characterization of the nanoparticles and nanostructures obtained by the synthesis procedure, focusing on their morphological, structural, chemical, electrical, optical and electronic properties by means of a wide variety of microscopies and spectroscopies.

The third objective has been the assembling of thin layers based on PEDOT:PSS

and most precisely, creating thin layers combining the synthesized nano-oxides and the polymer. To accomplish this objective, many different approaches have been tested and the best results are presented.

The fourth objective has been to test the applications of such materials. For that purpose, SnO_2 and TiO_2 have been tested as anodes for Li-ion batteries with collaboration with Dr. Neslihan Yuca from Enwair Energy Tech., Istanbul, Turkey. PEDOT:PSS and based composites have been tested as possible gas sensors, in this case thanks to the gas-sensing equipment designed by Dr. Javier Bartolomé from the group of Physics of Electronic Nanomaterials (Finegroup), Dpt. of Materials Physics at the University Complutense of Madrid. As part of a brief 3-month internship at the Institute for Energy Technology (*Institutt for Energiteknikk*, IFE) in Kjeller (Norway) under the supervision of Dr. Smagul Karazhanov, the possible use of the obtained composites as hybrid silicon solar cells have been tested, based on the study of the passivation properties of the silicon layer by means of PEDOT:PSS with and without nanoparticle addition of the silicon layer, as well of its behavior under illumination and irradiation. As a final proof of concept to test other miscellaneous applications, such as the use of the composites as thermoelectric, a setup for testing Seebeck effect has been designed, tested and error proofed. After carefully determining the validity of those results compared with the scientific literature, PEDOT:PSS-based thermally-induced voltage due to the Seebeck effect has been measured.

Furthermore, for each of the materials studied on this thesis (synthesized nanoparticles, PEDOT:PSS thin layers and its composites), their stability under different conditions such as temperature, UV laser irradiation and atmospheres have been analyzed.

Herein, a brief description of the chapter structure followed in this thesis is presented:

- **Chapter 1:** Introduction of physical properties and applications of the different materials SnO, SnO_2, TiO_2 and PEDOT:PSS, both separately and together forming composites.

- **Chapter 2:** Subdivided in two parts. Firstly, synthesis of the nanoparticles (SnO, SnO_2 and anatase TiO_2) and sample notation and properties are described. Also the procedures for assembling PEDOT:PSS thin layers and based composites are described. Secondly, the most notable characterization techniques are discussed briefly, emphasizing physical fundamentals and their usefulness for analyzing these materials as well as the conditions and equipment used in this thesis.

- **Chapter 3**: Undoped and Li or Ni doped SnO_2 nanoparticles synthesized via hydrolysis have been synthesized and their morphology, structure, electronic,

electrical and luminescent properties are described. Their possible use as anodes in Li-ion batteries has been also shown.

- **Chapter 4**: Undoped and Li or Ni doped anatase TiO_2 nanoparticles synthesized via hydrolysis have been synthesized and their morphology, structure, electronic, electric and luminescent properties are described. Their stability under UV irradiation or temperature as well as the transition from anatase to rutile phase have been also studied. Their possible use as anodes in Li-ion batteries has been also tested.

- **Chapter 5**: Undoped and Li or Ni doped SnO nanoparticles and platelets synthesized via hydrolysis have been synthesized and their morphology, structure, electronic, electrical and luminescent properties are described. In this case, special attention has been focused on their stability over time, as well as under thermal treatments or UV irradiation.

- **Chapter 6**: PEDOT:PSS thin layers have been assembled via spin coating as a passivation silicon layer for hybrid silicon solar cells. Their effects over the passivation on the silicon layer have been studied via the characterization of their optical and luminescent properties. The dependence on the silicon oxide layer, UV irradiation, materials and methods and the nanoparticle use to form hybrid composites on the final product have been also tested.

- **Chapter 7**: PEDOT:PSS composites with and without the use of nanoparticles properties are studied. However, in this chapter their study is focused on their possible use as either chemirresistive sensors or thermoelectric materials. In this chapter the study of the composites is focused on their electric behavior and surface morphology.

- **Chapter 8**: In this last chapter, the most notable conclusions inferred from this work are described.

Finally in the last section the most notable scientific reports from literature, which support this work, are cited.

Chapter 2.
Experimental methods

2.1. Sample fabrication

Two different kind of samples are studied in the research work presented in this dissertation. The first kind of investigated nanomaterials are TiO_2, SnO_2 and SnO nanoparticles either undoped or doped with Li or Ni. As indicated in chapter 1, the method used for the preparation of these nanoparticles was a soft chemical co-precipitation synthesis based on hydrolysis. This synthesis has been carried out using the facilities of Inorganic Chemistry group at the Chemistry Faculty of the Complutense University of Madrid under the supervision of Dr. Julio Ramírez-Castellanos.
This method allows to obtain a large quantity of material with good control of the size and final composition of the nanoparticles. The co-precipitation method is a soft chemistry route widely employed to synthesize nanomaterials. It can be used to prepare a variety of materials such as metals, semiconductors or insulators, allowing *in-situ* doping by using the adequate precursors. In this work, hydrolysis synthesis has been carried out at mild temperatures. For SnO_2 (and therefore, for SnO), pH has to be controlled as the reaction only occurs at certain pH, close to neutral.
The second type of samples consist of composites with a PEDOT:PSS polymeric host and SnO, SnO_2 or TiO_2 nanoparticles as a filler. These samples were deposited by spin coating in our Physiscs of Electronic Nanomaterials Group´s Laboratory or in the facilities of the Institute of Energy Technology (IFE) in Kjeller, Norway during my research stay abroad under the supervision of Dr. Smagul Karazhanov.

2.1.1. Synthesis of SnO and SnO_2 nanoparticles

Undoped SnO and SnO_2 nanoparticles were synthesized using $SnCl_2{\cdot}2\ H_2O$ (Sigma-Aldrich, purity 99.99%) as precursor. For each batch, 2.5 gr of $SnCl_2{\cdot}2\ H_2O$ were chosen. After dissolution of the precursor in water under continuous stirring at 50 °C, NH_4OH was added until pH = 8 was obtained distilled water was added until reaching 100 mL and hydrolysis occurs. Then, the temperature was raised up to 100 °C for 2 h. The obtained product was centrifuged until reaching neutral pH

and subsequently dried at 50 °C for 12 h. This hydrolysis product corresponds to romarchite SnO. To obtain SnO_2 this product was subsequently calcined at 350 °C for 20 h in order to obtain cassiterite SnO_2 nanoparticles. Fig.2.1 shows an overview of the synthesis process used for the fabrication of SnO and SnO_2 nanoparticles.

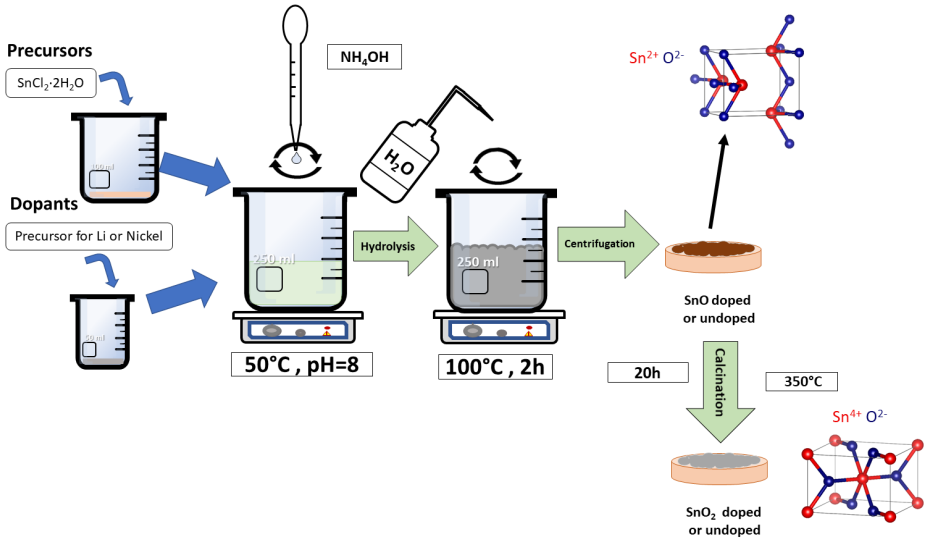

Fig. 2.1: Hydrolysis synthesis of undoped and doped SnO and SnO_2 samples.

Obtaining Ni or Li doped SnO and SnO_2 follows also a similar synthesis procedure. Stoichiometric amounts of $NiCl_2{\cdot}6H_2O$ (Probus) or LiCl (Labkem, purity 99%), respectively, were diluted in distilled water and added to the beaker containing $SnCl_2{\cdot}2\ H_2O$, before inducing the hydrolysis process. The rest of the synthesis is analogous to that followed for the undoped nanoparticles. The particles have been nominally doped with Li or Ni 20% or 30% in weight.

The corresponding sample nomenclature used for the synthesized nanoparticles is $SnO(_2)$:Y_x, where Y denotes the dopant (Li or Ni) and x= 0.2 and x= 0.3, denotes the selected nominal concentrations of the dopants precursor in the tin precursor mixture, corresponding to 20% or 30% weight. Hereinafter, the samples corresponding to doped SnO will be referred to as SnO:$Li_{0.2}$ or SnO:$Ni_{0.2}$ as shown in Table 2.1, and the samples corresponding to doped SnO_2 will be referred as SnO_2:$Li_{0.2}$, SnO_2:$Li_{0.3}$, SnO_2:$Ni_{0.2}$, and SnO_2:$Ni_{0.3}$ respectively, while the undoped samples will be named as SnO and SnO_2, as referred in Table 2.2.

Table 2.1: Notation for SnO samples.

Dopant	% wt	Notation
-	-	SnO
Lithium	20	SnO:$Li_{0.2}$
-	-	-
Nickel	20	SnO:$Ni_{0.2}$
-	-	-

Table 2.2: Notation for SnO_2 samples.

Dopant	% wt	Notation
-	-	SnO_2
Lithium	20	SnO_2:$Li_{0.2}$
Lithium	30	SnO_2:$Li_{0.3}$
Nickel	20	SnO_2:$Ni_{0.2}$
Nickel	30	SnO_2:$Ni_{0.3}$

2.1.2. Synthesis of TiO_2 nanoparticles

As for SnO_2 nanoparticles, TiO_2 samples have been synthesized following an analogous hydrolysis process as shown in the scheme of Fig.2.2.

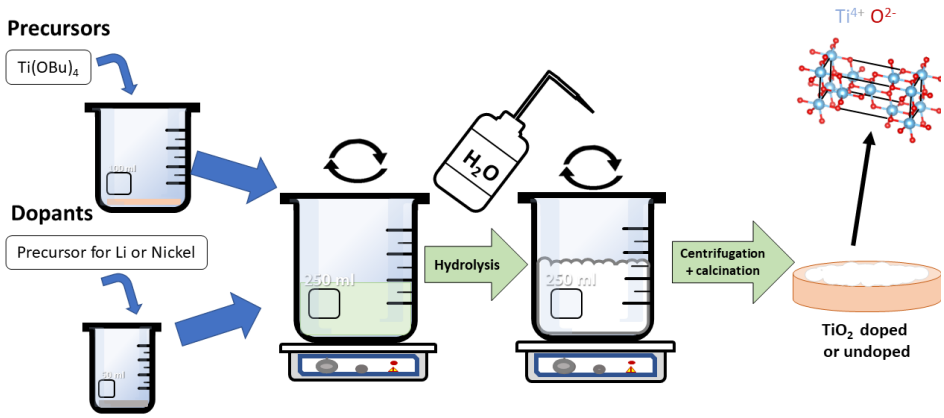

Fig. 2.2: Hydrolysis synthesis of undoped and doped TiO_2 nanoparticles.

Undoped anatase TiO_2 nanoparticles have been first synthesized as reference material. The desired amount of $Ti(OBu)_4$ (10 mL) (Sigma-Aldrich, purity 97%) is selected as Ti precursor and 1-butanol, 20 ml per 10 ml of precursor is added. The mixture is continuously stirred at room temperature. Distilled water is added to induce hydrolysis at its nominal pH value. The synthesis product is centrifuged with distilled water until neutral pH is reached and then dried in an oven at 50 °C for 12 h, obtaining a fine powder. A final treatment of this powder is carried out at 250 °C during 24 h to obtain crystalline material with the anatase phase.

Li or Ni doped anatase nanoparticles synthesis follows a similar procedure using $NiCl_2{\cdot}6H_2O$ (Probus) or LiCl (Labkem, purity 99%) as dopant precursors. The

desired stoichiometric amount of the precursor associated with the dopant is diluted in distilled water and introduced into a beaker with the Ti precursors before adding the distilled water to induce hydrolysis. The rest of the treatment is analogous to that followed for the synthesis of the undoped nanoparticles.

Samples will be referred to as TiO_2:Y_x, Y = Li, Ni and x = 0.2, 0.3 meaning 20 and 30% dopant weight as indicated in Table 2.3. Hereinafter, the samples will be referred to as TiO_2:$Li_{0.2}$, TiO_2:$Li_{0.3}$, TiO_2:$Ni_{0.2}$, and TiO_2:$Ni_{0.3}$ respectively, while the undoped sample will be named as TiO_2.

Table 2.3: Notation for TiO_2 samples.

Dopant	**% wt**	**Notation**
-	-	TiO_2
Lithium	20	TiO_2:$Li_{0.2}$
Lithium	30	TiO_2:$Li_{0.3}$
Nickel	20	TiO_2:$Ni_{0.2}$
Nickel	30	TiO_2:$Ni_{0.3}$

2.1.3. Thin layers obtained by spin coating

In this Doctoral Thesis, thin layers of composite material made of nanoparticles with a polymeric host, as well pristine polymer layers, have been prepared. Spin coating has been chosen as the main thin film deposition technique.
As main advantages, this deposition technique operates without need of vacuum atmosphere, at room temperature, and is a fast method to obtain thin layers of hundreds of nanometers. This solution-based process could be used to easily create thin layers of a variety of materials such as polymers or inorganic materials. This technique consists on pouring a liquid over an spinning substrate, thus the centrifugal force of the rotation allows uniformly liquid spread over the substrate, which creates a coating layer. By adapting different parameters of the spin process (speed, acceleration, time), the mixture which is being poured (viscosity, drop size) or the substrate (wettability), optimized layers can be obtained.

The spin coating setup is presented in Fig.2.3. Firstly, a syringe barrel is filled with a dispersion of the compound to be coated in a liquid phase. In our case, PEDOT:PSS was used both bare, and blended with SnO, SnO_2 or TiO_2 nanoparticles. Fortunately, PEDOT:PSS is an aqueous dispersion, very distinguished with a deep-blue color. To improve several properties of the polymer blend, some additives were used as well. The addition of organic compounds such as DMSO or EG enhances the electrical conductivity and prevents agglomeration of nanoparticles. In order to improve wettability Triton X-100 was chosen in some cases.

The spin-coating system used in chapter 7 is equipped with an automatic electronic dispenser controlled by means of a flow of compressed air. Usually, nominal gas flux is limited to 0.2-0.5 bar and the gas controller allows fine calibration avoid-

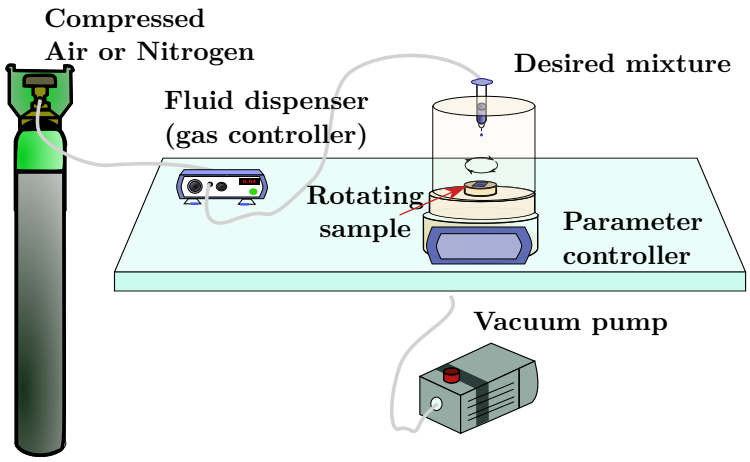

Fig. 2.3: Spin coating setup with gas controlled dispenser.

ing liquid reflux. This gas passes through a plastic tube to a syringe, filled with the mixture for the spin coating. The syringe has an interchangeable tip with different diameters, for this thesis the diameters ranged from to 0.33-0.61 mm. The spin coating station incorporates a sample holder which holds the coating substrate in place with help of vacuum generated by a rotary vacuum pump. Glass cover glasses or silicon wafers were used as substrates in this work. Table 2.4 shows the main properties of the employed substrates, which were different on the different chapters of this thesis.

Table 2.4: Properties of different substrates used in this thesis.

Material	Company	Method/Dopant Type/Orientation	Size	Thickness (μm)	Resistivity (Ω·cm)	Shown in
Silicon	Topsil	PV-FZ/Phos /N/(100)	(1/4 circle) 78.5 cm^2	280±20	1-5	chapter 6
Glass	-	-	(square) 2.2×2.2 cm^2	-	-	chapter 6
Silicon	Si-Mat	Intrinsic FZ/ (100)	(square) 1.5×1.5 cm^2	280±25	>5000	chapter 7
Glass	Deltalab	Ref D100002	(square) 1.5×1.5 cm^2	2000	-	chapter 7

Our system allows the control of different parameters and the creation of multi-step coating process, being the most relevant parameters of a deposition process the number of steps, spin revolutions, spin acceleration, time and delay-solution dispense time. Those parameters were optimized for the spin-coating process for each of the samples used in this work. For example, delay time was found to be fundamental to obtain a well-spread layer. For other substrate sizes, increasing the solution dispense time was necessary as higher mixture quantity was needed

to sufficiently cover the substrate. For that purpose, every parameter was changed independently. A deposition run can be programmed with the selected parameters.

As the deposition run is started, gas flux starts to flow and when the coating step is activated, the liquid is poured over the coating surface, which spins if the user selected so. The centrifugal force due to substrate spinning at high rates allows an effective solution spread over the coating surface, leading to a thin layer. The parameters used for the deposition of the layers on this thesis are described in the Table 2.6 and Table 2.5 for PEDOT:PSS layers. These parameters are the optimized parameters for the substrates used in this work.

Table 2.5: Thin layer deposition steps and parameters for PEDOT:PSS coatings at chapter 6.

Dynamic mode, 70-150μL of mixture used

Step	Speed (rpm)	Acceleration (rpm/s)	Time (s)	Deposition time(s)	Delay time(s)	Dispense time(s)
1	2000	1000	20	Manual	Manual	Manual
2	6000	1000	50			
3	Stopping	1000-0	until stop ~10s			

Table 2.6: Thin layer deposition steps and parameters for PEDOT:PSS samples at chapter 7.

$p = 0.04$ bar

Step	Speed (rpm)	Acceleration (rpm/s)	Time (s)	Deposition time(s)	Delay time(s)	Dispense time(s)
1	3000	1000	5	5	2	3
2	3000	1000	30			
3	4000	1000	20			

As the procedure which will be followed to mixture and create PEDOT:PSS thin layers is very similar in both chapter 6 and chapter 7, the process is summarized in Fig.2.4. The different steps will be discussed in their respective chapters but mainly in chapter 6 composites will be focused on their application in hybrid silicon solar cell and in chapter 7 on their possible implementation as TE and gas sensors.

Therefore, to summarize:

- Bare PEDOT:PSS films and the corresponding composites described in chapter 6 with nanoparticles were fabricated during author's stay at the Department of

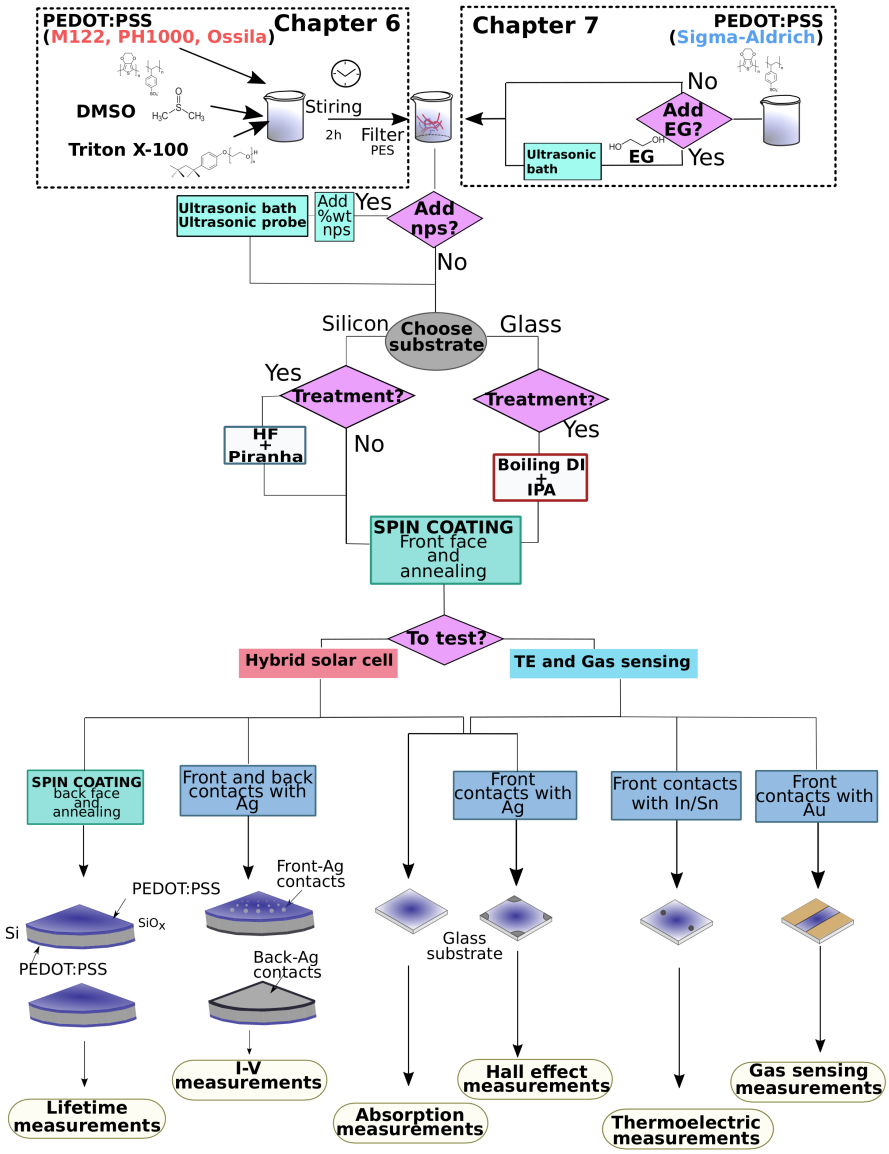

Fig. 2.4: Process diagram of the thin film method followed throughout this thesis.

Solar Energy, Institute for Energy and Technology (IFE), Kjeller, Oslo, Nor-

way, with a spin-coating system equipped only with manual dispenser. Liquids poured from a pipettor which was carefully placed at the same height for all preparations ($\sim$ 2 cm) and deposited during the first 5 seconds of spinning.

- Preparation of thin layers in chapter 7 via spin coating has been performed on a Spin Coating Polos Series Spin 150i with an automatic dispenser Nordson EFD PerformusVIII in our Physics of Electronic Nanomaterials Group´s Laboratory, at the Materials Physics Department, Physics Faculty, Complutense University of Madrid.

2.2. Characterization techniques

A set of techniques have been carried out to systematically characterize the samples. In many cases, not only spectroscopies have been applied but a combination with microscopy capabilities, offering spatial resolution of different properties at the micro and nano-scale.

Morphological information was mainly achieved by means of scanning and transmission electron microscopies (SEM and TEM), whereas structural or microstructural information was recorded by X-ray Diffraction (XRD), Raman spectroscopy and microscopy and Selected Area Electron Diffraction (SAD or SAED) in a TEM. Compositional characterization was achieved by energy dispersive X-ray spectroscopy in a SEM (EDS), as well as by inductively coupled plasma optical emission spectrometry (ICP-OES) and X-ray photoelectron spectroscopy (XPS) with synchrotron radiation, which also supplies information on the electronic structure with high surface sensitivity. X ray absorption spectroscopy (XAS) at the synchrotron facility was also employed to analyze deeper the elemental oxidation states and the presence of dopants, as well as enabling resonant photoemission spectroscopy (RPES) measurements to further characterize the valence band of the samples. The surface topography of the thin films was characterized by Atomic Force Microscopy (AFM). Optical properties such as luminescence emission and optical absorption were measured using Cathodoluminescence (CL) and Photoluminescence (PL) techniques and optical absorption spectroscopy on the UV-VIS range. Similarly, Photoluminescence and Photoluminescence Excitation (PL-PLE) was measured on a photoluminescence spectrometer. Electrical characterization were measured with a Hall effect equipment. Finally, both gas sensing and thermoelectric properties were tested on homemade setups.

These techniques can be divided in different groups according to their corresponding excitation source as shown in Table 2.7 and will be briefly described in the following sections.

Table 2.7: Classification of the experimental techniques according to the excitation source.

Source	Technique	Analyzed signal
e^-	SEM	Secondary e^-
	CL	$h\nu$ (IR-VIS-UV)
	EDS	$h\nu$ (X-Ray)
	TEM/HRTEM	Transmitted and diffracted e^-
$h\nu$ (Laser)	PL	$h\nu$ (IR-VIS-UV)
	Raman	Scattered $h\nu$
$h\nu$ (X-Ray)	XRD	$h\nu$ (Diffracted X-Ray)
	XPS	photoemitted e^-
	XAS	$h\nu$ (Absorbed X-Ray)

2.2.1. X-Ray Diffraction (XRD)

Crystalline structure can be determined by means of X-Ray Diffraction (XRD). The information collected by this technique is based on the interaction between an incident monochromatic X-ray beam and a crystalline sample (Fig.2.5(a)). Due to this interaction, a series of diffraction maxima can be observed in the corresponding directions which are determined by the *Bragg's Law*[77]:

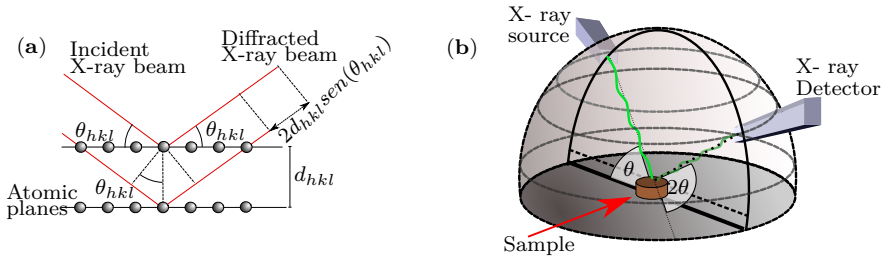

Fig. 2.5: (a) Bragg's law scheme (b) Scheme for obtaining diffraction pattern of a sample in θ-2θ mode.

$$n\lambda = 2d_{hkl}\ sen(\theta_{hkl}) \tag{2.1}$$

where n is an integer, λ is the wavelength of the incident X-rays, d_{hkl} is the inter planar distance between the diffraction planes with corresponding Miller indexes (h, k, l) and θ_{hkl} is the incident angle of the X-Ray beam.

XRD spectra was acquired at room temperature unless stated otherwise. However, XRD measurements as a function of the temperature (i.e Thermodiffractograms) have been also recorded for studying the anatase to rutile transition of the

TiO_2 nanoparticles as well the oxidation from SnO to SnO_2 as shown, respectively in chapter 4 and chapter 5.

Information relative to the crystalline grain size and distortion in the material can be obtained from the XRD analysis. When the particle dimension decreases, diffraction maxima widen and the average grain size D can be obtained with the *Scherrer equation*[78]:

$$D = \frac{K\lambda}{\beta cos(2\theta)} \tag{2.2}$$

where K is a dimensionless factor called shape factor. The shape factor has a typical value of about 0.89 but it can change depending on the crystalline structure and shape of the particles, λ is the X-ray wavelength; β is Full Width at Half Maximum (FWHM) without the instrumental background in radians and θ is the Bragg angle as shown in Fig.2.5(a).

The structural characterization of the nanoparticles was carried out by X-ray diffraction (XRD) in a PANanalytical X'Pert Powder equipment, using the copper K_α line where $\lambda_{Cu} = 1.5404$ Å and operating at 45 kV and 40 mA on a Bragg-Brentano[79] $\theta - 2\theta$ geometry, as observed in Fig.2.5(b). Measurements of Thermo diffractograms were performed with a X'Celerator detector. Respective step size and angle range, as well as temperature range are explained on the corresponding sections on chapter 4 and chapter 5. These measurements were performed at the X-ray Diffraction CAI facility at the UCM (Universidad Complutense de Madrid).

The software used to analyze the data was the X'Pert HighScore Plus (v.3.0.0, 2009) and Origin Pro 2019 (64bit).

2.2.2. Scanning Electron Microscopy (SEM)

A Scanning Electron Microscope (SEM) uses an electron beam to obtain information due to the interaction of the sample and the accelerated electron beam[80]. Schematics of a conventional SEM is represented in Fig.2.6. First, an electron gun generates an electron beam which is accelerated with a potential between 0.1 and 30 kV. The different scanning electron microscopes used during this thesis use thermionic effect of W (tungsten) filaments to generate the electron beam.

The electron beam passes through the microscope column, where electromagnetic condenser and objective lenses concentrate and collimate the beam. In the last step before arriving to the chamber, the electron beam passes through a set of apertures which diameters can be selected by the operator (between 50 and 500 μm). Then, the electron beam enters the chamber where the sample is placed over a conductive sample holder. Usually, SEM microscopes work in high vacuum ($\sim 10^{-6}$ Torr). By means of scan coils, electron beam *scans* the sample point per point, which generates different signals as electrons (both Secondary Electrons (SE) or BackScattered Electrons (BSE)), photons, X-ray, electric current... as observed in Fig.2.7.

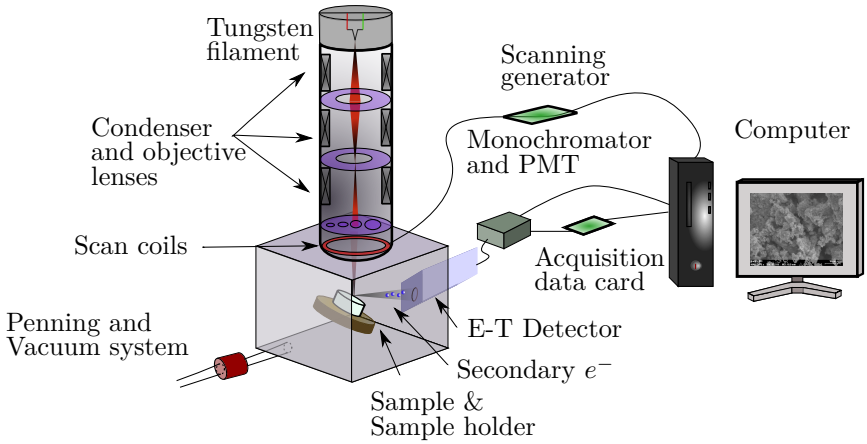

Fig. 2.6: Schematic diagram of a Scanning Electron Microscope.

Diverse signals are generated inside the region into which the electrons penetrate the sample, which is called interaction volume.

Depending on the atomic number of the specimen, Z, this volume is approximately a sphere when $15 < Z < 40$ and semi-spherical when $Z > 40$. Dimension on the Y axis of this volume is called *Gruen range* (R_G) which can be obtained from the *Kanaya-Okayama equation*[81]:

$$R_G = \frac{0.0276A}{\rho Z^{8/9}} E_b^{5/3} [\mu m] \tag{2.3}$$

where A is the atomic weight in g·mol^{-1}, ρ is density in g·cm^{-3}, E_b is electron beam energy in keV. To calculate and simulate the penetration ranges of different structures, a variety of software can be used such as *CASINO* (monte CArlo SImulation of electroN trajectory in sOlids)[82].

The signal intensity of interest is collected by its corresponding detector which transforms this signal to electric current and is processed by a computer synchronized with the scanning in order to form images or to collect spectral information. The main signal in SEM microscopes is formed by secondary electrons (SE), which are mostly low energy electrons (< 50 eV) generated by the electron beam interaction in the sample (emission mode). They are a result of inelastic interactions between the electron beam and the sample, in the most external electronic layers. These electrons gives substantial information about the topography of the sample.

SE are collected inside the SEM chamber by an scintillator-photomultiplier Everhart-Thornley (E-T) detector. This detector consists of an scintillator inside a Faraday cage. The scintillator produces photons due to the collection of electrons, enhanced by a positive voltage applied in the Faraday cage. E-T detector is at an angle in order to increase the detecting efficiency. These photons are transmitted through a light pipe and then are collected by a PhotoMulTiplier (PMT) which converts the optical signal into an electrical signal which can be amplified. Then,

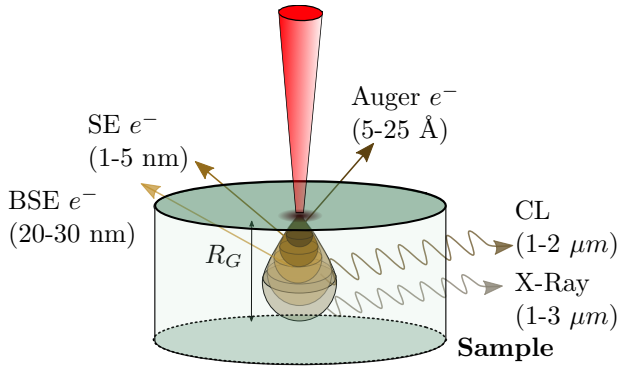

Fig. 2.7: Diagram of different processes and interaction of the electron beam with the specimen, according to the different interaction volumes.

this can be represented in a grey-scale image, for which color scale is proportional to the collected signal in each point. Other signals, which can be observed in Fig.2.7, come from different inelastic scattering at different sample depths, which is clearly dependent both on the specific material and the beam energy.

Scanning electron microscopes used during this thesis are a Hitachi S-2500, a Leica 440 Stereoscan and a FEI Inspect S, at the Physics of Electronic Nanomaterials Group´s Laboratory, Materials Physics Department, Faculty of Physics, Complutense University of Madrid.

2.2.3. Energy Dispersive Spectroscopy (EDS)

As mentioned in Fig.2.7, the interaction of the electron beam with the specimen in a SEM (or a TEM) can generate X-ray radiation as a result of inelastic scattering processes. Those X-rays carry atomic identification of the present elements besides its quantification, offering compositional information of the sample under study, which could be retrieved with spatial resolution by the so called micro X-ray analysis.

X-ray are produced inside the sample due to beam-sample interaction. If the beam energy is higher than the ionization energy of the atoms of the sample, electrons are ejected from the core electron levels following a process illustrated in Fig.2.8(a). Then, to bring back the atom to a ground level another electron from other energy level can occupy the empty electron state and two different scenarios can be considered: the energy difference between those two levels are emitted as X-ray radiation or another electron is ejected from the external levels (Auger electrons). X-ray intensity is displayed as a function of its energy in what is called EDX or Energy Dispersive X-Ray Spectroscopy (EDS).

In a EDS spectrum, as the one shown on Fig.2.8(b), different peaks are observed and each one is characteristic of different atoms. There is also a background contribution due to *Bremsstrahlung* (stopping radiation). The nomenclature used

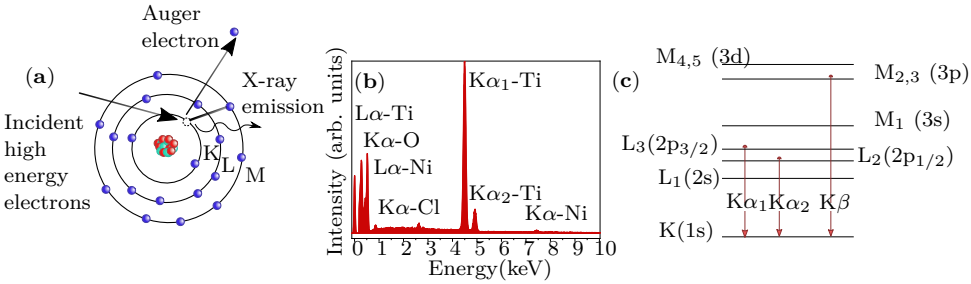

Fig. 2.8: (a) X-ray generation after an incident electron beam impact with an atom (b) Example of a EDX spectrum for the sample of TiO_2 doped with Nickel (c) Transitions between K, L and M shells of an atom leading to X-ray lines indicated following the Siegbahn notation.

for these electron transitions is called *Siegbahn notation* in which the layer which is initially ionized is designed by a letter (K, L, M...) accompanied by a Greek letter (α, β, γ, etc.) and with a sub-index which indicates transitions with similar energy as shown in the transitions of Fig.2.8(c) for illustration. A database to index these transitions can be found on the NIST website database[83].

Data acquisition system allows to quantify the composition of the material. This is performed with the *ZAF* correction which takes into account the atomic number (Z), self-absorption of X-rays (A) and Fluorescence (F). It is necessary to subtract the aforementioned *Bremsstrahlung* radiation, which measurement sensibility is really important for a correct subtraction and therefore a proper element quantification. Light elements with $Z < 4$ can not be detected with this technique. It is also possible to detect the presence of each element on a resolved area image what is so referred as *mapping* images. This is particularly important in order to assess the regions of the specimen which presents different elements than others.

Measurements in this thesis were performed using a system Bruker AXS Quantax coupled to SEM Leica Stereoscan, at the Physics of Electronic Nanomaterials Group´s Laboratory, Materials Physics Department, Faculty of Physics, Complutense University of Madrid. Energy resolution of the detector used in this work is around 123 meV. Data acquisition and quantification was performed using the Bruker ESPRIT 2 software.

2.2.4. Cathodoluminescence (CL)

Cathodoluminescence (CL) has been previously described as one of the effects that could occur due to the electron beam and sample interaction in a SEM chamber. This electron excitation generates photons that can be collected in a range between Infrared (IR) and Ultraviolet (UV). This phenomenon in a semiconductor occurs due the excitation of electrons from the Valence Band (VB) to the Conduction Band (CB), which generates electron hole pairs. These pairs can be radiative recombined which generates CL signal. Most common recombination processes are labeled on Fig.2.9. Among them, extrinsic transitions are related with defects or impurities

in the material, which origin can be partly related to the presence of dopants. Commonly, these transitions lead to wide band emissions with the exception of the intraionic transitions related with transitions metals or rare earths. In this work, the presented oxides mostly present a wide emission which covers a significant part of the visible spectrum.

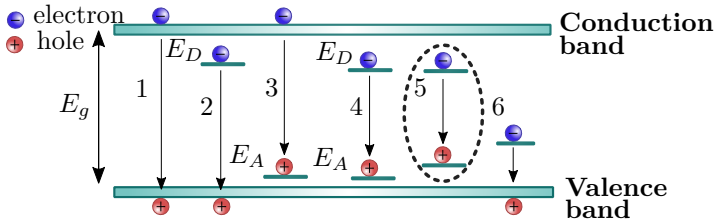

Fig. 2.9: Main radiative recombination processes for a semiconductor with a bandgap E_g (1) band to band, (2) donor level to valence band, (3) conduction band to acceptor level, (4) donor level to acceptor level, (5) bound exciton transition and (6) shallow or deep level to valence band.

Particularly, the CL signal is strongly dependent on different parameters such as the beam energy, crystalline orientation, dimensions or temperature. At Room Temperature (RT), phonon interaction leads to a competition between radiative and non radiative transitions. Phonon interaction can be diminished with lowering temperature, which enhances CL signal and induce narrower emission bands. To obtain low temperature measurements, an integrated system with a thermoresitance, a thermocouple and a cooling N_2 system is used, which allows a working temperature between 80 and 300 K.

To acquire CL spectra, light was harvested using a wave-guide collecting light proceeding from the SEM (Hitachi S-2500) chamber to a CCD camera Hamamatsu PMA-12, with an spectral range between 200 to 950 nm, obtained at the Physics of Electronic Nanomaterials Group´s Laboratory, Materials Physics Department, Faculty of Physics, Complutense University of Madrid. This CCD camera is directly communicated with the acquisition software.

2.2.5. Transmission Electron Microscopy (TEM)

A Transmission Electron Microscope (TEM) uses an electron beam with a higher energy range (typically between 100-300 keV) than in a SEM microscope. The transmitted electron beam and related signals are collected to display sample information on different kind of images, diffraction patterns or spectra depending on the selected technique. A schematic representation of a typical TEM is represented in Fig.2.10. In this thesis, a TEM was used to obtain two different measurements: Diffraction patterns and contrast images. Diffracted electron signal can be used to obtain contrast images with a much higher resolution than those obtained on a SEM microscope (nm). These images can be obtained with the transmitted electron beam (Bright Field (BF)) or with the diffracted beams (Dark Field (DF))[84].

These contrast images can be used to observe atomic ordering dislocation, grain boundaries etc. Moreover, crystalline structure can be obtained from the Selected Area (Electron) Diffraction (SAED) patterns (also called SAD) in which by modifying the lenses configuration we can study the reciprocal space instead the real space.

- *Diffraction mode*: To form Diffraction Patterns (DP), intermediate-system lenses have to be adjusted so that *Back-Focal Plane (BFP)* of the *objective lens* acts as the *objective plane* of the *intermediate lens*. The diffraction pattern is projected on the viewing screen (or a Charge-Coupled Device (CCD)).

- *Image mode*: To form image, intermediate lens have to be adjusted so that *object plane* of the *intermediate lens* acts as the *image plane* of the *objective lens*. Then an image is projected onto the viewing screen/CCD, as shown in Fig. 2.10.

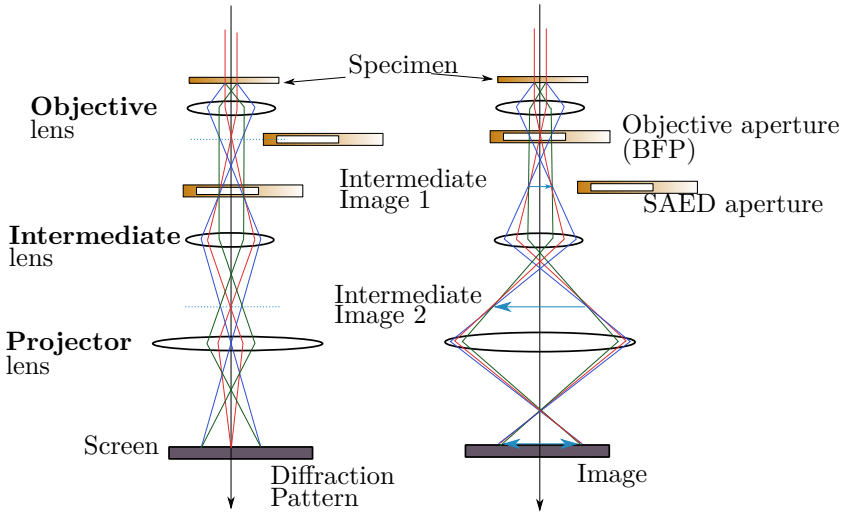

Fig. 2.10: The two basic operation modes of the TEM (a) diffraction mode: projecting the DP onto the viewing screen and (b) image mode: projecting the image onto the screen. This is a simplified diagram showing only three lenses.

Samples often require special preparation prior to obtain a thickness enabling electron transparency. In this thesis, all samples studied are in the nanometric range, thus no further preparation was needed. Samples were dispersed into a dispersing agent as IsoPropyl Alcohol (2-propanol) (IPA) in an ultrasonic bath and then deposited over a copper grid, coated with a carbon porous membrane.

The microstructural analysis was performed in a transmission electron microscope (SAED / TEM) JEM 1400 plus JEOL at the Centro Nacional de Microscopía, Universidad Complutense de Madrid.

To analyze the results, the size of the nanoparticles was estimated using ImageJ software. SAED diffraction patterns were analyzed using GMS 3 (SI viewer) with DIFPack from Gatan INC.

2.2.6. Induced Coupled Plasma-Optical Emission Spectroscopy (ICP-OES)

Induced Coupled Plasma-Optical Emission Spectroscopy (ICP-OES) is a technique based on the use of an Argon plasma generated by an induction coil, that can reach up to 10000 K. This plasma can excite atoms to excited energy levels. Those atoms decay to the fundamental level via the emission of radiation. The wavelength of this energy is characteristic of each atom as it is related to the ionization potential. Thus, samples will emit characteristic emission spectra as a function of the elemental composition. Intensity of these spectra is also proportional to the concentration of each chemical element. This technique is capable of detecting light elements such as lithium, even in a low concentration.

Samples have to be prepared before measurement with an acid digestion in order to be nebulized into the chamber. The sample is dissolved with different acids depending on the nature of the compounds, HNO_3 or HCl are commonly used.

Detection and semiquantification of lithium was performed by Optical Emission Spectrometry (ICP-OES) in an ARCOS equipment from SPECTRO with excitation source ICP, Perkin Elmer Optima 3300DV at the Geology CAI, Geology and Biology Faculty at the Universidad Complutense de Madrid. Each measurement was performed three times and averaged in order to diminish error.

2.2.7. Photoluminescence (PL)

Photoluminescence (PL) has been studied at room temperature in a confocal microscope using a He-Cd UV laser ($\lambda = 325$ nm) as an excitation source.

In Fig.2.11 the work principle of a confocal microscope can be observed. This microscope possesses an aperture called *pinhole* at the focal image point of the lens system, thus blocking light whose optical path is not exactly at the objective focus as observed in Fig.2.11(b). Confocal conditions allow to improve lateral resolution of the microscope.

Photoluminescence consists on the emission of light from a material due to the excitation by a light (photons) source. A photon source in the eV range produces electron-hole pairs after being absorbed by the sample. The de-excitation of the electrons through radiative transitions, as the ones represented in Fig.2.9, are measured in the visible or near infrared range. As illustrated in Fig.2.9, among the possible recombination processes, the ones involving crystalline defects, such as oxygen vacancies in oxides, play an important role in the luminescence properties of these materials.

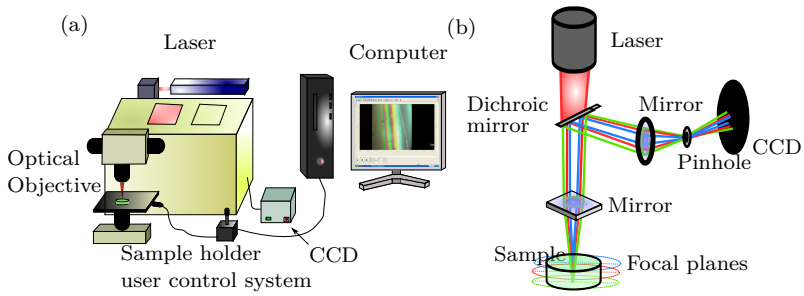

Fig. 2.11: (a) Confocal microscope experimental setup. This setup was both used to measure Raman spectroscopy and photoluminescence. (b) Schematic representation of a confocal microscope. Only rays which arrive from the focal point of the lens system can reach the detector. This configuration allows to achieve higher resolution than conventional optical microscopes.

In this thesis, emission spectra with spacial resolution (μ-PL) had been collected by means of a Horiba Jobin Yvon LabRam Hr800 confocal microscope using a He-Cd Kimmon IK Series ($\lambda = 325$ nm) UV laser. Different neutral filters were used in order to attenuate the total laser intensity, when necessary. In this configuration, nominal excitation light can be attenuated by using neutral filters (labeled as D^x with $x = (0, 0.3, 0.6, 1, 2)$ to reduce the total laser intensity by a factor of 10^{-x}, thus reducing the total intensity by a factor of 0.5, 0.25, 0.1, 0.01, etc. The generated light has been collected by an air-cooled CCD Synapse 354308 in a wavelength range between 300 and 800 nm, with a micrometric spatial resolution. All measurements have been performed at room temperature. Grating used for PL luminescence was 600 l/mm. The laser was focused onto the sample surface using a 40x objective (numerical aperture = 0.5, Thorlabs LMU-40X-NUV). The confocal microscope possesses a moving platform allows the sample holder to be displaced in the X and Y directions to analyze areas of around 300x300 $(\mu m)^2$. The program used for Photoluminescence and Raman data acquisition and analysis is LabSpec 6. These measurements have been obtained at the Physics of Electronic Nanomaterials Group´s Laboratory, Materials Physics Department, Faculty of Physics, Complutense University of Madrid.

2.2.8. Photoluminescence excitation (PLE)

Photoluminescence Excitation (PLE) is a specific type of photoluminescence in which the wavelength of excitation (λ_{ex}) light is varied and the change in the PL intensity is monitored at a fixed wavelength (λ_{em}). This signal is proportional to the number of photons generated by each incident photon. It is clear that this technique differs from PL as in that case the excitation wavelength (λ_{ex}) was maintained constant and the emitted luminescence (λ_{em}) was measured on a range between 300-750 nm. In the case of PLE, as the λ_{ex} varies, only photons with certain λ will be absorbed by the material, which can excite electron hole

pairs, which subsequently can recombine radiatively and produce the re-emission of photons. The PLE signal is calculated by comparing the excitation photon flux divided by the emitted photon flux.

The experimental setup consist on an excitation source formed by a variable-wavelength excitation source such as a Xe discharge lamp. Inside the system a monochromator guide the beam and a PMT recollect the PL signal which arise from the excited sample under the illumination, while a beam splitter redirects portion of the excitation light into another PMT to monitor the system response. The variable configuration allows not only to measure PLE but also obtaining other measurements such as PL. In particular, this equipment allows to decrease the temperature down to 4K.

PLE spectra were acquired with an FLS1000 system from Edinburgh Instruments, exciting with a 450W Xe lamp as excitation source in a variable range from 4-300K. The PMT allows measurement on a wide range from 240-750 nm. The system is connected to a cryostat and a close loop of liquid Helium pumped with a compressor HC-4E from Sumitomo Cryogenics, which allows to decrease the temperature within the sample holder down to 4K. The temperature system is controlled by an Intelligent Temperature Control (ITC) model MercuryiTC from Oxford instruments, which allows an steady-increase of the temperature up to RT. To decrease the temperature is necessary to create vacuum inside the chamber, which is obtained by a turbomolecular pump. To protect the PMT, different filters can be used, which allow up to 90% transmittance for certain wavelengths, close to the selected excitation wavelength. With this equipment also certain measurements of PL have been performed, as shown in chapter 4. These measurements have been obtained at the Physics of Electronic Nanomaterials Group´s Laboratory, Materials Physics Department, Faculty of Physics, Complutense University of Madrid.

2.2.9. Raman Spectroscopy

Raman spectroscopy is a non-destructive characterization technique based on the Raman effect, as a result of the inelastic scattering of light by a material. Inelastic scattering is produced due to the interaction of the incident photons with the phonons of the crystal lattice, molecular vibrations or other excitations.

As seen in Fig.2.12, a photon produced by a monochromatic source with energy $\hbar\omega_L$ interacts with the sample. The processes that can undergo with the interaction of the photon with the material lattice can be summarized as:

- When the incident photon, $\hbar\omega_L$, undergoes an elastic scattering and the dispersed photon possesses the same energy $\hbar\omega_L = \hbar\omega_s$, the process is called *Rayleigh scattering.*
- When photon is scattered inelastically, the scattering is called *Stokes scattering*, in which:
  - If the energy of the scattered photon, $\hbar\omega_s$, is lower than the incident

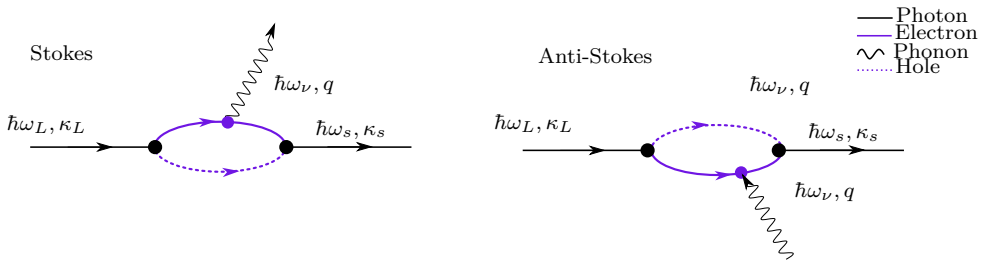

Fig. 2.12: Feynman diagram for Stokes Raman scattering process (emission of a phonon) and anti-Stokes scattering (absorption of a phonon).

photon energy ($\hbar\omega_L$) such as the scattered photon energy is $\hbar\omega_s = \hbar(\omega_L - \omega_\nu)$, its difference is passed to a phonon with energy $\hbar\omega_\nu$.

– If the energy of the scattered photon, $\hbar\omega_s$, is higher than the incident photon energy ($\hbar\omega_L$) such as the scattered photon energy is $\hbar\omega_s = \hbar(\omega_L + \omega_\nu)$, this processes is denoted as *Anti-Stokes scattering*, which energy difference is obtained from a phonon with energy $\hbar\omega_\nu$.

These two kinds of inelastic scatterings implies the creation or annihilation of either a phonon (1st order Raman interaction) or multiple phonons (2nd and successive Raman order). Depending on the symmetries of the different molecules, there is a criteria (Mulliken Symbols for Irreducible Representation) to name those rotations and vibrations, which can be found at different sources such as J.M. Hollas book[85].

In this thesis, Raman spectroscopy is coupled to the same confocal microscope as for Photoluminescence, an Horiba Jobin Yvon LabRam Hr800 using a Visible (VIS) red He-Ne ($\lambda = 633$ nm) or an UV He-Cd ($\lambda = 325$ nm) Kimmon IK Series laser, which allows to obtain photoluminescence and Raman spectra from the same area. The nominal laser power of each laser was 10 mW for the UV laser and 17 mW for the VIS laser. However, over time this power decreased and for most of this thesis their power were $\sim$ 5 mW for the UV laser and $\sim$13 mW for the VIS laser. The laser was focused onto the sample surface using a 40x objective (numerical aperture = 0.5, Thorlabs LMU-40X-NUV) which led to a laser spot diameter around ~ 1 μm for the UV laser and a few microns for the red laser. The scattered light was collected with the same objective and dispersed with a grating of 2400 l/mm for UV and 600 l/mm for VIS and finally acquired with an air-cooled CCD detector Synapse. Before each batch of measurements, the spectrometer was carefully calibrated employing the silicon Raman mode at 520 cm^{-1}. These measurements have been obtained at the Physics of Electronic Nanomaterials Group´s Laboratory, Materials Physics Department, Faculty of Physics, Complutense University of Madrid.

2.2.10. Photoluminescence based on Quasi-Steady State Photoconductance (PL-QSSPC)

Photoluminescence based on Quasi-Steady State Photoconductance (PL-QSSPC) allows to obtain calibrated photoluminescence lifetime images of the samples. The underlying principle is the radiative recombination of a CB electron and a VB hole that generates a photon which was already discussed as photoluminescence (PL) earlier in this chapter. The setup is described in Fig.2.13. A sample is introduced into the stage over a calibration RF coil and is illuminated with a laser. The RF bridge detects the changes on permeability of the sample which allows to deduce the sample conductance. Input values to perform these measurements are the thickness of the layer and the reflectance of the front layer. A more in depth explanation of this technique can be found on the following references[86,87].

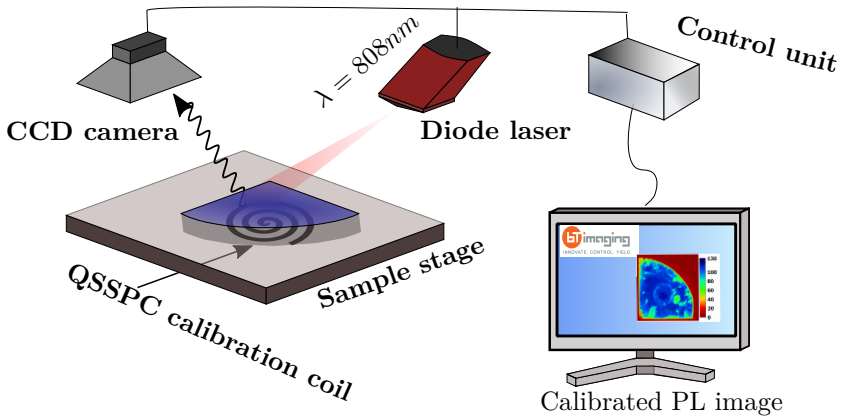

Fig. 2.13: PL-QSSPC setup to measure space-resolved PL imaging.

The underlying principle is as follows. Because each recombination (combination of an electron with a hole) event produces one photon, the PL emission rate, Φ_{PL}, is equal to the rate of radiative recombination:

$$\Phi_{PL} = B_{rad}(np - n_i^2) \tag{2.4}$$

Where B_{rad}, n and p are, respectively the material-specific radiative recombination coefficient and the electron or hole concentration. If we assume a n-type material we can insert $p = N_A + \Delta$n and $n = \Delta n$ as well as assume that n_i^2 is negligible for the most doping and injection conditions. The PL intensity:

$$I_{PL} = C_{cal} \cdot \Phi_{PL} = C_{cal} B_{rad}(N_A + \Delta n)\Delta n = C_{cal} B_{rad} N_A \Delta n + C_{cal} B_{rad} \Delta n^2 \tag{2.5}$$

where C_{cal} is a constant that describes the fraction of the emitted light detected by the camera and necessary to obtain a calibrated lifetime image.

The injection level can be obtained easily from eq.2.5 if we avoid the quadratic therm, which can be assumed for low injection,[86]:

$$\Delta n(x,y) = \frac{1}{C_{cal} B_{rad} N_A} \cdot I_{PL}(x,y) \tag{2.6}$$

These measurements are only valid if we assume quasi-steady state approximation (QSS) (where $\tau_{pulse} \gg \tau$) which means that the time constant of the flash decay was much longer than the carrier lifetime in the material, which implies that the excess carrier density is approximately in steady state at each point of the measurements.

To obtain C_{cal} and thus, the calibrated lifetimes, an integrated photoconductance (QSSPC) measurement is obtained by an inductively-coupled coil. From the measured lifetime vs injection level the correct C_{cal} is calculated by comparing the injection level in the point of calibration Δn_{cal} to the PL intensity in the region above the coil, $I_{PL,cal}$:

$$C_{cal} = \frac{I_{PL,cal}}{B_{rad}(N_A \Delta n_{cal} + \Delta n_{cal}^2)} \tag{2.7}$$

Correct quantification of the QSSPC measurement also requires knowledge of the thickness of the sample and the front side reflectance at the excitation wavelength (λ = 808 nm). Finally, the effective lifetime can be obtained from the injection level as:

$$\tau_{eff} = \frac{\Delta n(x,y)}{G} = \frac{\Delta n(x,y)}{(1 - R_f)\Phi_{ph}/W} \tag{2.8}$$

where G is the generation rate, R is the reflectance of the sample for a certain wavelength, Φ_{ph} is the photon flux from the excitation source and W is the width of the wafer.

The calibrated effective charge carrier lifetime values were calculated from the PL intensity based on the calibration due to the integrated Sinton QSSPC quasi steady state photoconductance (QSS-PC) measurements using an LIS-R1 PL imaging setup from BT Imaging with an excitation wavelength of λ = 808 nm under a constant illumination intensity of $4.2 \cdot 10^{-2}$ W cm^2. To calibrate PL images, the value of reflectance at λ = 808 nm of each sample was measured and used as input value.

These measurements were carried out during my predoctoral stay under the supervision of Dr. Smagul Karazhanov and Dr. Erik S. Marstein at the Solar Department of the Institute for Energy TechnologY (IFE) in Kjeller, Norway. Special thanks also to Dr. Halvard Haug and Dr. Chang Chuan You for their practical help in the laboratory.

2.2.11. X-ray Photoemission Spectroscopy (XPS)

In X-Ray Photoelectron Spectroscopy (XPS) measurements, a sample is illuminated with monochromatic light which induces, due to the Photoelectric effect, photoelectron emissions. Light can be generated by different sources, being the most used synchrotron radiation as it possesses several advantages such as a high photon

flux ($10^{10-12}\nu/s$), wide energy range (IR to X-ray), high collimation, short pulses... This technique is extremely-surface sensitive due to the small mean free path of photoelectrons which allows to obtain information of the first atomic layers of a sample. At the sample, the X-ray beam size is usually in the range of 1–5 μm. This technique requires Ultra-High Vacuum (UHV) ($10^{-10} - 10^{-11}$ Torr)[88]. An illustration of the experimental setup is shown in Fig.2.14(a). As it can be observed, emitted electrons are collected and analyzed with an energy analyzer being a common choice a Concentric Hemispherical Analyzer (CHA) which with a potential difference can deflect photoelectrons screening them based on their energy.

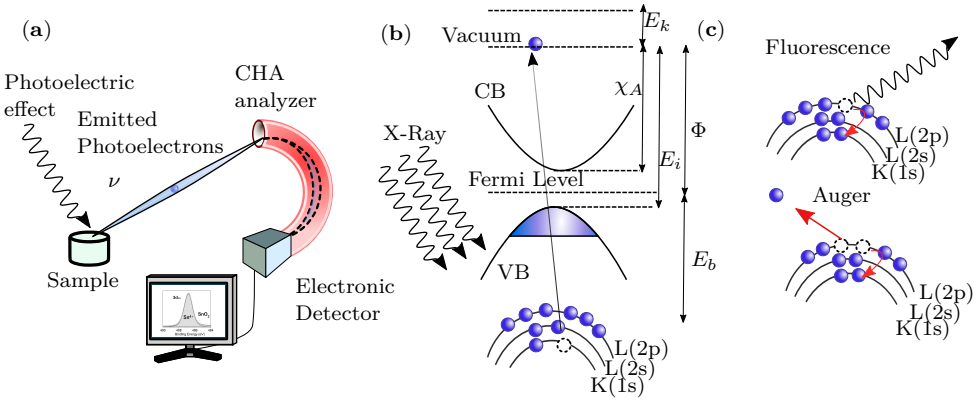

Fig. 2.14: (a) Scheme of the XPS measurement system (b) Electron photoemission scheme (c) Relaxation processes after hole generation.

When a photon beam with enough energy impinges a sample it can excite electrons from both the valence band (VB) or from deep atomic core levels to the vacuum level as observed in Fig. 2.14(b).

By measuring electron kinetic energy after ejection, the binding energy due to the *Photoelectric effect* can be calculated:

$$E_k = E_\nu - E_b - \Phi \quad or \quad E_k = E_\nu - E_b \quad \text{(if } E_F \text{ is used as the reference level)} \quad (2.9)$$

where E_k is the kinetic energy of the emitted photoelectrons, E_ν is the source photon energy and E_b is the binding energy of emitted electrons and Φ is the Work Function of the spectrometer.

Fig. 2.14(c) shows different processes that appear due to photoelectron generation such as Flourescence and Auger electron emission.

This technique allows to study the occupy states of a sample offering information about the elemental oxidation states and chemical composition of the sample. This can be determined due to the *Chemical shift* of the binding energy in the XPS spectra which increases due to the electron transfer to higher electronegative environment diminishing the photon kinetic energy. These data shifts are identify

and listed for a wide variety of compounds in databases such as on the NIST website[89]. Besides, the spin-orbit splitting of the different orbitals (*p,d,f,..*) can be observed, with intensities ratios of 1:2 for p levels, 2:3 for d levels and 3:4 for f levels[90], allowing an easy identification of the different core levels.

X-ray photoelectron spectroscopy (XPS) has been performed at the CNR Beamline for Advanced diCHroism (BACH)[91] of the Elettra synchrotron facility in Trieste, Italy. Photoemission spectra were acquired with a Scienta R3000 electron energy analyzer in normal emission geometry with a total energy resolution of 180 meV. All the photoelectron techniques realized in this thesis were obtained with the technical help of Igor Píš and Silvia Nappini, from the Elettra Elettra Sincrotrone facilites at Trieste, Italy.

To analyze XPS data, the NIST database[89] was used to determine the origin of the XPS peaks and to identify them (by comparing the *chemical shift* or the doublet splitting). KolXPD software was used to fit the different core levels, after Shirley background subtraction and fitting them using Voigt functions.

2.2.12. X-ray Absorption Spectroscopy (XAS)

When a photon beam of intensity I_0 hits a sample of thickness d, the intensity inside the sample decays following the *Beer-Lambert* law:

$$I(d) = I_0 e^{-d/\lambda}; \quad \frac{1}{\lambda} \, \alpha \, \mu \tag{2.10}$$

where λ is the mean free path, d denotes a distance and μ is the absorption coefficient, proportional to the material cross section.

X-Ray Absorption Spectroscopy (XAS) intensity is proportional to the probability of an electron undergoing through a transition from an initial state to a final state, following the *Fermi golden rule*,[92]:

$$I_{XAS} \, \alpha \, \left| \langle \Psi_f | \, \mathcal{H} \, | \Psi_i \rangle \right|^2 \tag{2.11}$$

where I_{XAS} is the XAS intensity, Ψ_f and Ψ_i are the wavefunctions corresponding to the final and initial state and $\mathcal{H}$ a Hamiltonian operator.

Fig.2.15(a) shows the absorption edges for XAS spectroscopy. In the process, a photon with enough energy can excite an electron from a deep level to a free site in the conduction band. The unoccupied states under the vacuum level give a finite value of the XAS intensity if it fulfills $E_F - E_i = h\nu$. Thus, XAS spectroscopy allows us to observe the empty states of the material. The experimental setup to obtain XAS spectrum is shown in Fig.2.15(b), which is based on Total Electron Yield (TEY). However, there are other setups:

- Transmission mode: X-ray beam intensity follows Beer-Lambert law, and after passing through the sample the intensity decays exponentially, where the intensity $I_{XAS} \; \alpha \; log\left(\frac{I_0}{I_s}\right)$ being I_s the transmitted X-Ray intensity. These measurements require thin samples in the order of μm.

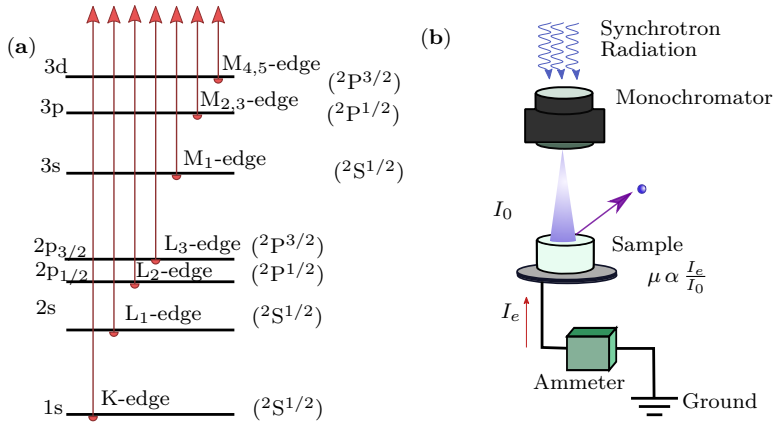

Fig. 2.15: (a) XAS edges and (b) representation of the TEY mode.

- TEY: In this mode the signal that is measured is a current intensity I_e generated to neutralize the charge of the material after the core electron emission. In this case, absorption coefficient shows a lineal dependence with intensity, $I_{XAS}\ \alpha\ \left(\frac{I_e}{I_0}\right)$, as it can be observed in Fig.2.15(b).

The XAS measurements included in this work were performed at the BACH beamline in total electron yield (TEY) by measuring the drain current through the sample. The photon energy resolution was set to 0.15 eV at Ni $L_{3,2}$-edge and O K-edge; 0.1 eV at Sn $M_{5,4}$ edge and 0.1 for Ti $L_{3,2}$. Measurements have been performed at high vacuum (10^{-10}-10^{-11} Torr) and at room temperature.

2.2.13. Atomic Force Microscopy (AFM)

Atomic Force Microscopy (AFM) is based on the detection of the forces experimented between a tip mounted on a cantilever and the studied surface. An optical system conformed by a laser and a photodiode is capable of measuring small deflections of the cantilever during the surface scanning. The cantilever can be placed over the sample in the (x, y, z) positions due to a system based on piezoelectric materials. A signal amplifier and a control unit allows to obtain high resolution topographic images. Schematic representation of an AFM is shown in Fig.2.16.

Forces between the tip and the sample are related to the material composition and the distance between them. Thus, they are elastic repulsive when the cantilever is in contact with the sample surface or either short/long range attractive forces (such as Van der Waals, adhesion forces, capillarity forces, magnetic forces...) when the cantilever tip is close to the surface.

There are also different modes to work. Either the force or the height between the tip and the sample can be kept constant and used as set-points during AFM measurements. Some of the most commonly used modes are:

- *Contact mode*: In this mode, cantilever tip is in contact with the sample and scans the surface. Contact generates repulsive forces. The user can maintain the height of the tip respective to the sample constant or maintain the detected force constant. This mode is one of the used in this thesis

- *Contactless mode or dynamic mode*: This mode allows to study soft samples. Amplitude, phase or vibration frequency are sensitive to the interaction between the tip and the sample. In particular the most used are frequency (FM-AFM; *Frequency Modulation Atomic* Force Microscopy) or amplitude (AM-AFM; *Amplitude Modulation Atomic Force Microscopy*). In AM-AFM, also known as *tapping mode*, the cantilever is oscillating at the resonance frequency.

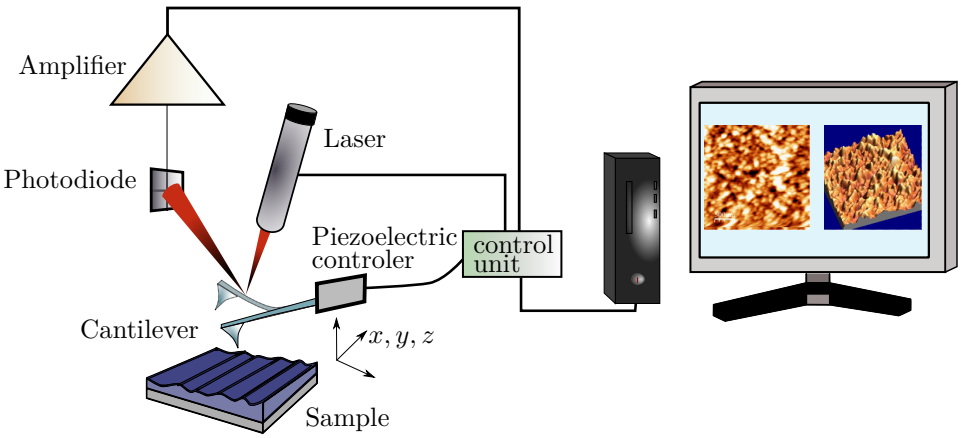

Fig. 2.16: Atomic Force Microscopy setup.

One important parameter used in AFM characterization is the root-mean-square (rms), which is the mean average of the square deviation of each of height (z_i) respective to the height average ($\bar{z}$) measured over the sample (enclosed on a area formed by n points):

$$R_{rms} = \sqrt{\frac{1}{n}\sum_{i=1}^{n}(z_i - \bar{z})} \tag{2.12}$$

AFM measurements were carried out in a Nanotec AFM controlled by Dulcinea electronics, using a silicon tip in contact mode at the Physics of Electronic Nanomaterials Group´s Laboratory, Materials Physics Department, Faculty of Physics, Complutense University of Madrid. Data acquisition and results analysis have been performed by means of the WSxM program[93].

2.2.14. UV-VIS spectroscopy

Ultraviolet and Visible spectroscopy allows to study the optical behavior of a material for different wavelengths, from near UV to even Near-InfraRed (NIR). For that purpose, three related magnitudes are studied: transmittance, reflectance and absorbance. We can define transmittance of a material as the fraction of the incident energy that passes through the material whereas reflectance is the fraction of the energy that is reflected. Therefore, absorbance consist on the energy fraction that is absorbed by a material.

These magnitudes can be described by the *Beer-Lambert* law, from where we can obtain that:

$$T(\%) = 100 \cdot \frac{I}{I_0} \tag{2.13}$$

$$A(\%) = log_{10}\frac{I_0}{I} = -log_{10}T \tag{2.14}$$

It is important to know that prior to the measurement, the equipment has to be carefully calibrated. Measurements must be performed with the minimum ambient light in darkness. In transmittance mode, detector is placed at a fixed position and 100% transmittance is calibrated. In reflectance mode, a material with practically 100% reflectance is used to calibrate. The different configurations are shown in Fig.2.17. Absorbance spectrum is obtained, considering minimum losses, by applying that:

$$T + R + A = 1 \tag{2.15}$$

Optical absorption was measured with a UV-VIS-NIR light source DH-200 ocean optics with a Deuterium and Halogen lamp at the Institute for Energy Technology (IFE), Norway, scanning in the range 150 to 1000 nm. Similarly, these measurements were performed at Materials Physics Department, Physics Faculty, Complutense Universidad de Madrid in a similar equipment (UV-1603 UV-Visible spectrophotometer, Simadzu (Izasa Sceintific)) but in a slightly smaller range between 250 to 900 nm. In this case, there is no need to change configuration and absorbance can be measured directly.

2.2.15. Contacts deposition

In some of the thin film samples on chapter 6, Ag contacts of 250-290 nm thickness were deposited with the aid of a mask on Kurt J Lesker FTC-2800 at IFE in order to measure I-V curves of the PEDOT:PSS samples deposited over silicon.

For other samples on chapter 7, gold contacts of 40 nm thickness were deposited with the aid of a mask on a Quorum Q150T ES evaporator at the Physiscs of Electronic Nanomaterials Group´s Laboratory, at the Materials Physics Department, Physics Faculty, Complutense University of Madrid. Gold contacts were fabricated in order to acquire Hall effect measurements of some of the PEDOT:PSS samples as well as to test sensing properties. Contacts for other samples to obtain Hall

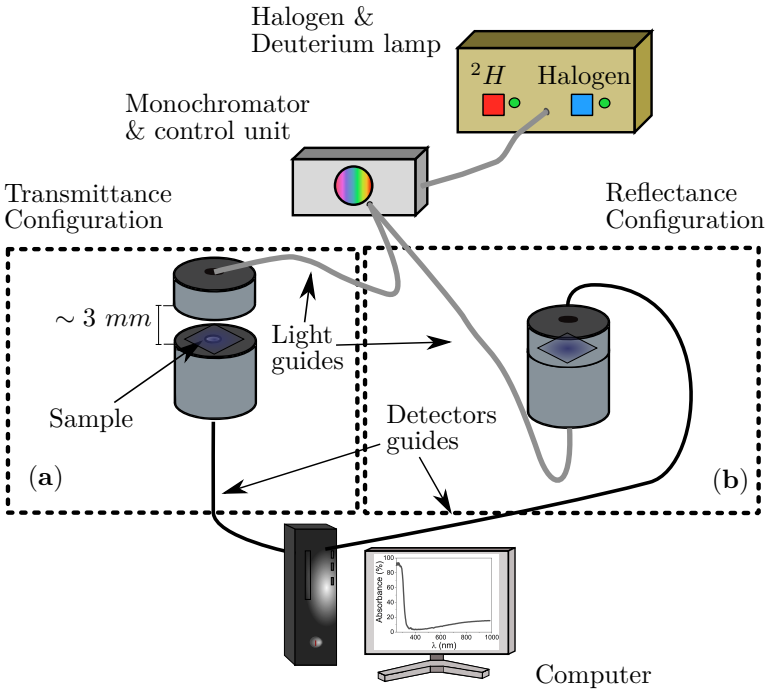

Fig. 2.17: UV-VIS-NIR spectrometer in (a) Transmittance configuration (b) Reflectance configuration.

effect were obtained using silver paste (RS Silver Conductive 186-3600). To measure the thermoelectric properties of the PEDOT:PSS layers, contacts with In/Sn (95%/5%) were welded.

2.2.16. Hall effect

The Hall effect is the appearance of a voltage difference (*Hall voltage*, V_H) across a sample, transverse to an electric current in the material and to an applied magnetic field perpendicular to the current as illustrated in Fig.2.18(a). The main equation ruling this effect is:

$$R_H = \frac{E_y}{j_x B} = \frac{V_H t}{IB} = -\frac{1}{ne} \tag{2.16}$$

where R_H is the hall coefficient, n the carrier density in cm^{-3}, t the material thickness. E_y and B_z are the electric and magnetic field, while j_x is the applied current density into the material

Hence, by obtaining the Hall coefficient we can determine parameters such as the carrier density of the material which is needed to calculate other relevant material properties as the magnetoresistivity, conductivity, sheet resistance, etc.

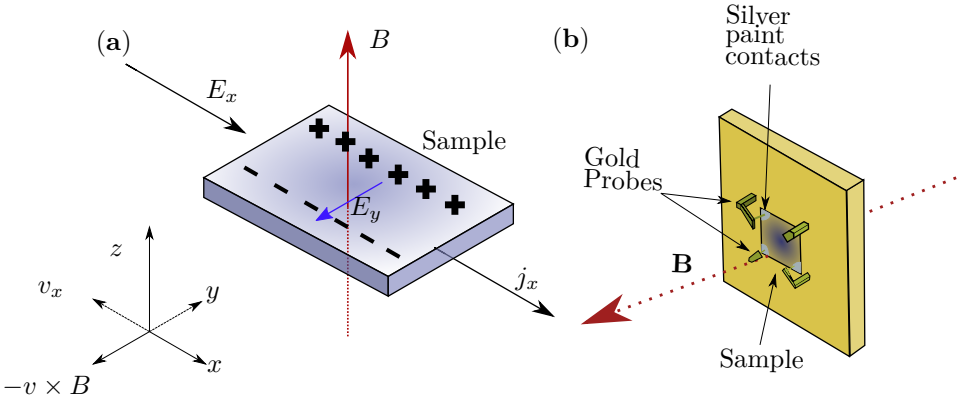

Fig. 2.18: (a) Hall effect principle and (b) 4-probes Hall effect setup in Van der Pauw configuration.

The experimental setup is based on the *Van der Pauw* configuration. With the square contact distribution, as close to the edges as possible, a current is generated to flow in one direction, for example I_{AB} and the voltage across the perpendicular direction is measured V_{CD}, thus $R_{AB,CD} = \frac{V_{CD}}{I_{AB}} = \frac{V_C - V_D}{I_{AB}}$

By reversing the polarity of the current and voltage through the different contacts we can calculate R_{vertical} and R_{vertical}, minimizing errors.

$$\begin{aligned} R_{vertical} &= \frac{R_{AB,CD} + R_{CD,AB} + R_{BA,DC} + R_{DC,BA}}{4} \\ R_{horizontal} &= \frac{R_{BC,DA} + R_{DA,BC} + R_{CB,AD} + R_{AD,CB}}{4} \end{aligned} \tag{2.17}$$

For the particular case $R = R_{ver.} = R_{hor.}$ we can obtain the sheet resistance as:

$$R_s = \frac{\pi R}{ln(2)} \tag{2.18}$$

If the thickness is known, we can obtain the resistivity, ρ, and therefore the conductivity, $\sigma = \frac{1}{\rho}$ by solving the following equation:

$$e^{-R_{hor.} \cdot \frac{\pi d}{\rho}} + e^{-R_{ver.} \cdot \frac{\pi d}{\rho}} = 1 \tag{2.19}$$

To calculate Hall coefficient and, subsequently obtaining carrier density among other parameters, measurements are repeated but in presence of a magnetic field on the $\hat{z}$ and $-\hat{z}$ directions (Designated by P and N subindexes) such as $V_{AC,P} = V_{C,P} - V_{A,P}$. Therefore:

$$\begin{cases} V_{AC} = V_{AC,P} - V_{AC,N} \\ V_{BD} = V_{BD,P} - V_{BD,N} \\ V_{CA} = V_{CA,P} - V_{CA,N} \\ V_{DB} = V_{DB,P} - V_{DB,N} \end{cases} \implies \begin{cases} V_H = \dfrac{V_{AC} + V_{BD} + V_{CA} + V_{DB}}{8} \end{cases}$$

Finally, we can determinate the value of the carrier concentration

$$n_s = \frac{IB}{q|V_H|} \tag{2.20}$$

The polarity of the Hall voltage is an indicator of the carrier type of the semiconductor. This means that, if positive, the main charge carrier consist of holes what is referred to as saying that the material possesses p-type behavior, and if it is negative, the material possesses n-type behavior, being the main charge carrier electrons.

Van der Pauw configuration Hall effect measurements were performed at room temperature using a Hall Ecopia AMP55T controlled with electronics HMS-7000 with 4 gold probes as shown in Fig. 2.18(b). This module allows to increase temperature up to 350K and decrease using liquid N_2 to approximately 120K. These measurements have been obtained at the Physics of Electronic Nanomaterials Group´s Laboratory, Materials Physics Department, Faculty of Physics, Complutense University of Madrid.

2.2.17. Gas sensing setup

As a proof of concept, PEDOT:PSS layers were evaluated as possible candidates for chemiresistive gas sensing devices. For that purpose, PEDOT:PSS layers were introduced into a sealed chamber where a gas carrier was introduced, and the surface-response of the layer was measured. Experimental setup used for this work is shown on Fig.2.19 and was designed by Dr. Javier Bartolomé to whom the author express gratitude for his practical help. The system consists on eight valves controlled by an programmable circuit board, which allows to open or close the valves as desired, allowing the gas to enter the chamber or not. This gas will pass through a blubber where the analyte gas to study (ethanol, water vapor) will start to bubble and will flow to the chamber where the sample is placed and connected to a Keithley 2400 to measure the changes on conductivity. The measuring process is as follows.

1. A gas flow, referred to as carrier gas (Dry air, N_2) will pass through the system during variable time, often 1200 s. During this time oxygen will be absorbed by the surface.

2. A mixed gas flow formed by the carrier gas and the analyte gas to study will enter the chamber in which the surface of the sample and the previously absorbed oxygen will react with the material. The duration of these cycles were varied taking into account if the material is saturated or not in periods of 300, 480 and 600 s.

3. During the same time span than for the previous sample, the analyte flow is cut and only the gas is allow to pass. The cycle is repeated a few times.

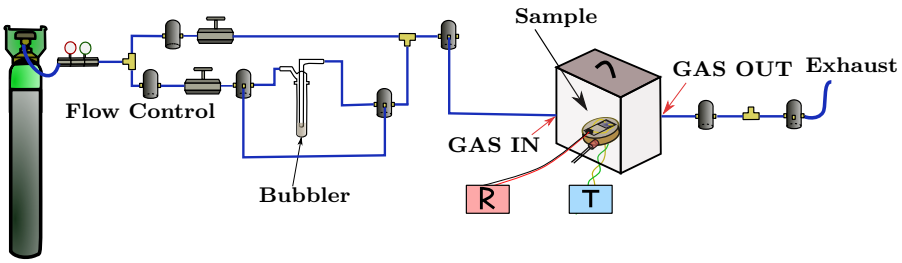

Fig. 2.19: Gas sensing setup.

Chapter 3.
SnO_2 nanoparticles doped with Li or Ni

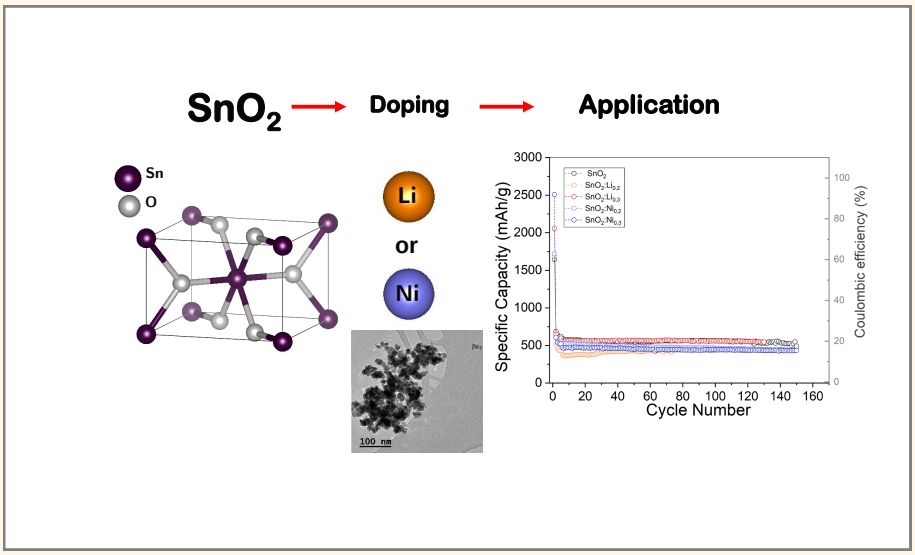

Abstract: In this chapter, undoped and Li or Ni doped SnO_2 nanoparticles synthesized via hydrolysis are studied. Firstly, a morphological, structural and compositional characterization was performed based on several techniques such as XRD, Raman spectroscopy, EDS, ICP-OES, SEM, and TEM. Optical and electrical properties were studied by PL and Hall effect measurements, respectively. Finally, the electronic properties of the nanoparticles were analyzed by means of XPS, XAS and resonant XPS in a synchrotron radiation facility. To conclude, the application of these nanoparticles as anodes in Li-ion batteries were evaluated.

This chapter includes adapted material from: A. Vázquez-López et al., Influence of doping and controlled Sn charge state on the structural stability and performance of SnO_2 nanoparticles as anodes in Li-ion batteries, *J. Phys. Chem. C*, **2020**, 124, 34, 18490–18501[94].

3.1. Synthesis, morphological, structural and compositional characterization

SnO_2 nanoparticles were synthesized via hydrolysis, as described in subsection 2.1.1. Undoped and Li or Ni doped SnO_2 nanoparticles were obtained by combining the stoichiometric amounts of the selected precursors and mixed with vigorous agitation at 50 °C into a basic medium. Distilled water was added and then it was left for stirring 2h at 100 °C. The obtained mixture was rinsed and centrifuged until reaching neutral pH. Finally, the dry powder was introduced into a furnace at 350 °C for 20 h.

3.1.1. XRD characterization

XRD patterns from both undoped and doped (Li, Ni) SnO_2 nanoparticles are displayed on Fig.3.1. All the XRD patterns can be indexed according to the cassiterite structure of SnO_2 ,which possesses a tetragonal unit cell and belongs to the $P4_2/mnm$ symmetry group, with lattice parameters close to a = b = 4.738 Å and c = 3.186 Å (Inorganic Crystal Structure Database (file) (ICSD) nº: 00-001-0625).

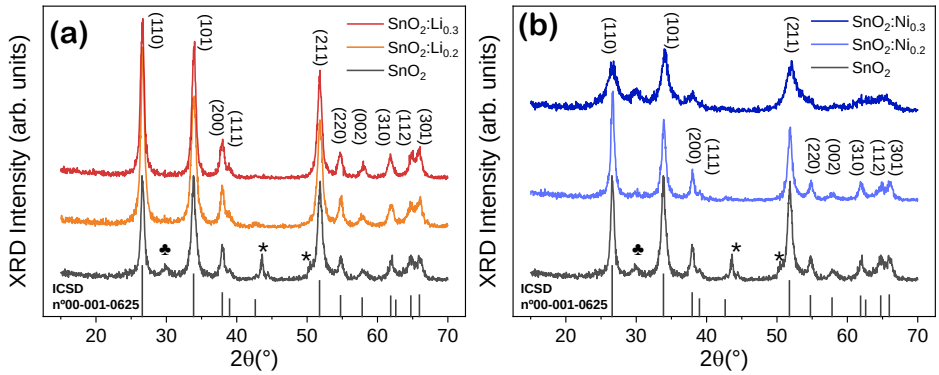

Fig. 3.1: XRD patterns of both undoped and (a) Li or (b) Ni doped SnO_2 nanoparticles. Peaks corresponding to SnO are marked with (♣) whereas peaks due to the sample holder are marked with (*). Histograms correspond to the spectra of the ICSD file nº00-001-0625 corresponding to SnO_2.

The XRD results confirm the high crystallinity of the as-synthesized nano-

particles, even for those with the highest amount of dopants. Peaks from the precursors or different secondary compounds were not observed for Li doped samples. For the undoped and the Ni doped SnO_2 samples, a weak peak around 30° corresponding to a small amount of romarchite SnO (ICSD nº: 01-072-1012) obtained during the synthesis can be observed, as marked with (♣) in Fig. 3.1.

By using thermal treatment temperatures higher than that employed in this work, 350 °C, the presence of SnO could be completely removed, although larger SnO_2 nanoparticles will be obtained instead. Peaks observed in 43.5-44.5° and 50° are due to the sampleholder, maked with (*) in Fig.3.1.

The broadening of the XRD peaks, mainly for the SnO_2:$Ni_{0.3}$ sample, indicates the low dimensions obtained for the synthesized nanoparticles. No peak shift was observed for the doped samples. The average crystallite dimensions (D) were estimated from the XRD patterns analysis by using the Scherrer formula shown in eq.2.2. Results are displayed on Table 3.1.

Table 3.1: Size estimation of the undoped and doped SnO_2 nanoparticles and the corresponding lattice parameters obtained from XRD analysis

Sample	**Size (nm)**	**a(Å)**	**c(Å)**	**ratio c/a**	**V^3(Å^3)**
SnO_2	10.45 ± 0.05	4.73(8)	3.19(4)	0.674±0.001	71.70±0.26
SnO_2:$Li_{0.2}$	9.76 ± 0.03	4.74(2)	3.18(3)	0.671±0.001	71.58±0.09
SnO_2:$Li_{0.3}$	11.19 ± 0.03	4.73(0)	3.18(6)	0.673±0.001	71.28±0.12
SnO_2:$Ni_{0.2}$	10.62 ± 0.05	4.73(3)	3.18(7)	0.673±0.001	71.40±0.19
SnO_2:$Ni_{0.3}$	7.29 ± 0.05	4.72(3)	3.16(4)	0.670±0.001	70.59±0.13

To obtain the cell parameters a and c, two planes with different Miller indexes (101) and (200) were chosen from the XRD patterns and taking into account the tetragonal structure of the unit cell:

$$\frac{1}{d_{hkl}^2} = \frac{1}{a^2}\left[h^2 + k^2 + l^2\left(\frac{a}{c}\right)^2\right] \tag{3.1}$$

As observed in Table 3.1, the averaged dimensions of the crystallite sizes are around 10 nm. The SnO_2:$Ni_{0.3}$ nanoparticles exhibit the lowest dimensions. Cell parameters of the tetragonal structure (a and c) are also indicated in Table 3.1, as well as the calculated cell volume ($V = a^2 \cdot c$ [Å^3])

3.1.2. EDS and ICP-OES characterization

To analyze the chemical composition of the sample under study, EDS measurements have been performed. For that purpose, nanoparticles were deposited on carbon tape over a Cu substrate. EDS measurements have been performed using a SEM microscope with an electron beam of 15 kV and 1.5 nA.
Normalized spectra can be observed in Fig.3.2 for the SnO_2 nanoparticles doped with lithium or nickel, respectively.

In both doped and undoped samples we can clearly observe emission lines attributed O $K_{\alpha 1}$(range 0-1 keV) and Sn L_{α}, L_{β}(range 3-4 keV). In some spectra a weak contribution corresponding to the lines $K_{\alpha 1}$ and $K_{\alpha 2}$ from Cl can be also appreciated, probably due to the use of Cl-containing precursors $SnCl_2{\cdot}2H_2O$, LiCl or $NiCl_2{\cdot}6H_2O$ to introduce the doping species. Nickel doped samples present Ni peaks corresponding to K_{α} and L_{α} at 7.4 and 0.8 keV[83]. Inset in Fig.3.2(b) shows detailed region between 7 and 8 keV, showing that the presence of nickel is different in both samples.

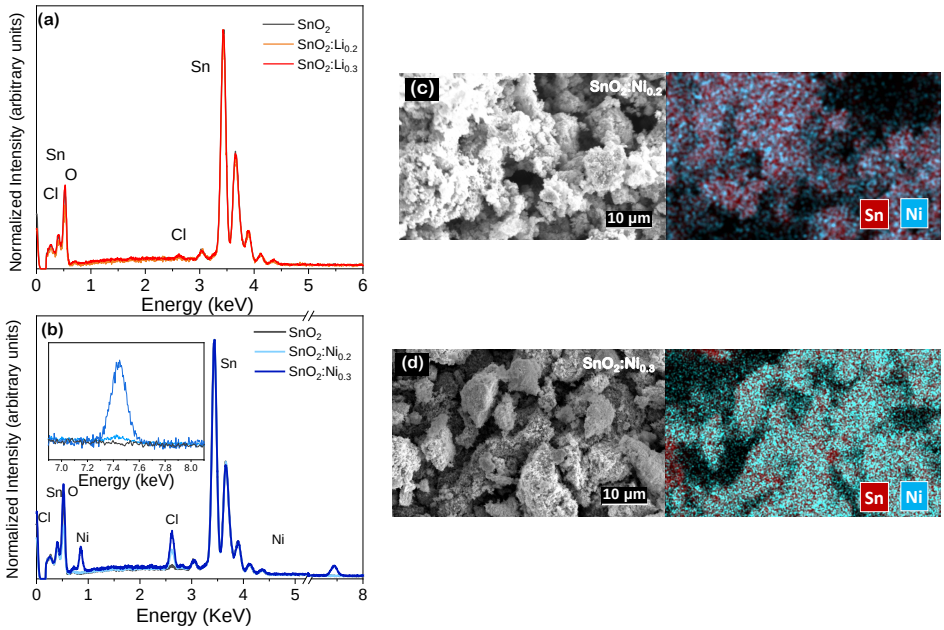

Fig. 3.2: Normalized EDS spectra acquired for undoped and (a) Li and (b) Ni doped SnO_2 nanoparticles. Inset in (b) shows detailed region between 6.5 and 8.5 keV. Figures (c) and (d) show the SE and EDS mapping of Ni and Sn corresponding to samples SnO_2:$Ni_{0.2}$ and SnO_2:$Ni_{0.3}$

Quantification of the present elements were performed as described in subsection 2.2.3. The atomic ratio Sn/O is close to the theoretical one from SnO_2 (33% /66%) based on the individual values of such elements shown in Table 3.2.

To quantify the presence of Lithium in Li-doped samples, the technique used was ICP-OES as this technique allows to detect light elements. Table 3.2 shows the quantification results for ICP-OES for the samples SnO_2:$Li_{0.2}$ and SnO_2:$Li_{0.3}$. For the sample SnO_2:$Li_{0.2}$ only 0.06 % at has been introduced. For the sample SnO_2:$Li_{0.3}$ almost 1% has been introduced. Notice that the estimation obtained

Table 3.2: Atomic percentages of Sn, O and Ni obtained by EDS and Li obtained by ICP-OES

Technique	(% at)	SnO_2	$Li_{0.2}$	$Li_{0.3}$	$Ni_{0.2}$	$Ni_{0.3}$
EDS	**Sn**	22.4 ±2.6	23.9 ± 2.7	21.2 ± 2.5	24.6 ± 2.9	21.7± 2.6
	O	77.1± 4.7	75.6 ± 5.6	78.3 ± 5.2	74.2 ± 5.1	73.3 ± 5.0
	Ni	-	-	-	0.5 ± 0.1	3.8 ± 0.3
ICP-OES	**Li**	-	0.06 ±0.03	0.95 ±0.02	-	-

through EDS for this samples does not take into account the presence of lithium and slightly overestimate and oxygen content.

3.1.3. TEM characterization

Fig.3.3 shows the TEM images of the undoped (SnO_2) and the doped nanoparticles with the highest dopant concentration, SnO_2:$Li_{0.3}$, SnO_2:$Ni_{0.3}$, as representative examples of the doped samples. As observed in the TEM images shown in Fig.3.3 the nanoparticles exhibit a rounded appearance and dimensions of 10 nm. Nanoparticle size was estimated from the TEM images, and the particle size dispersion is presented on the corresponding histograms as inset of Fig.3.3(a)-(c). The estimated averaged dimensions correspond to 10.8 nm for SnO_2, 11.9 nm for SnO_2:$Li_{0.3}$ and 5.4 nm for SnO_2:$Ni_{0.3}$. These results are in agreement with XRD measurements, which also indicated the lowest dimensions for the highest Ni doping and similar size tendency. The corresponding SAED patterns, shown in Fig.3.3(d)-(f) confirm the crystallinity of the undoped and doped SnO_2 nanoparticles. The main crystalline planes obtained from the analysis of the SAED patterns are in agreement with those observed in XRD: (110), (101) and (200) planes.

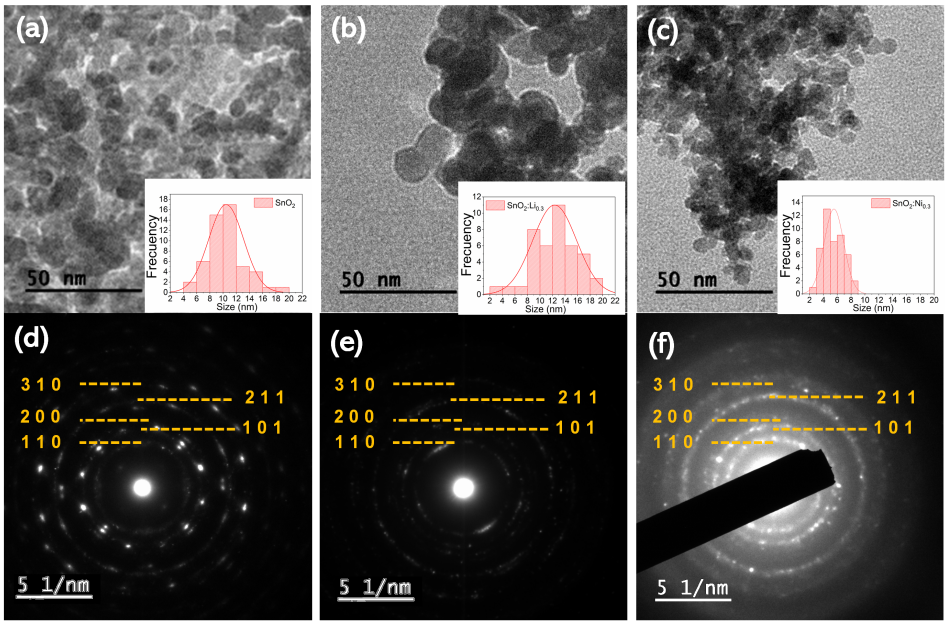

Fig. 3.3: TEM images corresponding to (a) SnO_2, (b) SnO_2:$Li_{0.3}$ and (c) SnO_2:$Ni_{0.3}$ nanoparticles. Insets show histograms with the average particle size distribution. (d),(e),(f) shows their corresponding SAED patterns.

3.1.4. Raman spectroscopy characterization

Samples were studied in a confocal microscope Horiba Jobin Yvon LabRam Hr800 using a He-Cd laser $\lambda = 325$ nm as excitation source.

SnO_2 belongs to the space group D_{4h}^{14}, as shown in section 1.1, which normal lattice vibration modes at the Γ point of the Brillouin zone are given by $\Gamma = 1\cdot A_{1g} + 1\cdot A_{2g} + 1\cdot A_{2u} + 1\cdot B_{1g} + 1\cdot B_{2g} + 2\cdot B_{1u} + 1\cdot E_g + 3\cdot E_u$[95]. This representation presents two IR active modes (A_{2u}, E_u), four Raman active modes (A_{1g}, B_{1g}, B_{2g}, E_g) and two inactive modes (A_{2g}, B_{1u})[96].

Usually, the dominant Raman modes are E_g (∼490 cm^{-1}), A_{1g} (∼640 cm^{-1}) and B_{2g} (∼760 cm^{-1}). These vibrational modes are associated with the movements of Sn and O, in particular, E_g is associated with the movement of O anions along the c axis, while A_{1g} and B_{2g} are associated with elongation (expansion and contraction) of O-Sn-O bonds and movement of the anions in a symmetric and asymmetric manner, respectively, orthogonal to the c axis as represented in Fig.3.4(a)-(d). Modification and activation of certain Raman modes can be promoted by many factors such as the reduction of dimensions of the SnO_2 lattice. To observe the difference in the Raman spectra of the synthesized nanoparticles, they were compared to the Raman signal from commercial SnO_2 nanoparticles (Tin(IV) oxide,-325 mesh, 99.9%, Sigma-Aldrich). Raman spectra of commercial and as-synthesized nanoparticles are presented at Fig.3.4(e). Both spectra present main

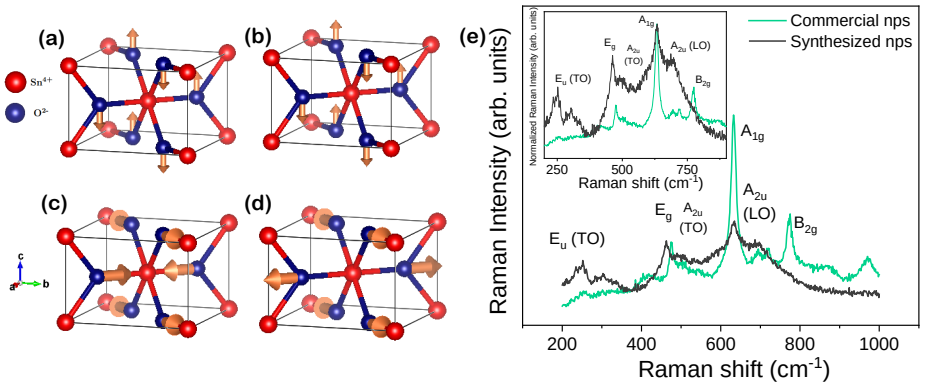

Fig. 3.4: Graphic representation of common rutile vibrational modes on SnO_2 (a) E_{1g}, (b) E_{2g}, (c) A_{1g} and (d) B_{2g} modes and (e) Raman spectra from commercial (Sigma-Aldrich) and synthesized SnO_2 nanoparticles. Inset in(e) shows the 225-725 cm^{-1} region normalized to the A_{1g} region for both samples.

contributions at around 240 cm^{-1}, 460 cm^{-1} and 640 cm^{-1}, which can be associated with E_u(TO), E_g and A_{1g} modes, respectively. E_u mode consists on the vibration of both Sn and O atoms in the plane perpendicular to the c axis[29]. As observed in Fig.3.4(e) Raman spectra for the obtained nanoparticles in comparison to commercial nanoparticles are wider which can be attributed to the reduced size of the nanoparticles.

In addition to these vibrational modes, other weak peaks at around 500 cm^{-1} and 690 cm^{-1} can be also observed in the Raman signal from the nanoparticles as observed in Fig.3.4(e), which can be assigned to the IR active A_{2u}(TO) and A_{2u}(LO), respectively. In particular, these modes appear due to the relaxation of the selection rules owing to the reduced dimensions of the nanoparticles or increasing lattice disorder. In this case the B_{2g} mode is not observed for the undoped SnO_2 nanoparticles, contrary to the usual SnO_2 Raman signal, possibly because the presence of defects could hinder this vibrational mode. The position of the main vibrational modes from the SnO_2 nanoparticles and commercial samples are indicated in Table 3.3. Positions obtained from Diéguez et al.[96] are also included for comparison. As it can be observed on the Table 3.3, B_{2g} is absent in the synthesized nanoparticles and a shift on the E_g mode to lower wavenumber is also observed in the synthesized nanoparticles.

Raman spectra for the undoped and doped nanoparticles are shown in Fig.3.5. It is clearly noticeable that Raman spectra from SnO_2 is strongly modified by the presence of dopants. Li doping induces an increase in the relative intensity of the E_g mode which dominates the corresponding spectrum for SnO_2:$Li_{0.2}$, as shown in Fig.3.5(a). In SnO_2:$Li_{0.3}$, a decrease in the relative intensity of the E_g and A_{2u} modes can be observed, while the A_{1g} mode increases and dominates the corresponding Raman signal. Contrary to the rest of the samples, the B_{2g} mode

Table 3.3: Frequencies (cm^{-1}) of the different vibrational modes observed for commercial and synthesized SnO_2 as compared with the literature[96].

	Vibrational modes						
	E_u			A_{2u}			
Sample	TO	LO	E_g	TO	LO	A_{1g}	B_{2g}
SnO_2 commercial nps	254.2	-	474.6	501.6	695.1	632.4	775.1
SnO_2 synthesized nps	249.7	-	462.7	490.0	691.9	634.6	-
Diéguez et al.[96]	244	-	476	477	705	638	782

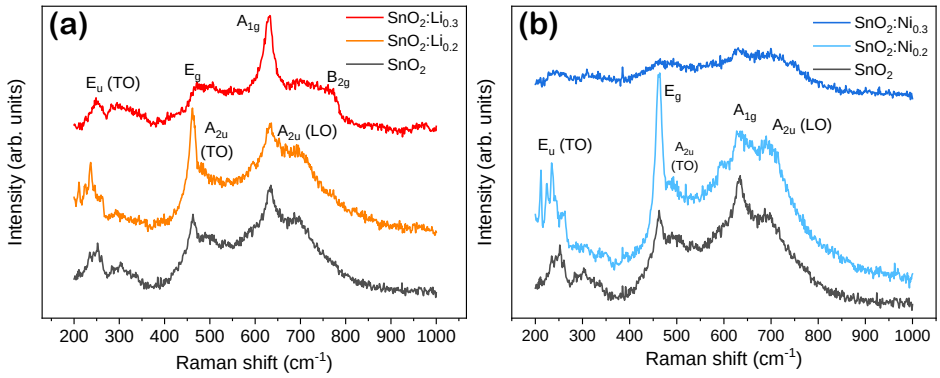

Fig. 3.5: Raman spectra from undoped and (a) Li or (b) Ni doped SnO_2 nanoparticles. These spectra have been recorded with the UV laser as excitation source.

at around 780 cm^{-1} can be distinguished for SnO_2:$Li_{0.3}$. As previously stated, this mode is related to comprising motions of O anions with respect to Sn cations perpendicular to the c-axis.

Table 3.4: Frequencies (cm^{-1}) of the different vibrational modes for undoped and doped SnO_2 nanoparticles as compared with the literature[96].

	Vibrational modes						
	E_u			A_{2u}			
Sample	TO	LO	E_g	TO	LO	A_{1g}	B_{2g}
SnO_2	249.7		462.7	490.0	691.9	634.6	-
SnO_2:$Li_{0.2}$	237.8	-	462.7	486.2	691.9	633.5	-
SnO_2:$Li_{0.3}$	251.9	-	476.8	-	699.5	630.3	769.4
SnO_2:$Ni_{0.2}$	234.6	-	462.7	487.6	688.6	633.5	-
SnO_2:$Ni_{0.3}$	-	-	-	-	-	-	
Diéguez et al.[96]	244	-	476	477	705	638	782

On the other hand, the Raman spectra from nickel doped samples are presented in Fig.3.5(b). Low Ni doping induces an increase in the relative intensity of the E_g mode at 460 cm^{-1} and a decrease in the relative intensity of the A_{1g} mode, which allows to distinguish a weak contribution at around 600 cm^{-1}. SnO_2:$Ni_{0.3}$ presents a quenched signal and the modes are weakened.

3.2. Optical properties analysis

In this section the optical response of the doped and undoped nanoparticles are studied based on different excitation sources, measuring photo luminescence (PL) at RT (T=298 K) and cathodoluminescence (CL) at RT and lower temperatures (down to to 120 K).

3.2.1. Photoluminescence

The luminescent properties of the SnO_2 nanoparticles were analyzed by photoluminescence at room temperature using and UV laser (λ = 325 nm) as excitation source, as shown in Fig.3.6. PL spectra were acquired using a D_1 filter (as described in subsection 2.2.9) and a confocal pinhole of 950 μm.

Fig.3.6(a) shows the PL spectra of the synthesized nanoparticles and commercial SnO_2. There is a shift on the main peaks on synthesized nanoparticles in comparison with commercial nanoparticles. Moreover, the intensity of the former is much lower.

Undoped SnO_2 nanoparticles show a broad PL spectrum from the near-IR to the UV range centered around 2.3 eV. Deconvolution of the PL signal to Gaussian contributions has been performed after background subtraction which indicates the presence of bands at $\sim$ 1.6 eV, 1.9 eV, 2.3 eV, 2.6 eV and 2.9 eV. Band at 1.6 eV is omitted in the figure as it is near to the limit of detection of the CCD and near to the laser modulations. Also, the presented SnO_2:$Ni_{0.3}$ is not normalized due to low signal. The high relative intensity of the orange and green bands (1.9, 2.3 eV) associated with oxygen vacancies confirms the presence of these native defects in the probed SnO_2 nanoparticles. The low energy band at 1.6 eV has been also reported for doped SnO_2 and could be attributed to intrinsic defects related to the presence of Sn-interstitial defect level promoted by doping[97]. The high energy emission at 2.9 eV can be related to recombination of an electron from the conduction band with a $V_O^{\bullet\bullet}$.[98]. These main emissions from SnO_2 and their possible origin are summarized in Table 3.5.

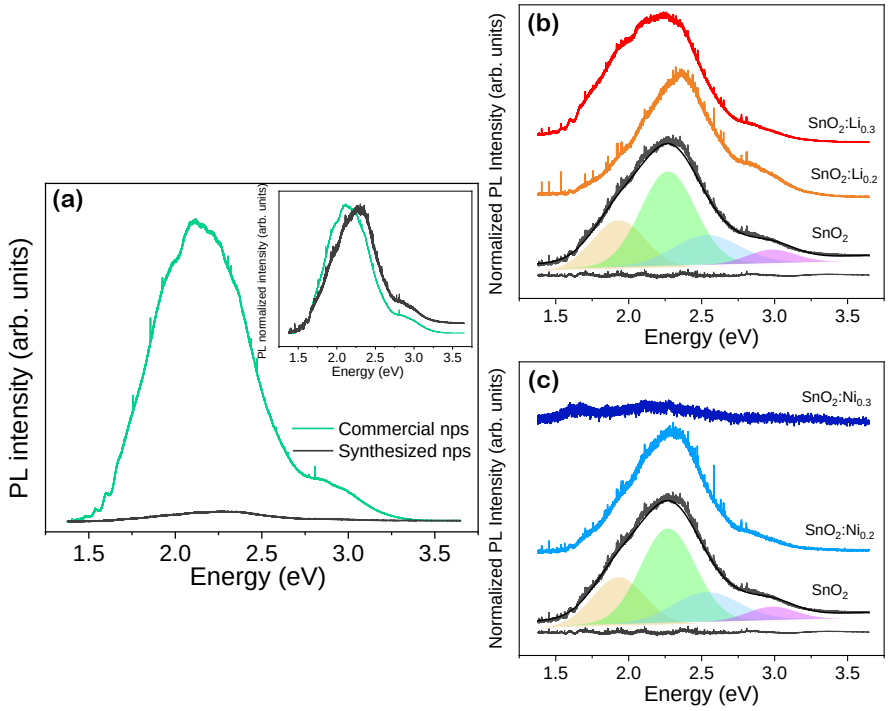

Fig. 3.6: PL spectra from commercial and synthesized nanoparticles where inset shows normalized photoluminescence spectra. Normalized PL spectra of undoped and (b) Li or (c) Ni doped SnO_2 nanoparticles.

Table 3.5: SnO_2 luminescence bands, as proposed in the literature.

Name	E (eV)	λ (nm)	Origin
Infrared band	~ 1.6	~ 775	-Intrinsic defects promoted by doping which mechanism could be explained by the presence of Sn-interstitial defect level.[97]
Orange band	~ 1.9	~ 652	-Associated with defect states due to oxygen vacancies[99], acting as a donor levels.
Green band	~ 2.3	~ 539	-Normally associated with oxygen vacancies with two adjacent oxygen atoms missing[100] or to Self-Trapped Holes (STH).
Blue band	~ 2.6	~ 476	-Transitions involving surface states.
Violet band	~ 3.0	~ 427	-Associated with recombinations of an electron from the CB with vacancies $V_O^{\bullet\bullet}$.[98]

3.2.2. Cathodoluminescence

Cathodoluminescence (CL) was measured using a SEM Hitachi S-2500 Microscope at RT and lower temperatures using an acceleration voltage of 15 kV. Optical properties of a semiconductor such as luminescence depends on the temperature. This temperature variation will modify the electron-phonon interactions as well as induce changes on the band structure of the material. At low temperatures, the efficiency yield of radiative processes is increased versus the dominant non-radiative processes at high temperature, therefore decreasing the temperature will enhance the signal of the luminescence.

As observed in Fig.3.7, at RT commercial nanoparticles posses a wide emission on the visible range, with a high green emission centered at ~ 2.2 eV. Synthesized nanoparticles however posses two clear shoulders where the blue band predominates. Li doped SnO_2 presents luminescence mainly at ~ 2 eV.

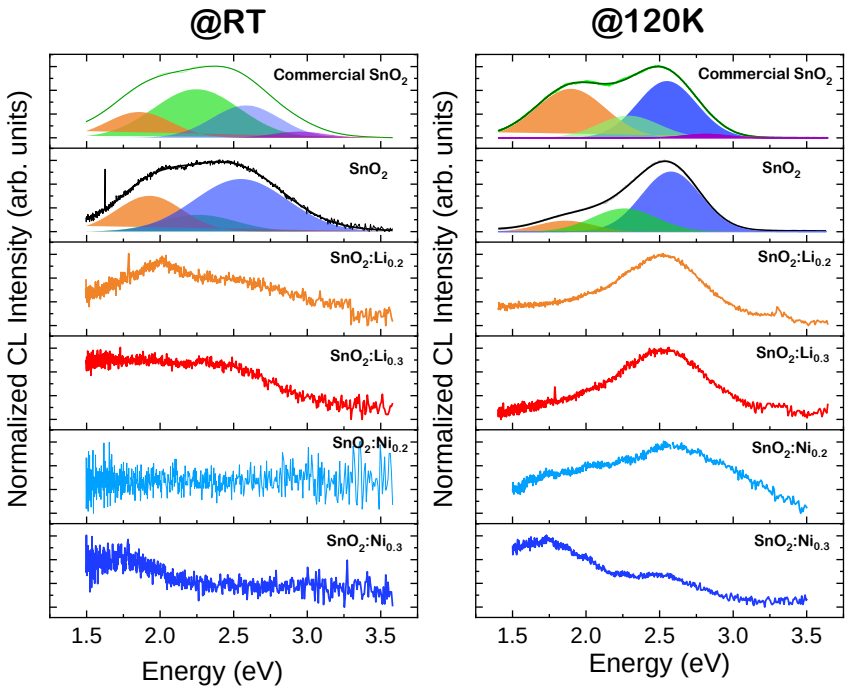

Fig. 3.7: Normalized CL spectra at (a) 298K and (b) 120K corresponding to the doped and undoped nanoparticles. The first spectra show the CL corresponding to the commercial SnO_2 nanoparticles as a reference.

The spectra corresponding to the CL signal at low temperatures are shown on Fig.3.7(b). Commercial nanoparticles show a wide emission on the visible range, with two clear shoulders and similar contributions of the orange and blue band. Synthesized SnO_2 nanoparticles show a predominately blue band at ~ 2.5 eV. Li

doped SnO_2 nanoparticles show a similar spectrum that undoped nanoparticles with a main blue band contribution. Ni doped SnO_2 luminescence is really weak.

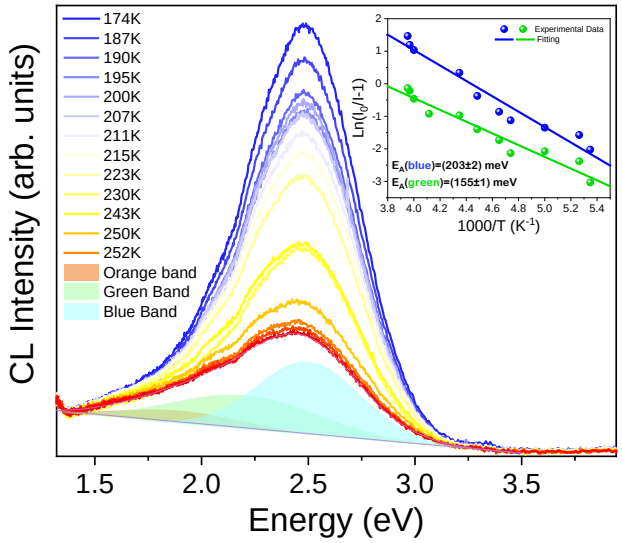

Fig. 3.8: Evolution of cathodoluminescence of undoped SnO_2 nanoparticles as a function of temperature. Inset shows linear fit to obtain the activation energy corresponding to the emission band centered at 2.5 and 2.2 eV.

Fig.3.8 shows spectra acquired of SnO_2 nanoparticicles obtained between 170-250 K. It can be observed how the total CL signal is quenched when the temperature of the sample increases, due to increasing non-radiative recombination. Thus, this quenching of the total luminescent intensity could be explained with the contribution of a non-radiative process which is thermally activated.

It can be also observed in Fig.3.8 that the temperature also affects the relative intensity of each of the luminescence bands, which can be divided in three main emissions, similar to the observed emission bands for photoluminescence which are drawn on Fig.3.8 as orange ($\sim$ 1.9 eV), green ($\sim$ 2.2 eV) or blue ($\sim$ 2.5 eV). At low temperatures, a weak contribution at $\sim$ 3.0 eV appears as well. The origins of these luminescence bands have been described on the previous section. This intensity-temperature evolution of the aforementioned bands can be described by *Configuration coordinate model*[101]:

$$I = \frac{I_0}{1 + A \cdot e^{\frac{-E_A}{k_B \cdot T}}} \tag{3.2}$$

Where I_0 is the intensity at the lowest temperature, A is a pre-exponential factor, E_A is the activation energy (in meV), k_B is the Boltzmann constant and T is the temperature. This equation is often referred as the *Arrhenius equation*. Inset on

Fig.3.8 shows the fitting to the Arrhenius equation of the blue band (i.e $\sim$ 2.5 eV) which leads to an activation energy of 203±2 meV while the analysis of the green band ($\sim$ 2.25 eV) leads to an activation energy of 155±1 meV. The differences between the activation energies is a clear indicator on the different mechanisms involved in these emissions.

3.3. Electric characterization

3.3.1. Hall Effect

Hall effect measurements were performed on the samples in order to investigate their electrical properties at room temperature. For that purpose, the nanoparticles were pressed into pellets using a hydraulic press Mega KP30A and silver paint contacts were prepared over the pressed pellets.

The calculated values corresponding to the conductivity and charge carrier concentration are shown in Table 3.6. SnO_2 exhibits n-type conductivity, as indicated with the negative sign on the carrier concentration, due to the formation of oxygen vacancies and Sn interstitial defects, which energy levels are close to the conduction band[102]. SnO_2 doping with different elements, such as Sb as an example, can increase the n-type behavior. This is due to the introduction of donor centers near the CB, and this leads to charge carrier concentrations up to 10^{20} cm^{-3} .

Table 3.6: Variation in the charge carrier concentration and the conductivity of the undoped and doped SnO_2 nanoparticles..

Sample	**D** (μm)	σ ($S \cdot cm^{-1}$)	**Δn** (cm^{-3})
SnO_2	700	(2.91±0.78)·10^{-1}	(-4.58±0.73)·10^{17}
SnO_2:$Li_{0.2}$	800	(4.56±0.58)·10^{-1}	(-2.65±0.20)·10^{17}
SnO_2:$Li_{0.3}$	1100	(2.00±0.15)·10^{-5}	(-1.59±0.29)·10^{12}
SnO_2:$Ni_{0.2}$	1650	(1.13±0.01)·10^{-2}	(-5.94±0.34)·10^{15}
SnO_2:$Ni_{0.3}$	1600	(1.18±0.16)·10^{-5}	(-1.34±0.35)·10^{11}

Undoped SnO_2 sample shows averaged conductivity of 2.91·10^{-1} S·cm^{-1} and carrier concentration of 4.58 10^{17} cm^{-3}, which is in accordance with typical values around 10^{17} -10^{20} cm^{-3} reported for SnO_2 nanoparticles[46,94]. Low Li or Ni doping either improves or decreases, respectively, the corresponding electrical conductivity values. In particular, the sample SnO_2:$Li_{0.2}$ shows the highest conductivity value. By increasing the dopant concentration, a lowering of the conductivity is caused both for Li and Ni doping. In that case, values around 10^{-5} S·cm^{-1} were obtained for SnO_2:$Li_{0.3}$ and SnO_2:$Ni_{0.3}$.

3.4. Electronic characterization

3.4.1. XPS

XPS spectra were calibrated using the C($1s$) core level from adventitious carbon at 284.6 eV. After Shirley background correction, Voigt functions were used for the deconvolution of the spectra. In Fig.3.9 XPS surveys for (a) Li doped and (b) Ni doped samples are represented. XPS spectrum from undoped SnO_2 is also included in Fig.3.9(b) as a reference. For the Li doped nanoparticles a beam photon energy of 253 eV was used in order to observe Li($1s$) core level, whereas for undoped and Ni doped SnO_2 a photon beam energy of 650 eV was employed.

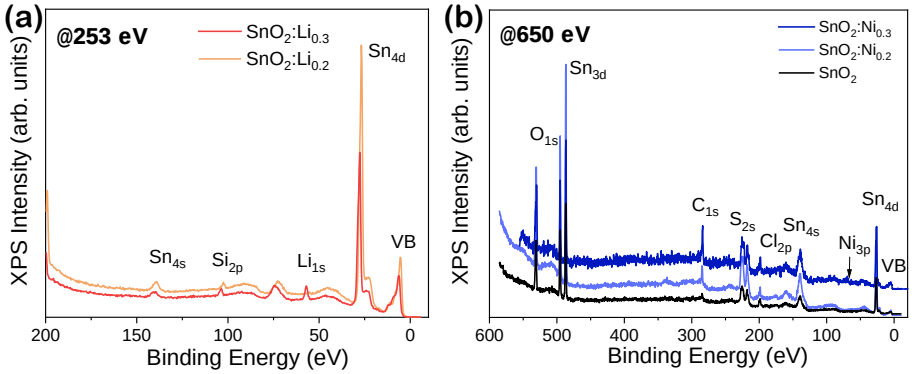

Fig. 3.9: XPS surveys from (a) Li and (b) Ni doped SnO_2 nanoparticles acquired with a beam energy of 253 and 650 eV, respectively. In (b) survey from undoped SnO_2 is shown for comparison.

Fig.3.10 shows the Sn ($3d_{5/2}$) and ($3d_{3/2}$) core levels from the analyzed samples, for both undoped and doped (Ni, Li) samples, Sn ($3d_{5/2}$) and ($3d_{3/2}$) contributions appear at binding energies about 486.8 eV and 495.2 eV[89], respectively, with an energy difference around 8.41 eV with binding energies corresponding to the main charge state of Sn^{4+} in rutile type SnO_2[103,104].

Voigt fitting of the Sn ($3d_{5/2}$) is displayed on insets of Fig.3.10 in which one only contribution at 486.8 eV due to Sn^{4+} in rutile SnO_2[104] can be observed both for undoped and doped (Ni, Li) SnO_2 nanoparticles. Some works[105]commonly reported an unavoidable presence of a Sn^{2+} contribution at lower binding energies in the XPS spectra from SnO_2, which is usually related to regions with electronic environment similar to SnO due to a high oxygen deficiency. In this case, neither the presence of Ni nor Li doping induces reduced states of Sn, at least within the detection limit of the technique, and only Sn^{4+} is observed in the XPS study, which confirms the high crystalline quality of the as-synthesized SnO_2 nanoparticles, even for the highest amount of doping.

Fig.3.11 shows the O($1s$) core levels for undoped and doped samples. The spec-

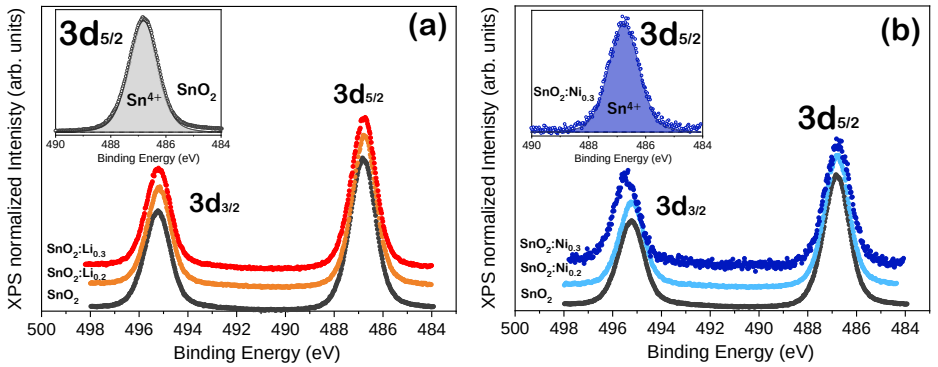

Fig. 3.10: XPS Sn($3d$) core levels from undoped and (a) Li or (b) Ni doped SnO_2 nanoparticles acquired with a beam energy of 650 eV. Deconvolutions corresponding from Sn($3d_{5/2}$) core level from SnO_2 and SnO_2:$Ni_{0.3}$ are shown in the inset in (a) and in (b).

tra can be deconvoluted in two main contributions named as O_I and O_{II} centered at 530.6 eV and 531.7 eV, respectively. A third contribution at higher binding energies named O_{III} centered at 533.4 eV is observed for Ni doped samples. First contribution is due to oxygen in SnO_2 lattice, while the latter, at higher binding energy, is associated with the presence of adsorbed oxygen at the surface and oxygen deficiency[103]. This second contribution and the contribution at higher energy, are often wider and can be attributed to other oxygen species. In some works the high energy peak is also associated with the presence of –OH groups[29]. The relative intensity of the O_I contribution at 530.6 eV due to lattice oxygen decreases with the addition of both Ni and Li dopants, as observed in Fig.3.11.

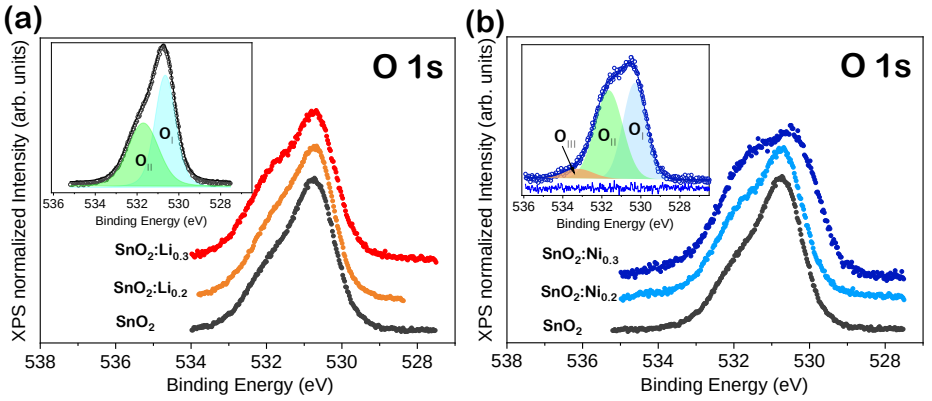

Fig. 3.11: XPS O($1s$) core levels from undoped and (a) Li or (b) Ni doped SnO_2 nanoparticles acquired with a beam energy of 650 eV. Deconvolutions corresponding to O($1s$) core level from SnO_2 and SnO_2:$Ni_{0.3}$ are shown in the inset in (a) and in (b).

The Li($1s$) core levels from the Li doped SnO_2 samples are shown in Fig. 3.12(a). The XPS spectra are centered at around 55 eV, which corresponds to Li^+, thereby confirming Li presence on the samples surface. XPS spectra in Fig. 3.12(a) are not normalized, hence based in the comparison of the corresponding Li($1s$) intensity ratio, Li concentration is lower for the SnO_2:$Li_{0.2}$ as expected, in agreement with the ICP-OES measurements. In particular, the Li($1s$) core level is centered at 54.96 eV for the sample SnO_2:$Li_{0.2}$ and at 55.34 eV for SnO_2:$Li_{0.3}$. This shift in the binding energy from Li($1s$) could be due to the variable incorporation of Li in the SnO_2 lattice, as interstitial and/or substitutional[106,107], being this variable incorporation relative to the amount of dopant. This effect is in agreement with the Raman and PL results, as will be discussed later in section 3.6. Based on these results, interstitial Li could be promoted by low Li doping, while higher Li doping would also induces substitutional Li.

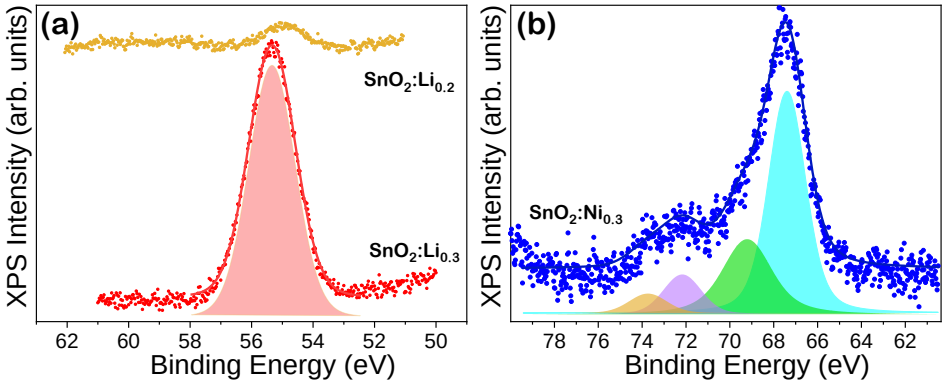

Fig. 3.12: XPS core level (a) Li($1s$) and (b) Ni($3p$) from Li-doped and Ni-doped SnO_2 nanoparticles, respectively, acquired with a beam energy of 650 eV for Ni($3p$) and beam energy of 253 eV for Li($1s$).

Fig.3.12(b) shows the Ni($3p$) core level for SnO_2:$Ni_{0.3}$ in which the splitting of Ni($3p$) into Ni($3p_{1/2}$) and Ni($3p_{3/2}$) can be observed. Ni($3p$) core level for SnO_2:$Ni_{0.2}$ is not represented due to the low signal as nickel concentration is lower. Peaks centered at 67.4 eV and 69.2 eV can be attributed to the main presence of Ni^{2+}, while the contributions at higher energy could be partially assigned to a lower amount of Ni^{3+}[108]. The proposed peaks match with the position, doublet separation and intensity of a doublet due to spin orbit interaction. This result confirms that Ni is incorporated with a variable oxidation state in SnO_2, although due to the complexity of the Ni($3p$) signal, Ni quantification is avoided in this case.

The valence band region of the samples under study is composed of three main contributions centered at ∼5 eV, 8 eV and 10.5 eV, as shown in Fig.3.13. The low energy bands at 5 and 8 eV correspond to the O($2p$) states and hybridization from the O($2p$) and Sn($5p$) orbitals, respectively, as commonly reported for SnO_2[109]. The shoulder at ∼10.5 eV can be related to the hybridization between the O($2p$)

and Sn(5s) orbitals[110]. Only for the samples with the highest amount of dopants, a decrease in the position of the Fermi level with respect to the maximum of the valence band was observed, as compared with undoped SnO_2. The E_F-E_{VBM} decreases about 0.2 eV and 1.2 eV for the samples doped with Li ($x = 0.3$) or Ni ($x = 0.3$), respectively. Hence lower n-type character can be induced by Li or Ni doping ($x = 0.3$) at the surface.

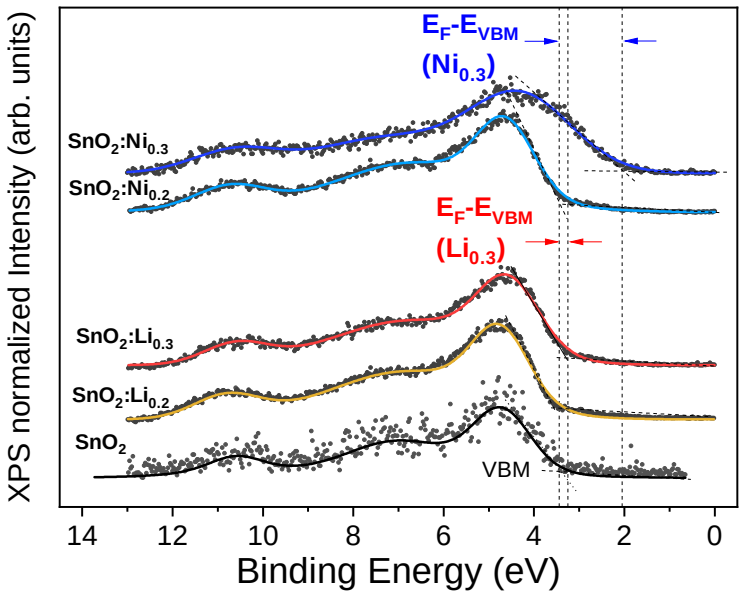

Fig. 3.13: Valence band region of SnO_2 and doped (Li,Ni) SnO_2 samples.

3.4.2. XAS

Surface sensitive XAS measurements in total electron yield (TEY) were performed in order to study the electronic structure of the samples.

Fig.3.14 shows the Sn $M_{5,4}$ edge of the undoped and doped (Ni, Li) SnO_2 nanoparticles. The features observed in the corresponding XAS spectra correspond to rutile SnO_2. The Sn $M_{5,4}$ edge consists of two groups of peaks in the region 490-496 eV and 498-504 eV and a pre-peak at 487 eV. The first peaks (M_5) correspond to Sn($3d_{5/2}$)→Sn($5p$) transitions, while the latter peaks (M_4) are due to Sn($3d_{3/2}$)→Sn($5p$) transitions. M_4/M_5 ratio is slightly enhanced for the nanoparticles with higher concentration of dopants. Sn $M_{5,4}$ is less resolved than O K-edge because of the relatively small $M_{4,5}$-edge cross section with respect to the O K-edge[72]. The first set of triplets is more sensitive not only to the local atomic structure and O-coordination but also with the valence state of Sn atoms[72,111].

The latter peaks are attributed to M_4-edge resonances, characteristic of rutile SnO_2[42].

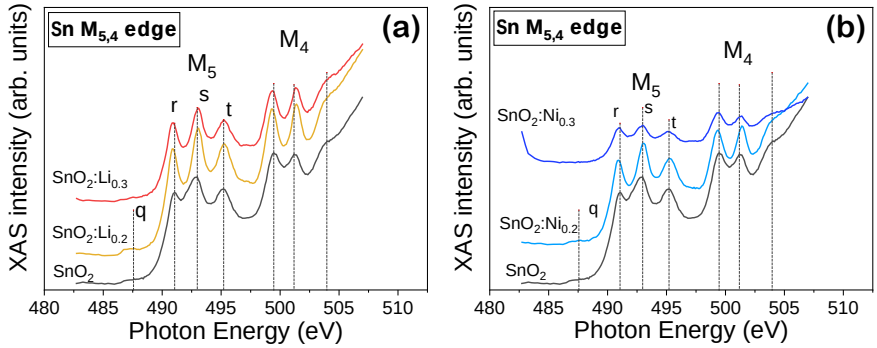

Fig. 3.14: XAS spectra showing Sn $M_{5,4}$ edge from undoped and (a) Li or (b) Ni doped SnO_2 nanoparticles.

Fig.3.15 shows the O-K edge from the analyzed samples originated from the electronic transitions from the O($1s$) core level into the unoccupied electronic states above the Fermi level; i.e., the O K-edge spectrum measures the O-related p-projected states in the conduction band[42]. The first peak ∼533.6 eV (labeled as x) can be assigned to the a_g resonance. This spectral feature appears due to the hybridization of O($2p$) orbitals with the Sn($5s$) orbitals and forms the bottom of the conduction band. The second high energy peak ∼539.5 eV (y) corresponds to the b_u resonance and originates due to the hybridization of O($2p$) orbitals with Sn ($5p$) orbitals. Among those peaks we can distinguish two low intense shoulders at ∼536.3-537.8 eV (u, v), which are due to the b_{1u} and b_{2u} bands and their appearance is related to surface defects, e.g., oxygen deficiency. The higher energy features at 550 eV- 570 eV, are due to the hybridization of O($2p$) orbitals with Sn($5d/4f$) states.

The XAS spectrum corresponding to the Ni $L_{3,2}$-edge from the sample SnO_2:$Ni_{0.3}$ is shown in Fig.3.16 formed by L_3 ($2p_{3/2} \rightarrow 3d$) and L_2 ($2p_{1/2} \rightarrow 3d$) transitions[112]. In our case, peak positions are placed for the L_3-edge at 852.9 eV and for L_2–edge at 870 eV. From the spin-orbit splitting, peak positions and intensity are in reasonable agreement with a Ni^{2+} oxidation state. As the concentration of lithium is low, the Li K edge was not observed for the probed samples.

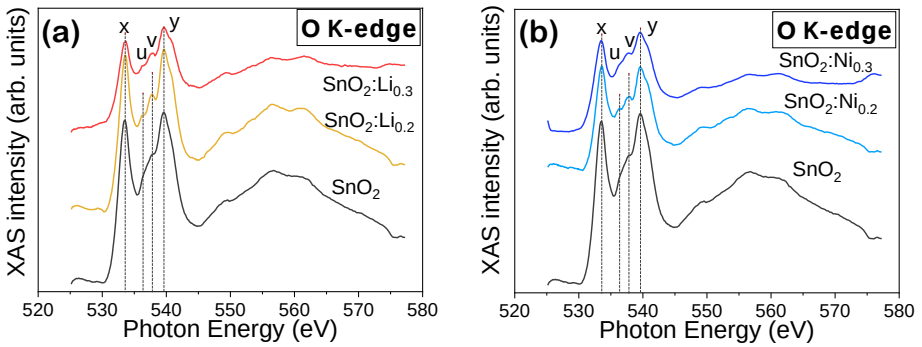

Fig. 3.15: XAS spectra showing O-K edge from undoped and (a) Li or (b) Ni doped SnO_2 nanoparticles.

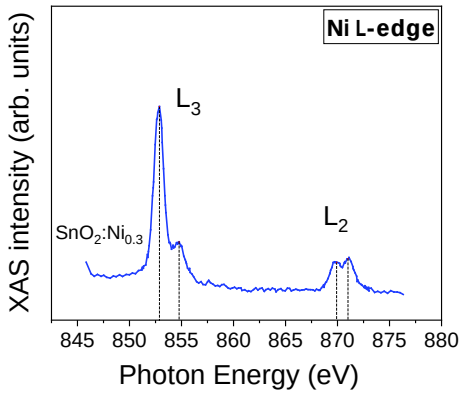

Fig. 3.16: XAS spectrum showing Ni $L_{3,2}$ edge corresponding to the sample SnO_2:$Ni_{0.3}$.

3.4.3. RPES

In order to better understand the states in the valence band closer to the Fermi level, Resonant PhotoEmission Spectroscopy (RPES) was employed. RPES provides element-specific information on electronic states in the valence band. The electronic states can be enhanced when the incident photon energy is slightly higher than the binding energy of the selected core level[113,114]. On-resonance RPES, spectra for Ni and Li states were acquired using energies of 852.9 eV for SnO_2:$Ni_{0.3}$ and 59 eV for SnO_2:$Li_{0.3}$ (based on the XAS measurements shown in Fig.3.16). For the off-resonance XPS spectra energies of 848 eV and 50 eV, respectively, were used.

Fig.3.17(a) indicates that there are no clear Li-related states which resonate in the valence band region for SnO_2:$Li_{0.3}$, as both on-resonance and off-resonance spectra are similar.

On the other hand, differences can be appreciated in the region closer to the Fermi level from the SnO_2:$Ni_{0.3}$ sample (Fig.3.17(b)) due to Ni-related states which resonate, thus showing higher relative intensity due to the enhanced absorption at 852.9 eV, as enlarged in the inset. The O($2p$)-Ni($3d$) hybridization could be related to the increase in the relative intensity of the contribution around 8 eV[115].

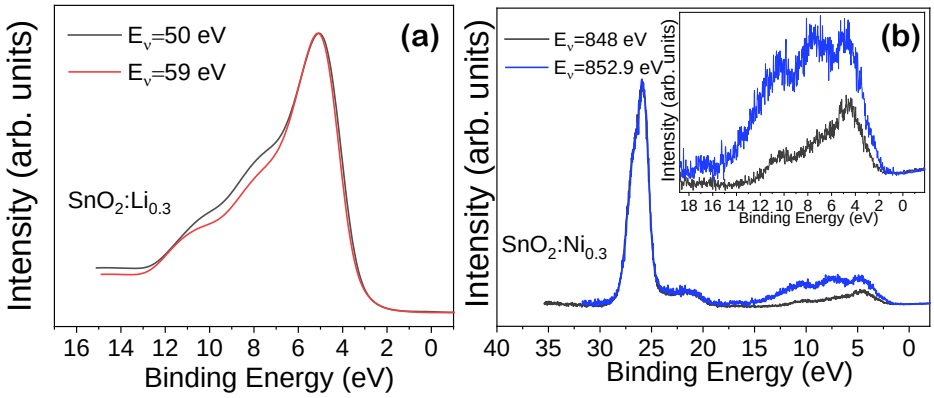

Fig. 3.17: (a)Valence band spectra of the sample SnO_2:$Li_{0.3}$ acquired under conditions of *off-resonance* (E_ν = 50 eV) and *on-resonance* (E_ν = 59 eV) and (b) Valence band spectra of the sample SnO_2:$Ni_{0.3}$ acquired under conditions of *off-resonance* (E_ν = 848 eV) and *on-resonance* (E_ν = 852.9 eV) according to the Ni-$L_{3,2}$ edge XAS spectrum.

3.5. Applications in Li-ion batteries

The implementation of the SnO_2 nanoparticles as anodes in ion Li-batteries was performed at Enwair Energy Technologies Corp., Istanbul Technical University, Istanbul Turkey supervised by Dr. Neslihan Yuca. In order to study the possible use of the undoped and (Li, Ni) doped SnO_2 nanoparticles as electrodes in batteries, battery cells were prepared and assembled. For the cell preparation, Celgard 2400 separator obtained from Celgard and Poly(Acrylic Acid) (PAA), (Mw: 450.000, Sigma-Aldrich) was utilized as binder. Lithium-ion electrolyte was purchased from BASF, which includes 1.2 M lithium hexafluorophosphate ($LiPF_6$) in Ethylene Carbonate (EC), DiEthyl Carbonate (DEC) (EC/DEC = 3:7 by weight), and 30% by weight of FluoroEthylene Carbonate (FEC) were added. After testing different compositions for the electrode, the results presented here correspond to SnO_2 based active materials, binder, and Carbon Black (CaB) mixed in water with the optimized weight ratio of SnO_2 nanoparticle/(PAA)/CaB = 70/20/10 for 3 hours. Slurries were coated on copper foil by using a doctor blade. After electrodes dried, they were cut as disk for coin cell assembling. They were placed under a controlled atmosphere in the glovebox overnight and further dried in the vacuum oven at 90°C for 12 h to completely remove the water. Fig.3.18(a) shows the specific capacity

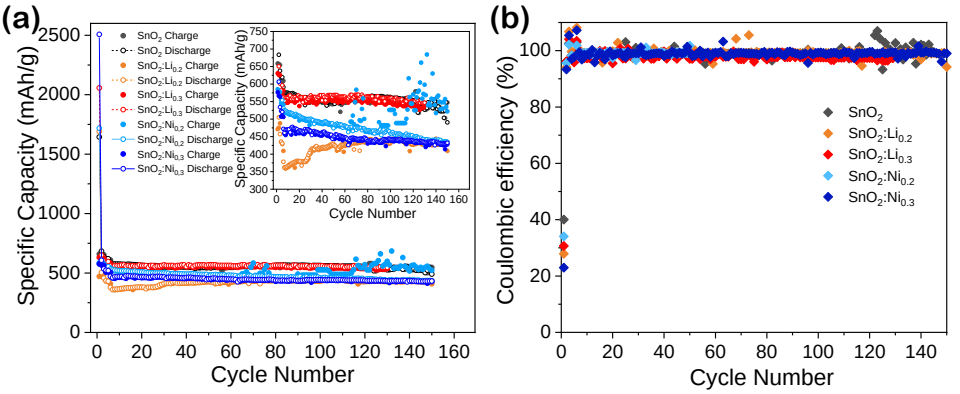

Fig. 3.18: (a) Specific capacity values upon cycling from LiB with anodes based on undoped and doped SnO_2 nanoparticles and (b) calculated couloumb efficiency. Inset in (a) shows detailed region of specific capacity between 300-750 $mAhg^{-1}$.

upon cycling from the LiB with anodes based on the undoped and doped nanoparticles. For all the samples, high initial capacity values were achieved, followed by stable capacity profiles around 500 $mAhg^{-1}$. These apparently high capacity values could be understood due to the small size of the employed nanoparticles[116], as confirmed by XRD and TEM, as well as due to the highly conductivity and high mobility of the blend. The nanoparticles used in this work offer short distances for charge carriers diffusion and are able to better withstand the volume change, hence improving the capability, although nanoparticles aggregation after several cycles can also lower the cyclability. Actually, J. Chen[117] reported that 10 nm is the critical size to prevent pulverization and aggregation of nanoparticles which degenerate the electrochemical performance in LiB. According to the results shown in Fig.3.18, SnO_2 based cells exhibit an initial specific capacity of 1644 mAh/g while SnO_2:$Li_{0.2}$, SnO_2:$Li_{0.3}$, SnO_2:$Ni_{0.2}$ and SnO_2:$Ni_{0.3}$ based cells show initial specific capacity values of 1690, 2057, 1718 and 2507 $mAhg^{-1}$, respectively. Therefore, high initial capacity values were obtained in this work for the samples with the highest dopant concentration, for example for SnO_2:$Li_{0.3}$, which could be associated with the improved initial Li intercalation and subsequent alloy formation in these samples[118]. Similar results of Nickel-doped SnO_2 based anodes[119] have been measured with other binders, showing high initial specific capacity but a decrease over time. However, the cells based on anodes with the highest doping also exhibit the main decrease in the initial capacity after the first cycles Fig.3.18. As observed in Fig.3.18(b) couloumbic efficiency is close to 100% what confirms the good electrochemical performance of the obtained anodes.

3.6. Discussion

The synthesis of SnO_2 has been widely studied in the scientific literature. There are many different methods to synthesize high-quality nanoparticles such as hydrothermal[120] sol-gel[45,95,121], Chemical Vapor Deposition (CVD)[99,122], co- precipitation[42,43,53,123], laser pyrolysis or synthesis methods based on polymeric precursors[124], among others. Significant efforts have been made in the optimization of the synthesis methods leading to SnO_2 with controlled dimensions, morphology and concentration of dopants. Actually, doping with Li and transition metals (such as Ni) can lead to variations in the SnO_2 electrical conductivity and the optical absorption[53,54]. In addition, incorporation of dopants can also alter the synthesis process favoring or hindering the growth of nanoparticles and the formation of defects[125,126]

SnO_2 has dragged an on-going attention in the energy related industry mainly as a Li-[94,118,127] or Na-ion[128] based anodes either composed of SnO_2 itself or its composites with organic counterparts, mainly due to the ability of inserting lithium and its great electrochemical behavior, being abundant, low-cost, environmental friendly and safe during performance[127]. A continuous research on the improvement of the capacity and performance/cyclability of LiBs, for which different materials and strategies are considered such as reducing sizes to the nanoscale,[129,130] controlling the morphology and aspect ratio,[131] using nanocomposites materials,[132] or doping with different elements[15,126] is currently undergoing. Li doped SnO_2 has demonstrated promising performance in Li-ion batteries based on the enhanced lithiation and insertion-disinsertion of lithium. Moreover, the use of some other metal dopants can also improve the battery response. Questions remain such as how lithium is incorporated into the lattice, both on substitutional or intersititial positions[106,107]. Some authors[15,126] exposed that the use of iron or cobalt doped SnO_2 involves good specific capacity and enhanced coulombic efficiency. This interest goes far beyond the applicability on Li-ion batteries, as in the last decade it has been an interest in obtaining p-type conductivity for semiconductors, such as SnO_2, which are natively n-type. Different authors claim to have obtained p-type conductivity[133], assumption that remains as a controversial issue.

Herein, the use of both Li doped SnO_2 and Ni doped SnO_2 has been evaluated in order to assess the role played by these dopants in the modification of the SnO_2 properties and the performance of LiB devices. Both Li or Ni doped SnO_2 has not been extensively studied in depth yet, contrary to other dopants such as Sb. Previous reports on Li doped SnO_2[125] has shown potential in LiBs as previously mentioned. Also, Ni doped SnO_2 has been used as many other dopants to modify optical response, which has been limited to applications such as to gas sensing[124] due to the band narrowing obtained through doping[54] which has also been exploited in photocatalysis.

The synthesis method employed in this work is adequate to obtain high crystalline SnO_2 in rutile phase with homogeneous dimensions as it has been observed

by means of XRD and TEM. Small size and high quality of the nanoparticles are obtained. By using this method is clear that the conditions have to be carefully controlled in order to achieve high control of the final product.

As observed in Table 3.1, undoped SnO_2 nanoparticles show averaged crystallite dimensions around 10 nm. Slight changes were detected in the estimated crystallite sizes as a function of the doping. This effect is more noticeable for the case of the Ni doped nanoparticles for which the crystallite dimensions decreases down to 7.29 nm for the nanoparticles with the highest amount of Ni (SnO_2:$Ni_{0.3}$). Previous studies indicated that the inhibition or promotion of the growth kinetics of nanoparticles depends on the precursors used during hydrolysis, which could retard the kinetics of the growth process, as also reported for other doped SnO_2 nanoparticles[53]. The size of the SnO_2 unit cell slightly decreases with the incorporation of both Li and Ni, although the decrease in the lattice parameters is higher for Ni doping. Considering the ionic radii of Li^+ and Sn^{4+} in octahedral coordination and high spin configuration ($R_{Li^+} = 0.59$ Å, $R_{Sn^{4+}} = 0.71$ Å)[134] this effect can be due to the incorporation of Li^+ as substitutional of Sn^{4+} ions. The ionic radius of Ni^{2+} is similar to that from Sn^{4+} ($R_{Ni^{2+}} = 0.69$ Å)[135] hence in this case partial incorporation of Ni as Ni^{3+}, with a lower radius than Ni^{2+}, should be also considered. Both Li or Ni incorporation does not modifies cell parameters strongly. This could be attributed to the aforementioned similar relative relation of the ionic radii of the dopant respective to the tin in octahedral configuration. Compared with other synthesis methods, hydrolysis is the least costly in terms of effort and time. With this method we have therefore obtained crystalline nanoparticles, as well as efficient insertion of the doping and a large amount of material, since the synthesis has a very high yield. The synthesis procedure could avoid the formation of SnO by increasing the calcination temperature or time, but most likely will end with slightly higher nanoparticles, which for this work was unintended.

Raman spectra assures the nature of rutile type SnO_2 nanoparticles obtained for both doped or undoped materials, although it shows complex behavior with dopant addition. Incorporation of Li in the SnO_2 lattice in a low concentration promotes vibrational modes related to motion of O along the c- axis (E_g), while a higher amount of Li induces an increase in the vibrational modes perpendicular to the c-axis (A_{1g} and B_{2g}, respectively). Moreover, the appearance of the B_{2g} mode only in the samples with the highest amount of Li can be associated with a decrease in the concentration of lattice defects, which mitigates this vibrational modes.

Samples doped with Ni show a more complex contribution around 240 cm^{-1} together with weak modes at 300 and 340 cm^{-1}. These modes could be related to TO (and even LO) E_u modes, which is triple-degenerated. For high nickel doping, a less defined Raman signal is obtained, with a decrease on the relative intensity of certain modes as E_g or A_{1g}, which are still detected. A higher concentration of defects on the SnO_2:$Ni_{0.3}$ nanoparticles, which are also the particles with smaller crystallite size, can be related to the decrease of the corresponding Raman signal.

Sn^{4+} substitution by Ni^{2+}, with similar ionic radii ($R_{Ni^{2+}} = 0.69$ Å, $R_{Sn^{4+}} = 0.71$ Å), is commonly reported for Ni doping, although the presence of Ni^{3+} should be also considered in this case, in agreement with XRD measurements, thus inducing variable structure of defects in SnO_2 in order to achieve charge balance. Vibrational modes related to secondary phases or ternary compounds (e.g. Li_2SnO_3) have not been observed, within the resolution of the technique.

To unambiguously observe and analyze the presence of the dopants mainly two different techniques were used: EDS to observe Ni and ICP-OES to observe Li presence. EDS analysis shows that the ratio Sn/O is consistent in all samples and that Ni is clearly well distributed over the doped sample which assures that the procedure allows good homogeneity. Ni concentration varies for the different concentrations from 0.49 to 3.84 % at. in SnO_2:$Ni_{0.2}$ and SnO_2:$Ni_{0.3}$ respectively which can be perfectly observed on both the EDS spectra and mapping, presented on Fig.3.2.

Furthermore, Lithium has been also quantified with both ICP-OES and observed, but only relatively quantified via XPS. As observed in Table 3.2 lithium concentration varies from 0.06 to 0.95 % at. for SnO_2:$Li_{0.2}$ and SnO_2:$Li_{0.3}$, respectively. These values are in agreement with the relative difference observed for those samples on the corresponding Li($1s$) core level by XPS. Because of this, hydrolysis can be established as a good method to obtain Li doped samples with dopant control until a certain extent. However, XPS does not distinguish between different atomic positions and it is limited only to the surface of the sample. As previously mentioned, some authors point out that Lithium is incorporated as interstitial, whereas others assure that is substitutional[106,107]. This is confirmed in both ways with first principle calculations, which also differ in interstitial[52] or substitutional[136] positions accordingly to the similar ionic radii previously described. On top of that, theoretical studies point out that higher lithium concentrations could increase also particle size[137] due to migration of Lithium to the surface of the nanoparticles, which could explain the slight changes on the nanoparticles sizes, as function of the dopant concentration.

Optical characterization based on PL has been performed on the undoped and doped nanoparticles. Dopant effects can be associated with the differences observed on the corresponding luminescence signal. SnO_2 characteristic luminescence exhibits a wide band covering the VIS region, from NIR to UV. Normally, it can be deconvoluted to 4-5 bands, as described in Table 3.5. Full information about the Gaussian deconvolution can be observed in Table 3.7 where the energy center of each band as well as the FWHM and the relative area (relative, %) are described.

Total PL signal is also affected by doping. Variable Li doping leads to changes in the SnO_2 luminescence signal. Either a decrease or an increase of the relative intensity from the bands, related to oxygen vacancies, was induced by low or high Li doping, respectively. Hence, different incorporation of Li into the SnO_2 lattice, as well as related defects, should be promoted as a function of the amount of Li, in agreement with the analysis of the Raman signal. Actually, incorporation of Li

Table 3.7: Peak deconvolution of the normalized PL spectra.

Sample	Position (eV)	FWHM (eV)	Relative area (%, arb units)
SnO_2	1.93	0.422	24.7
	2.27	0.443	50.1
	2.53	0.530	18.8
	2.98	0.388	6.3
SnO_2:$Li_{0.2}$	1.93	0.383	11.6
	2.30	0.446	58.6
	2.52	0.395	17.5
	2.90	0.379	12.3
SnO_2:$Li_{0.3}$	1.93	0.432	34.2
	2.28	0.438	52.6
	2.53	0.405	9.0
	2.89	0.331	4.2
SnO_2:$Ni_{0.2}$	1.98	0.434	23.1
	2.29	0.422	57.2
	2.60	0.503	17.4
	2.99	0.277	2.3
SnO_2:$Ni_{0.3}$	1.64	0.431	23.2
	2.26	0.648	56.1
	2.90	0.800	20.7

in substitutional Sn^{4+} sites can induce formation of oxygen vacancies to maintain charge neutrality, whose related emission is enhanced for SnO_2:$Li_{0.3}$.

Doping with a low amount of Ni only induces slight changes in the corresponding PL signal, dominated by the green emission (2.25 eV), with respect to undoped SnO_2. However, by increasing the amount of Ni a drastic quenching of the luminescence is observed. This dopant effect on the luminescence is known as *killer effect*, characteristic of the transition metals of the Fe group, highlighting a strong effect for the Ni^{2+} ions[138]. Hence, the decrease of the emission intensity for SnO_2:$Ni_{0.3}$ may be a result of the formation of a large number of non-radiative recombination centers by Ni incorporation[139].

Complementary to PL measurements, CL results give an insight on the radiative luminescent transitions of the synthesized samples. The observed emissions at 1.9, 2.2 at 2.5 eV (orange, green or blue) have been reported as the main luminescence bands of SnO_2[99] associated, respectively, for the former contribution with the presence of oxygen vacancies, for the green also related with the presence of oxygen vacancies and the blue band with the presence of other structural or stoichiometric defects. It should be noted that the commercial nanoparticles present a high energy contribution at 2.9 eV which resembles the violet band observed in photoluminescence. CL of the doped nanoparticles at RT is really weak. At

120K it is observable, Li-doped nanoparticles posses a dominant blue band and to a lesser extent an increase in the green band, which is also associated with the presence of oxygen vacancies. These results point out to that Li-doping increasing the oxygen-vacancies related defects, which also agrees with PL. Ni-doping quenches strongly the luminescence which could be related as previously mentioned killer effect. At 120K apparently, there is a presence on both samples of the blue band, while for SnO_2:$Ni_{0.3}$ the orange band dominates. Compared with the commercial nanoparticles, our synthesis method produced particles with a higher concentration of surface defects and oxygen vacancies. As suggested by different authors, the green band (often placed 2.25-2.48 eV) evolution with respect of the temperature could be analyzed with a coordinate-configurational model[99]. CL spectra for the undoped SnO_2 sample was acquired between 174-252 K. Inset on Fig.3.8 shows the fitting to the Arrhenius equation of the blue band (i.e $\sim$ 2.5 eV) and the green band (i.e $\sim$ 2.25 eV), which clearly have different slope indicating that not only the activation energy is different, also pointing out that the mechanism related to both emissions are different.

Electric properties of the synthesized nanoparticles were measured using Hall effect. For that purpose, nanoparticles were pressed under the same conditions into pellets. Hall effect results show that SnO_2 exhibits n-type conductivity, as expected, which is maintained even with the presence of dopants. The n-type nature of SnO_2 is commonly associated with the formation of oxygen vacancies and Sn interstitial defects, which energy levels are close to the conduction band[102]. SnO_2 doping with different elements, such as Sb as an example, can increase the n-type behavior as it has been commented before. This is due to the introduction of donor center near the CB, and this lead to concentrations up to 10^{20} cm^{-3}[46].

In this case undoped SnO_2 sample shows averaged conductivity of $2.91 \cdot 10^{-1}$ $S{\cdot}cm^{-1}$ and carrier concentration of $4.58 \cdot 10^{17}$ cm^{-3}. Conductivity mechanism of SnO_2 is often studied in thin films. As nanoparticle material, conductivities are usually in the order of 10^{-1} or 10^{-2} $S{\cdot}cm^{-1}$[140] while carrier concentration ranges between 10^{17}-10^{20} cm^{-3}[46]. The increase of conductivity in SnO_2 is often related to an increase on the concentration of oxygen vacancies. However at the nanoscale, some aspects related to the interface-related processes, hopping mechanisms or percolation effects should be also considered[45].

Low Li or Ni doping either improves or decreases, respectively, the corresponding electrical conductivity values. In particular, the sample SnO_2:$Li_{0.2}$ shows a slight increase of the conductivity value. This is in accordance with others authors observations with similar lithium concentrations[50]. However, by increasing the dopant concentration, a lowering of the conductivity is caused both for Li and Ni doping. The incorporation of Li and Ni dopants in the amounts considered in this work does not give rise to p-type conductivity, although some compensation effect on the conductivity is observed for the nanoparticles with the highest concentration of Li and for both Ni doped samples, showing a reduced conductivity when compared with the undoped sample. This compensating effect is in agreement with the reduced n-type character detected by XPS results on the valence

band measurements for Li(x=0.3) and Ni(x=0.3) doped samples. Theoretical DFT calculations[136]also support that Li acts as a donor when incorporated as a interstitial, which could explain the small increase in the conductivity for sample Li (x=0.2), whereas it acts as an acceptor when incorporated as a substitutional atom in the SnO_2 lattice compensating the carriers in the SnO_2 and reducing the conductivity for Li (x=0.3) sample. Therefore in this work, Li could be incorporated as an interstitial for low contents, whereas for higher contents substitutional positions could be preferred.

Electronic structure and surface properties of the samples were studied using photoelectron spectroscopies. By measuring the Sn($3d$) core level it was observed that, despite the small amount of SnO detected by XRD in the samples, in this case contributions from Sn with oxidation states lower than Sn^{4+} were not detected, which could be due to the surface sensitivity nature of XPS rather than XRD. Moreover other possibilities can be contemplated as a possible SnO/SnO_2 core shell structure formed in some nanoparticles due to the easy oxidation of SnO, or the low presence of SnO-like domains in intergranular regions could be considered. Either way, presence of SnO should be very weak and most of the nanoparticles correspond only to SnO_2, as confirmed by XPS. This single-Sn valence was observed for all the different samples, regardless of the dopant presence.

O($1s$) deconvolutions show different behavior with increasing doping. Thereby, in this case higher dopant concentration induces an increase in the O_{II}/O_I ratio, for both the Li and Ni doped SnO_2, which can be related to a slight increase in the concentration of oxygen vacancies at the surface of these doped nanoparticles as well as, in the case of SnO_2:$Ni_{0.3}$ nanoparticles an enhanced oxygen adsorption due to their lower dimensions and higher surface-to-volume ratio, as demonstrated by XRD and TEM.

A detailed study of the Ni($3p$) core level could provide information on the oxidation state of the nickel. However, the decomposition of the spectrum into different contributions and their association with the different oxidation states of nickel is still debatable. It should be noted that the fitting at higher energies with the proposed peaks is not matching completely the total XPS signal, as the region of higher energies could contain satellite peaks[141]. Atomic multiplet splitting and charge transfer effects could contribute to satellite peaks about 5 to 6 eV from the Ni($3p$) main peaks[142], which in this case have not been added to the deconvolution for the sake of clarity. Still, some controversy remains about the multivalence of Nickel analysis in Ni($3p$) spectra, as some authors attribute peaks between 67 and 69 for both Ni^{2+} and Ni^{3+}[143], while in some other cases only Ni^{2+} is considered. In this case, the Doublet Separation (DS) is in accordance with the bibliography[89] of around 1.8 eV for Ni^{2+}.

In the VB region observed by XPS, the Fermi level is shifted towards the VB minimum $\sim$ 0.2 eV for the sample of SnO_2:$Li_{0.3}$ as compared to SnO_2. Substitutional Li is considered to be promoted by increased Li doping acting as an aceptor and thus leading to lower n-type character of the samples. As suggested by XPS measurements, similar phenomena have been previously reported for Li doped

SnO_2[125] indicating a substitutional incorporation of Li atoms in SnO_2. This effect is accentuated in the case of Nickel where the shift is $\sim$ 1.2 eV. Reduction of Ni^{3+} to Ni^{2+} by capturing a free electron could be associated with the lower n-type character observed for the Ni (x=0.3) doped samples.

From XAS spectra of the Sn $M_{5,4}$ edge, the expected peaks corresponding to rutile tin oxide were observed. To clarify subtle changes induced due to dopant/defects can be related with the area under XANES/XAS spectra, as these features have been found comparable with the unoccupied partial density of states[42]. Deconvolution of the first two peaks of the first triplet (labeled r and s) in Fig.3.14,3.19 and particularly, increase on the relative intensity of r indicates formation of unoccupied p/f density of states upon doping. Maximum intensity is observed for the lower doping, similarly observed by Eu-doping by Sharma et al.[42]. This could be understood as for higher doping, Ni or Li atoms are expected to fill Density Of States (DOS) through the creation of defect levels. A pre-peak resonance, below

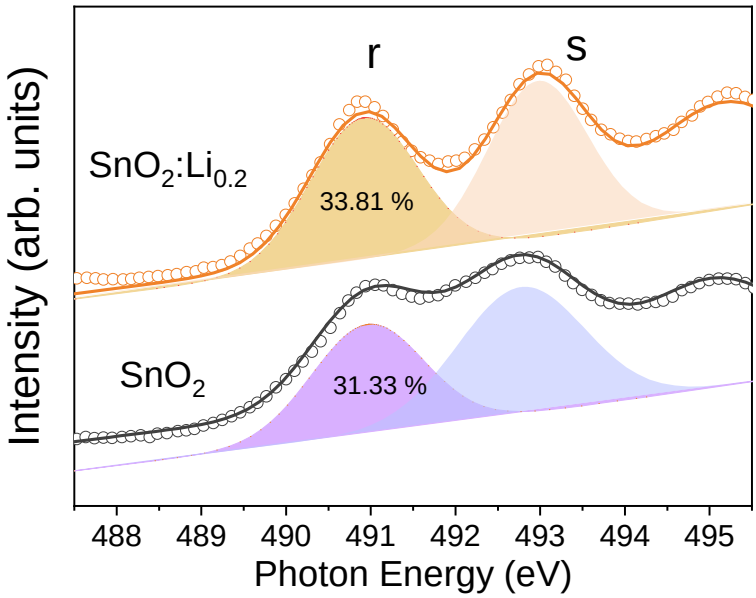

Fig. 3.19: XAS spectra deconvolution of Sn $M_{5,4}$ edge.

the M_5 edge, labeled as q in Fig.3.14 has been reported to be associated with surface or defects states caused by unsaturated coordination of surface Sn ions due to oxygen vacancies.[42,72,111]. This peak is normally absent in commercial SnO_2 but present in SnO. Other authors attribute this peak, along with the following resonance peak labeled as t, to the presence of surface states, as this surface state

resonance is due to a fraction of coordination unsaturated surface Sn ions resulting from oxygen vacancy/deficiency or Sn interstitial and surface reconstruction of the SnO_2 nanostructure[144]. In this case pre-peak is absent for SnO_2:$Ni_{0.3}$ and very weak for all samples, except for SnO_2:$Li_{0.2}$.

O K-edge spectra contains different features which notation is explained by De Groot et al.[145]. The energy difference between the x and y is ∼6.3 eV which is close to the previously reported value in the O K-edge spectra for rutile SnO_2 compound (i.e., Sn^{+4}). All the XAS spectra are similar, except for the weak peaks around 538 eV which are better resolved for the doped samples which could indicate higher presence of oxygen deficiency. There is a decrease on the x and y peak with dopant concentration, which indicates a decrease in the O($2p$) and Sn($5s/5p$) hybridization. This could be understood due to formation of Sn vacancies or O deficiency, which could be attributed to the dopant inclusion.

To determine the valence of the Ni advantage can be taken from the measurement of Ni L-edge. The branching ratio, which is defined as $L_3/(L_2 + L_3)$ (L_i signifies the integrated intensities for the Li-edge peak), is another integrated spectral property that can be analyzed. L_3 centroid is an indicator of oxidation states while the branching ratio reflects the electronic spin states for $3d$ metal complexes. In this case, branching ratio is approximately 0.78 for a centroid position average of 853.8 eV which is near to the expected value for Ni^{+2}[112]. This is assured via simulated spectra simulated using CTM4XAS *Charge Transfer Multiplet program for X-ray Absorption Spectroscopy* program, v.5.5[92,146] as shown in Fig.3.20. This software allows the analysis of transition metal $2p$ and $3p$ core level excitations, either Electron Energy Loss Spectroscopy (EELS) or X-ray Absorption Spectroscopy (XAS)[147], based on Charge Transfer Multiplet (CTM) approach. This approach states that there are effects of charge fluctuations on both initial and final states, which can be described by combination different ground and final state configurations, which is particularly useful for transition-metal oxides. The most important charge transfer is the transition for a configuration $3d^N$ to $3d^{N+1}L$, where an electron (ligand electron) is transferred to the metal site and thus, a ligand hole (designated by L) is created. The charge transfer multiplet method is the most prevalent and conventional theoretical approach for the analysis of transition metals $L_{3,2}$ XANES[146]. This program allows to simulate $L_{3,2}$ edge with the use of certain (semi-empirical) parameters. For octahedral symmetry (O_h), the crystal field splitting $10Dq$ and additional parameters such as the charge transfer parameter energy Δ (eV) or the Hubbard potential U_{dd} can be modified. To match experimental results, the best results were obtained with the parameters shown in Fig.3.20, with and small adjustment on the energy position, probably shifted on the experimental spectra. Charge transfer parameter, Δ, was added as it clears the peak feature of L_2 spectra, which fits with the experimental results. This spectra resembles previous reports on NiO, which could explain the possible Ni^{2+} valence. However the weak increase in the relative intensity of the L_3 shoulder at 853.8. eV can be related to a low presence of Ni^{3+}[148].

As a final proof of concept in this chapter, the undoped and Li or Ni doped SnO_2

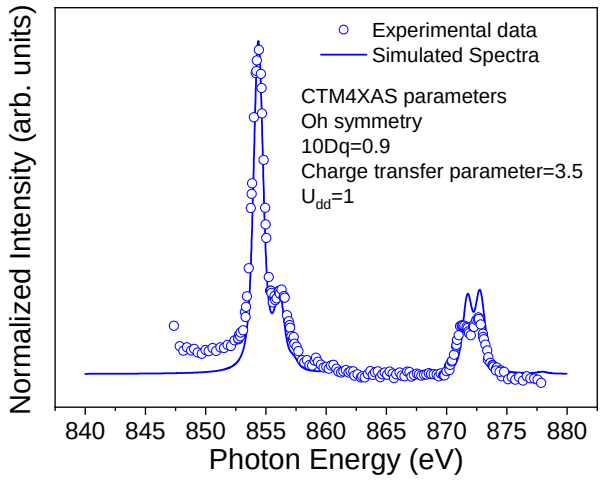

Fig. 3.20: Simulation of the Ni^{2+} $L_{3,2}$ edge using the CTM4XAS program[146].

nanoparticles have been tested as possible electrodes in LiBs. After the assembly of the half cells, they were tested by measuring capacity fading over performance. Firstly, a decrease of the initial capacity values was observed, which it has been already observed in SnO_2-based anodes, attributed to an irreversible conversion reaction of Li with SnO_2[16]which is always followed by a capacity fading after the first 30–50 cycles, attributed to the SnO_2 structural instabilities due to the volume expansion/reduction and reactions that may undergo during lithiation/delitiation processes. In fact, the irreversible conversion reaction causes the initial drop in capacity,[149] and the allowed reactions (which mostly are reversible), lead after few cycles to less Sn^0 reversely converted to SnO_x and the incomplete SnO_2 reduction occurred during lithiation and delithiation, which causes a steady decrease on the specific capacity. It has been recently suggested that the conversion and alloying reaction can overlap upon cycling and different intermediate compounds could be formed, composed by Li-Sn-O[116]. Other possible explanations on the capacity fading is attributed to the interfacial charging of lithium at the phase boundaries of nanoparticles in the SnO_2 electrode and even the possible formation of Solid Electrolyte Interphase (SEI)[150]. Nonetheless, in our case the capacity fading with increasing number of cycles is not abrupt, as observed in Fig.3.18, upon cycle number most of the capacity is retained. The absence of Sn^{2+} on the particle surfaces, confirmed by XPS, could retard some of these intermediate reactions, leading to enhanced cyclability and electrochemical response. For all the cells, reversible capacity values between 500 – 600 $mAhg^{-1}$ are retained upon 150 cycles and beyond, which is significantly higher than the theoretical capacity of a graphite anode commercialized ($\sim$ 372 $mAhg^{-1}$)[151] , thus confirming excellent cyclability performance. The stability of these batteries are comparable with pre-

vious reports[152] in which SnO_2 was combined with either carbon black, carbon nanotubes or as GO/SnO_2 composites[73], although in the latter case the good conductivity and mechanical properties of graphene oxide played a key role. Besides, in the present work, coulombic efficiency values near 100% were obtained, which confirms the good electrochemical performance of the SnO_2-based cells.

In order to compare the performance of the different anodes, as well as their relative efficiency, it is useful to compare the specific capacity values for a particular cycle, after a large number of cycles where the performance is stable. Capacity values after 100 cycles corresponding to the cells with anodes based on undoped or doped SnO_2 nanoparticles are indicated in Table 3.8. After 100 cycles, the undoped SnO_2 sample shows 562.9 $mAhg^{-1}$ specific capacity and a very stable profile. SnO_2:$Li_{0.2}$ based anodes exhibit a large initial decrease in the capacity followed by a recovery during the followed cycles, although better performance is always achieved for SnO_2:$Li_{0.3}$ anodes, which after 100 cycles are around ∼560.5 $mAhg^{-1}$.

Table 3.8: Specific capacity at 100 cycles.

Sample	**Step**	$\mathbf{C_{esp}(mAhg^{-1})}$
SnO_2	Charge	557.1
	Discharge	562.9
SnO_2:$Li_{0.2}$	Charge	431.2
	Discharge	438.3
SnO_2:$Li_{0.3}$	Charge	547.0
	Discharge	560.5
SnO_2:$Ni_{0.2}$	Charge	526.1
	Discharge	458.6
SnO_2:$Ni_{0.3}$	Charge	439.7
	Discharge	442.8

In this case, Li doped SnO_2-based anodes show improved capacity for higher Li doping (SnO_2:$Li_{0.3}$), while for Ni doping the opposite behavior was observed. Low Ni doping involves slightly higher capacity as compared with high SnO_2:$Ni_{0.3}$ samples, although slightly better stability is achieved for the latter. It should be remarked that in the present work the capacity fading upon cycling is weaker as compared with some other works[153], which can be partially explained based on the homogeneity, high crystallinity, and low size of the particles, shortening the diffusion path of lithium and enhancing charge/discharge processes[116,117]. Nevertheless, some other aspects such as the presence of dopants and the related structure of defects should be also investigated and considered among the aspects governing the cell performance, which motivates this study.

PL and Raman measurements confirmed a high concentration of defects for these nanoparticles, which could hinder the electrochemical performance of the SnO_2:$Ni_{0.3}$ based anodes. Variable incorporation of dopants in SnO_2, even in a

very low concentration, clearly modifies the battery performance, as it has been observed in this section. According to our results, interstitial Li could be favored at the low doping values, SnO_2:$Li_{0.2}$, while higher doping levels lead also to substitutional. The incorporation of Li in variable positions, as function of dopant concentration, has been reported on the literature. Wang et al.[154] analyzed Li doped SnO_2 thin films and proposed the presence of Li interstitials at low Li doping, due to their lowest formation energy, as well as enhanced Li incorporation in Sn sites at higher Li doping, which agrees with our results. Rahman et al.[136]studied by first principle calculations the incorporation of Li in the rutile SnO_2 lattice and the relation with native defects from the oxide. According to their reported calculations, energy formation of Li interstitials is the lowest, although incorporation of Li at Sn sites is also favorable as lowers the lattice distortion. Li incorporation also reduces the formation energy of native defects in SnO_2 and favors their stabilization. Variable incorporation of dopants as interstitial and/or substitutional has been also reported by other authors, which should be also considered for the Ni doped SnO_2 nanoparticles analyzed in this work. In this case, higher Ni doping induces more defective nanoparticles with decreased conductivity.

The presence of a low amount of Li, preferentially as interstitial, could worsen the lithiation/delithiation processes leading to lower battery performance, as compared with undoped SnO_2, while these processes would be recovered in SnO_2:$Li_{0.3}$ based anodes, for which the presence of Li in Sn sites, involving higher oxygen vacancies concentration and lower n-type character due to Li-related acceptor levels have been proposed. Ni doping involves combined oxidation states and higher formation of defects leading to lower n-type character and worse conductivity values as compared with undoped SnO_2, although good cyclability is achieved in the Ni doped SnO_2 based LiB anodes.

3.7. Conclusions

In this chapter, undoped and Li or Ni doped SnO_2 nanoparticles have been synthesized via a co-precipitation method based on hydrolysis. A characterization of morphological, structural, compositional, electrical, electronic and optical properties has been carried out throughout this chapter. These nanoparticles have been tested as possible candidates in lithium ion battery anodes.

- Hydrolysis synthesis has been proved as a good, fast and reliable method to obtain high-crystalline and single-phase rounded nanoparticles around 10 nm, as measured by XRD and TEM. Among the different synthesized nanoparticles, SnO_2:$Ni_{0.3}$ have shown the smallest size, at 7.29 nm, being this decrease in size attributed to the effect of the dopant on the kinetics of the reaction during the hydrolysis process. EDS and ICP-OES results ensure the presence of the dopant on the structure and its homogeneous distribution, being for Li 20% the lowest observed concentration, at 0.06% at, which nonetheless induces changes on the optoelectronic properties of the doped nanoparticles. A range of techniques (XRD, TEM, Raman) have shown that

the obtained nanoparticles present rutile structure with variable properties attributed to the effects of dopant incorporation.

- Raman spectroscopy obtained with an UV laser, shows significant variations in the SnO_2 vibrational modes even for the lowest concentration of the dopants and even most noticeable changes with their highest concentration. High Ni doping induces an increase in the concentration of defects, mostly oxygen vacancies, while variable Li incorporation induces changes mainly in the E_g or A_{1g} and modes, promoted depending on the dopant concentration, thus showing that low Li doping triggers modes related to motion of O along the c- axis, while higher amount induces an increase of modes perpendicular to the c- axis. PL spectra shows an increase of oxygen vacancies concentration with higher Li content whereas Ni doping quenches the luminescence due to the formation of non-radiative recombination centers.

- XPS results shows the only presence of Sn^{4+}, detected by the inspection of the Sn($3d$) core level for both doped and undoped nanoparticles. Ni($3p$) core level from Ni doped samples shows possible mixed Ni^{2+}/Ni^{3+} charge states. Li doping shows changes in the Li($1s$) state which can be attributed to different dopant incorporation as interstitial (low doping) or substitutional (high doping). The valence band region shows a lower n-type behavior for the samples doped with higher dopant concentrations. There is a present ongoing debate on how lithium is incorporated into the lattice, both on substitutional or intersititial sites[106,107] in which our work[94] has shed some light on the effect in the most stable positions as a function of the dopant concentration.

- Moreover, these nanoparticles have been used as a proof of concept, as an active material for anodes in LiBs, in which both an study on their specific capacity over number of cycles as well as the possible mechanism which may affect their performance were discussed. It was observed that the electrochemical cells showed not only a high capacity but stability over 150 cycles. In particular, both SnO_2 and SnO_2:$Li_{0.3}$ showed the highest values at $\sim$560 $mAhg^{-1}$ after 100 cycles. In this sense, on top of those results fundamental knowledge has been obtained on the study of the effects of tin charge state on the overall performance of the batteries, which apparently indicates that low amount of Li, preferentially as intersitial, could worsen the lithiation/delithiaton processes. Based on these results, the defect structure associated with the Li or Ni doping, variable Li incorporation as interstitial and substitutional, mixed Ni oxidation states, and the lack of Sn^{2+} confirmed by XPS, could retard some of the intermediate reactions occurring in the LiB, which can be related to the improved cyclability and electrochemical response observed in this case. These aspects should be considered in order to design LiB batteries with enhanced performance.

Chapter 4.
TiO_2 nanoparticles doped with Li or Ni

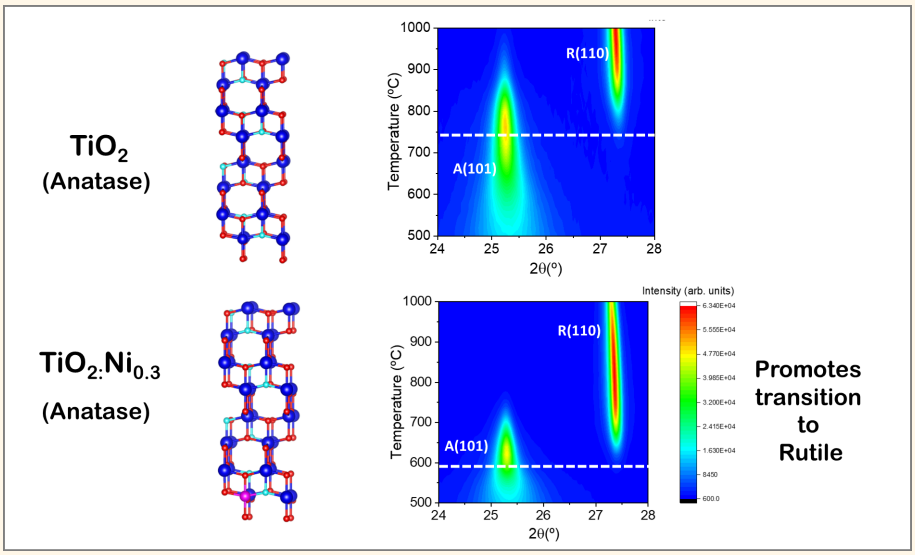

Abstract: In this chapter, undoped and Li or Ni doped anatase TiO_2 nanoparticles have been synthesized by a soft chemistry co-precipitation method based on hydrolysis. Firstly, a characterization of their morphological, structural and compositional properties was performed. Optical and electrical properties have been also studied. Deeper insight on the Li or Ni doping effects were achieved by Photoelectron spectroscopy as well as first principle calculations. A possible application of these doped nanoparticles has been tested as possible part of anodes in Li-ion batteries. The dopant effect on the anatase-to-rutile transition (ART), which has been induced via thermal treatments as well as by UV-irradiation, has been also evaluated, leading to a dopant-promoted faster ART, which occurs at lower temperatures.

This chapter includes adapted material from:

- A. Vázquez-López et al., Hybrid Materials and Nanoparticles for Hybrid Silicon Solar Cells and Li-Ion Batteries, *Journal of Energy and Power Technology*, **2021**, 3, 2.[155]

4.1. Synthesis, morphological, structural and compositional characterization

TiO_2 nanoparticles were synthesized via hydrolysis, as described in subsection 2.1.2. Undoped and Li or Ni doped TiO_2 nanoparticles were obtained by combining the stoichiometric amounts of the selected precursors and mixed with magnetic stirring at room temperature. Distilled water was added and then it was left for stirring a few seconds. The obtained mixture was rinsed and centrifuged until reaching neutral pH. Finally, the dry powder was introduced into a furnace at 250 °C for 24 h.

4.1.1. XRD characterization

Anatase TiO_2 with variable Li or Ni content were initially characterized by XRD, as shown in Fig.4.1.

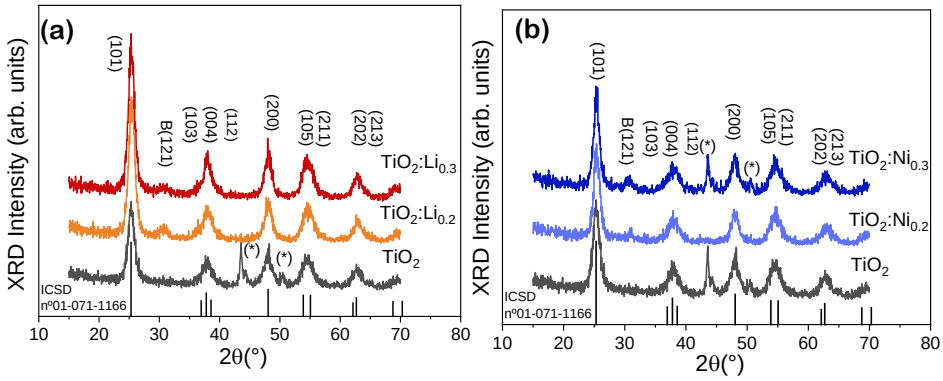

Fig. 4.1: XRD patterns of both undoped and (a) Li or (b) Ni doped TiO_2 nanoparticles. Peaks corresponding to brookite are marked with the letter B, whereas peaks due to the sample holder are marked with (*). Histogram correspond to the spectra of the ICSD file nº01-071-1166 corresponding to TiO_2.

XRD analysis from the powder samples can be indexed to the anatase structure of TiO_2 (ICSD nº01-071-1166) with no presence of precursors or other Ti-based compounds. Peaks observed at 43.5-44.5° and 50° are due to the Cu sample holder. Doped samples present a weak peak at around 30.8° which can be attributed to brookite (ICSD nº:00-015-0875) due to low annealing temperature. This peak

disappears by increasing the temperature used during the synthesis. In this work, low temperature was chosen to prevent increasing grain size. It should be pointed out that the main (101) peak of anatase can overlap with the (120) and (111) from brookite.

Size effects are clearly noticeable in the XRD patterns as the peaks present a widening which is related to the low size of the crystalline domains. Phase stability is present on all the samples, even up to 30% Ni or Li weight percentage.

Similarly as described on section 3.1, from the XRD signal, the average of the crystalline size can be estimated from the Scherrer formula (Equation 2.2). To calculate that, the signal from the planes (101) and (200) was employed and the corresponding results are presented on Table 4.1. Average size is below 7 nm for all the samples and slightly increases with dopant incorporation. Li doped samples samples present higher size up to 6.34 nm with lower dopant concentration. However, the size of the Ni doped samples increases with dopant inclusion. Lattice parameters and the estimated unit cell volume are indicated in Table 4.1.

Table 4.1: Size estimation of the undoped and doped TiO_2 nanoparticles and the corresponding lattice parameters obtained from XRD analysis

Sample	**Size (nm)**	**a(Å)**	**c(Å)**	**ratio c/a**	**V^3(Å^3)**
TiO_2	5.92±0.03	3.76(9)	9.35(2)	2.481±0.006	132.85±0.64
TiO_2:$Li_{0.2}$	6.34±0.02	3.76(8)	9.26(5)	2.459±0.005	131.56±0.56
TiO_2:$Li_{0.3}$	6.24±0.02	3.78(1)	9.45(9)	2.502±0.002	135.25±0.15
TiO_2:$Ni_{0.2}$	6.49±0.03	3.76(1)	9.39(3)	2.497±0.001	132.87±0.08
TiO_2:$Ni_{0.3}$	6.69±0.03	3.76(6)	9.32(5)	2.476±0.001	132.23±0.10

4.1.2. EDS and ICP-OES characterization

The chemical composition of the samples was analyzed with EDS on a SEM microscope where the nanoparticles were deposited on carbon tape over a Cu substrate. EDS spectra were acquired with a beam energy of 15 kV and 1.5 nA. Normalized spectra can be observed in Fig.4.2(a)-(b) for samples doped with lithium or nickel respectively. Both for doped and undoped samples emission lines attributed Oxygen $K_{\alpha 1}$(range 0-1 keV), Ti K_α (range 4.5 keV) and L_α (0.45 keV)[83] can be clearly observed. In some of the samples weak lines $K_{\alpha 1}$ and $K_{\alpha 2}$ from Cl can be observed, which can be attributed to the dopant precursors LiCl or $NiCl_2{\cdot}6H_2O$. Nickel doped samples, whose spectra is depicted in Fig.4.2(b), present Ni peaks corresponding to $K_{\alpha 1}$ and L_α at 7 and 0.8 keV. Averaged concentration from Ti, O and Ni estimated from the analysis of EDS signal are indicated on Table 4.2. Also, SEM images and mappings corresponding to TiO_2:$Ni_{0.2}$ and TiO_2:$Ni_{0.3}$ are presented in Fig.4.2(c)-(d) where it can be observed that Ni is homogeneously distributed in the sample.

As mentioned on section 2.2.6, ICP-OES allows to detect light elements such as lithium. Table 4.2 shows the ICP-OES quantification results for the samples.

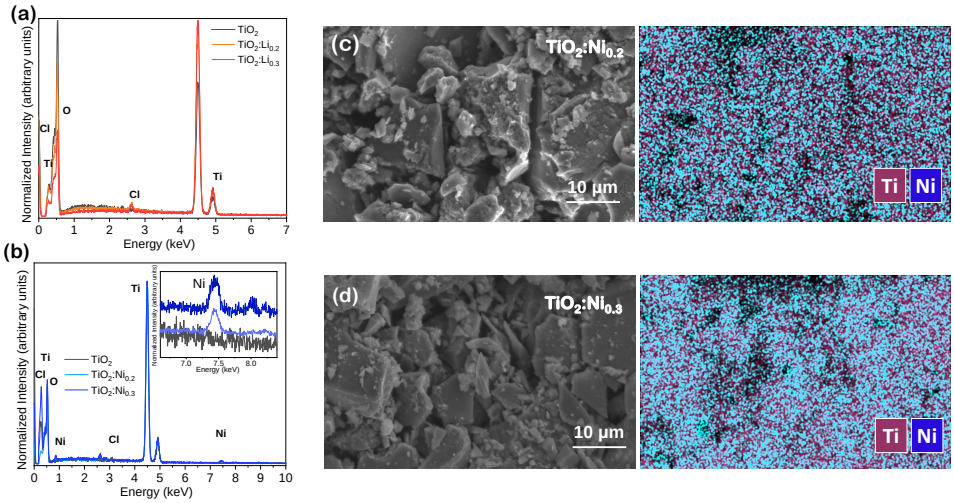

Fig. 4.2: Normalized EDS spectra acquired for undoped and (a) Li and (b) Ni doped TiO_2 nanoparticles. Inset in (b) shows detailed region between 6.5 and 8.5 keV. Figures (c) and (d) show the SE and EDS mapping of Ni and Ti corresponding to samples TiO_2:$Ni_{0.2}$ and TiO_2:$Ni_{0.3}$

Low Li concentration of 0.50 % and 0.65% atomic were estimated for the samples TiO_2:$Li_{0.2}$ and TiO_2:$Li_{0.3}$, respectively.

The atomic ratio Ti/O is close to the theoretical one from TiO_2 (33% /66%) for all the samples, as shown in Table 4.2, although small variations can be observed in the doped samples. Apart from the low amount of Cl, no other elements were detected in the analyzed nanoparticles within the resolution of this technique.

Table 4.2: Atomic percentages of Ti, O and Ni obtained by EDS and Li obtained by ICP-OES

Technique	% at	**TiO_2**	**$Li_{0.2}$**	**$Li_{0.3}$**	**$Ni_{0.2}$**	**$Ni_{0.3}$**
EDS	**Ti**	38.7± 2.0	25.9 ± 1.3	36.3 ± 1.8	39.1 ± 1.9	35.8 ± 1,7
	O	61.3±30.7	74.1 ± 24.8	62.86 ± 30.2	59.56 ± 15.2	62.06 ± 22.4
	Ni	-	-	-	1.4 ± 0.1	1.5 ± 0.2
ICP-OES	**Li**	-	0.50 ±0.03	0.65 ±0.02	-	-

4.1.3. TEM characterization

Fig.4.3(a)-(c) shows the TEM images of the undoped TiO_2 and doped TiO_2 with the highest dopant concentration, TiO_2:$Li_{0.3}$ and TiO_2:$Ni_{0.3}$, in which we can observe that nanoparticles exhibit rounded shape and dimensions in the range of 10 nm. Each TEM image includes an histogram showing the average size of the nanoparticles calculated from the analysis of the images. For TiO_2 the average size is 6.72±1.78 nm while for TiO_2:$Li_{0.3}$ is 7.88±2.14 nm and for TiO_2:$Ni_{0.3}$ is 8.65±2.50 nm. This is in agreement with XRD measurements which also showed lower size for the undoped nanoparticles.

The corresponding SAED patterns Fig.4.3)(d)-(f) confirm the crystallinity of the undoped and doped TiO_2 nanoparticles. The observed crystalline planes are in agreement with those observed in XRD,

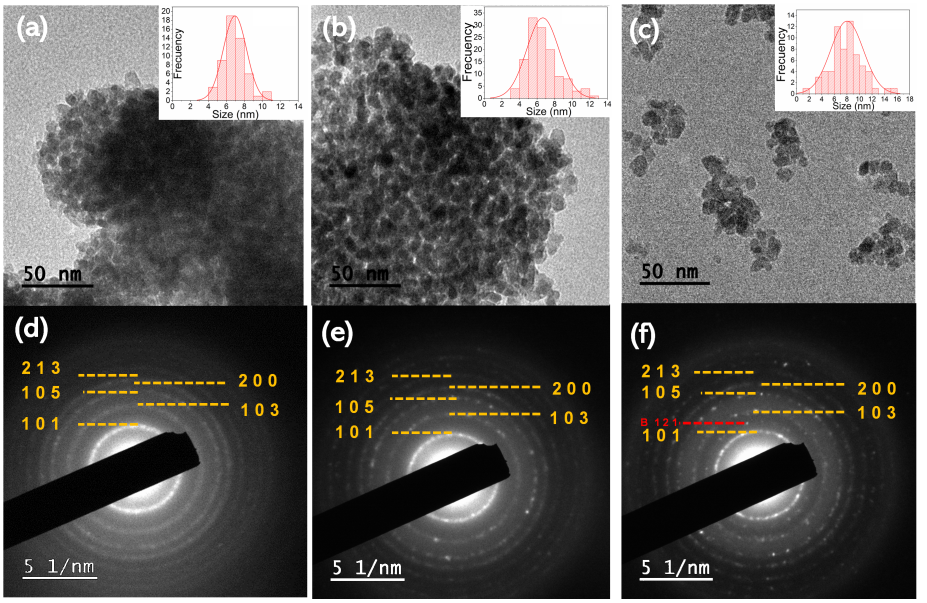

Fig. 4.3: TEM images corresponding to (a) TiO_2, (b) TiO_2:$Li_{0.3}$ and (c) TiO_2:$Ni_{0.3}$ nanoparticles. Insets show histograms with the average particle size distribution. (d),(e),(f) shows their corresponding SAED patterns.

4.1.4. Raman spectroscopy characterization

4.1.4.1. Undoped TiO_2

Raman spectroscopy was used to analyze the effect of the dopant and dimensions. A red laser ($\lambda = 633$ nm) (VIS) and an Ultra-Violet laser ($\lambda = 325$ nm) (UV) were used, which energies are lower and higher than the anatase band gap. Anatase TiO_2 phase is metastable as has been previously discussed. Thus, it is mandatory to control the laser intensity to avoid phase transition during data acquisition. Hence, a neutral filter was used in order to diminish the nominal intensity to $0.1 \cdot I_0$, specially important when the UV laser was employed.

Anatase TiO_2 possesses 15 optical modes with an irreducible representation of $1 \cdot A_{1g} + 1 \cdot A_{2u} + 2 \cdot B_{1g} + 1 \cdot B_{2u} + 3 \cdot E_g + 2 \cdot E_u$. Among these modes, A_{1g}, B_{1g}, and E_g, are Raman active (6 total Raman active modes) and the modes A_{2u}, and E_u, are infrared active. The B_{2u} mode is inactive both in the Raman and infrared spectra[156]

Firstly, undoped synthesized TiO_2 anatase nanoparticles were compared with commercial anatase nanoparticles (Sigma-Aldrich, 325 mesh, 99% purity, d=3.900), as shown in Fig.4.4 using both (a) a visible laser and (b) UV laser. Spectra were normalized as the commercial sample possesses higher Raman intensity. The relative position of the peaks are described on Table 4.3. Only peaks from anatase TiO_2 are observed in the Raman spectra. Size effects can be appreciated in the Raman signal of Fig. 4.4 as a wider E_g is observed for the nanoparticles in addition to a shift towards higher wavenumber, observed with both lasers. Inset on Fig.4.4(a) shows the region around 150 cm^{-1} where this effect can be clearly observed.

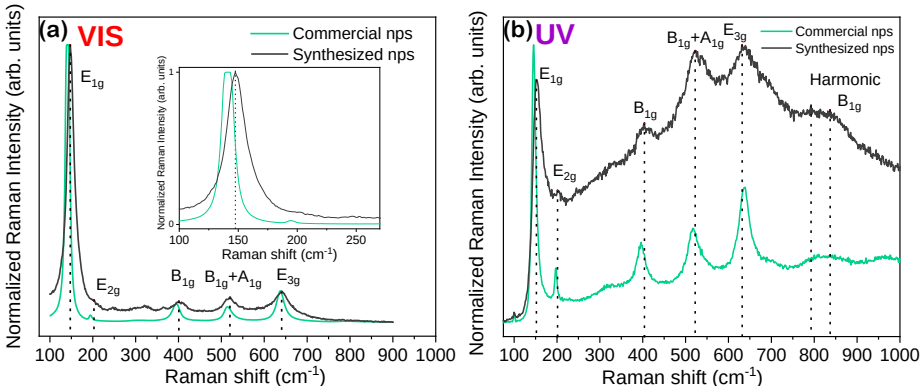

Fig. 4.4: Normalized Raman spectra of both anatase TiO_2 commercial (Sigma-Aldrich) and synthesized nanoparticles, acquired with a (a) VIS ($\lambda = 633$ nm) or an (b) UV ($\lambda = 325$ nm) laser.

In the Raman spectra of the synthesized nanoparticles acquired with the UV laser, shown in Fig.4.4(b), there is a contribution at 800-840 cm^{-1}, which was not observed under Raman spectra obtained with the VIS laser. This mode is often

disregarded on the literature, due to the difficulty of its observation. It should be mentioned that after the Gaussian-Lorentz deconvolution, it was composed by two contributions centered at 792 and 836 cm^{-1} for the synthesized nanoparticles.

The former contribution can be associated with the first harmonic B_{1g} overtone, while the latter contribution has been associated with stretching modes of short Ti-O bonds at the TiO_2 surface[157].

In this case, the presence of this contribution is the most remarkable change between both lasers as well as the change on the relative intensity of the peaks, as is clear that for the VIS laser the most intense peak is the E_g. Also, remaining Raman modes (B_{1g}+ A_{1g}, E_{3g}) not only change position, but also become the most intense modes. The position of the Raman peaks is listed in Table 4.3.

Table 4.3: Vibrational Raman modes measured with either the UV or VIS laser for both the commercial and synthesized TiO_2 nanoparticles. In both cases laser energy density was $0.1 \cdot I_0$.

Mode	**VIS**		**UV**	
cm^{-1}	Commercial	Synthesized	Commercial	Synthesized
E_{1g}	142	149	145	152
E_{2g}	193	199	199	203
B_{1g}	394	403	396	404
A_{1g} +B_{1g}	514	521	516	521
E_{3g}	637	646	638	632
Harmonic B_{1g}	-	-	811-848	792-836

4.1.4.2. Doped TiO_2

To asses the differences that may be due to the dopant addition, Raman spectra from undoped and doped samples are analyzed in the following section. Firstly, spectra were obtained with the VIS laser and then with the UV laser.

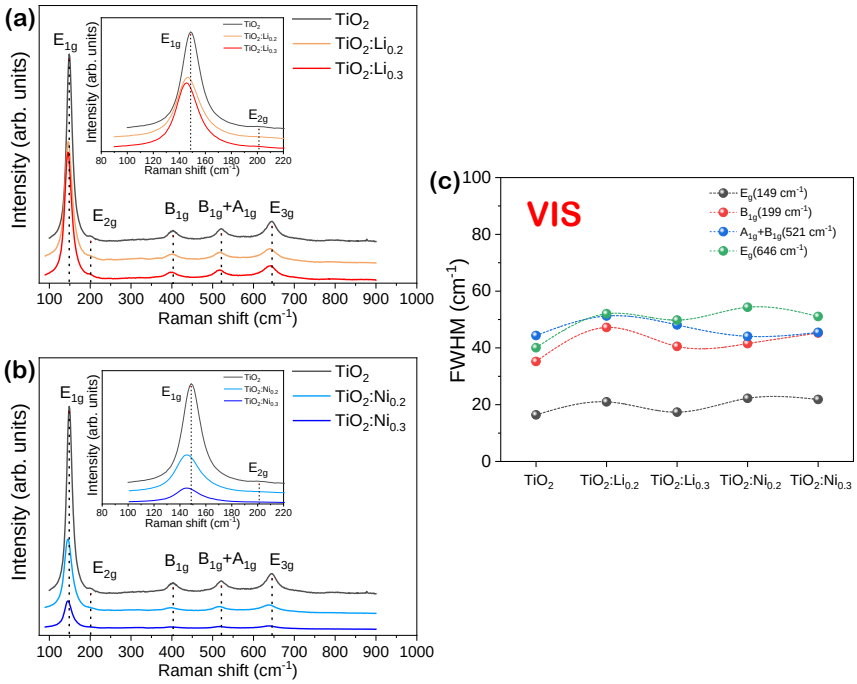

Fig. 4.5: Raman spectra from undoped TiO_2 and doped with (a) Li or (b) Ni and (c) FWHM of the different modes of each sample. These spectra have been recorded with the VIS laser as excitation source.

Fig.4.5(a)-(b) shows Raman spectra obtained with the VIS laser for the samples doped with 20% and 30% of Lithium or Nickel, respectively. Raman signal from undoped TiO_2 nanoparticles is also included as a reference. Even for the highest dopant concentrations, only anatase TiO_2 modes are observed. As the dopant concentration increases, Raman modes tend to diminish their relative intensity.

The E_g mode, which for undoped TiO_2 is around 149 cm^{-1} shifts to lower wavenumber with dopant addition. Table 4.4 shows the relative positions of the peaks. FWHM were obtained by deconvoluting the Raman spectra to Gaussian-Lorenzt functions (G-L). Wider peaks are observed for lower dopant concentrations as shown in Fig.4.5(c), which can be related to the lower dimensions of the doped samples, as confirmed by XRD and TEM analysis.

Fig.4.6 shows Raman spectra obtained with the UV laser of both undoped and doped anatase with lithium or nickel. There are also differences in the position of

Table 4.4: Vibrational VIS Raman modes of undoped and doped TiO_2 nanoparticles.

Mode cm^{-1}	VIS					UV				
	TiO_2	$Li_{0.2}$	$Li_{0.3}$	$Ni_{0.2}$	$Ni_{0.3}$	TiO_2	$Li_{0.2}$	$Li_{0.3}$	$Ni_{0.2}$	$Ni_{0.3}$
E_{1g}	149	148	147	146	144	152	151	152	150	150
E_{2g}	199	200	198	195	196	203	204	200	203	200
B_{1g}	403	401	396	399	398	404	394	400	404	395
A_{1g}+B_{1g}	521	519	520	517	515	521	522	523	520	522
E_{3g}	646	639	642	641	639	632	636	640	636	634
Harmonic B_{1g}	-	-	-	-	-	792	792	792	792	792
	-	-	-	-	-	836	856	853	860	853

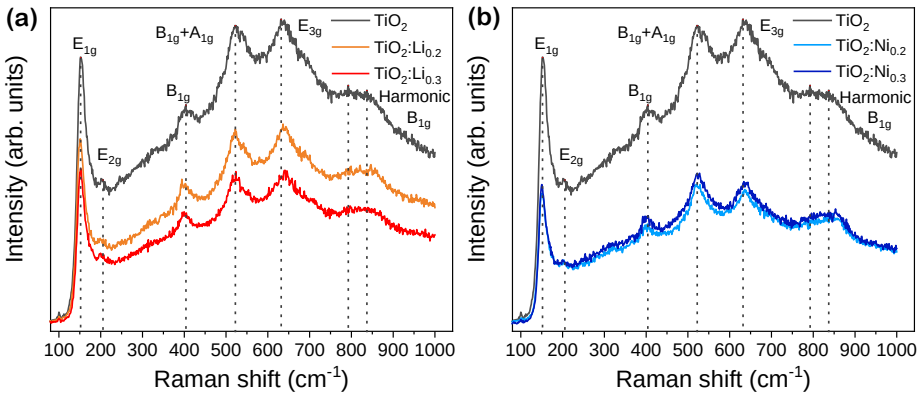

Fig. 4.6: Raman spectra from undoped TiO_2 and doped with (a) Li or (b) Ni nanoparticles. These spectra have been recorded with the UV laser as excitation source.

the Raman modes, which are summarized also in Table 4.4. According to Raman results, the modes which apparently are more sensitive to the dopant presence are E_{3g} (∼631 cm^{-1}) and the Raman mode centered at ∼836 cm^{-1}. E_{3g} mode is shifted towards higher wavenumber with dopant concentration, similarly to the contribution at ∼836 cm^{-1}. When the dopant concentration increases however, the shift is smaller for the contribution ∼836 cm^{-1}, as compared for low dopant concentration. It should be mentioned that the remaining E_g modes suffer also position shifts showing an opposite behavior, as E_{1g} and E_{2g} are shifted towards lower wavenumber. This second Raman mode is remarkably weak, notably for Ni-doped samples.

4.2. Optical characterization

4.2.1. Photoluminescence

Luminescence properties of the samples were studied by means of Photoluminescence (PL) measured at room temperature with an UV laser (λ=325 nm) and a filter D_1, as described in subsection 2.2.9 which diminished the laser intensity that reaches the sample by $0.1 \cdot I_0$. The objective of this chapter is studying the dopant influence on the anatase properties.

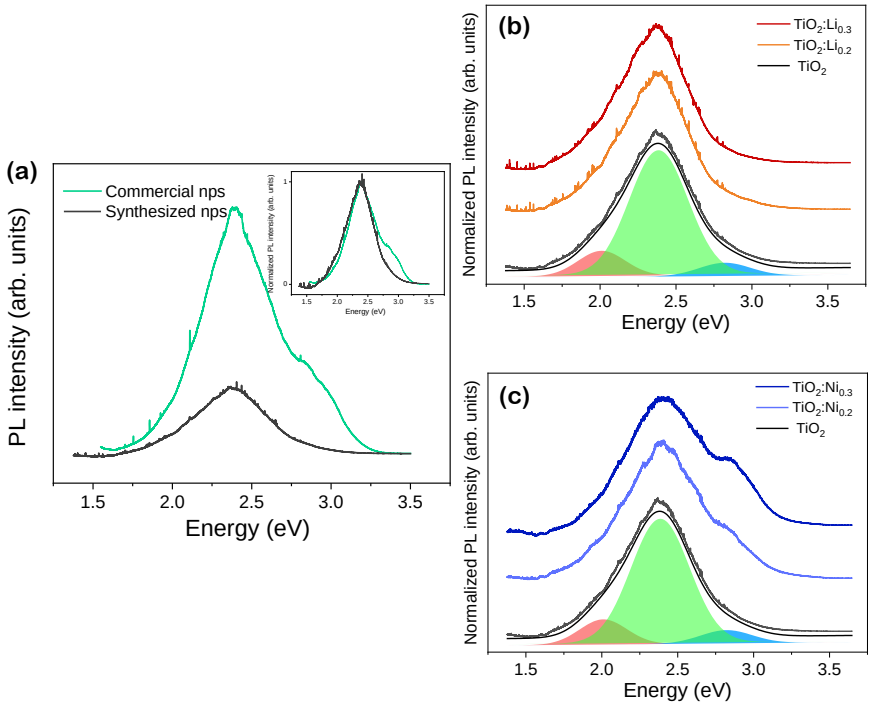

Fig. 4.7: PL spectra from commercial and synthesized nanoparticles where inset shows normalized photoluminescence spectra. Normalized PL spectra of undoped and doped with (b) Li or (c) Ni TiO_2 nanoparticles.

Fig.4.7(a) shows PL spectra without normalization and normalized (as an inset on the figure) of the undoped synthesized nanoparticles and commercial anatase nanoparticles (Sigma-Aldrich, 325 mesh, 99% purity, d=3.900). These spectra show characteristic wide emission around 2.3 eV, on top of a weak contribution around 2 eV and other shoulder at higher energy around 2.9 eV. The possible mechanism of those emissions are described in Table 4.5, where it can be observed that the main contribution at 2.3 eV, which covers a substantial part of the visible spectra, is attributed to surface defects, which are created due to oxygen deficiency. The

emission at $\sim$ 2.9 eV is attributed to self-trapped excitons, which are located in the TiO_6 octahedron, which were shown on chapter 1. The synthesized nanoparticles has lower PL emission intensity than the commercial sample, as it can be observed in Fig.4.7(a). The most noticeable change between the commercial and the synthesized nanoparticles is the strong enhancement of the contribution $\sim$2.9 eV in the PL signal, observed in Fig.4.7(a).

Table 4.5: Possible Anatase TiO_2 luminescence bands as suggested on the literature.

E (eV)	**λ (nm)**	**Origin**
~ 2	~ 620	Electrons which are promoted from the VB to shallow subgap states, which relax by occuping states below the CB[158] or oxygen vacancies related defects and undercoordinated Ti[157].
~ 2.3	~ 527.6	Surface defects normally associated with oxygen deficiency[157].
~ 2.9	~ 413.3	Normally associated with Self-Trapped Excitons (STE) localized at the TiO_6 octahedron[48].

Normalized spectra from the doped nanoparticles are displayed in Fig.4.7(b)-(c). All spectra show similar characteristics, which consist of a broad band around 2.35 eV which dominates the PL spectra, with the exception of the nickel-doped samples, which exhibit enhanced emission near 2.9 eV.

PL spectra contributions were fitted to Gaussian functions and results are presented on Table 4.9. Unlike Li doped samples, which all present a similar behavior on the band spectra for the PL signal, Ni doping enhances high energy contributions. It is observed that the contribution at 2.86 eV is enhanced by the Nickel addition. This band is related to the presence of STE.

4.2.2. Cathodoluminescence

TiO_2 luminiscent properties were as well studied via Cathodoluminiscence at Room Temperature and 120K, between 300 and 900 nm, acquired in a SEM microscope using an acceleration voltage of 15 kV.

CL spectra acquired for the undoped and doped samples are shown in Fig.4.8. As a reference, the CL signal corresponding to the commercial sample is also shown, as marked on the graph. CL signal is strongly affected by the temperature and so both spectra at room conditions and low temperature (120K) are shown. Similarly to what was observed by PL, mainly two/three contributions centered in ∼1.5 eV and in the VIS region at 2.32 eV dominate the spectra. In the case of TiO_2:$Ni_{0.2}$ (as well for the commercial nanoparticles) there is a clear contribution at ∼3 eV, which particularly for the low Ni-doped is the main contribution of the spectra.

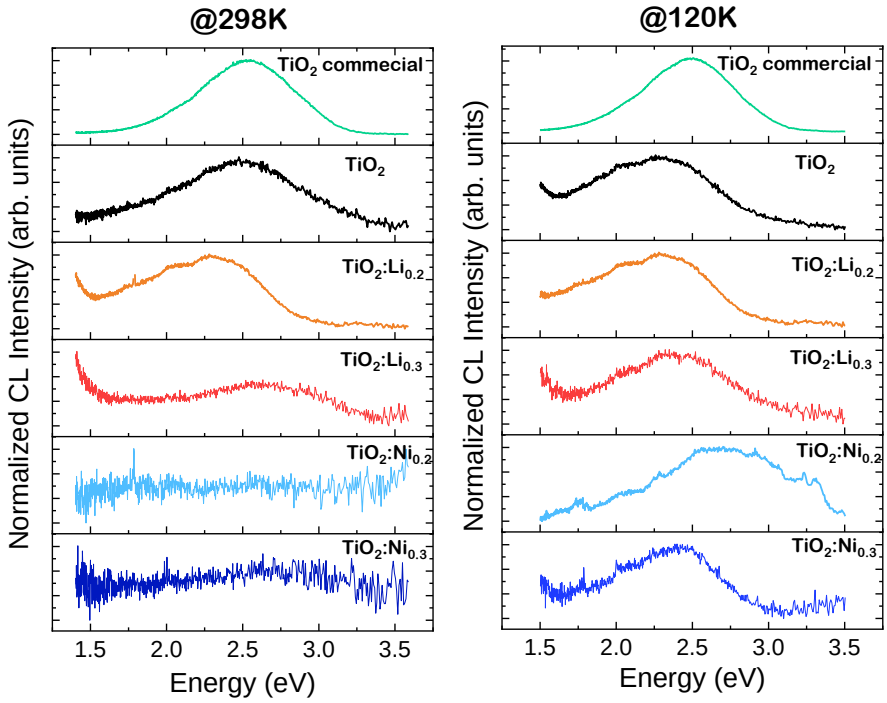

Fig. 4.8: Normalized CL spectra at (a) 298K and (b) 120K corresponding to the doped and undoped nanoparticles. The first spectra show the CL corresponding to the commercial TiO_2 nanoparticles as a reference.

Cathodoluminescence as a function of the temperature, can be also analyzed following the configuration coordinate model, as explained on the previous chapter. By fitting the relative intensities as a function of the temperature, it led to an activation energy of 407±20 meV for the orange band (∼2 eV) and 220±15 meV

for the green band (∼2.25 eV), demonstrating that each of the emissions is due to different mechanisms

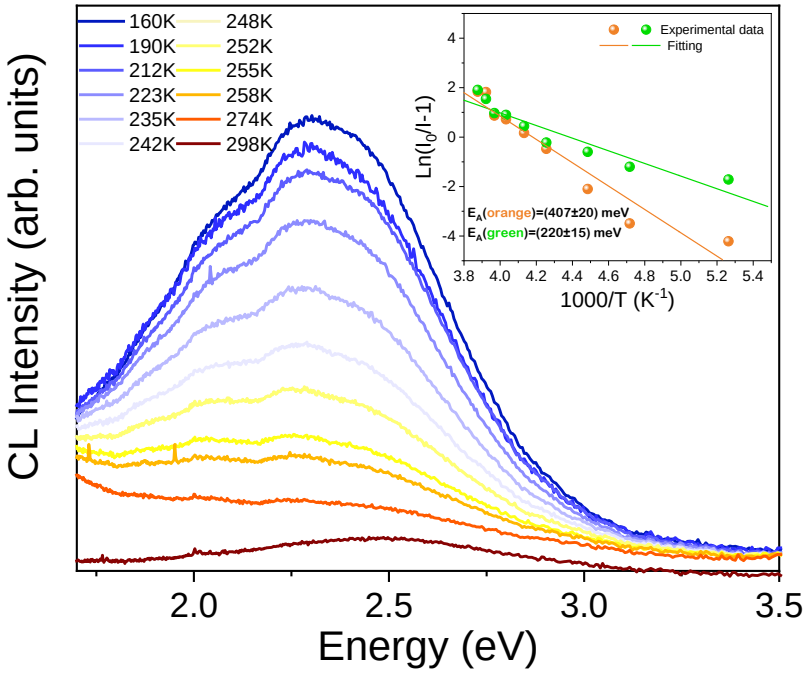

Fig. 4.9: Evolution of cathodoluminescence of undoped TiO_2 nanoparticles as a function of temperature. Inset shows linear fit to obtain the activation energy corresponding to each contribution on the spectra.

4.2.3. PLE

Photoluminescence (PL) and photoluminescence excitation (PLE) spectra were acquired with an Edinburgh Instruments FLS1000 system, exciting with a 450W Xe lamp as excitation source in a variable range from 10-300K.

First, both PL and PLE signals were measured in a wide band region (from 240-750 nm) and over different temperatures. For PLE measurements, obtained with an λ_{em}=540 nm, only a clear contribution from a band near 420 nm is observed, for both doped or undoped nanoparticles Fig.4.10.

Using the Xenon discharge lamp, it is possible to obtain PL signal by exciting with shorter wavelengths than with the UV laser as performed in the photoluminescence section. Not only that, but in this equipment it is possible to perform the measurements, lowering the temperature down to ∼4 K. In the Fig.4.11 the PL signal obtained with λ_{ex} = 290 nm, wavelength which possesses higher energy than the anatase band gap, from room temperature to 10 K (for the samples with

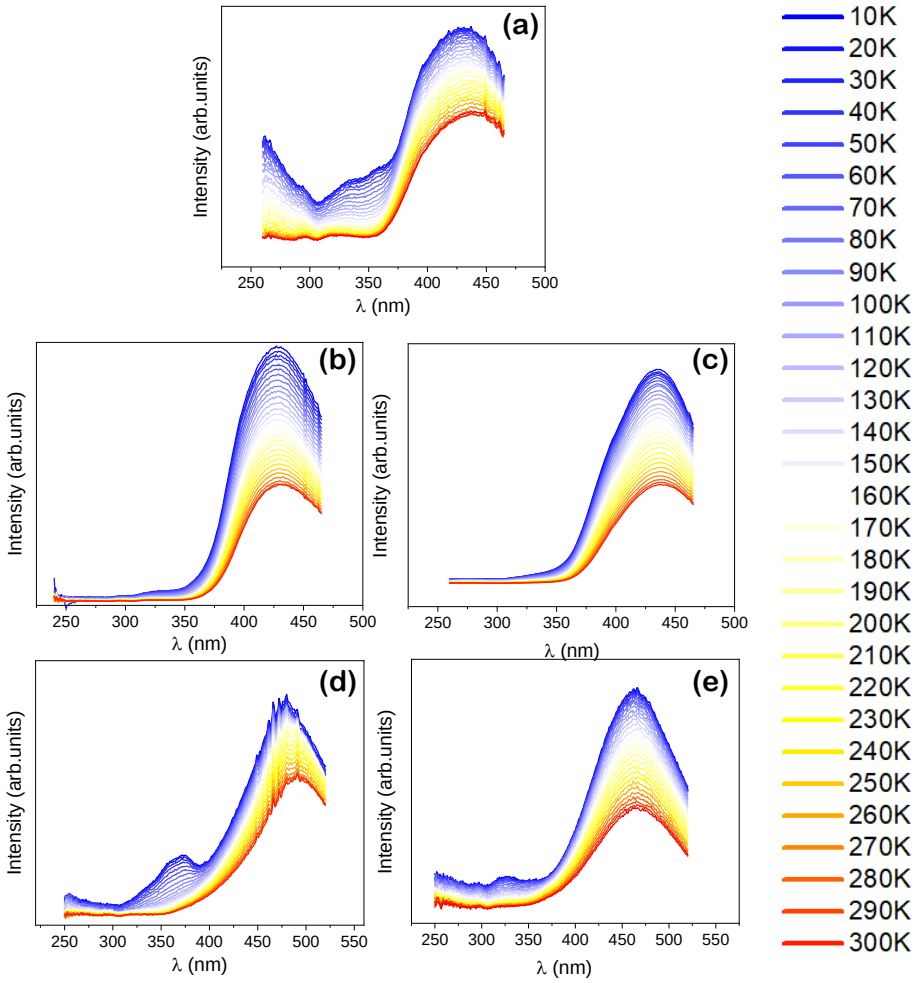

Fig. 4.10: PLE spectra corresponding to (a) TiO_2, (b) TiO_2:$Li_{0.2}$, (c) TiO_2:$Li_{0.3}$, (d) TiO_2:$Ni_{0.2}$ and (e) TiO_2:$Ni_{0.3}$ acquired for an emission wavelength of λ_{em}=540 nm in a temperature range between 10-300K.

the highest dopant concentrations). Their fitting to the Arrhenius equation led to the activation energies shown in Table 4.6. In this case, the complete spectrum was fitted to the equation which, for some of the samples, needed to be adjusted by adding other contribution with its corresponding activation energy E_B and pre-exponential factor B:

$$I = \frac{I_0}{1 + A \cdot e^{\frac{-E_A}{k_B \cdot T}} + B \cdot e^{\frac{-E_B}{k_B \cdot T}}} \tag{4.1}$$

Where I_0 is the intensity at the lowest temperature, A, B are two pre-exponential factor, E_A, E_B are the activation energy (in meV), k_B is the Boltzmann constant and T is the temperature. Note that, particularly for TiO_2:$Ni_{0.3}$, is the only case where the fitting was successful with only one activation energy.

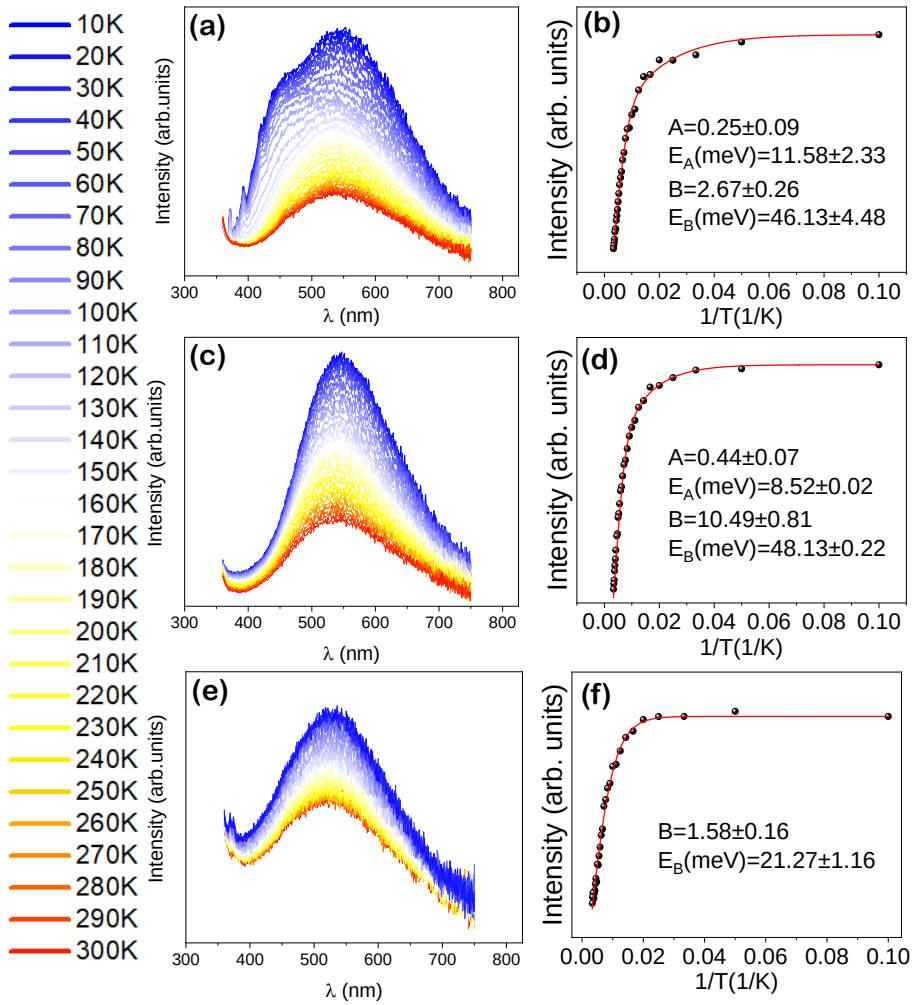

Fig. 4.11: PL spectra corresponding to (a) TiO_2, (c) TiO_2:$Li_{0.3}$ and (e) TiO_2:$Ni_{0.3}$ acquired for an excitation wavelength of λ_{ex}=290 nm on a temperature range between 10-300K and (b), (d), (f) their respective fittings to the Arrhenius equation.

Table 4.6: Activation Energies obtained from the fitting from spectra acquired at λ_{ex} = 290 nm.

Sample	A	E_A(meV)	B	E_B(meV)
TiO_2	0.25±0.09	11.58±2.33	2.67±0.26	46.13±4.48
TiO_2:$Li_{0.3}$	0.44±0.07	8.52±0.10	10.49±0.81	48.13±2.12
TiO_2:$Ni_{0.3}$	-	-	1.58±0.06	21.27±0.61

4.3. Electrical characterization

4.3.1. Hall effect

Hall effect measurements were performed on the samples in order to investigate their electrical properties at room temperature. Similarly than on the previous chapter, before measuring their electric properties, samples were pressed into pellets with silver paint contacts. Obtained values corresponding to the conductivity are shown in Table 4.7. Samples were highly resistive, which difficult their measurement, which was obtained with I=10 nA. High Li-doping presented the highest conductivity, which is almost one order of magnitude higher than for undoped TiO_2.

Table 4.7: Variation in the charge carrier concentration and the conductivity of the undoped and doped TiO_2 nanoparticles.

Sample	σ $(S \cdot cm^{-1})$
TiO_2	(-1.19±0.10)·10^{-7}
TiO_2:$Li_{0.2}$	(-8.26±0.92)·10^{-7}
TiO_2:$Li_{0.3}$	(-2.24±0.1)·10^{-6}
TiO_2:$Ni_{0.2}$	(-1.87±0.77)·10^{-6}
TiO_2:$Ni_{0.3}$	(-3.15±0.84)·10^{-7}

4.4. Electronic characterization

4.4.1. XPS

Synchrotron radiation X-ray photoelectron (XPS) and soft X-ray absorption (XAS) spectroscopy have been performed at the CNR Beamline for Advanced diCHroism (BACH) of the Elettra synchrotron facility in Trieste, Italy. The photoelectron spectra were acquired using a Scienta R3000 electron energy analyzer. All core-levels and valence band spectra were recorded with a total energy resolution of 180 meV. For those measurements, samples were prepared as pellets. Photoelectron spectra of Ti($2p$) and O($1s$) were calibrated referenced to Ti(IV)($2p_{3/2}$) peak set

at 458.6 eV due to charging effects in the probed samples. Valence band spectra were referenced to the 7.1 eV peak from the Valence Band. Ni($3p$) and Li($1s$) were calibrated to the Ti($3s$) (62.5 eV)[159]. XPS and XAS measurements can be extremely sensitive to the variations promoted in the anatase TiO_2 nanoparticles even for low differences in the concentration of dopants.

In Fig.4.12 XPS surveys for (a) Li doped and (b) Ni doped samples are represented. XPS spectrum from undoped TiO_2 is also included in Fig.4.12(b) as a reference. For the Li doped nanoparticles a beam energy of 253 eV was used in order to observe the Li($1s$) core level, whereas for undoped and Ni doped TiO_2 a beam energy of 650 eV was employed.

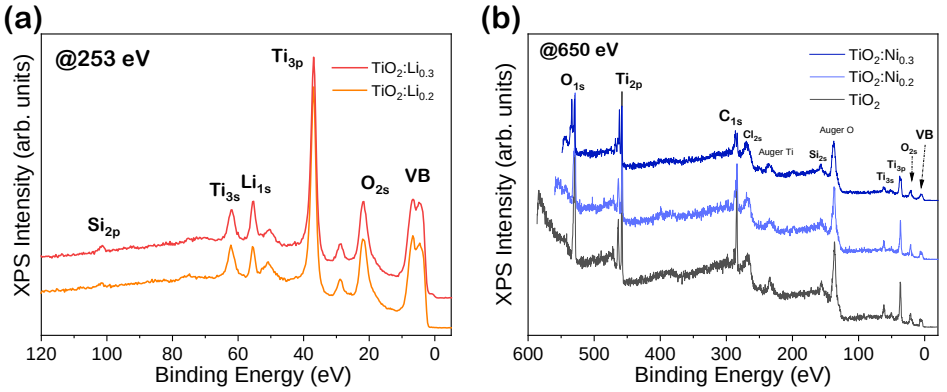

Fig. 4.12: XPS surveys from (a) Li or (b) Ni doped TiO_2 nanoparticles acquired with a beam energy of 253 and 650 eV, respectively. In (b) survey from undoped TiO_2 is shown for comparison.

After Shirley background subtraction, XPS peaks were fitted with Voigt functions. Ti($2p$) and O($1s$) spectra were normalized to the peak heights. On the other hand, Li($1s$) and Ni($3p$) were normalized with respect of Ti($3s$) level. An initial beam energy of 653 eV was used for the acquisition of the Ti($2p$) core level. Both for undoped and doped samples, Ti($2p$) spectrum exhibits the usual splitting into Ti($2p_{1/2}$) and Ti($2p_{3/2}$) at energies around 464.4 and 458.6 eV, respectively[89]. The XPS spectra from the undoped and doped samples can be fitted with only one contribution associated with Ti^{4+} in TiO_2, as shown in Fig.4.13. Other contributions due to the presence of Ti with lower oxidation states were not detected in this case, within the resolution of the technique, which indicates high crystallinity for the analyzed nanoparticles.

Fig.4.14 shows the O($1s$) core level for the undoped and the doped TiO_2. Two main contributions, centered at 529.7 eV (O_I) and 531.3 eV (O_{II}), can be observed in the XPS spectra. The O_I contribution is due to the O^{2-} in the anatase TiO_2 lattice (529.7 eV), while O_{II} (531.3 eV) is a complex contribution commonly associated with the presence of oxygen vacancies related defects[160], hydroxyl groups or chemisorbed oxygen[137]. A slight decrease in the relative intensity of the high en-

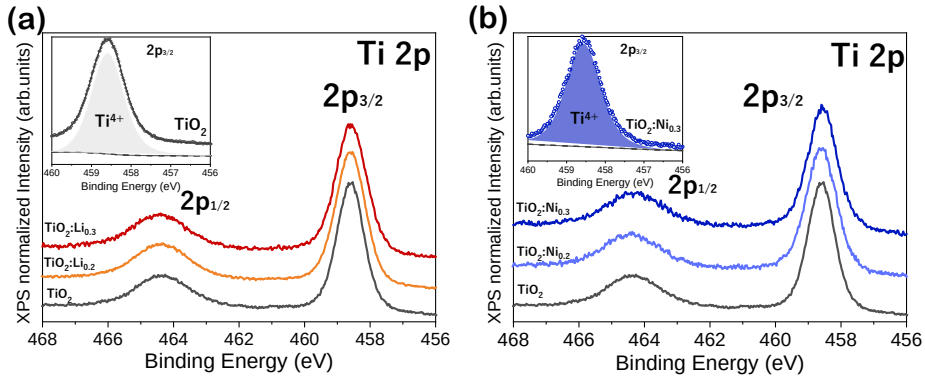

Fig. 4.13: XPS Ti($2p$) core levels from undoped and doped with (a) Li or (b) Ni TiO_2 nanoparticles acquired with a beam energy of 650 eV. Deconvolutions corresponding from Ti($2p_{3/2}$) core level from TiO_2 and TiO_2:$Ni_{0.3}$ are shown in the inset in (a) and in (b).

ergy band (O_{II}) is promoted by doping with Li or Ni. This effect is more noticeable for lithium doping.

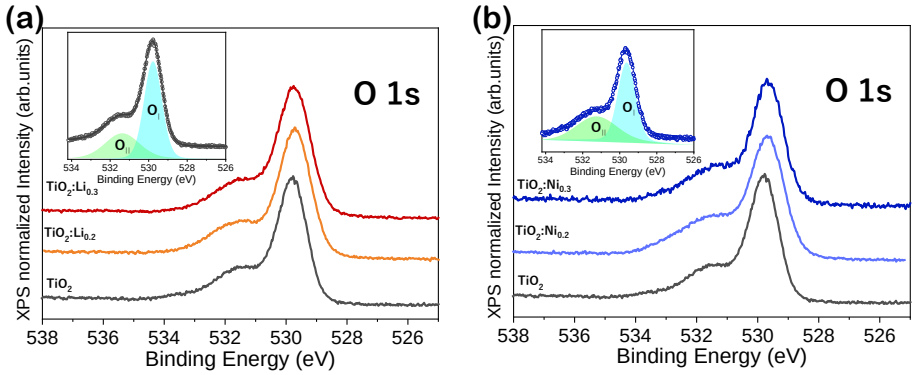

Fig. 4.14: XPS O($1s$) core levels from undoped and doped with (a) Li or (b) Ni TiO_2 nanoparticles acquired with beam energy of 650 eV. Deconvolutions corresponding to O($1s$) core level from TiO_2 and TiO_2:$Ni_{0.3}$ are shown in the inset in (a) and in (b).

The Li($1s$) core levels from the Li doped TiO_2 samples are shown in Fig.4.15(a). The XPS spectra are centered at 55.8 eV for TiO_2:$Li_{0.2}$ and 55.9 eV for TiO_2:$Li_{0.3}$, which energies correspond to Li^+, thereby confirming Li doping in these samples. As expected, the analysis of the Li($1s$) signal confirms the lower Li concentration for the sample TiO_2:$Li_{0.2}$, in agreement with the ICP-OES measurements. Fig.4.15(b) shows Ni($3p$) and Ti($3s$) core levels from the Ni doped nanoparticles. The broad contribution in Fig.4.15(b) centered at around 68 eV can be associated with Ni($3p$), thus confirming Ni doping in the samples.

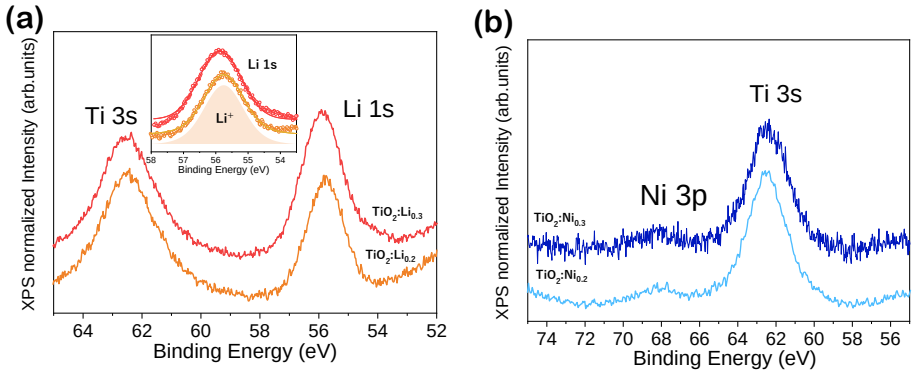

Fig. 4.15: XPS core level (a) Li($1s$) and (b) Ni($3p$) from Li-doped and Ni-doped TiO_2 nanoparticles, respectively, acquired with a beam energy of 650 eV for Ni($3p$) and beam energy of 253 eV for Li($1s$). Inset in (a) shows Li($1s$) spectra for Li doped samples without normalization.

The valence band region for the undoped and doped TiO_2 nanoparticles are shown in Fig.4.16. The spectra position was calibrated using as reference the O($2p$)-Ti($3d$) bonding peak at ∼7.1 eV. The energy difference between the Fermi level and the maximum of the valence band (E_F -E_{VBM}) is similar for the undoped and Li doped samples. Nonetheless, Ni doped samples show E_F-E_{VBM} values lower than undoped TiO_2 about 0.35 and 0.5 eV for the TiO_2:$Ni_{0.2}$ and TiO_2:$Ni_{0.3}$ samples respectively, showing a lower n-type character induced by Ni doping. In that case, the presence of acceptor levels induced by Ni doping should be considered. Each VB region is characterized by two broad peaks at ∼4.7 and ∼7.1 eV mainly related to non-bonding and bonding O($2p$) orbitals, respectively, in accordance with the scientific literature[49]. Differences between the spectra can be observed in the low energy region below 3 eV, as marked with an arrow in the inset of Fig.4.16.

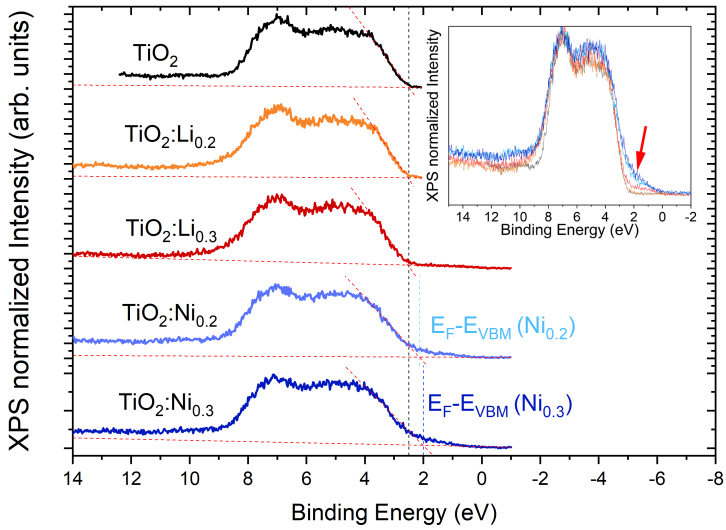

Fig. 4.16: Valence band region of TiO_2 and doped (Li,Ni) TiO_2 samples. Inset shows detailed region between 0-14 eV.

4.4.2. XAS

To deeply study the electronic structure and the so-related TiO_2 defects induced by doping, XAS measurements have been performed. As shown in Fig. 4.17,4.18,4.19, the absorption edges corresponding to Ti $L_{3,2}$, O K and Ni $L_{3,2}$, respectively are represented for each sample.

Fig.4.17 shows the XAS spectra of doped TiO_2 nanoparticles as well as undoped TiO_2 as a reference. Ti $L_{3,2}$-edge is associated with transition of the core electrons from the Ti($2p$) to unoccupied Ti($3d$) states[107]. Absorption spectra in this work are in good accordance with previous studies on anatase TiO_2 nanostructures[161–163].

Peaks labeled as A and B in Fig.4.17 belong to the L_3 edge while peaks labeled as C and D belong to the L_2 edge. The splitting of the $L_{3,2}$-edge is due to spin orbit coupling in $L_3(2p_{3/2})$ on the range between 454-462 eV, and L_2 $(2p_{1/2})$ on the range between 462-467 eV, which are also further split due to crystal field into t_{2g} (d_{xy}, d_{xz}, d_{yz}) and e_g $(d_{z^2}, d_{x^2-y^2})$ orbitals. The first two peaks in Fig.4.17, labeled as A and A', are two small pre-peaks related to a transition which is forbidden in LS-coupling, but becomes allowed because of the multi-pole $2p-3d$ interactions[162]. Peak B_2 confirms the presence of the anatase phase, as the intensity ratio of this doubly-splitted e_g is reversed in anatase and rutile due to the difference of their crystal symmetries[164], being the intensity of B_2 higher than B_2' for anatase, with a ratio $B_2/B_2' > 1$[165], as observed in this case. It can be noticed that there are small, but not negligible, variations in the XAS spectra among the probed

samples, as observed for the B_2 peaks. It has been reported that either changes or the disappearance of the shoulder B_2 may be due to the structure distortions and the chemical changes in anatase TiO_2. In this case, slight variations on the ratio of the relative intensities $B_2/B_2' > 1$ are observed with dopant addition. These weak distortions in the XAS spectra observed in the doped nanoparticles could be associated with small changes in the oxygen deficiency, in agreement with Raman and PL measurements.

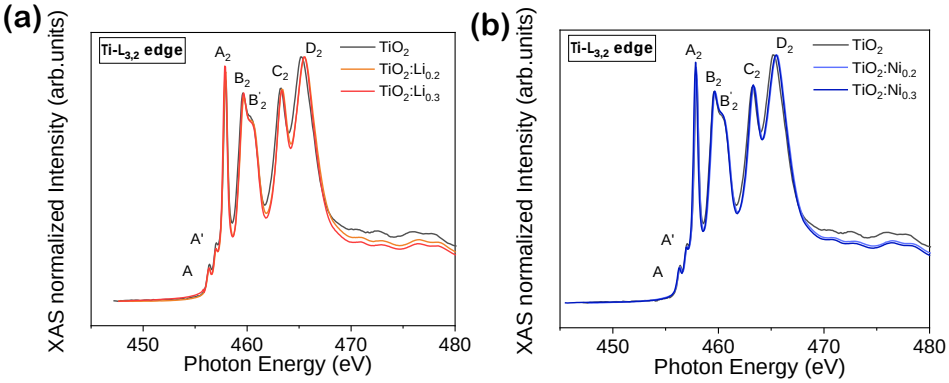

Fig. 4.17: XAS spectra showing Ti $L_{3,2}$ edge from undoped and (a) Li or (b) Ni doped TiO_2 nanoparticles.

Fig.4.18 represents de O-K edge spectra which describe the electronic transition from O($1s$) to unoccupied O($2p$) states primarily hybridized with Ti-($3d$) unoccupied states. In this case the XAS spectra can be divided in two main regions. The first region which possesses lower energy, ranges between 530-536 eV. This region reflects the O($2p$)-Ti($3d$) hybridization where due to crystal field, Ti($3d$) splits into t_{2g} π- antibonding states and e_g σ-antibonding states respectively, placed at 530.6 and 533.3 eV (P and Q peaks). These states are related to the splitting of d orbitals from titanium due to the crystal field Dq. The second region, at higher energies >536 eV (R and S peaks), is due to transitions in hybridization of O($2p$) and Ti($4sp$)[162]. This region has two clear contributions labeled as R and S. These two features reflect oxygen and titanium antibonding states[165].

The XAS spectrum is sensitive to the electronic environment of the oxygen atoms. Small variations in the relative intensities of the XAS peaks are observed in the XAS spectra from the doped nanoparticles, as compared with undoped TiO_2. Almost no peak broadening is observed which indicates the high crystallinity of the samples even after the dopant inclusion into the crystal lattice. The decrease in the relative intensity of these peaks could indicate variations in the oxygen chemical surrounding, as the titanate octahedron can be distorted due to the dopant inclusion. Groot et al.[92] have studied the oxides of transition metals in which a considerable amount of information can be obtained from both the intensity ratio and the peak position which are related not only to the hybridization of the states

in both VB and CB but also with the projection of the DOS of empty states O($2p$).

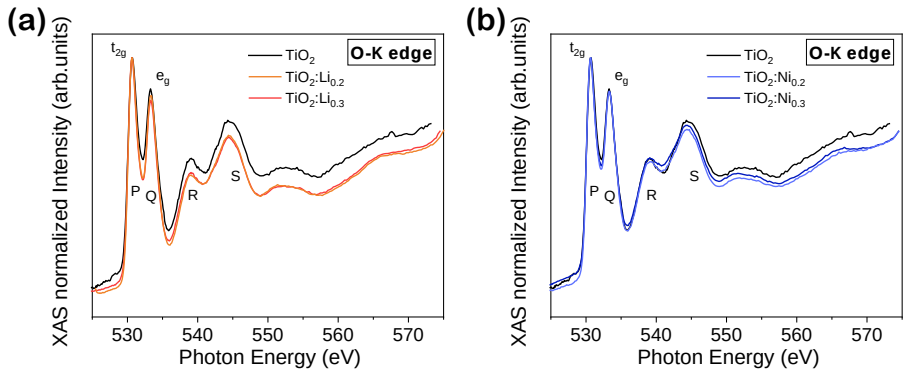

Fig. 4.18: XAS spectra showing O-K edge from undoped and (a) Li or (b) Ni doped TiO_2 nanoparticles.

Fig.4.19 represents the Ni $L_{3,2}$ edge of the nickel-doped TiO_2 samples. Similarly to Ti $L-$edge, the spectra correspond to the allowed transitions from Ni($2p$) to Ni($3d$) states. The splitting in the L-edge is due to spin orbit coupling by approximately 17 eV in L_3 ($2p_{3/2}$) in the range between 850-855 eV and L_2 ($2p_{1/2}$) 865-875 eV range[112]. Coulomb and exchange interaction between the core holes and the $3d$ shell produces a splitting on the L_3 (U and V) and L_2 (W and X) peaks. Ni(II) high spin spectrum is in agreement with our spectra, as it presents a high-energy side of the L_3 peak and a splitted L_2-edge[166]. This is further in agreement after estimating the ratio $L_3/(L_2 + L_3)$ that agrees with Ni(II), not shown here[112], which indicates that Ni is incorporated in the TiO_2 lattice mainly as Ni^{2+} .

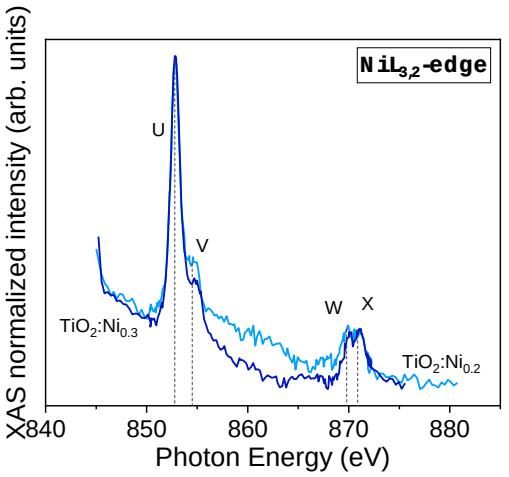

Fig. 4.19: XAS spectrum showing Ni $L_{3,2}$ edge corresponding to the sample TiO_2:$Ni_{0.3}$.

4.4.3. RPES

In order to get a deeper insight in the origin of some of these contributions in the VB region, mainly in the low energy region below 3 eV, resonant photoemission spectra were also acquired. This technique is based on the changes of the intensity of the photoemission under excitation with certain photon energies, which allows to identify the origin of the features observed associated with the atomic bonding on our structure. By tuning the incident photon energy across the element specific core-level, it is possible to enhance the related states in the valence band or in the band gap. On-resonance resonant photoemission spectra (RPES) for Ni and Li states were acquired using energies of 852.8 eV, for the sample TiO_2:$Ni_{0.3}$,and 56 eV for TiO_2:$Li_{0.3}$ based on the XAS measurements shown in Fig.4.20(a)-(b). For the off-resonance XPS spectra energies of 847 eV and 52 eV, respectively, were used.

Fig.4.20(a) shows RPES spectrum for TiO_2:$Li_{0.3}$. There are two clear resonant features around ∼4.7 and ∼7.1 eV, respectively related to non-bonding and bonding O($2p$) orbitals as previously mentioned, and a weak resonant peak at ∼1 eV, marked with arrows in Fig. 4.20(a). The first peak at ∼4.7 eV shows a range off-resonance between 55 and 62 eV, approximately, whereas the second peak at ∼7.1 eV resonates until higher energies as 66 eV.

Resonances appear also in the VB region for the TiO_2:$Ni_{0.3}$ sample (Fig.4.20(b)). We observe not only that the aforementioned peak on ∼4.7 eV becomes dominant but also a shoulder at ∼2.5 eV that can be observed on the inset on Fig.4.16 becomes significant due to the resonating Ni-related states.

According to XPS and XAS results as well as previous PL and Raman measurements, the as-synthesized nanoparticles exhibit high crystallinity. Doping process

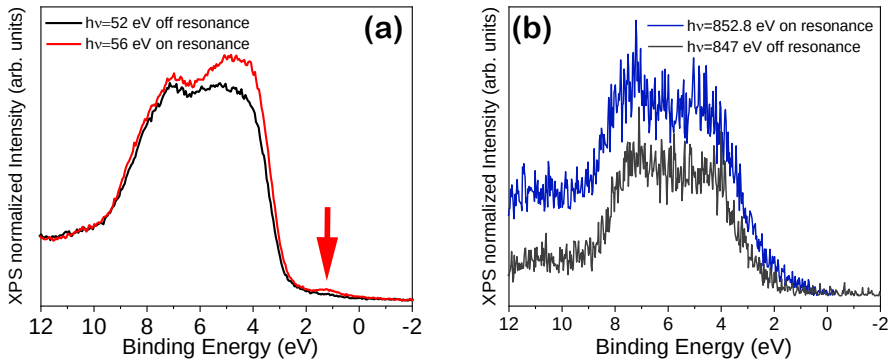

Fig. 4.20: (a) Valence band spectra of the sample TiO_2:$Li_{0.3}$ acquired under conditions of *off-resonance* (E_ν = 52 eV) and *on-resonance* (E_ν = 56 eV) and (b) Valence band spectra of the sample TiO_2:$Ni_{0.3}$ acquired under conditions of *off-resonance* (E_ν = 847 eV) and *on-resonance* (E_ν = 852.8 eV) according to the Ni-$L_{3,2}$ edge XAS spectrum.

leads to higher concentration of oxygen vacancies in Li doped TiO_2, while Ni doping induces in addition some other defects, as observed by PL, some of them probably associated with acceptor levels. Dopant-related states were also promoted in these nanoparticles. In particular Li or Ni-related states were observed in the VB region at ∼1 and 2.5 eV, respectively.

4.5. DFT calculations

To assess the effect of both the dopants and the oxygen vacancies on the electronic structure of anatase, first principles calculations were performed within the DFT method in collaboration with Dr. Ruth Martínez-Casado. Lattice parameters of $a = 3.76$ Å and $c = 9.65$ Å have been obtained in agreement with the experimental results presented in Table 4.1. The considered concentration of Li and Ni dopants can be seen in Table 4.8, which have been slightly overestimated with respect to the ones obtained by ICP-OES and EDS (Table 4.2) to observe more clearly the effect of the dopant concentration on the DOS.

Table 4.8: Band gap and cell parameters of the different samples obtained by DFT.

Sample	%at dopant	Band gap (eV)		Cell parameters	
		Without $V_O^\bullet$	With $V_O^\bullet$	a(Å)	c(Å)
TiO_2	-	3.61	4.51 (0.9)	3.767	9.655
TiO_2:$Li_{0.2}$	1.04	3.82	3.90 (0.08)	3.771	9.644
TiO_2:$Li_{0.3}$	1.69	3.71	3.85 (0.14)	3.768	9.659
TiO_2:$Ni_{0.2}$	1.04	3.99	4.18 (0.19)	3.767	9.655
TiO_2:$Ni_{0.3}$	2.08	4.0	4.26 (0.26)	3.760	9.594

Several substitutional positions have been studied in order to find the most stable configuration. A 12.5% of oxygen vacancies were introduced in each sample to match the experimental concentration. The most stable structures and projected DOS are shown in Fig.4.21 for (a) TiO_2 (b) TiO_2:$Li_{0.3}$ and (c) TiO_2:$Ni_{0.3}$. Fig.4.21(a) shows that undoped TiO_2 under the presence of oxygen vacancies promotes the formation of middle gap states coming from oxygen. Li doping does not seem to play a major role on the electronic structure of anatase as it can be seen in Fig.4.21(b), where the appearing states are due to the oxygen atoms. However, Ni introduces a variety of states on the band gap and close to the valence band (Fig.4.21(c)), reaffirming the results observed by XPS. Ni doped TiO_2 shows a rather complex role on the VB, in combination with oxygen vacancies, which may play a role on its ferromagnetic effects[167]. Previous studies had shown that the increasing of Ni doping favors rutile structure over anatase[168].

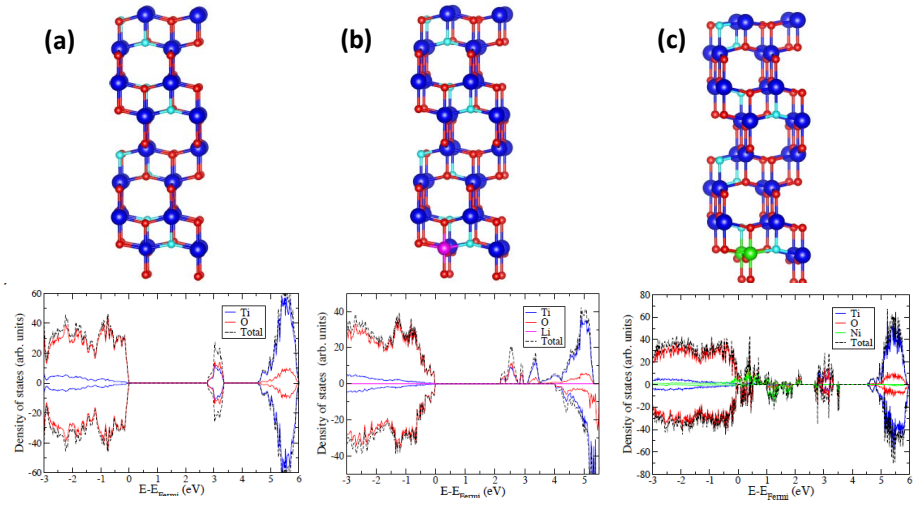

Fig. 4.21: Most stable structures and projected DOS for (a) TiO_2 ,(b) TiO_2:$Li_{0.3}$ and (c) TiO_2:$Ni_{0.3}$ with Ti, O, Li or Ni represented as blue, red, magenta or green circles, respectively. Oxygen vacancies are plotted in cyan.

Ni has been reported to decrease the band gap as well as to introduce intra-band gap states. This effect has been observed with our calculations as it can be clearly observed in Fig.4.21(c). The band gap values estimated by DFT calculations are shown in Table 4.8. In all cases the bandgap for anatase was overestimated, however a clear tendency of band gap narrowing in the doped samples is observed when oxygen vacancies are considered.

4.6. Anatase-to-rutile transition for doped TiO_2 with Li or Ni

In Chapter 1, it has been mentioned that the anatase phase is a metastable phase and the stable phase of TiO_2 is rutile. The transition from anatase to rutile is commonly denominated as ART. This transition is irreversible and occurs around 700 °C but it may vary depending on many factors such as the growth atmosphere, defects, particle dimension or addition of dopants during the synthesis process[39].

Herein, we have been able to transform anatase to rutile nanoparticles by two different methods, following results from previous reports[157,169]. The first method consists on enhancing the temperature and studying the transformation by measuring XRD diffractograms (Thermodifractometry as described in subsection 2.2.9). Second method is based on triggering the reaction via laser irradiation, analyzed by Raman spectroscopy.

4.6.1. Thermally-induced ART

In order to analyze the dopant influence on the anatase-to-rutile transition, thermodiffractometry has been performed by measuring XRD diffraction patterns at controlled temperatures from 500°C until reaching 1000°C. This complete process was therefore composed by 599 steps. Temperature profile increases with a 3 minutes slope and maintain constant temperature for 13 minutes. The studied θ and 2θ region, comprised between 19.9970 - 40.0171° with step size of 0.0334 °C has been scanned. In this selected region the ART can be tailored based on the monitor of the diffraction peaks at 25.28° and 27.51° which correspond to the diffraction planes of (101) for anatase and (110) for rutile phase (ICSD n°00-001-1292), respectively.

Fig.4.22(a) shows the evolution as a function of the temperature of the diffraction patterns corresponding to the TiO_2 sample, while the diffractograms under the same conditions for Li doped samples and Ni doped samples are presented, respectively, on Fig.4.22(b)-(c) and Fig.4.22(d)-(e). Maxima related to other oxides were not observed.

The rutile phase is observed in the images due to the appearance of diffraction maxima corresponding to the (110) planes of the rutile, which appears at approximately 27.51°. For undoped TiO_2, the beginning of the transition is around 740°C. As the annealing temperature increases, the maximum of the diffraction patterns from anatase (101) became narrower due to the increase of size of the nanoparticles, while its relative intensity decreased, as observed in Fig.4.22. Even up to 1000°C, undoped TiO_2 did not complete full phase transition. The relative information extracted from Fig.4.22 is found in Fig.4.23, on which we will focus our attention to determine the differences in the transition due to the presence of the dopants.

Fig.4.23 shows the temperatures at which the formation of the rutile phase begins, as well as the temperature range during which this transition takes place, being understood as the difference at which the diffraction planes corresponding

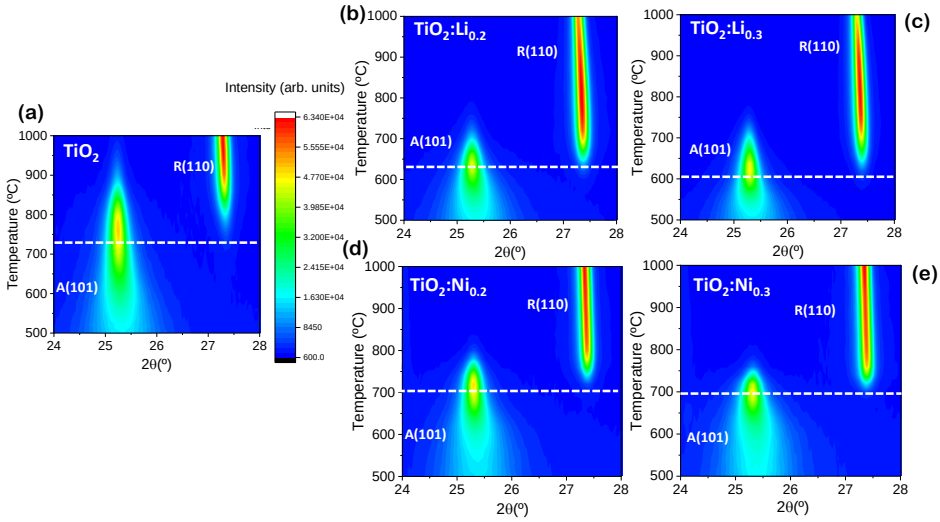

Fig. 4.22: X-ray Thermo diffractograms on the range 500-1000°C from samples (a) TiO_2, (b) TiO_2:$Li_{0.2}$, (c) TiO_2:$Li_{0.3}$, (d) TiO_2:$Ni_{0.2}$, (e) TiO_2:$Ni_{0.3}$

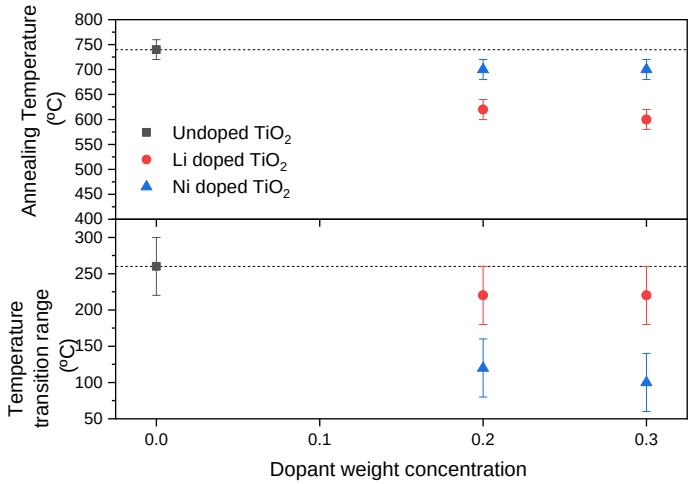

Fig. 4.23: Annealing temperature and range in which the transition from anatase to rutile occurs as a function of the dopant concentration corresponding to the undoped and doped anatase nanoparticles with either Li or Ni.

to rutile (110) begin to be significant up to the temperature at which the planes of anatase (101) are negligible. Not only is the type of dopant significant in the transition to rutile, it has been observed that the relative concentration of the

dopant modifies the transition to rutile, as observed in Fig.4.23. Doping with lithium in 20% and 30% concentration changes the temperature in which rutile starts to appear from 620 to 600 °C, while for Ni doping remains almost equal, within the uncertainty of these measurements. Nonetheless, among different Ni dopant concentrations, the range in which the transition takes place also decreases, from 120 to 100°C for 20% or 30% dopant concentration, respectively.

4.6.2. Laser-induced ART

4.6.2.1. UV laser effect on the Raman modes

It has been observed that Raman spectra acquired with UV laser changed as a function of irradiation conditions. For that purpose, neutral filters were selected to reduce the overall intensity by factors of 0.5, 0.25 and 0.1. Spectra acquired until this moment for the study of the anatase phase were acquired using 0.1 reduction factor to prevent undesired transition during data acquisition.

Therefore, we can promote rutile transition by means of appropriate laser irradiation. To asses how the laser intensity affects Raman spectra, UV Raman spectra were acquired with the complete set of neutral filters, and its effect on particular Raman modes has been analyzed, as shown in Fig.4.24 which shows the E_g mode. E_g mode was dominant on the Raman spectra, and it is sensitive to UV irradiation.

The commercial sample shows the most substantial changes, as not only E_g mode is shifted towards higher wavenumber with increasing laser intensity, when irradiated with the highest intensity (I_0), the E_g mode is less defined and clearly wider. The same effect was observed with the undoped TiO_2 nanoparticles, but with a less pronounced shift. Regarding doped synthesized nanoparticles, similar behavior is observed, but with subtle changes. For both Li or Ni doping, increasing intensity shifts the Raman spectra towards higher wavenumber, but this effect is most notably for Ni doped samples.

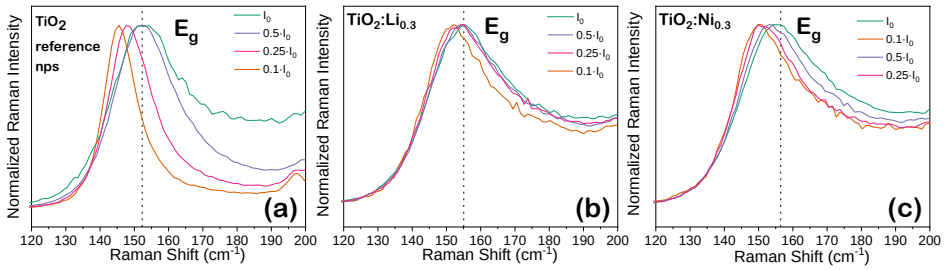

Fig. 4.24: TiO_2 Raman UV spectra centered on the E_g mode of the undoped (commercial) and Li or Ni 30% doped samples acquired with different laser intensity I_0 which varies by a reduction factor of 0.5, 0.25 or 0.1.

Some modes, as E_g, are more sensitive to laser irradiation: they shift towards higher energy as the laser power intensity increases, as shown in Fig.4.24. To discern

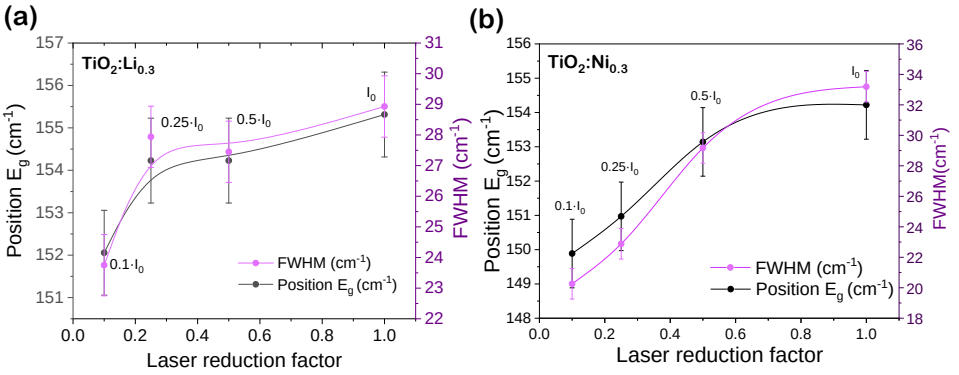

Fig. 4.25: Dependence of position and FWHM of the E_g mode on the laser intensity for the (a) Li 30% and (b) Ni 30% doped samples.

these small changes in the spectra of the doped samples, the E_g mode was fitted to Gaussain-Lorentz functions and its position as well of FWHM was obtained, as observed in Fig.4.25. Peak widening of the mode can be observed. This effect can be attributed to thermal effects related with the temperature increase due to higher energy and spot size. For some of the samples the effect is most noticeable, as for example for Ni 30% sample (Fig.4.25(b)).

4.6.2.2. Time dependence

The laser intensity is not the only factor to be taken into account to provoke the transition from anatase to rutile, since other factors, such as the exposure time, strongly affect the formation of the rutile phase. Therefore, samples were irradiated with the highest laser intensity I_0 during controlled time periods. After irradiation, Raman spectra were acquired with $0.1 \cdot I_0$ to assess the differences.

First, the Raman spectra from commercial anatase TiO_2 nanoparticles were acquired with maximum UV laser irradiation, to have a reference of the irradiation process. After 40 min of irradiation with the UV laser it is clearly observed that modes, which can be attributed to rutile phase, are observed mainly around 245, 447 and, most notably, at 615 cm^{-1} (A_{1g}) which can be indexed unequivocally to rutile by comparing with the rutile commercial nanoparticles, shown also in Fig.4.26. In particular, commercial rutile posses modes at (in cm^{-1}) 154 (B_{1g}), 263 (Multiphonon process) 414 (E_g), 613 (A_{1g}), as well as a shoulder 700 cm^{-1} which is a multiphonon process can be observed in Fig.4.26(a). Raman signal from anatase possesses higher relative intensity thus spectra are normalized. The strong decrease of the anatase E_g mode at $\sim$ 145 cm^{-1} is also a clear indicator of the undergoing transition. This mode strongly decreases over the first minutes of irradiation, as observed in Fig.4.26(b), while over longer periods of time it decreases much more slowly, which could indicate that the transition occurs within the first moments of irradiation.

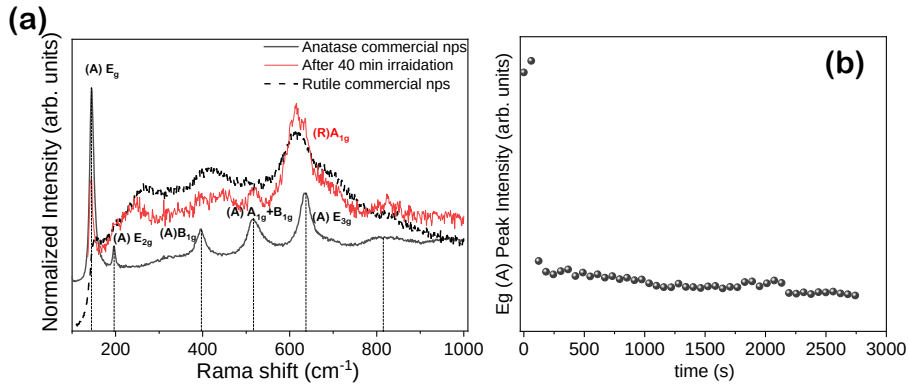

Fig. 4.26: (a) Raman UV spectra of anatase commercial nanoparticles before and after being irradiated with I_0 for 40 min. (b) Intensity evolution of the E_g corresponding to commercial anatase.

The synthesized nanoparticles, both doped or undoped, were also irradiated as shown in Fig.4.27. Undoped nanoparticles were irradiated for the longest time period, approximately during 2 hours as shown in Fig.4.27(a), which clearly induces a phase transition, as it can be observed by the shift on the E_{3g} mode at ∼630 cm^{-1} to ∼615 cm^{-1}, which corresponds to the rutile A_{1g} mode. Similarly than for commercial nanoparticles, the main mode from anatase (E_{1g}, ∼ 152 cm^{-1}), decreases upon UV-exposure time, as observed in Fig.4.27(b). Nonetheless in this case it is observed that the decay slope is lower, as well as continuous, which indicates that the transition occurs at a slower path. The time-dependency on the UV-induced phase transition was also studied for Li and Ni doped samples, with the highest dopant concentrations. Raman spectra from lithium with the highest dopant concentration are observed in Fig.4.27(c)-(d). Similar decay over time of the E_g is observed, and the transition to rutile apparently occurs at a similar path. The main change occurs for the Ni-doped samples, as they apparently are more stable under laser irradiation. After 30 min, the decay on the relative intensity of E_g of anatase is really small, as well as no other changes were observed on the spectra apart from a low decrease on its relative intensity, as observed in Fig.4.27(e)-(f).

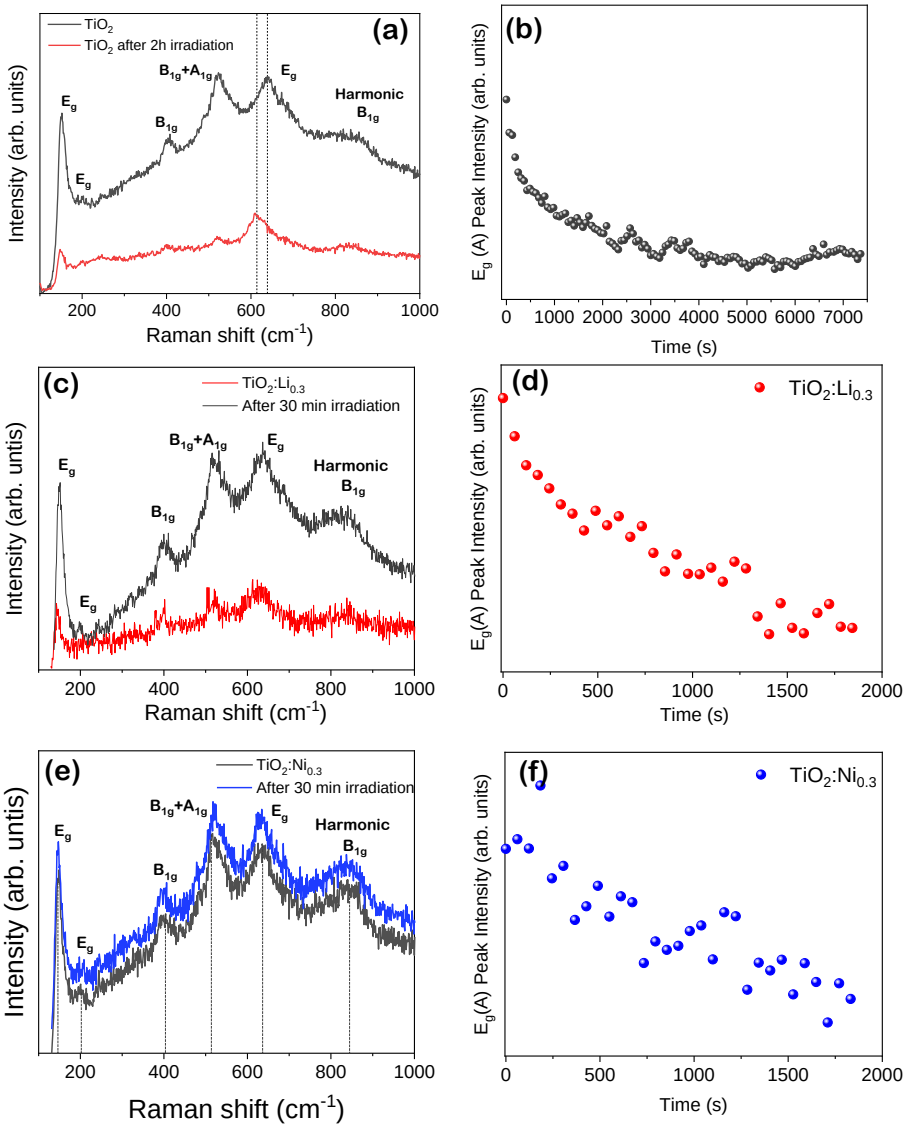

Fig. 4.27: (a) Raman spectra before and after 2h of laser irradiation with I_0 corresponding to TiO_2, (c) before and after 30 min of irradiation corresponding to TiO_2:$Li_{0.3}$ and (e) before and after 30 min of irradiation corresponding TiO_2:$Ni_{0.3}$ nanoparticles and (b),(d),(f) its corresponding intensity evolution of the E_g corresponding to anatase.

4.7. Applications in Li-ion batteries

The possible implementation of the TiO_2 nanoparticles as anodes in Li-ion batteries was performed at Enwair Energy Technologies Corp., Istanbul, Technical University, Istanbul Turkey in collaboration with Dr. Neslihan Yuca.
In this case, active materials, binder and carbon black (CaB) were mixed in water (weight ratio of TiO_2/(PAA)/CaB = 70/20/10) for 3 hours. Slurries were then coated on the copper foil by using a doctor blade. After electrodes dried, they were cut as disk for coin cell assembling. They were placed in the glovebox overnight and further dried in the vacuum oven at 90 °C for 12 h to completely remove the water. Celgard 2400 separator was obtained from Celgard. PAA (Mw: 450.000, Sigma-Aldrich) was utilized as binder. Lithium-ion electrolyte was purchased from BASF, including 1.2 M lithium hexafluorophosphate ($LiPF_6$) in EC, DEC (EC/DEC = 3:7 by weight), and 30% by weight of FEC were also added. The electrodes were used to assemble the coin cells. As a counter electrode, the Li metal was used. The performance of the assembled 2032 coin cells was evaluated with Neware Battery Test system. The cut-off voltage of cell testing is between 1.2 V and 0.01 V, assuming a theoretical value of 330 $mAhg^{-1}$ for TiO_2. Half cells were cycled at C/25 for 2 cycles, at C/10 for 2 cycles and at C/5 for following cycles[i]. Only undoped and Li-doped TiO_2 results are show, as Ni-doped samples shown very poor battery performance in terms of specific capacity.

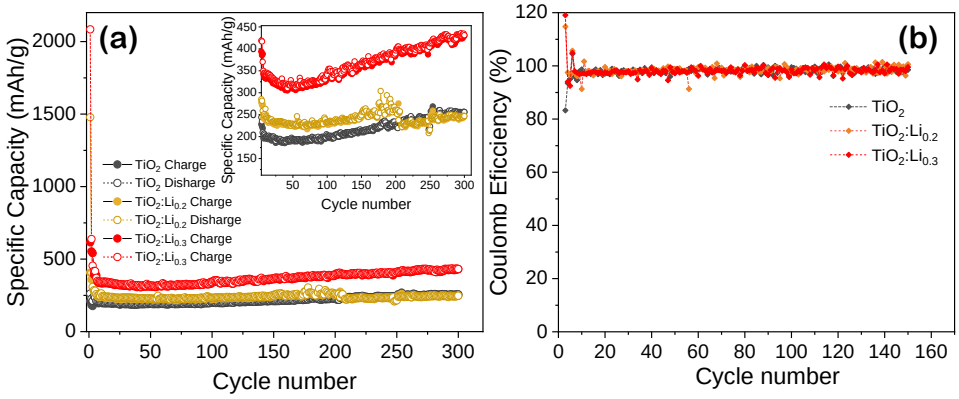

Fig. 4.28: (a) Specific capacity and (b) coulombic efficiency values upon cycling from LiB with anodes based in undoped and doped TiO_2 nanoparticles. Inset in (a) shows detailed region of specific capacity between 80-450 $mAhg^{-1}$.

The specific capacity and Columbic efficiency of TiO_2, TiO_2:$Li_{0.2}$ and TiO_2:$Li_{0.3}$ are shown in Fig.4.28. It was found that, initially the tested cells show capacities, after the initial 4 cycles at C/25 and C/10, respectively, of ∼198, ∼238 and ∼345 $mAhg^{-1}$ during discharge, respectively, as shown in Fig.4.28(a).During the following

[i]C-rate measures the rate at which a battery is discharged relative to its maximum capacity. In this case initially different C-rates were used for testing.

cycles the capacity decays, most notably for the TiO_2:$Li_{0.3}$ anode reaching ∼315 $mAhg^{-1}$ at 50 cycles.

However, after this initial decay the capacity of each sample increases over cycle number. After 200 cycles at C/5, cells with TiO_2, TiO_2:$Li_{0.2}$ and TiO_2:$Li_{0.3}$ electrodes showed 225, 261 and 396 $mAhg^{-1}$ specific capacity, respectively. Specific capacity of the anode containing TiO_2:$Li_{0.2}$ suddenly drops at 200 cycles, whereas TiO_2:$Li_{0.3}$ continuous to increase over time. Coulombic efficiency is close to 100% in all cases as observed in Fig.4.28(b) where the coulombic efficiency over the first 140 cycles are shown.

4.8. Discussion

During the last decades TiO_2 (titania) has become one of the most extensively-used wide-band gap semiconductors. Titania possesses different polymorphs, being the most notable: brookite, anatase and rutile. Anatase and rutile phases are both a tetragonal structure ($I4_1/amd$ and $P4_2/mnm$ respectively) but differ on their physical and chemical properties such as the refractive index, band gap or electrical conductivity, which determine its applicability.

In fact, anatase TiO_2 has been widely exploited in photocatalysis, solar cells, and lithium-based batteries[9,33,41] where it exhibits excellent optoelectronic properties and better photocatalysis effect than rutile TiO_2[6]. However, anatase can transform into rutile under certain operation conditions mainly because of its metastable nature, which should be considered in the design of anatase-based devices.

Different methods have been reported to synthesize anatase TiO_2[9,10,12,13,41] such as hydrothermal,[40,170] *Liquid-Mix*,[157,169] sol-gel,[48,137,160,171] mechanical alloying.[55] co-precipitation,[168] hydrolysis,[127] solvothermal,[172] CVD,[173] or Pulsed Laser Deposition (PLD)[49]. Among the most common methods to synthesize TiO_2, hydrolysis comprises significant advantages, as it is a low cost method for both undoped and doped nanoparticles, which presents a certain level of doping control on the final product. In most applications, enhanced properties of TiO_2 are determined not only by the crystallographic phase, but also by the dimensions, defects and doping. Recent attention has been focused on the investigation based on using transition metals dopants, such as Cr, Fe, Al[47,157], Co[48,174], Mn[117], Mo[175] or non-metals such as N, C, F, B[41] among many others[39,176]. In this work a transition metal (Ni) and a light element (Li) were selected as dopants in anatase TiO_2 nanoparticles. Nickel doping has shown remarkable results as a TiO_2 dopant in photocatalysis[55,168,170]and solar cells, while light metal dopants such as lithium have also demonstrated promising results for TiO_2 in catalysis[7], photocatalysis[40], electrode[177] or transport layer[178] in PeSC. In addition to the selection of the adequate dopant, its concentration should be also controlled as very low differences in the amount of dopant could lead to variable TiO_2 properties, which should be taken into account in the performance of TiO_2 in diverse devices. Doping anatase with different cations can control the ART and promotes or hinders the formation of rutile nanoparticles at low temperatures, which should be considered in the

development of TiO_2 based devices.

Via XRD analysis the only phase observed in the nanoparticles synthesis by hydrolysis in this work was anatase TiO_2 and a weak contribution of brookite on the Ni-doped samples with the highest dopant concentration, due to the low temperature on the synthesis process. No further oxides, precursors or secondary phases were observed. Furthermore, no peak shift was observed and neither peak broadening was observed. The obtained cell parameters were summarized on Table 4.1 (ICSD nº 01-071-1166). Nanoparticle sizes were always below 7 nm but the dopant effect respective to size is different for the different dopants. Li doped samples present higher dimensions up to 6.34 nm with lower dopant concentration. However, Ni doped samples linearly increases with dopant inclusion. Some authors had pointed out that occasionally lithium could migrate to the surface which could be a reason for the observed higher particle size[137].

Li^+ and Ti^{4+} possess similar ionic radii (R_{Li^+}=0.59 Å, $R_{Ti^{4+}}$=0.60 Å), hence Li^+ could substitute Ti^{4+} in the anatase TiO_2 lattice without substantial changes in the lattice parameters. In the case of the Ni doped nanoparticles, despite the larger Ni^{2+} ionic radius ($R_{Ni^{2+}}$=0.69 Å), a peak shift was neither observed, which could indicate that Ni is incorporated with variable oxidation states, Ni^{2+} and Ni^{3+}, as they possess a higher and lower ionic radius, respectively. Variable concentration of defects due to each dopant and its concentration should be also considered. The similar parameters observed could be understood due to the similar ionic radii[134] as $R_{Li^+}/R_{Ti^{4+}} \sim 0.98$ and $R_{Ni^{2+}}/R_{Ti^{4+}} \sim 1.15$.

Both EDS and ICP-OES assure the presence of the dopants. Ni-doped samples present an homogeneous distribution of Ni as observed in Fig.4.2(c)-(d). Despite the variable concentration of the dopant-based precursors in the synthesis procedure, similar concentrations of dopants were detected for both weight concentrations. This effect could be related to a near-solubility limit of the dopant on the anatase phase. The solubility limit of Li in anatase is related with different effects such particle size and oxygen stoichiometry[179], and for high concentrations it can not be omitted that Li appears to migrate towards the surface. Still, anatase structure has been conserved, being reported for 7 nm anatase particles able to host up to Li/Ti=0.21[180].

TEM measurements confirm that rounded and homogeneous particles with similar sizes were obtained. TiO_2:$Ni_{0.3}$ SAED shows the presence of brookite, in agreement with XRD results. It should be pointed out that anatase peak (101) on XRD could hide (120) and (111) peaks of brookite, which could be attributed to a lower temperature synthesis or an undesired effect due to the high dopant concentration.

Structural characterization was also studied by Raman spectroscopy. For all the samples analyzed in this work, the dominant peak is the E_g mode from anatase TiO_2 centered at 149 cm^{-1}. This mode is more sensitive to the concentration of oxygen vacancies in anatase TiO_2[157]. Firstly, the obtained nanoparticles were analyzed using both VIS and UV laser and compared with commercial anatase TiO_2 nanoparticles, which were used as reference. Intensity of Raman modes on commercial nanoparticles was higher as compared with synthesized ones. As well,

a slight shift towards higher wavenumber of the principal modes were observed. More clear was that every mode was less defined, most notably E_g, which is related to O-Ti-O symmetric stretching vibrations, mode observed with both lasers and the harmonic B_{1g} mode observed with UV. This is due to the high sensibility of distortions of both modes. The general lower mode definition is due to the multiple structure defects in the synthesized nanoparticles which is clearly observed on the following luminescence measurements.

Raman spectra obtained with the VIS laser show that the total intensity decreases for the doped samples, especially for the Ni doped ones. Moreover, for the doped samples there is a small redshift in all the modes, mainly for the E_g mode (149 cm^{-1}). This weak redshift is more noticeable for the nickel doped nanoparticles, together with a peak widening, as observed in the insets in Fig. 4.5. This redshift could be attributed to phonon confinement and non-stoichiometric defects in the doped nanoparticles probably due to the variable presence of oxygen vacancies[181]. Fig.4.5(c) shows the variation of the FWHM from the main Raman peaks, obtained by a deconvolution of each Raman mode to Gauss-Lorentz functions after background correction. It can be appreciated that the width of the peaks is higher for the doped samples, despite their slightly higher dimensions. For most of the modes, the FWHM increases for low doping and decreased for higher amount of dopant. These effects in the Raman signal from the doped nanoparticles can be related to the disruption and contraction of the TiO_2 lattice due to the substitution of Ti^{4+} for Ni^{2+}[182] or Li^+ creating oxygen vacancies. This broadening and peak shift have been also observed in Mn[183]or Mo[175]doped anatase TiO_2 which assures the effect on the oxygen vacancy generation to maintain overall charge neutrality after the dopant inclusion.

UV laser measurements were performed to obtain deeper information on the high energy region. This high sensibility is due to the relaxation fo the selection rules due to the low nanoparticle dimension. Fig.4.6 shows that, similarly to the results observed with VIS laser, the intensity of the Raman signal is dependent of the doping, being the lowest for Ni-doped samples. In this case, we can observe high energy contributions around 800-850 cm^{-1} Fig.4.6(b)-(c), which are summarized on Table 4.4. The former contribution is related to the 1st harmonic of the B_{1g} mode ($\sim$400 cm^{-1}) while the second mode is often disregarded. Undoped samples posses a lower contribution of both modes, being dominant the first contribution, however doping specially Ni-doping enhances the second contribution similarly to the results reported for Fe-doped samples[169]. These contributions are also shifted.

Normalized PL spectra of doped and undoped samples are shown in Fig.4.7. All the spectra can be deconvoluted to three main Gaussian contributions, at $\sim$2.0, 2.3 and 2.8 eV as shown in Table 4.9. The emission centered at $\sim$2.3 eV, which dominates the PL spectra from all the samples, has been usually attributed to surface defect associated with oxygen deficiency in anatase TiO_2[48,157,183–185]. The high-energy emission around 2.8 eV can be attributed to the presence of self-trapped excitons[48,157,183–185]usually observed in titanates formed for octahedral TiO_6, while the low-energy emission around 2 eV can be attributed to localized excitons[184].

Li doping does not affect significantly the luminescence as compared with anatase TiO_2 (Fig.4.7). However, the total intensity of the PL signal slightly decreases for the TiO_2:$Li_{0.2}$ sample, whereas increases for the nanoparticles with the highest amount of lithium (TiO_2:$Li_{0.3}$). This effect could be related to a disorder induced with Li^+ or the creation of recombination center of photogenerated electrons and holes[185]. Ni doping promotes and increases the relative intensity of the emission centered at 2.85 eV (Fig. 4.7), attributed to self-trapped excitons, as also reported for Fe-doped anatase TiO_2[157]. In this case, no significant variations were observed between sample TiO_2:$Ni_{0.2}$ and TiO_2:$Ni_{0.3}$. In both cases Ni-doping induces a decrease in the total intensity of the PL emission, as compared to undoped TiO_2, contrary to the effect observed for Li doping. Some authors reported a decrease in the PL signal for Co-doped TiO_2 related to the formation of non-radiative levels, although for Ni doping the localization of Ni trapping levels in the band gap should be also considered[55]. This effect is also supported by DFT calculations which points out to a possible reduction of the bandgap and the presence of impurity states for anatase TiO_2 doped with transition metals[186]

Table 4.9: Deconvolution parameters of the PL spectra to Gaussian functions acquired at RT from undoped and Li or Ni doped TiO_2 nanoparticles.

	Position (eV)	**FWHM (eV)**	**Relative Area (%, arb.units)**	**Reduced χ^2**
TiO_2	2.01	0.366	13.0	$1.09{\cdot}10^{-4}$
	2.39	0.454	79.6	
	2.82	0.400	7.5	
TiO_2:$Li_{0.2}$	2.00	0.379	14.7	$1.05{\cdot}10^{-4}$
	2.38	0.444	78.4	
	2.82	0.481	6.9	
TiO_2:$Li_{0.3}$	2.00	0.383	15.0	$1.06{\cdot}10^{-4}$
	2.37	0.448	79.8	
	2.86	0.454	5.2	
TiO_2:$Ni_{0.2}$	2.00	0.383	10.4	$2.01{\cdot}10^{-4}$
	2.40	0.484	74.5	
	2.86	0.391	15.1	
TiO_2:$Ni_{0.3}$	2.03	0.341	8.1	$1.60{\cdot}10^{-4}$
	2.42	0.468	79.9	
	2.85	0.403	21.0	

Cathodoluminescence results show similar luminescent bands than in Photoluminescence. Synthesized and commercial TiO_2 samples spectra are centered at $\sim$ 2.5 eV. Low Li-doping enhances the luminescent signal at $\sim$ 2.5 eV which is related to the presence of V_O,$V_O^{\bullet\bullet}$, while higher Li-doping luminescence is shifted towards $\sim$ 3 eV, and therefore shows the opposite behavior to what was observed in photoluminescence. This discrepancy on high-Li doping as compared with photoluminescence could be attributed to the poor CL signal which only triggers emission of certain radiative or non radiative centers. Ni-doping signal is extremely small but high-Ni doping wears a contribution towards 3.0 eV can be observed, which may be related to STE, as observed for PL. Decreasing temperature enhances lumines-

cence on the samples as it can be clearly observed in Fig.4.9. Moreover, the CL shift towards lower energy and the main contribution shifts from 2.5 eV to $\sim$ 2.33 eV and $\sim$ 2 eV is in overall the most enhanced feature with decreasing temperature. Reaching the minimum temperature of 120K all spectra were normalized as shown in Fig.4.8(b). At 120 K, undoped and Li-doped TiO_2 present a similar spectra, while Ni (especially low Ni-doping), shows a higher-energy contribution. These results are in good agreement with the observed by photoluminescence: Ni-doping enhances high energy contributions at $\sim$ 2.9 eV, related to STE. Battiston et al.[187] measured CL for TiO_2 anatase layers, and observed emissions at 500 nm ($\sim$ 2.48 eV), 550 nm ($\sim$ 2.25 eV) and 610 nm ($\sim$ 2.03 eV) which are in similar position to our observations. In our case, it is clear that the synthesis method creates a lower concentration of STE for Li and undoped samples, whereas Ni doping mostly in low concentrations, enhances these STE. The spectra of Ni at high concentration was very weak and the observed contribution which is similar to undoped anatase, could be misinterpreted.

PL and PLE were also obtained using a discharge Xe lamp at a variable range of temperature from which the activation energy were estimated. In all the samples we observe an activation energy E_B that is nearly five times larger than E_A (if present), while the order between samples the pre-exponential factor is similar which agrees with previous results on anatase layers growth on the (110) direction[101]. Concerning the model used, it has been already reported that PL emission intensity at low temperature for anatase nanocrystals fits better with the use of two activation energies[101], as show in Equation 4.1. In this equation the pre-exponential factor can be described as $A = \tau_R/(\tau_i - \tau_{i\downarrow})$ which are coefficients given by the ratio of the luminescent radiative lifetime τ_R and the inverse transition probabilities of the non-luminescent states $i = (a, b)$ to the luminescent one $\tau_{i\downarrow}$ and to the ground state τ_i. This study on doped nanoparticles has not been extensively studied on the bibliography. The different radiative processes that undergo on the different samples are clearly different, most notably for the TiO_2:$Ni_{0.3}$ sample. It has been regarded that the PL behavior in anatase under temperature changes can be fully explained by the dissociation of weakly bound self-trapped excitons where each of the two carriers strongly distorts the lattice.

Hall effect measurements allow to determine the conductivity of the pressed-into-pellets nanoparticles. Commonly reported values for TiO_2 nanoparticles range between 10^{-4}-10^{-8} S·cm^{-1}[188–190], where these discrepancies are due to the different particle size, porosity, oxygen stoichiometry or percolation effects that may undergo during measurements. TiO_2 conductivity is often studied in form of thin layers obtained either via sol-gel or CVD, rather than as nanoparticles and higher conductivities are usually reported. Li-doped samples present higher conductivity than undoped particles, similar to Ni-doped but in this case increasing Ni doping tends to decrease the conductivity. This increase on the conductivity, mediated by Li-doping, is attractive to use these nanoparticles in electronic devices.

According to the Raman, CL and PL analysis, only slight changes are induced by Li or Ni doping in the structure and the luminescence properties of the TiO_2 nanoparticles, in accordance with the minor variations in the concentration of dopants. Variable structure of defects, mainly associated with oxygen deficiency, were considered as a function of the type and amount of dopant. In particular, Ni doping seems to promote more defective TiO_2 nanoparticles. However, as the variation of the dopant concentration in the samples under study is small, these changes are not very noticeable and their analysis require more sensitive techniques. Hence, in order to deeply assess possible changes related to the doping process, in this work complementary XPS and XAS measurements were performed to determine changes on the chemical structure of the undoped and doped samples.

Mostly Ti($2p$), O($1s$) core levels and for the doped samples Li($1s$) or Ni($3p$) were studied. Position, intensity and DS from the Ti core level allows to attribute the valence of the present Ti to Ti^{4+}, without traces of other valences. It should be mentioned that other works[171], and most notably after introducing dopants on the anatase structure, observe a presence of Ti^{3+}, which is also regarded as an effective approach to improve its photocatalytic activity as Ti^{3+} acts as active site. The presence of Ti^{3+} is more commonly observed in rutile nanoparticles[191]. In our case not only Ti^{3+} is not observed by XPS, complementary techniques such as CL did not observe any contribution which could be related to Ti^{3+} defects, which further aims towards the absence of Ti^{3+} on the samples.

O($1s$), shown in Fig.4.14 shows differences upon dopant concentration. The presence of Li or Ni mostly promote the high energy contribution (O_{II}), which is often attributed to the presence of oxygen vacancies as well of other hydroxyl groups, as we have discussed on the previous chapter. The specific dopant core levels, such Li($1s$) also bring valuable information on the dopant related effects on the chemical environment. Li($1s$), shown in Fig.4.15(a), demonstrated in first instance that there is Li presence on the sample, particularly on a high concentration. The slight differences on both the spectra corresponding to TiO_2:$Li_{0.2}$ and TiO_2:$Li_{0.3}$, indicates that there is a small difference on the dopant concentration among both samples, but non negligible. By comparing the Ti($3s$) and Li($1s$) peaks, which posses similar height as well as almost the same cross section at 230 eV, a rather high Li concentration on the surface is deduced. This could imply that most of the lithium is present on the surface or even formatting a LiO_x shell surrounding the TiO_2 core. Some authors reported that a large amount of Li^+ was doped onto the surface of TiO_2, probably by the formation of Ti-O-Li bonds[7], and occasionally the lithium migrated to the surface could justify higher nanoparticle size[137], as compared with undoped nanoparticles. This could explain the higher size of the doped Li-samples compared with the undoped TiO_2.

Regarding Ni($3p$), the low concentration of the dopant as compared with the previous chapter, in which the possibility of multiple Ni valence as Ni^{3+} or Ni^{2+} was discussed, hinders its quantification, as observed in Fig.4.15(b) as Ni($3p$) peak height is really small. Nonetheless, qualitatively we can determine the presence of Ni on the samples. Previous reports show that Ni doping can preserve Ti^{4+} charge

state[160], which could explain the observations on the Ti($2p$) core level, in which only Ti^{4+} was observed on our samples.

The VB region suffered a shift towards the Fermi level for the samples containing Nickel, similarly to the effect observed for the Ni-doped SnO_2 nanoparticles on the previous chapter, which indicates a lower n-type behavior for both Ni-doped samples. It should be remarked that the valence band region corresponding to the Ni-doped samples presented a different contribution than the undoped samples. Undoped TiO_2 presented mainly two contributions: a main contribution at $\sim$ 7.1 eV, which in fact was used to center the spectra position and other contribution at $\sim$4.7 eV. Ni doped samples presented differences in the low energy region below $\sim$3 eV, which is marked with an arrow in the inset of Fig.4.16. The origin of this contribution will be discussed on the resonant spectra, as this effect is further enhanced.

XAS spectra was described carefully on this chapter. Fig.4.17 shows the Ti $L_{3,2}$-edge, which it was pointed out to be very similar to previous reports. The relative intensity on the B_2' peak confirmed that the samples were anatase TiO_2, as the relative intensity of this peak is considered the fingerprint to detect anatase or rutile structure. While this qualitative study on the XAS spectra leads to conclude that the dopant in fact affects the electronic environment and the crystal structure, there are subtle changes between different absorption spectra on the Ti-L edge. One initial approach, and as stated on the previous chapter, was the use of the CTM4XAS software, as Ti L-edge can be simulated, due to the final titanium configuration as a transition metal. However, this subtle changes, and especially the B_2' is not successfully represented by this approach, so this idea has to be dismissed.

To assess the origin of these defects, the region between 457 and 462 eV, which corresponds to the Ti($2p$)$L_{3,2}$ region, represented in Fig.4.17 has been analyzed in depth. This absorption edge is divided in two regions, as previously discussed (L_3 and L_2, due to spin-orbit coupling). Each edges are divided into two regions, due to the crystal field effect. The first region is composed by d orbitals with t_{2g} symmetry at positions $\sim$457.9 eV, as well as two pre-peaks which origin was discussed as multipole $2p$-$3p$ interactions. The second contribution at this first region is composed by e_g orbitals, which are placed around 459.5 eV. In this region, the most notable changes are observed, primarily on the B_2 peaks (e_g) intensity with the dopant addition, which may be attributed to small changes in the oxygen deficiency, in agreement with Raman and PL measurements.

In order to describe the different energetic levels associated with d orbitals is necessary to introduce parameters known as *crystal field parameters* Dq, and Ds and Dt. Thus, the energy associated with the orbitals t_{2g} and e_g are separated by an energy of $10Dq$, where $+6Dq$ is due to e_g and $-4Dq$ for t_{2g}. $10Dq$ is defined as the energy difference between the t_{2g} states and the e_g states[147] as observed in Table 4.10.

Energy difference between orbitals b_{1g} and b_{2g} has been found to be comparable to the crystal field splitting parameter $10Dq$. Difference between $b_{1g}(d_{x^2-y^2})$ and

Table 4.10: Crystal field energy positions of the different orbitals[145].

	Energy as a function of D	Orbital
b_{1g}	$6Dq + 2Ds - 1Dt$	$d_{x^2+y^2}$
a_{1g}	$6Dq - 2Ds - 6Dt$	d_{z^2}
b_{2g}	$-4Dq + 2Ds - 1Dt$	d_{xy}
e_{1g}	$-4Dq - 1Ds + 4Dt$	$d_{xx,yz}$

$a_{1g}(d_{z^2})$ is defined to be $\delta_1 = 4Ds + 5Dt$ and the sign of this parameter determines the type of tetragonal distortion as compression for $\delta_1 < 0$ and stretching (elongation) if $\delta_1 > 0$ respective to the z axis. By fitting the spectra to Gauss-Lorentz (G-L) functions (labeled as A, B, C and D) as shown in Fig.4.29(a) we can obtain $10Dq$ and $\|\delta_1\|$[92], as shown in Table 4.11.

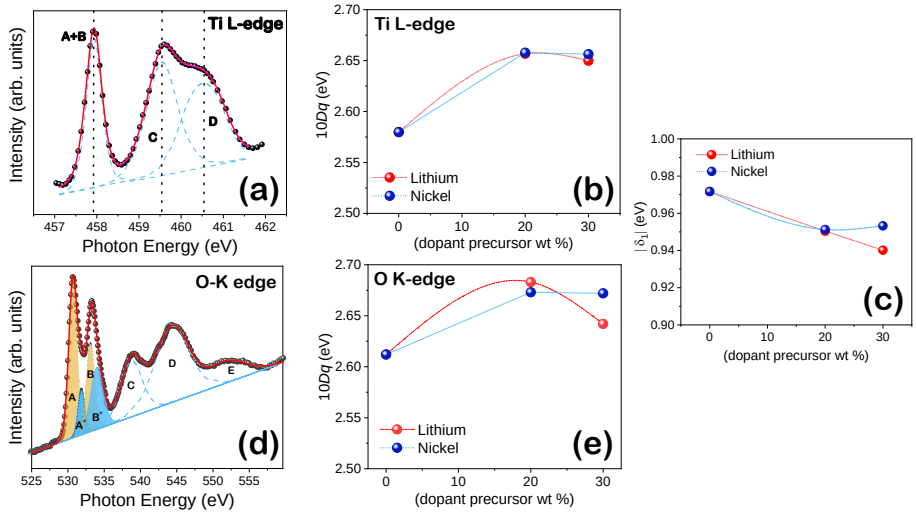

Fig. 4.29: (a) Ti L_3 edge G-L deconvolution for the sample of TiO_2 (b) $10Dq$ crystal field splitting for the different samples obtained from the deconvolution G-L of the Ti($2p$) L_3 (c) Tetragonal distortion parameter $\|\delta_1\|$ for the different samples obtained from the deconvolution G-L of the Ti($2p$) L_3 edge and (d) O-K edge G-L deconvolution for the sample of TiO_2 (e) crystal field splitting for the different samples obtained from the deconvolution G-L of the O($1s$) K-edge.

A similar study can be obtained from the absorption edges of O($1s$) K. In this case, the two main regions described previously can be fitted using 4 (A, A^*, B, B^* and 3 (C, D, E) in bands respectively and the most representative are summarized in Table 4.12 and observed in Fig.4.29(d). As observed, small changes on the peak

Table 4.11: Ti($2p$)-$L_{3,2}$ deconvolution parameters to G-L functions.

	$\mathbf{E_{A+B}}$ **(eV)**	$\mathbf{E_C}$**(eV)**	$\mathbf{E_D}$**(eV)**	$\mathbf{E_D}$-$\mathbf{E_C}$ $\sim \lvert\delta_1\rvert$	$\mathbf{E_D}$-$\mathbf{E_{A+B}}$ $\sim 10Dq$
TiO_2	457.93	459.54	460.51	0.97	2.58
TiO_2:$Li_{0.2}$	457.91	459.62	460.57	0.95	2.66
TiO_2:$Li_{0.3}$	457.88	459.59	460.53	0.94	2.65
TiO_2:$Ni_{0.2}$	457.91	459.62	460.57	0.95	2.66
TiO_2:$Ni_{0.3}$	457.84	459.54	460.50	0.95	2.66

positions are obtained (< 0.1 eV).

Table 4.12: Deconvolution of the O($1s$)-K edge obtained from G-L functions.

	$\mathbf{E}_A$ **(eV)**	$\mathbf{E}_{A^*}$ **(eV)**	$\mathbf{E}_B$ **(eV)**	$\mathbf{E_B}$-$\mathbf{E_A}$ $\sim 10Dq$
TiO_2	530.73	531.51	533.34	2.61
TiO_2:$Li_{0.2}$	529.68	530.47	532.37	2.68
TiO_2:$Li_{0.3}$	529.71	530.52	532.35	2.64
TiO_2:$Ni_{0.2}$	529.66	530.43	532.33	2.67
TiO_2:$Ni_{0.3}$	529.66	530.42	532.33	2.67

Fig.4.29 shows the crystal splitting ($10Dq$) and $\|\delta_1\|$ differences between the samples mainly due to doping. The ($10Dq$) splitting is both obtained from the calculation with the positions on Ti $L_{3,2}$-edge and O-Kedge shown in Fig. 4.29(b)-(d), where Ti($2p$)L_3 (E_D-E_{A+B}) and O($1s$) K (E_B-E_A), respectively. While for the Ti-L edge the results of the $10Dq$ is almost the same similar tendencies are obtained but from O K-edge the values are slightly overestimated, which can be clearly observed on the differences obtained when estimating the values of the crystal field parameter for 20% concentration for each dopant. Ti-L edge lead to a very similar result, while for O-K edge there is a discrepancy of 0.03 eV. Tetragonal distortion $\|\delta_1\|$ as a function of dopant is shown in Fig. 4.29(c). In this case an increase in the dopant concentration decreases the tetragonal distortion, which is not what is observed for the $10Dq$ parameter. These values are in agreement with the results reported by other authors[162].

Regarding Ni-doped samples, the splitting of L_3 and L_2 into two contributions is very sensitive to Ni oxidation state and charge transfer[148]. An increase on the relative intensity of these peaks could denote an increase in the hole concentration and thus an increase in the Ni^{3+} concentration[148]. Both TiO_2:$Ni_{0.2}$ and TiO_2:$Ni_{0.3}$ spectra possess comparable relative intensity, thus confirming similar Ni doping in both cases.

After measuring the XAS spectra, to obtain deeper knowledge on the VB region, mainly on the region below 3 eV, XPS was measured under resonance conditions. TiO_2:$Li_{0.3}$ contributions at ∼7.1 eV and 4.7 eV posses a resonance maximum at 58 eV, while the resonant peak at ∼1 eV becomes significant in the range 54-66 eV, with a maximum at ∼55 eV, as observed on the contouring plot in Fig.4.30, showing the VB region acquired on a variable range of photon energies between 52 and 66 eV. These features can be observed on the Constant Initial State (CIS) plots, shown in Fig.4.30(b)-(d). Therefore, the feature around 0.9 eV could be due to the transition from Li(1s). Some authors pointed out the presence of a feature around 0.9 eV, similar to that observed in this work for Li doped TiO_2, can be associated with Ti(3d) defect state[49] due to the probability of transition between Ti(3p)→Ti(4s). As Ti(2p) $L_{3,2}$ was not measured under resonance conditions, it is not possible to completely obviate the presence of Ti^{3+}, although the rest of the techniques performed up to this point apparently support its absence in our samples. Giordano et al.[177] demonstrated that the for Li-doped TiO_2 of Ti(3s) there was a presence of Ti^{3+}, which indicates a partial reduction of Ti^{4+} to Ti^{3+}, which should be clear as an asymmetry on the Ti(3s) spectra in this work, which is not present.

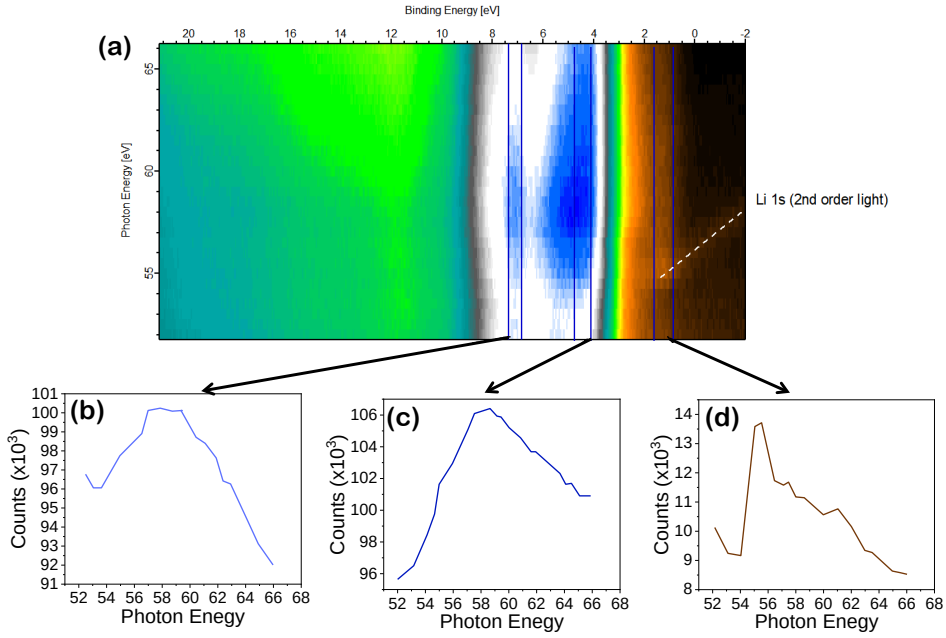

Fig. 4.30: (a) Contour plot showing TiO_2:$Li_{0.3}$ VB region acquired with photon energy between 52-67 eV and CIS spectra of the regions with binding energy between (b) 1-1.5 eV (c) 4-4.5 eV (d) 7-7.5 eV .

Ni-doped samples, precisely the TiO_2:$Ni_{0.3}$ sample, shows a clear shoulder at ∼2.5 eV could be related to Ni(3*d*) states[192]. A similar feature was reported for Fe-doped TiO_2[49] attributed as Fe-3*d* and Ti-3*d* derived states. In our case Ni could play a role similar to Fe(3*d*). Hence, RPES measurements shed light to the Li-related states (∼1 eV) and Ni-related states (∼2.5 eV) in the VB region promoted by doping in the nanostructures.

Ab-initio calculations based on DFT were obtained to assure the effect of the dopants on the anatase structure. Firstly, to observe more clearly these effects, it was needed to add a relatively high concentration of oxygen vacancies to match with experimental results. The presence of Ni introduced a high level of mid-gap band states, which could explain the previous results observed by RPES. However, for Li-doped samples there is no presence of Li-related sub-band gap states, which in fact has been reported on the literature[177]. Both Ni and Li decreased the band gap of anatase, if we consider a high presence of oxygen vacancies, what has been reported on the literature[176] as observed on Table 4.8.

Anatase stability is limited due to its metastability which tends to transit to rutile. This non-reversible transition occurs most commonly at around 600-700 °C for undoped TiO_2 in absence of impurities or dopants[39], but reported transition temperatures vary in a wide range precisely depending on the different synthesis methods materials, dopants, particle size or atmosphere. It has been reported that with sizes around 10 nm anatase becomes more stable than rutile[193]. The ART can be modified by doping, as previously reported by diverse authors,[39,47,169,182,193,194]which is an important aspect to be considered in the potential applicability of the anatase phase in devices operated at high temperatures.

In our case, the ART begins at around 740 °C for undoped TiO_2, while this transition is initiated at lower temperatures, around 600 (620) and 700° C, for the Lithium and Nickel doped TiO_2, respectively, being in agreement with the values reported by other authors[193,194]. Li and Ni-related defects may contribute to the formation of oxygen vacancies as Ni^{2+} ions may enhance nucleation and growth by two different effects, breaking and creation Ti-O bonds, enhanced by the absence of O_2 and providing energy mass transport route accelerating the growth process of rutile[182]. This is also in agreement with DFT calculations which show that nickel promotes rutile over anatase[168]. To qualitatively quantify this transition, one approach was suggested by Spurr and Myers[195] in which the fraction of the volume of rutile could be estimated from the XRD data. These equation has been slightly modified[175,196], reaching:

$$F_R = \frac{1}{1 + 0.8\left[\frac{I_A(101)}{I_R(110)}\right]} \tag{4.2}$$

where F_R, $I_A(101)$ and $I_R(110)$ are the rutile phase percentage, intensity of anatase (101) peak and intensity of rutile (110) peak. This results can be used qualitatively, as for obtaining reliable results a constant background should be carefully subtracted from each spectra.

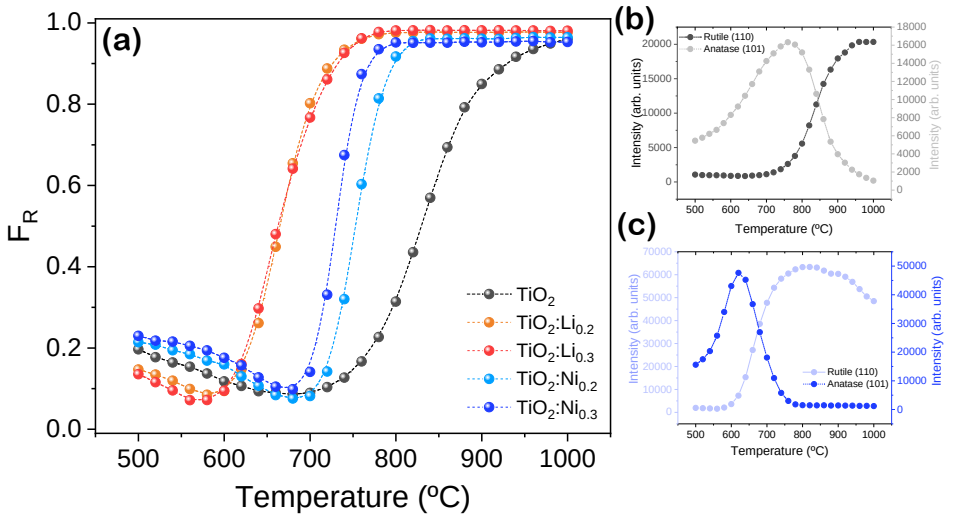

Fig. 4.31: (a) Rutile fraction estimated with the Spurr-Myers equation for each of the samples and comparison of the relative intensity of the diffraciton peaks corresponding to Rutile (110) and Anatase (101) with increasing temperature for (b) TiO_2 and (c) TiO_2:$Ni_{0.3}$.

Fig.4.31(a) shows the comparative fraction of rutile obtained with increasing temperature. Three different behaviors are observed for the set of samples. TiO_2 has a slower slope and did not reach a percentage of rutile of 100%. For the Ni doped samples the slope is higher and the maximum value of the rutile fraction is reached faster, but at higher temperature than for Li-doped samples. Fig.4.31(b)-(c) shows the relative intensity of the corresponding to Rutile (110) and Anatase (101) for TiO_2 and TiO_2:$Ni_{0.3}$ respectively. It is clear that for the doped samples anatase is transformed faster to rutile. The limitations on the quantification rutile (as a percentage) with the use of Equation 4.2 is given due to the fact that at lower temperatures it suppose there are a substantial presence of rutile ($\sim$ 20%), which is not reliable. Anyhow, the different slopes on the observed curves is a clear indicator on the different speed in which rutile is obtained, which is evident on Fig.4.31(b)-(c).

Previous results show that doping with transition metals as Fe tends to lower this temperature, arguably due to precipitation of the excess of dopants in the highly doped samples, which can facilitate the phase transition[169]. As mentioned, similar ionic radii of Ni^{2+} and Li^{+} respective to Ti^{4+} could be translated on dopants incorporation as substitutional and, to maintain charge balance, oxygen vacancies are created. Besides, Ni^{2+} and Li^{+} eases the break and creation of Ti-O bonds and provides a energy mass transport routes, as the number of Ti-O bonds decrease, the nucleation and growth process of rutile is promoted. Many factors could affect the anatase stability such as the grain size, its morphology or the synthesis atmosphere.

The idea of inducing ART via laser irradiation has been discussed on the literature over the last 5 years[157,174,197,198], as it offers a method to obtain complex anatase/rutile structures without the use of any mask. Laser conditions to trigger this reaction are often based in high-power lasers under vacuum or inert environments, distinguishing among continious-wave or pulsed lasers. This transition has been obtained with the use lasers which cover a great extent on the UV-NIR range, such as UV lasers with wavelengths of 266 nm[197] or 325 nm[157], VIS lasers (green, 532[174,198] and red 785[198]) and higher wavelengths-lasers such as a Nd:YAG, 1064 nm[199]. While anatase TiO_2 laser-induced transition has been widely reported, the dopant effect on this transition has not been as widely considered. Vasquez et al.[157] analyzed the effect of Al and Fe, with Fe-doped samples clearly inhibiting the transition. Dauksta et al.[197] induced the transition on Nb-doped TiO_2, which was stabilized by the Nb doping, on a different approach as suggested in this work, as the authors used a pulsed laser, which led to the phase change from anatase to rutile with 10000 laser pulses. Gaur et al.[174] observed the phase transformation of Co-doped TiO_2, remarking that the lattice expansion plays a major role on the controlled transition. Recently, Labadini et al.[198] used dye-pretreated anatase TiO_2 films in which via Raman spectroscopy induced the ART transition when excitation of the dye sensitizer caused an electron injection from dye molecule-excited state to the TiO_2 conduction band.

In our case, it has been mentioned that some of the Raman modes such as E_g are sensitive to laser irradiation as observed in Fig.4.27, where both the FWHM and position are affected by different laser densities. However, the effect of the UV irradiation will be clearly affected by the dopant type (Li or Ni) as well as the nanoparticle type (synthesized or commercial). When increasing the laser intensity from the UV laser to the highers value, I_0, the E_g mode was shifted towards higher wavenumber, which responds to two different effects: thermal heating from the UV irradiation and UV light interaction with the sample. Nonetheless, both Li and Ni responded in different manner. Li doping does not modify the position or FWHM of the E_g mode until reaching $0.5 \cdot I_0$ which could indicate that most of the laser irradiation is not enhancing the temperature of the sample, and it is rather affecting the Ti-O bonds of the sample, which could affect the nucleation process of the rutile growth from broken bonds, favoring the transition. On the other hand, Ni-doping was observed to thermally induce the transition at lower energies (as compared with undoped TiO_2) but when using laser irradiation, this transition does not occur as easily. Other explanations could be related to the UV-induced transition does not exclusively triggers the transition via thermally increasing the temperature of the lattice. Some authors have proposed that the laser-induced phase transition is dominated by a thermal mechanism related with processes of absorption and desorption of surface oxygen which is on the anatase surface[200]. Dauksta et al.[197] pointed out that the phase transition occurs due to the nonlinear absorption of the laser light and an explosive re-solidification of the surface layer. In their observations, the presence of anatase on the edge of the formed crater after the laser ablation suggest that there is still mostly anatase. With the power densities used in this thesis, there were no morphological changes observed after

the UV irradiation, and it is more likely that the localized structural transformation takes place within the same particle, as suggested by other authors[174]. This should be considered as a possible explanation on the different behavior observed for the Ni-doped samples. Nanoparticle surface is very different among doped and undoped samples, as clearly observed for the Li-doped samples, where a high concentration and bigger size could indicate segregation of lithium. The possibility of a different surface structure could led to different structural transformations under laser irradiation. From these methods, is clear that the design of a mask-free pattern via laser irradiation, which combine anatase and rutile is possible. In our case we have observed that Li-doped TiO_2 showed improved electronic properties and variable luminescence, which makes this material appealing for optoelectronic device design. The use of combined anatase and rutile have already shown potential application, due to their photocatalytic and antibacterial properties, in which irradiation induces the decrease in the colonization intensity of bacteria[199].

Finally, contemplating a possible application of the nanoparticles synthesized and characterized throughout this chapter, we have considered their application in lithium-ion battery anodes. Transition metal oxides have been regarded as an important anode candidate for achieving high-performance LIBs, where titanium dioxide, is considered one of the main candidates, as it has been widely investigated based on its cycling stability, chemical inertness and high safety[10]. It is well known that the optoelectronic properties of nanoparticles are related with its morphology, size or volume-surface ratio. To vary those properties, one well-established approach consists on doping those nanomaterials with other elements which can strongly modify the final properties. Doped titania nanoaparticles have shown increased capacity compared to undoped nanoparticles, as specific capacity obtained in this work is higher than the expected nominal capacity of undoped TiO_2 of $\sim$200 $mAhg^{-1}$ and higher compared to previous reports $\sim$125 $mAhg^{-1}$[10,127]. Li-diffusion simulations have shown that conductivity in TiO_2 strongly depends on the titania polymorph and nanoparticle size where conductivity changes from dual ionic and electronic to pure ionic[201].

Fig.4.13 showed that Li doping increases the LiB capacity stability TiO_2-based anodes with their excellent stability can be an important candidate with many modifications or combination of other materials such as graphene or silicon[10,11]. TiO_2:$Li_{0.3}$ capacity increases over cycle time even after 300 cycles, reaching 433 $mAhg^{-1}$, which is an improvement, respectively to the lowest capacity measured in this sample close to 309 $mAhg^{-1}$, of an 40%.

As observed, specific and volumetric capacity of TiO_2:$Li_{0.3}$ are superior than for undoped particles (341.1 and 202.6 $mAhg^{-1}$ in discharge at 100 cycles as shown in Table 4.13, respectively) by a factor of 1.68 which suggests that the distortions created by Li ions substituted on the titania lattice and the higher conductivity of the nanoparticles enhanced cycling performance. Li-doped nanoparticles have shown higher conductivity than undoped particles (10^{-6} $S{\cdot}cm^{-1}$) which could be also attributed to the higher specific capacity. The pre-lithiated titania, which is clearly distorted taking into consideration the results obtained in the previous

Table 4.13: Specific and volumetric capacity at 100 cycles.

Sample	Step	$C_{esp}(mAhg^{-1})$	$C_{vol}(mAhcm^{-3})$
TiO_2	Charge	201.6	140.1
	Discharge	202.6	140.8
TiO_2:$Li_{0.2}$	Charge	228.1	164.3
	Discharge	233.7	168.4
TiO_2:$Li_{0.3}$	Charge	336.6	138.6
	Discharge	341.1	140.4

section, which migrated Li-to the surface could be a most favorable host to the Lithium which is inserted during the battery testing. No changes are observed as a function of the dopant on the cell stability, which might indicate that the volumetric expansion in the lithiation-delithiaton processes is small.

4.9. Conclusions

In this chapter, single-phase anatase TiO_2 nanoparticles doped with either Li or Ni and synthesized via hydrolysis have been studied. A characterization of morphological, structural, compositional, electrical, electronic and optical properties has been carried out. These nanoparticles have been tested as possible candidates in lithium ion battery anodes. The transition from anatase-to-rutile has been induced both by laser irradiation and by thermal treatments.

- Nanoparticles present high crystallinity and homogeneous dimensions around 6-7 nm. Dopant incorporation has been successfully introduced in two different concentrations (20% or 30% in weight of the dopant precursor), obtaining similar final atomic concentrations in the range of 1.5% at for Ni doping and 0.6% for Li doping.

- Via Raman spectroscopy, effects due to the low dimension, dopant incorporation and the presence of defects in the nanoparticles have been observed. VIS Raman has shown that E_g modes are quenched for the doped samples. Other modes, such as the mode at $\sim$ 849 cm^{-1} is affected by the dopant presence, attributed to Ti-O bonds at the surface. Li or Ni doping does not affects strongly the Raman signal, as the main vibrational modes do not vary significantly on position or intensity.

- PL, PLE and CL measurements presented the expected luminescence bands corresponding to anatase TiO_2. Undoped and Li doped samples did not show any significant difference, while Ni-doping enhances an emission band $\sim$3 eV which is attributed to STE, which was enhanced with increasing Ni content.

- XPS analysis has given fundamental knowledge on the sample surface, as well on their electronic properties. Ti^{4+} presence at the surface in both doped and undoped samples has been shown, independently on the dopant concentration. Particularly remarkable is the high concentration of lithium observed on the sample surface, which could suggest a possible Li migration towards the sample surface. DFT calculations have demonstrated that Ni doping creates a variety of levels near the valence band, whereas Li doping does not affect much the band structure of TiO_2, except for a low contribution at $\sim$1 eV which was observed via RPES and, while for most of the authors is related to Ti^{3+}, its origin could be also related to lithium.

- XAS results on the Ti-L edge shows slight differences among the undoped and doped samples. After a deconvolution of the O($1s$) K-edge as well of the Ti($2p$)-L it was possible to estimate the crystal field parameters $10Dq$ as well as the tetragonal distortion ($\|\delta_1\|$), showing small discrepancies on their value depending on the edge used for their calculation (< 0.03 eV) but with clear differences for the doped samples, which indicates distortions on the TiO_6 octahedron.

- ART transition has been observed both, induced by laser irradiation as well as thermally activated, the former observed by measuring XRD on the range between 500-1000°C. Taking into consideration PL results of the doped samples, showing a higher presence of oxygen vacancies, could enhance the ART transition due to the creation of new Ti-O bonds, following rutile symmetry. The distortions on the anatase structure, attributed to the XAS results support this idea, which in fact agrees with thermodiffractometry observations: both dopants enhance the ART by boosting it to lower temperatures and completing it through a narrow range. This responds to the higher concentration of defects and oxygen vacancies observed by PL and Raman spectroscopy, which could be centers for the formation of the rutile Ti-O bonds upon increasing temperature. ART has been also induced by UV-irradiation, as TiO_2 have been clearly affected by continuous-laser irradiation, as observed by the strong quenching on the E_g after prolonged irradiation as well as its shift under variable laser intensity. For most of the samples, the transition was almost instantaneous, while for Ni-doped samples is much slower. This effect is related to the different mechanism to trigger the ART under laser irradiation, where different parameters such as the thermal conductivity of the material which dominates the thermalization process or the surface of the nanoparticles, in which the transition occurs via the recrystalization after the abrasive laser irradiation, might be different for these samples as compared with undoped samples.

- Undoped and Li-doped TiO_2 nanoparticles have been tested as candidate for anodes in Li-ion batteries. Anodes show low capacity but outstanding stability over 300 cycles, which also improved over cycle times, being the best results obtained for the TiO_2:$Li_{0.3}$ sample, which after a slight decrease

on the specific capacity, steadily increase up to 300 cycles, being superior than undoped TiO_2 as well as graphite. Therefore, Li-doped TiO_2 is a possible anode candidate.

Chapter 5.
SnO nanoparticles doped with Li or Ni

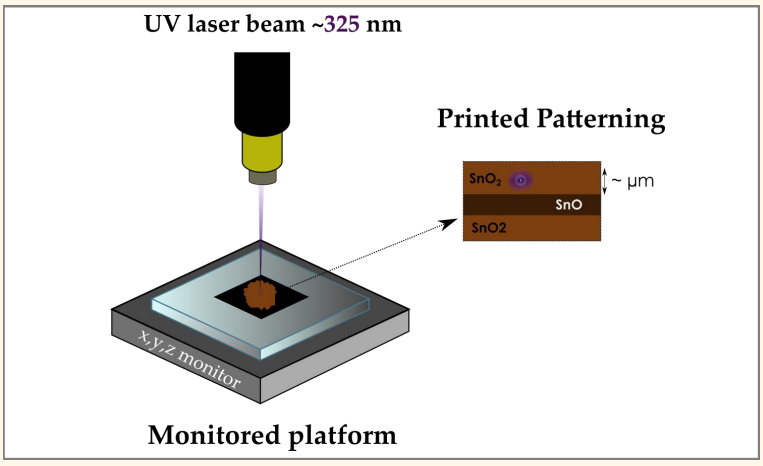

Abstract: In this chapter, undoped and Li or Ni doped tin(II) oxide (SnO) nanoparticles and platelets have been synthesized at room conditions via a hydrolysis procedure. The x-ray diffraction (XRD) and transmission electron microscopy (TEM) confirm the high crystallinity of the as-synthesized romarchite SnO nanostrucutres with dimensions ranging from 4 to 22 nm. The stability of the initial SnO and the controlled oxidation to SnO_2 are studied based on either thermal treatments or controlled laser irradiation using a UV and a red laser in a confocal microscope. Thermal treatments induce the oxidation from SnO to SnO_2 without a substantial formation of intermediate SnO_x, as confirmed by thermodiffraction measurements, while by using UV or red laser irradiation the transition from SnO to SnO_2 can be controlled, assisted by formation of intermediate Sn_2O_3, as confirmed by Raman spectroscopy. Finally, a tailored spatial SnO/SnO_2 micropatterning can be achieved by controlled laser irradiation with potential applicability in optoelectronics and sensing devices.

This chapter includes adapted material from: A. Vázquez-López et al., In situ local oxidation of SnO induced by laser irradiation: A stability study, *Nanomaterials*, **2021**, 11, 4, 976[202].

5.1. Synthesis, morphological, structural and compositional characterization

During the previously-discussed synthesis of SnO_2 reported in section 2.1.1, SnO was obtained as an initial product before the final step in which the powder was thermally treated at 350°C. This SnO precursor powder was left untreated and stored on glass vessels after each of the synthesis and measured after 1-2 years of storage. Once that time passed, the following study was carried out for both undoped and Li or Ni doped with 20%wt SnO powders.

5.1.1. XRD, SEM and TEM characterization

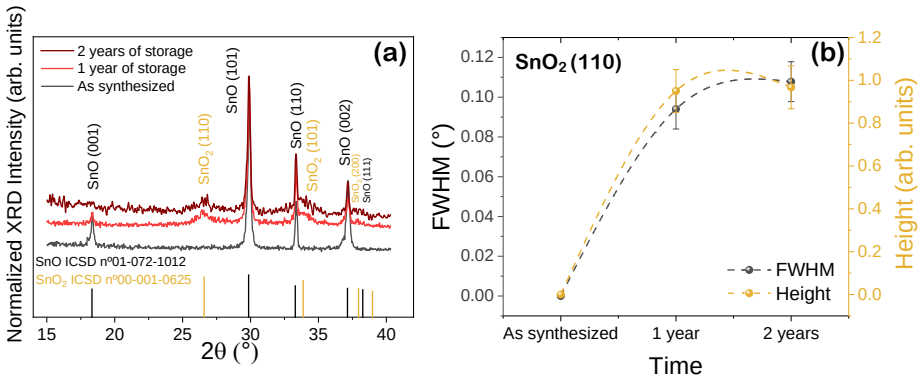

Fig. 5.1: (a) Normalized XRD patterns from SnO nanopowders over the period of two years where the histograms represent the ICSD file nº01-072-10125 (black) corresponding to SnO and ICSD file nº00-001-0625 (yellow) corresponding to SnO_2, (b) FWHM and intensity of SnO_2 (110) peak.

XRD results confirm that the synthesized nanoparticles mainly consist of high crystalline romarchite[i] tin monoxide SnO (ICSD: 01-072-1012), with a dominant (101) peak. Only a weak maximum corresponding to SnO_2 (110) (ICSD: 00-001-0625) is observed at 26.5° in the XRD diffractograms. The as-synthesized SnO was stable under room conditions. Fig.5.1(a) shows the XRD patterns acquired from SnO as synthesized and after 1 or 2 years of storage, where peaks from SnO

[i]In this section to prevent any misconceptions, tin monoxide (SnO) will be named after its mineral name *romarchite* to clearly differentiate from other oxides and, specially, from tin dioxide (rutile, SnO_2). Note that the mineral *romarchite* in nature, could present not only SnO as other species could be in form of impurities.

still dominate the diffractograms after long storage and the maximum from SnO_2, observed at 26.5°, increases.

Other maxima which can be attributed to SnO_2 such as (101) at 33.9° are slightly observed. In that time span, the weak contribution corresponding to SnO (001) is quenched, which may be related to the formation of small domains of SnO_2. Diffraction peaks related to metallic Sn or other Sn-based oxides are not detected in this case. Fig.5.1(b) shows the evolution of the SnO_2 (110) intensity and FWHM over time, showing that a steady-state formation of SnO_2 was achieved during the first year of storage.

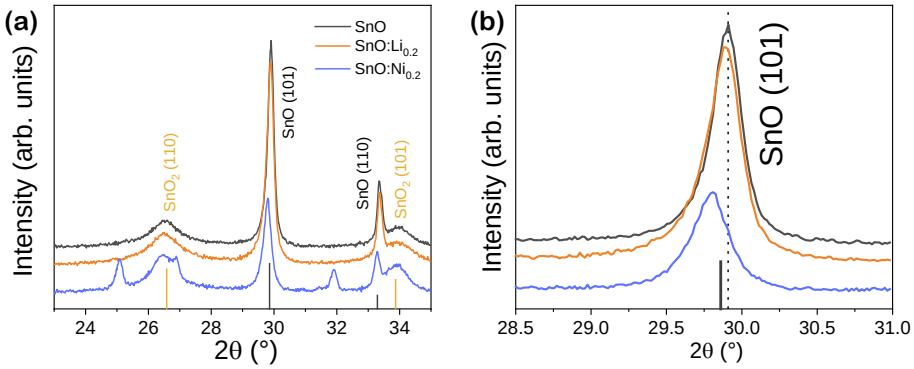

Fig. 5.2: (a) XRD diffractograms from SnO, SnO:$Li_{0.2}$ and SnO:$Ni_{0.2}$ (b) shows detailed region of SnO (101) peak between 28.5 and 31°.

XRD diffractograms corresponding to the doped nanopowders (SnO:$Li_{0.2}$ and SnO:$Ni_{0.2}$) acquired at room temperature are shown on Fig.5.2(a). Very similar patterns are observed for the Li-doped nanopowders whereas for Ni-doped other peaks are observed. For undoped SnO diffraction peaks from metallic Sn or other oxides such as Sn_2O_3 and Sn_3O_4 were not detected, while for SnO:$Ni_{0.2}$ the diffraction pattern presents a few different diffraction peaks placed at $\sim$ 25.1°, 26.9° and 31.9°. The former contribution at $\sim$ 25.1° is probably due $NiCl_2{\cdot}6H_2O$ (ICDS n°:00-001-0200) from the precursor. There is also the contribution of $\sim$ 26.5° that was attributed to SnO_2 in the other samples that in this case present a shoulder at 26.9° which, as well as the diffraction peak at 31.9° could be attributed to Sn_2O_3 (ICDS n°:00-025-1259), with the latter contribution also probably related with Sn_3O_4 (ICDS n°:00-016-0737).

Fig.5.2(b) shows the detailed region between 28.5-31.0° in which it is possible to observe with detail the SnO(101) peak. Both Li and Ni doped present a peak shift towards lower angle, in undoped SnO the peak is centered at 29.90°, for SnO:$Li_{0.2}$ it appears at 29.88° and for SnO:$Ni_{0.2}$ the SnO (101) reflection is located at 29.80° thus showing differences in the host SnO lattice due to the dopant addition.

The lattice parameters for both undoped and doped SnO were estimated from the analysis of the corresponding XRD patterns using the SnO planes (101) and (110), as indicated in Table 5.1.

Table 5.1: Averaged dimensions and lattice parameters from undoped SnO and doped SnO estimated from XRD measurements.

Sample	a(Å)	c(Å)
SnO	3.79(7)	4.84(3)
SnO:$Li_{0.2}$	3.79(7)	4.85(2)
SnO:$Ni_{0.2}$	3.80(1)	4.86(9)

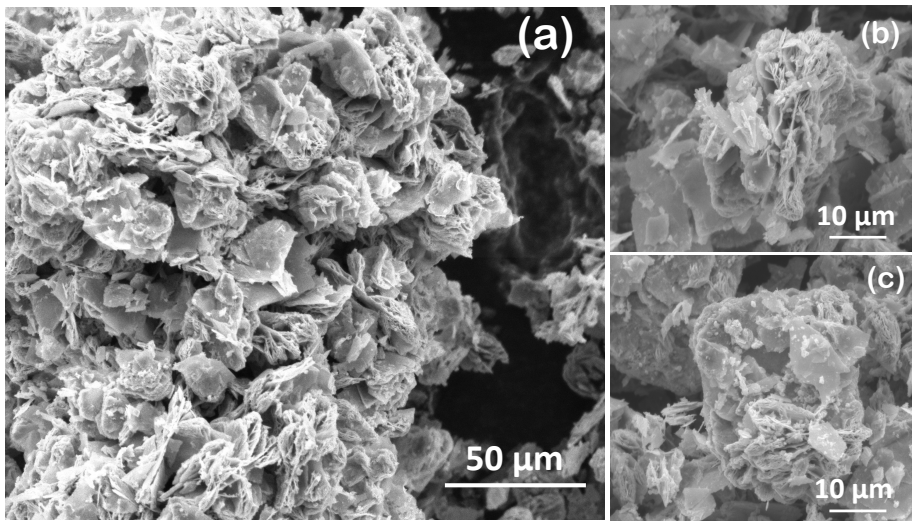

Fig. 5.3: SEM micrographs of the SnO samples showing (a) platelets (b) flower-like morphologies and (c) square-like microstructures.

SEM images corresponding to the SnO sample shows the presence of platelets that grow intercalated and pile up to form agglomerates of several microns in size as observed in Fig.5.3(a). Detailed regions are shown in Fig.5.3(b)-(c), where not only platelets can be observed as the piling of these structures may cause other growths such as square-like microstructures.

SEM images corresponding to the doped samples are presented in Fig.5.4. While Li-doped SnO presents a similar morphology than undoped SnO, composed mostly by micro-size platelets/planes, Ni-doped SnO presents a higher presence of nano-size particles.

Complementary to SEM analysis, low magnification TEM images were acquired and are shown in Fig.5.5. It can be observed that the dimensions of the undoped nanoparticles range from 4 to 22 nm, with averaged dimensions around 11 nm, as confirmed in the histogram presented in Fig.5.5(a) as an inset. In addition, larger platelets with dimensions of hundreds of nm can be also observed in Fig.5.5(b).

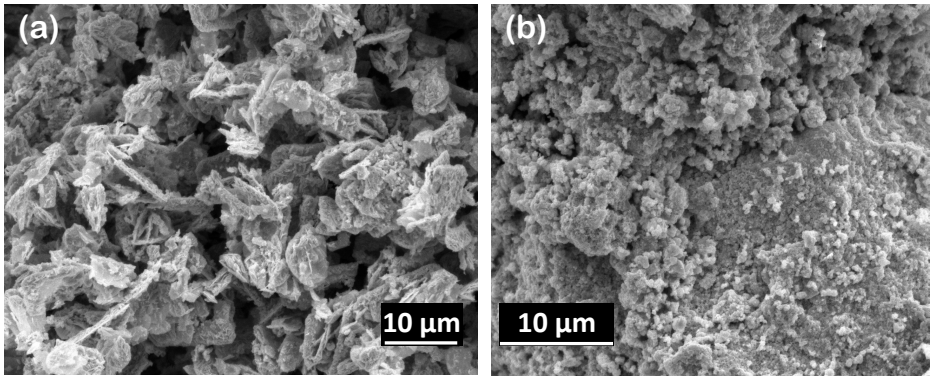

Fig. 5.4: SEM micrographs corresponding to (a) SnO:$Li_{0.2}$ and (b) SnO:$Ni_{0.2}$.

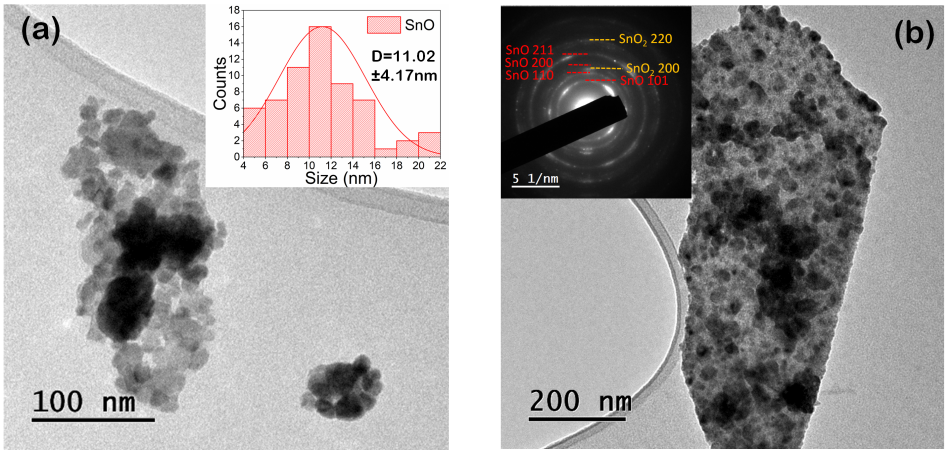

Fig. 5.5: TEM image of the as-synthesized SnO nanopowder, showing (a) nanoparticles and (b) platelet-like structures. Inset in (a) shows the histogram with the average dimensions, while inset in (b) shows the corresponding SAED pattern.

SAED pattern included in the inset in Fig.5.5(b) confirms that the nanocrystals correspond to SnO, although a low amount of SnO_2 is also observed in some regions, as confirmed by the weak spots in the SAED pattern, in agreement with the XRD results.

HRTEM images show that some regions corresponding to certain nanoparticles present both SnO and SnO_2 as observed in Fig.5.6. Fast Fourier Transform (FFT) included as an inset in the image shows that the image is in fact acquired along the $[1\bar{1}\bar{1}]$ direction. Inset in the upper right corner shows spots in red confirming that rutile is present in the sample with parameters of 3.82 and 4.97 Å.

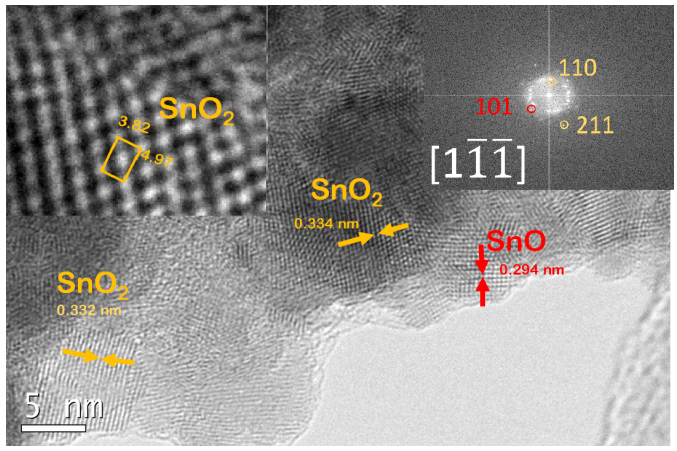

Fig. 5.6: HRTEM images from SnO nanoparticles. Inset on the upper left corner shows the I-FFT image of the region where SnO_2 is observed while inset on the upper right corner shows the FFT of the image.

5.1.2. EDS and ICP-OES characterization

As aforementioned, SnO synthesis is the former part of the described SnO_2 synthesis. After the hydrolysis process, the obtained powder (SnO) was heated on a furnace to obtain SnO_2. For those tin dioxide (SnO_2) nanoparticles we have shown the results of both ICP-OES and EDS, where different concentration of Li or Ni were detected and shown on Table 3.2. It is obvious that the dopant is present on SnO if it is present on the final SnO_2 product. As EDS is a non-destructive technique and easily comparable, Fig.5.7(a) confirms the presence of Ni on the SnO:$Ni_{0.2}$ sample, due to the observation of the Ni K transition. The presence of Nickel is homogeneously distributed Fig.5.7(c). Nonetheless, ICP-OES results were not repeated on SnO:$Li_{0.2}$ due to the destructive nature of this technique. Quantification on this samples had not been performed as the relative high intensity of the electron beam (15kV, 1.5nA) needed to detect Nickel will most likely transform SnO to SnO_2 providing misleading information about the element quantification.

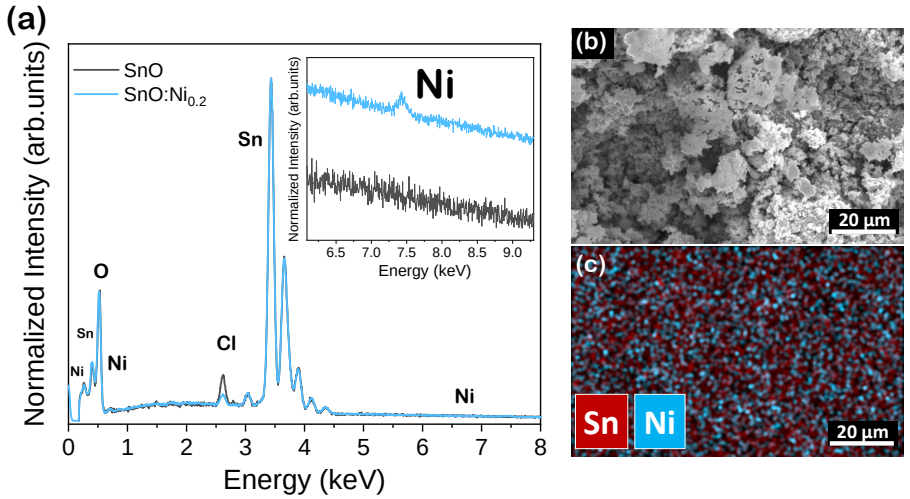

Fig. 5.7: (a) EDS spectra from undoped SnO and Ni doped SnO powders. Inset shows detailed region between 7 and 8 keV (b) SE image and (c) EDS mapping of Ni and Sn.

5.1.3. Thermo XRD

To determine the stability of the SnO nanopowders under the influence of increasing temperatures and its oxidation into SnO_2, XRD patterns have been acquired *in-situ* during a controlled annealing process in air, as described in the experimental section 2.1.1. Fig.5.8 shows the diffraction patterns acquired in the range of angles 15°–70° at two temperatures, 25 °C and 900 °C for both undoped and Li or Ni doped SnO. Peaks at 39.4 and 45.8° (marked with *) correspond to the Pt sample-holder. Before the annealing, the XRD pattern of the three samples can be indexed mostly to SnO (ICSD nº 01-072-1012) and to a lesser extent, to SnO_2 (ICDS nº 00-001-0625). After reaching 900 °C, the three samples are mostly composed by SnO_2, while a minimum presence of SnO remains.

Fig.5.9 represents the contouring plot of the intensities from the XRD signal between 23-35° corresponding to the different steps in the annealing process from 25 to 900 °C. It can be observed that oxidation from initial SnO nanopowder into SnO_2 starts at around 400 °C for undoped SnO. This oxidation process is nearly completed at temperatures above 800 °C, as observed in Fig.5.9. Similar results are observed for the Li doped samples, whereas for the Ni doped the transition starts at lower temperatures around 300°C and occurs faster.

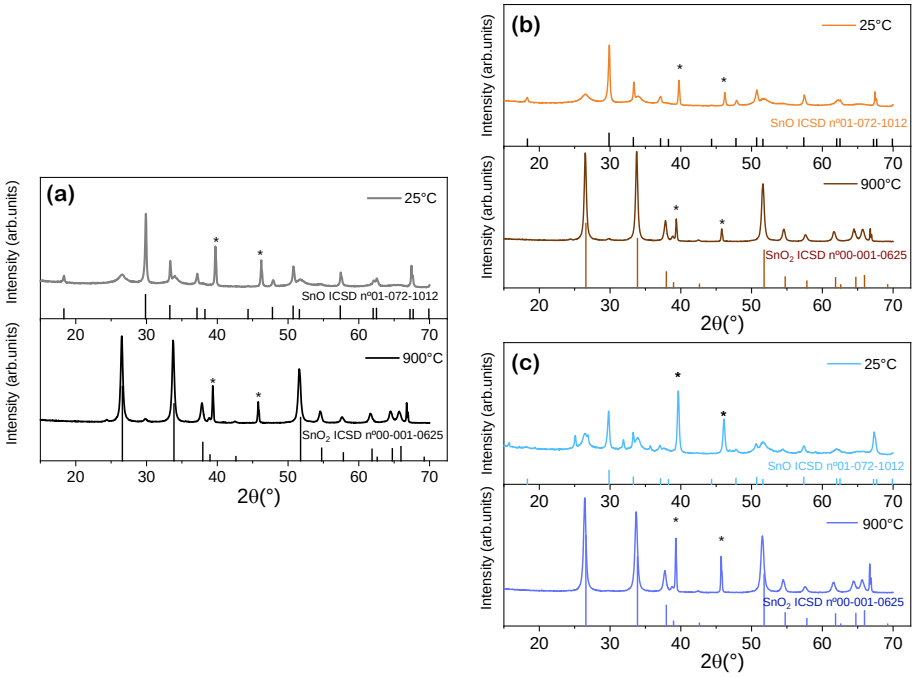

Fig. 5.8: XRD diffraction patterns of (a) undoped SnO (b) Li and (c) Ni doped powders acquired at 25 and 900 °C. Histogram patterns correspond to the ICSD files labeled in each of the figures. Peaks at 39.4 and 45.8° (marked with *) correspond to the Pt sample-holder.

Based on the results depicted in Fig.5.9, it is observed that when increasing the temperature up to 300 °C there is no strong oxidation or phase transition and, in addition to a weak SnO_2 (110) maximum at around 26.5°, only minor shifts to lower angles in the XRD peaks from SnO are observed, mainly the peak corresponding to the SnO (101) planes at around 30°. This particular region is depicted with more detail on Fig.5.10. Fig.5.10(a) shows the decrease of the peak with increasing temperatures which height and position are represented in Fig.5.10(b). It is clear that the peak maximum intensity and position reaches a minimum near 500°C. The peak height increases again near 750°C. This could be an indicator that the lattice undergoes to different transitions during the thermal treatment.

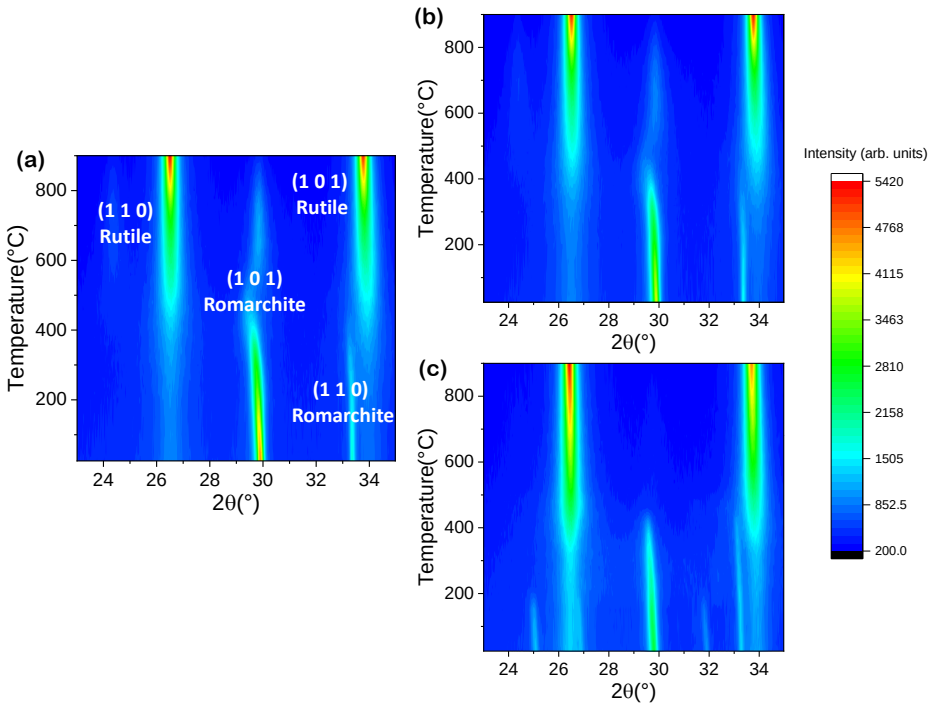

Fig. 5.9: Thermo XRD patterns in the range of 23 to 35° represented in a contouring plot of intensities for (a) SnO (b) SnO:$Li_{0.2}$ and (c) SnO:$Ni_{0.2}$.

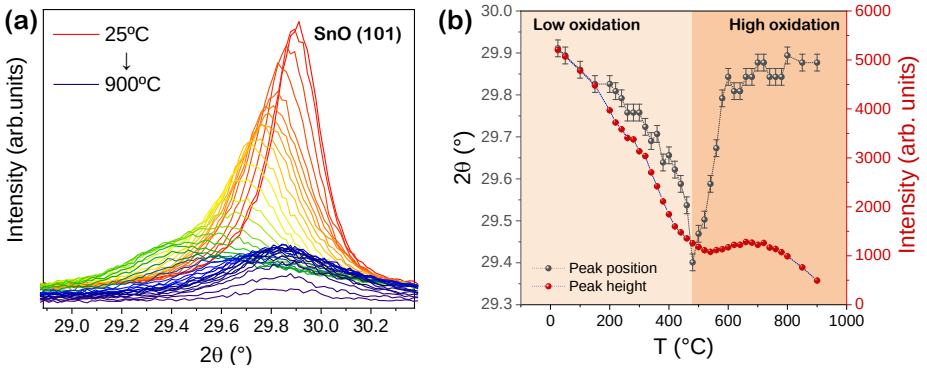

Fig. 5.10: (a) XRD diffraction patterns detailed region between 28.8 and 30.4° of SnO powders between 25 to 900 °C and (b) corresponding peak height and position.

5.1.4. Raman spectroscopy

In order to study the SnO samples and their stability under laser irradiation and the possible laser-induced formation of SnO_2 from SnO, Raman spectra from SnO

nanopowder have been analyzed using either a red (λ = 633 nm) or an UV (λ = 325 nm) laser, as well as with variable laser conditions based on the employed neutral filters and controlled irradiation duration.

5.1.4.1. Raman excited by a VIS laser $\lambda = 633$ nm

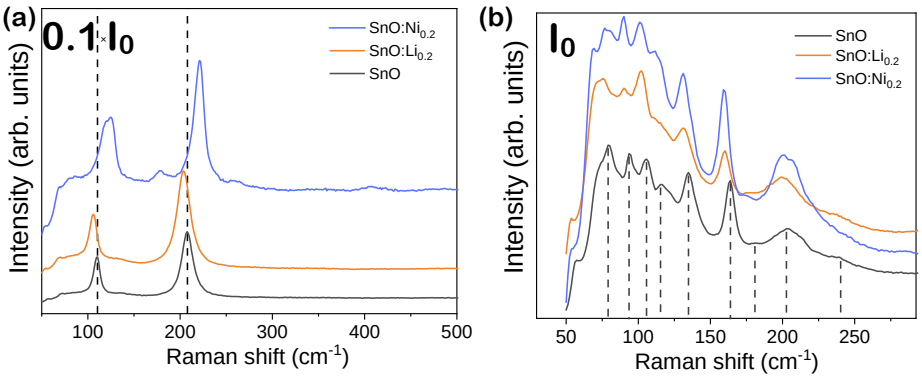

Fig. 5.11: Raman obtained with the VIS laser λ=633 nm with two different energy densities (a) 0.1·I_0 and (b) I_0 for the corresponding SnO, SnO:$Li_{0.2}$ and SnO:$Ni_{0.2}$ powders.

SnO commonly shows two main Raman modes at around 110 and 208 cm^{-1} which correspond to the B_{1g} (or E_g) and A_{1g} modes, respectively[19,203]. Tin dioxide (SnO_2) modes had been described previously in section 3.1.4.

For the Raman spectra measured with the VIS laser, an irradiation time of 200 s and variable neutral filters were used to compare its effect on the final spectra. Fig.5.11 shows the spectra obtained for each of the samples (SnO, SnO:$Li_{0.2}$ or SnO:$Ni_{0.2}$) with two different laser power density (0.1·I_0 or I_0). When using the lowest laser power density (0.1·I_0), see Fig.5.11(a), the formation of SnO_2 is avoided, as only Raman peaks from SnO centered at 110.5 and 208.6 cm^{-1} can be clearly distinguished in the corresponding Raman spectrum. However, when using higher laser power densities, in addition to these SnO vibrational modes, some other new Raman peaks can be observed mainly in the range between 100-200 cm^{-1} as depicted on Fig.5.11(b).

For each sample also the comparative effect of each laser power density (0.1·, 0.25·, 0.5· or 1·I_0) is shown in Fig.5.12(a)-(c). Two main peaks centered at 136 and 165 cm^{-1} are clearly distinguished either using higher power intensity (I_0) or increasing exposition time with lower power intensity (0.1·I_0) (not shown here). The number of modes increases with the maximum laser power intensity, I_0, and its possible origin are discussed on Table 5.2. Particularly, it is observed that when the energy density is high (I_0), modes are observed on the region between 400-800 cm^{-1}, which origin is also discussed on Table 5.2, but are mostly related to SnO_2 as we have discussed on chapter 3.

Noticeable changes are observed on the Ni-doped sample. In this case not only

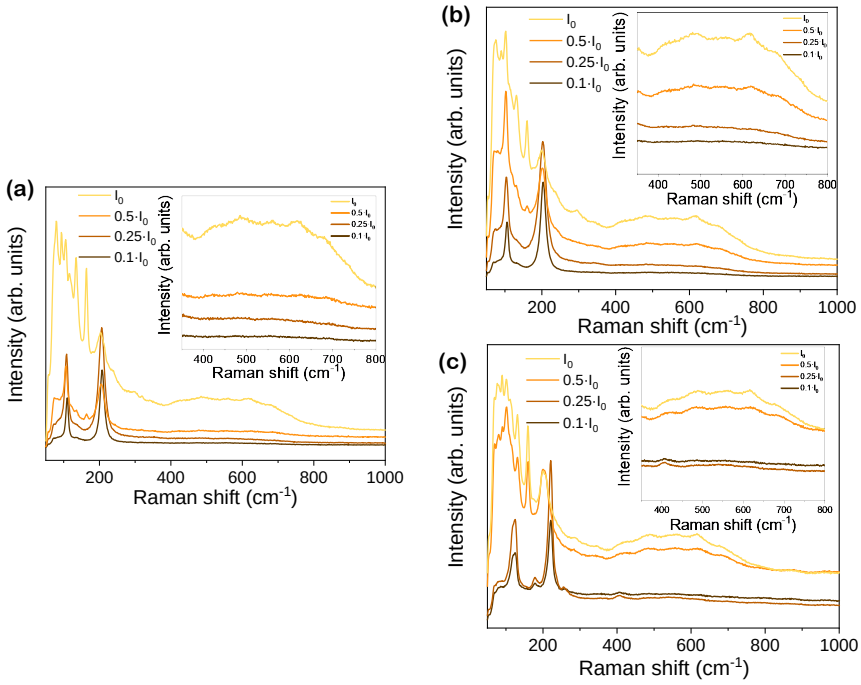

Fig. 5.12: Raman spectra obtained with the VIS laser λ=633 nm with different energy densities (from 0.1·, 0.25·, 0.5· or 1·I_0) corresponding to (a) SnO, (b) SnO:$Li_{0.2}$ and (c) SnO:$Ni_{0.2}$ nanoparticles. Inset shows detailed region between 375-800 cm^{-1}.

the B_{1g} and A_{1g} are wider, they are shifted ∼20 cm^{-1} as well as new modes are observed at the following positions 180.1, 259.1 and 408.7 cm^{-1}. $NiCl_2$ has an E_g mode at ∼ 175 cm^{-1} and A_{1g} at ∼270 cm^{-1} which might be a possible origin of those two peaks[206].

Table 5.2: Raman peaks acquired with VIS laser $\lambda = 633$ nm with maximum irradiation energy observed for the SnO sample. The values collected from the literature that correspond to theoretical/calculated modes are marked with (†), whereas (‡) indicates both theoretical and experimental modes. Remaining values represents experimental modes.

Raman shift (cm^{-1})		
This work	Proposed origin	Literature
79	Sn_2O_3	76 (Sn_2O_3)[204], 76† (Sn_2O_3)[205]
93	Sn_3O_4	90 (Sn_3O_4)[204], 90† (Sn_2O_3)[205]
105	Sn_2O_3	101-109†(A_g and B_g, respectively, Sn_2O_3)[205]
115	SnO, E_{1g}	115(SnO, E_{1g})[32,204,205], 114(SnO, B_{1g})[19],116.3 ($SnCl_2$)[203]
134	Sn_3O_4	130,132†,140(Sn_3O_4)[204,205]
164	Sn_3O_4	170‡(Sn_3O_4)[204,205]
204	SnO, A_{1g}	211,211,212,209.5,204† (SnO, A_{1g})[19,32,203–205]
235	Sn_3O_4	240, 238(Sn_3O_4)[204,205],234.3 ($SnCl_2$)[203], 240(E_u(TO))[94]
296	Sn_3O_4	300(Sn_3O_4)[204]
485	SnO_2	480 (SnO)[205],480 (Sn_3O_4,A_g mode), Disorder from SnO_2[204], 480, 490(SnO_2, E_g)[94,204,205]
558	SnO_2	Disorder from SnO_2[204]
620	SnO_2	640(SnO_2, A_{1g})[94,204]
680	SnO_2	690(disorder from SnO_2, A_{2u}(LO))[94,204]

5.1.4.2. Raman excited by an UV laser $\lambda = 325$ nm

Fig.5.13 shows Raman spectra acquired with the UV laser in different spots on the SnO sample using different neutral filters which can tailor the laser power densities and using irradiation times of 60 s. Raman peaks from romarchite SnO are not observed when irradiating with the UV laser, even with the lowest power density ($0.1 \cdot I_0$), at least within the resolution of the technique. As the laser power density increases the Raman signal obtained with the UV laser is dominated only by vibrational modes from SnO_2, the intensity of which raises, which confirms the improved crystallinity of the formed SnO_2 during laser irradiation. After the UV irradiation, the E_g and A_{1g} modes from SnO_2 at ~ 469 and ~ 615 cm^{-1}, respectively, are clearly observed in the Raman spectra.

Fig.5.14 shows Raman spectra acquired using the same filter but with variable irradiation time (60 or 600s) where peaks from SnO_2 increase for longer irradiation and other features are observed mainly due to the different energy density of the UV laser. In this case with this longer exposure peaks from SnO (A_{1g}) becomes visible. New modes appear and are summarized on Table 5.3.

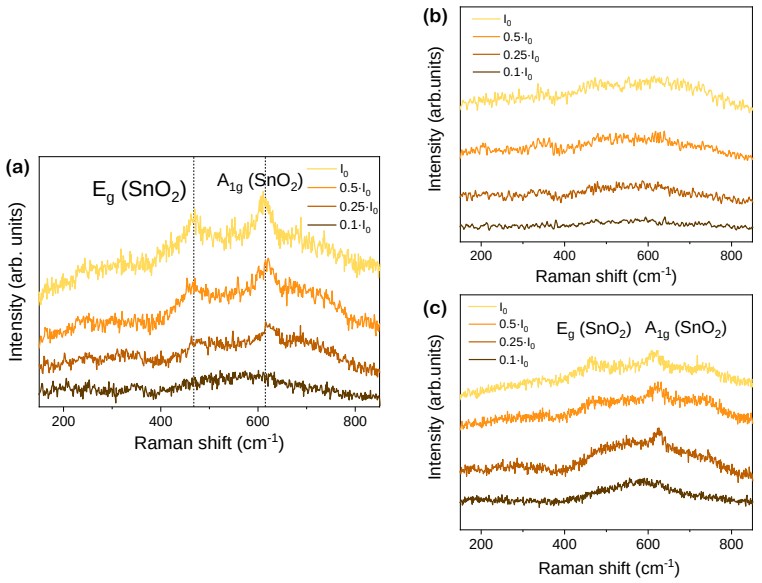

Fig. 5.13: Raman obtained with the UV laser λ=325 nm with different energy densities (from $0.1{\cdot}I_0$ to I_0 corresponding to (a) SnO, (b) SnO:$Li_{0.2}$ and (c) SnO:$Ni_{0.2}$ nanoparticles.

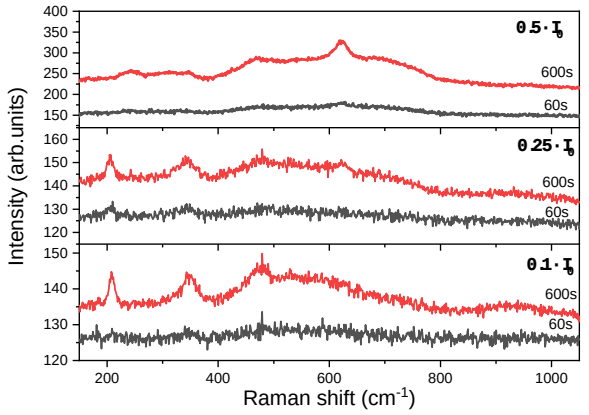

Fig. 5.14: Raman spectra acquired using different filters and variable irradiation time (60 or 600s), where peaks from SnO_2 increase for longer irradiation.

Advantage can be taken from the laser-induced oxidation from SnO into SnO_2 in order to achieve spatial controlled SnO/SnO_2 micropatterning. Based on a monitored stage, the UV laser with the highest laser intensity (I_0) can irradiate different areas in the sample composed by SnO powders with micrometric resolution

Table 5.3: Raman modes observed for variable laser irradiation energy during 600s.

Raman shift (cm^{-1})				
Laser energy density			Proposed origin	Literature
$0.1{\cdot}I_0$	$0.25{\cdot}I_0$	$0.5{\cdot}I_0$		
209	209	-	SnO, A_{1g}	211,211,212, 209.5,204† (SnO, A_{1g})[19,32,203–205]
-	-	244	SnO_2, E_u(TO)	240(SnO_2, E_u(TO))[94]
348	348	-	SnO, B_{1g}	347†-350 (SnO, B_{1g})[205]
480	480	470	Depends on the irradiation energy	480 (SnO)[205], 480 (Sn_3O_4, A_g mode),490(SnO_2, E_g)[94,204,205]
-	625	621	SnO_2,A_{1g}	640(SnO_2, A_{1g})[94,204]

$\sim 1-10\ \mu m$, as a function of the laser spot size, thus leading to a spatial controlled formation of SnO_2. Following this process, SnO or SnO_2 regions can be promoted in the samples as a function of the selected irradiation conditions. In this case, Fig.5.15(a) shows the bright (SnO_2) or dark (SnO) stripe-patterning formed on the surface of the sample after a controlled irradiation with the UV laser only in the bright areas, with a laser intensity of I_0. After the controlled UV irradiation, Raman spectra were acquired in selected points from the regions in Fig.5.15(a) using the UV laser and the lowest power density ($0.1{\cdot}I_0$) in order to avoid formation of SnO_2 during measurements. The spectra acquired in region (i) corresponds to the Raman signal from SnO_2, which confirms the oxidation from SnO to SnO_2 only in the irradiated regions, as shown in Fig.5.15(b).

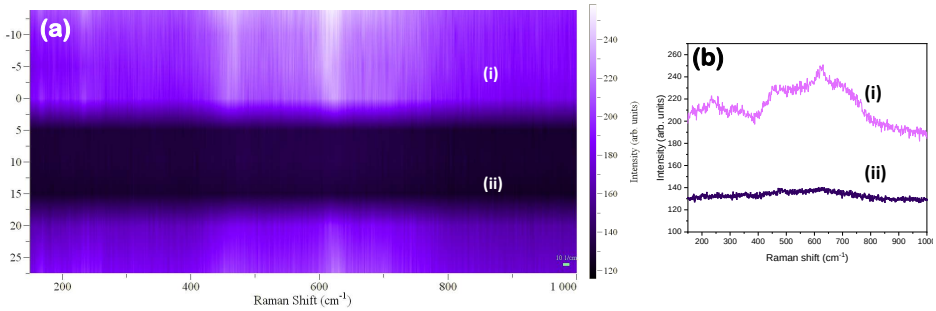

Fig. 5.15: (a) Line patterning induced by UV irradiation. Two clear different zones can be observed corresponding to (i) SnO_2 obtained after UV irradiation and (ii) SnO in the non-irradiated region. (b) Raman spectra acquired with the UV laser on regions (i) and (ii) as marked in (a).

Similarly, a larger cross-like pattern was created by irradiating first on the X axis a strip between -30 and 30 μm, with step of 2.5 μm during 3 minutes using the UV laser with the highest power (I_0) and then repeated with the same

parameters on the Y axis. To assess the difference of the irradiated/non irradiated zone, a square-like pattern (30×30 μm^2) was measured with a step size of 5μm with power (0.1·I_0) and the obtained image is shown in Fig.5.16. In this image, it can be perfectly observed the irradiated strips, represented on a clear violet color which are formed by SnO_2 while the remaining dark zones are conformed of mostly SnO. Therefore, with this method is easy and reasonably fast to obtain SnO/SnO_2 micropatternings, with accuracy.

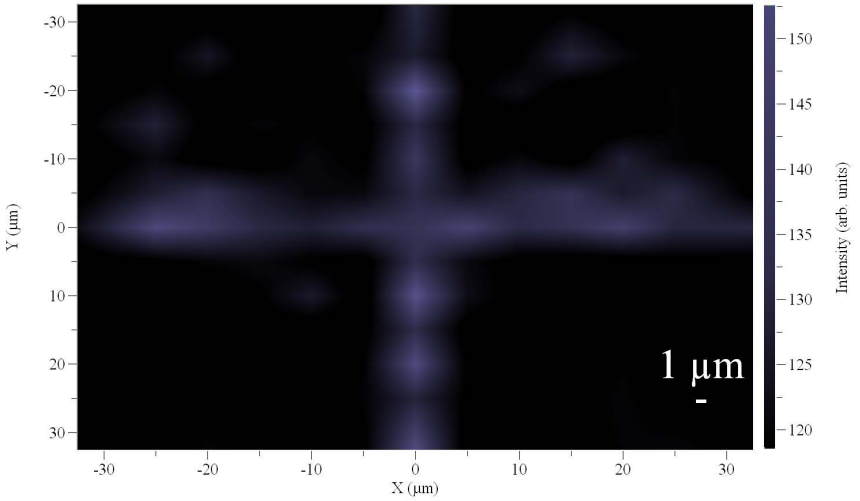

Fig. 5.16: Cross-like patterning induced by UV irradiation. The bright area correspond to the irradiated region (SnO_2) while the dark area correspond to non-irradiated region (SnO).

Increasing UV laser irradiation has shown to induce a phase transition from SnO to SnO_2 with minimum exposure time. Increasing this time enhances the oxidation process and promotes SnO_2 formation. In order to get a deeper insight of the oxidation process, SnO nanopowder was irradiated continuously with a UV laser using a power density of 0.5·I_0, while Raman spectra were acquired in the same point each minute for 25 minutes. As observed in the inset in Fig.5.17 continuous laser irradiation leads to higher intensity spectra and narrow and well-centered peaks corresponding to the SnO_2 modes such as A_{1g}. Oxidation induced by laser-irradiation and thermal effects have been monitored by measuring Raman spectra for other oxides[207]. Peak intensity of the A_{1g} mode as a function of the irradiation duration Fig.5.17, can be fitted to the *Johnson-Mehl-Avrami-Kolmogorov* (JMAK) equation[208]:

$$X = 1 - e^{-Kt^n} \tag{5.1}$$

In this equation, X is referred to the volume fraction that is transformed in

the irradiation zone, K is the effective rate constant and n is the Avrami exponent. This exponent depends on the mechanism of nucleation and growth. In this case we consider that the volume transformed is proportional to the measured Raman intensity obtained after subtracting a linear profile background. This JMAK equation has been often employed to describe laser-induced phase transitions from metastable phases[208,209]or to describe crystallization kinetics. The transformation from SnO to SnO_2 cannot be described with this equation as the transformation for high laser energy densities occurs very fast. However, evolution and crystallization of the SnO_2 formed during the initial irradiation stages can be described with the fit depicted in Fig.5.17(b). Increasing the irradiation time not only increases the intensity of certain modes, but also these modes become narrower. Corresponding to the SnO sample, the calculated Avrami exponent has a value close to $n = 1$ which corresponds to a diffusion controlled bi-dimensional reaction with nucleation site saturation[208]. Hence, increasing irradiation time enhances SnO_2 crystallinity, as expected.

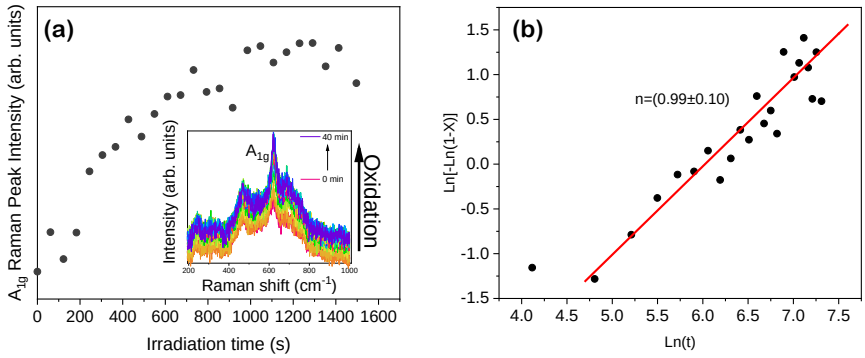

Fig. 5.17: (a) Evolution of the A_{1g} Raman peak corresponding to SnO_2 with increasing irradiation time, using the UV laser and the D_{03} filter ($0.5 \cdot I_0$). Inset in (a) shows the spectra acquired using UV laser irradiation from 0 to 25 minutes. (b) Avrami plot from the data in (a).

5.2. Optical characterization via Photoluminescence

As the SnO bandgap has commonly been reported to be between 2.5 eV (∼ 496 nm) and 3.4 eV (∼ 364 nm), the UV laser of $\lambda = 325$ nm (∼ 3.81 eV) was used as excitation source in order to get information from all the luminescent processes. The SnO oxidation to SnO_2 by UV irradiation takes place very fast, as observed during Raman analysis, thus the obtained photoluminescence signal resembles the characteristic luminescence spectrum from SnO_2. With the assistance of neutral filters, the laser power intensity was reduced, similarly as on the previous sections. Fig.5.18(a) shows the PL spectra from SnO nanopowders acquired with the UV laser using $0.1{\cdot}I_0$ laser power density, before any irradiation and with minimum exposure time during measurement, to prevent undesired irradiation. Fig.5.18(b) shows the corresponding deconvolution of the PL spectra to gaussian functions. Three main contributions can be observed, a dominant band centered around ∼2.3 eV, a high energy contribution at ∼3 eV and at lower energy at ∼1.94 eV. For Li or Ni doped, the main contribution is slightly shifted towards lower and higher energy, respectively.

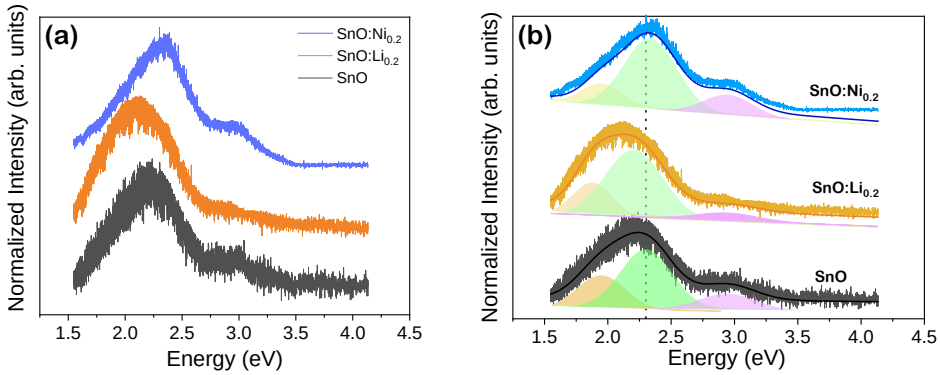

Fig. 5.18: (a) PL of undoped SnO and Li or Ni doped SnO powders before irradiation (acquired with a $0.1{\cdot}I_0$ neutral filter) (b) their corresponding deconvolution to gaussian functions.

Fig.5.19(a) shows PL spectra from SnO acquired with the UV laser using $0.1{\cdot}I_0$ laser power density in the same spot, before and after irradiating the sample with the maximum (I_0) intensity for 10 s for the undoped sample, whereas for doped samples the corresponding PL spetra are shown in (c) or (e), respectively. The total intensity of the PL signal was increased when using higher laser power densities, as expected, and resembles the PL spectra observed in chapter 3 corresponding to SnO_2. For the PL spectrum acquired with the highest laser intensity (I_0), the dominant emission is centered at around 2.3 eV as shown in Fig.5.19.

The differences on the PL spectra acquired with the complete set of filters are shown on Fig.5.19(b)(d)(f) represented as chromaticity coordinates calculated from the PL spectra according to the *Commission Internationale de l'Eclairage (CIE)*

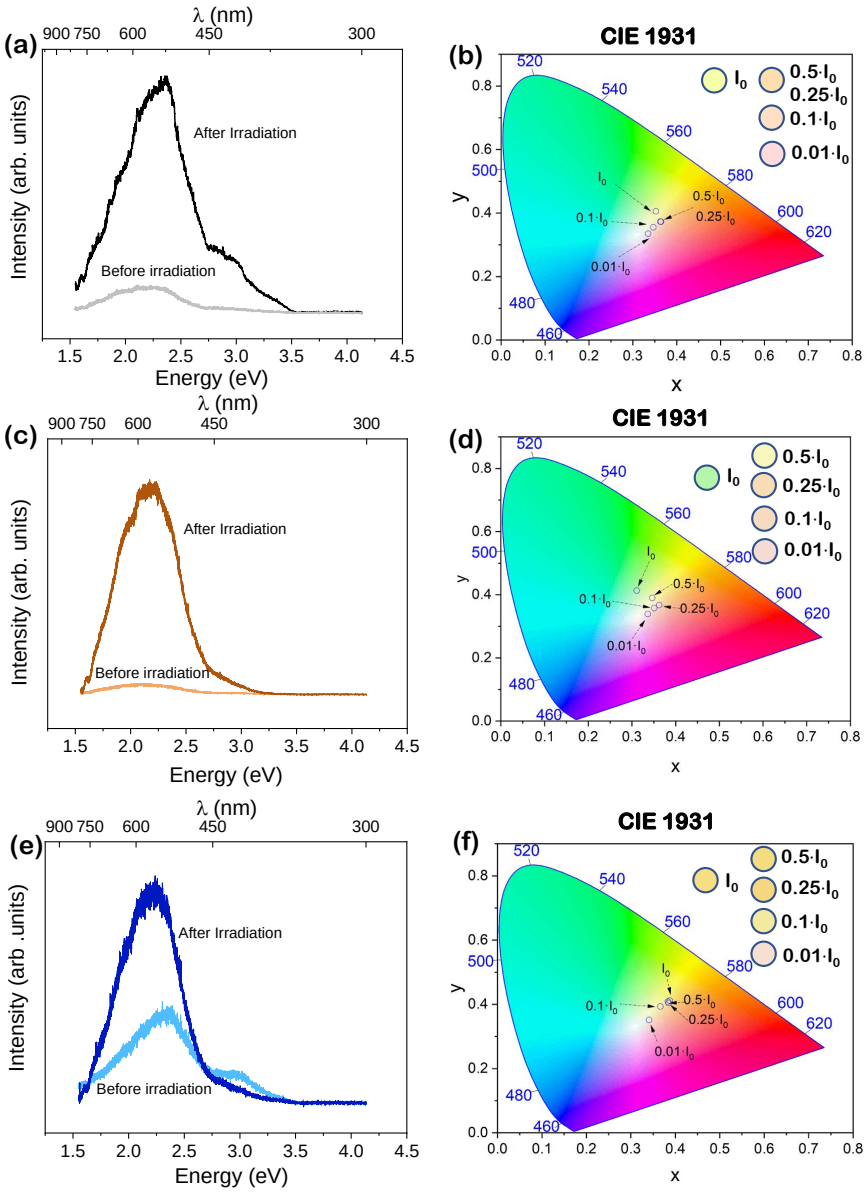

Fig. 5.19: PL before irradiation (acquired with a $0.1 \cdot I_0$ neutral filter) and after irradiation with I_0 for 10 s (acquired with a $0.1 \cdot I_0$ neutral filter) corresponding to (a) SnO, (c) SnO:$Li_{0.2}$, (e) SnO:$Ni_{0.2}$ samples and (b),(d),(f) their respective CIE 1931 plot corresponding to PL intensity of SnO nanoparticles using different neutral filters.

following CIE 1931 standard[210,211]. Note that the PL intensity is shifted towards

a yellow-ish emission with increasing irradiation energy, yet the different samples present different behavior.

5.3. Electric characterization via Hall effect

Hall effect was used to test the electrical properties of the obtained particles. Li-doped sample present higher conductivity as well as higher carrier concentration as observed in Table 5.4. The dopant effect on the electrical properties of SnO resembles the observed behavior on SnO_2, in which the presence of Li in 20% increased its conductivity but with a clear major difference, as expected, SnO presents p-type behavior. Ni-doped samples presented a high resistivity and thus, low conductivity which could not be measured with the resolution of the equipment ($\sim 10^{-7}$ $S \cdot cm^{-1}$), which is most likely to the insulator behavior of the chlorine precursors, such as $NiCl_2$.

Table 5.4: Hall effect results obtained with I=100μA corresponding to SnO and SnO:$Li_{0.2}$.

Sample	σ $(S \cdot cm^{-1})$	**Δp** (cm^{-3})
SnO	$1.82 \pm 0.21 \cdot 10^{-2}$	$2.98 \pm 0.66 \cdot 10^{16}$
SnO:$Li_{0.2}$	$3.38 \pm 0.89 \cdot 10^{-2}$	$3.71 \pm 0.21 \cdot 10^{16}$

5.4. Discussion

As discussed in chapter 1, tin oxide is a well-known semiconductor oxide which commonly appears in two crystalline forms, tin dioxide (SnO_2, cassiterite) and tin monoxide (SnO, romarchite)[212], being the former most commonly used as it is the stable polymorphic form. Despite the potential applicability of SnO in some fields of research, its use is commonly hindered as it is easily oxidized to the most stable SnO_2.

Tin monoxide, (tin(II) oxide, stannous oxide) (SnO, Sn^{2+}) romarchite, possesses p-type conductivity and often exhibits a layered structure with tetragonal space group $P4/nmm$ (129) with lattice parameters $a = b = 3.803$ Å and $c = 4.838$ Å, corresponding to a litharge-type structure[213]with a variable optical band gap, ranging between $E_{GAP} \sim$ 2.5-3.4 eV[51,212,214,215]. These properties have sparked growing interest on tin monoxide in the last lustrum as photocatalyst[216,217], gas sensing[51], as well as potential thermoelectric candidate, supported by first principle calculations[31,218]in part due to low toxicity and abundance, compared with other thermoelectric materials. Despite SnO_2 is considered a potential candidate as anode material for LiBs[16,94,116,117,153], some authors as Gervillié et al.[36] affirm that SnO appears as a better candidate concerning irreversible capacities and coulombic efficiency, whereas SnO_2 possesses best gravimetric capacity. SnO layered-type structure with sizeable c size could overcome one of the main drawbacks in Li-ion batteries, the lattice expansion, leading as well to improved Li diffusion[219] or Na diffusion[20] as SnO can form a layered structure in the [001] direction with an Sn-O-Sn sequence with large c parameter, with high theoretical capacity reaching 1150 $mAhg^{-1}$[20]. Furthermore, as one of the few p-type oxides, SnO is also considered as a candidate for hole injection layer in optoelectronic devices. However, its use is still under-explored due to limitations concerning its synthesis in a pristine form without other Sn-based oxides and its easy oxidation to SnO_2. To obtain high crystalline tin(II) oxide, common synthesis methods include hydrothermal[51,217,220]and microwave-assisted synthesis[221] whereas other methods such co-precipitation or hydrolysis remain understudied. Furthermore, most of the synthesis procedures deal with controlled atmospheres, such as Ar[214,222] or N_2[219], remarking that the synthesis must be performed on a poor oxygen atmosphere. Research concerning the growth and synthesis of SnO is primarily focused on the creation of thin films of SnO or SnO_x by techniques such as spray pyrolysis[223], sputtering[18], oxidation of Sn layers[224], PLD, template-free hydrothermal growth or mechanical exfoliation[213].

High efficiency performing devices require stability over long periods of time, being this aspect one of the main drawbacks for the widening of the SnO-based applicability. A natural oxidation process occurs on SnO which leads to the formation of crust-like or micro domains of SnO_2 which eventually become a full oxidation of the SnO domains into SnO_2. Actually, in most synthesis methods a mix of both tin oxides is formed, while the achievement of pure SnO is not straightforward being for the most part preferred to obtain SnO_x rather than searching for pure SnO. Understanding the thermodynamics and limits of existence of this phase under dif-

ferent conditions (atmosphere, temperature, UV light irradiation) is fundamental in order to overcome some of the challenges that faces the applicability of SnO and then broaden the potential use of this oxide.

Hence, in this chapter we have synthesized SnO romarchite powders both undoped and doped with Li or Ni in one weight concentration, 20% wt. Doping SnO remains understudied due to the inherent instability of this material. Despite, doping engineering could led to optimized properties such modifiable luminescence, different morphology or boosted conductivity.

As observed by XRD, SnO nanoparticles remained stable up to two years under storage at room conditions inside glass vessels. In that time span, a minimum oxidation occurred as observed on Fig.5.1 via the evolution of the SnO_2(110) peak, which in combination with the SnO (101) have been employed widely in this chapter to describe the oxidation processes, and are depicted on Fig.5.20. SnO_2(110) increases both height and FWHM during the first and a half year of storage, after which it starts to stabilize.

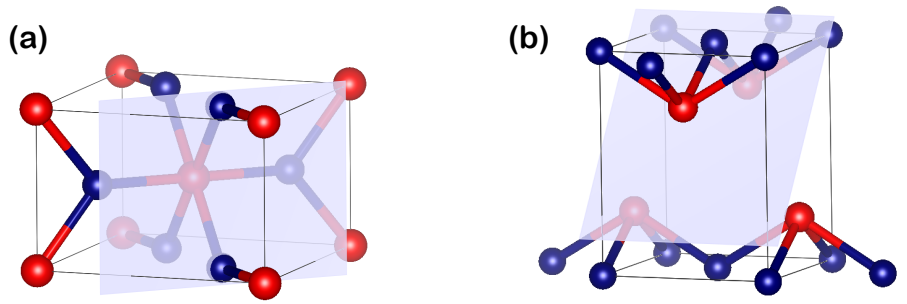

Fig. 5.20: (a) (110) plane of SnO_2 and (b) (101) plane of SnO .

Other peaks which are related with SnO_2 appear on the diffractogram as peak shoulders of other SnO position-close peaks such as SnO_2 (101) near SnO (110). Also the disappearance of the SnO (001) peak should not be ruled out, which is clearly diminished due to general oxidation of the sample. This is reasonable as this plane possesses only a 5.1% of relative intensity on the XRD pattern from SnO (ICSD 01-072-1012). Oxidation of SnO to SnO_2 is analyzed based on the works of different authors such as Leitner et al.[225] where they developed the thermodynamic diagram of the oxidation of tin and its other intermediate transition and proposed two oxidation processes: a method of core-shell like oxidation or the formation of two-single components where non-oxidized and oxidized particles coexist. Either method could agree with the observation of increasing SnO_2 on the

X-Ray diffractograms.

XRD patterns of Li or Ni doped SnO powders were shown in Fig.5.2(a)-(b) as well as on Fig.5.8. In both cases there is a clear presence of SnO but in the case of Ni there is a considerable shift of the SnO (101) peak as well the contribution of other compounds. Ni doped show contributions probably other oxides as well of other products formed by precursor reaction that may undergo due to annealing temperatures.

To further address the possible origin of the different diffraction peaks observed on the sample SnO:$Ni_{0.2}$, it is useful to observe the wider angle range presented in Fig.5.8 rather than Fig.5.2(a)-(b). In this diffractogram we observe novel peaks different to the already discussed peaks at positions around 25.1°, 26.9° and 31.9°, which origin was attributed most likely to $NiCl_2{\cdot}6H_2O$ (ICDS n°:00-001-0200) for the first peak and for the other two Sn_2O_3 (ICDS n°:00-025-1259), being the latter also probably related with Sn_3O_4 (ICDS n°:00-016-0737). These other remarkable peaks with low intensity are observed at 15.8°, 18.2° and 35.7°. This peaks could be correspond also $NiCl_2{\cdot}6H_2O$ (ICDS:00-001-0200) used as precursor. Unambiguously attribute the origin of this peak is non-trivial, as their positions are very close on the XRD diffractograms, and most likely in this sample there is a combination of the different tin oxides, most likely due to the dopant effect.

SEM and TEM analysis confirm the presence of SnO nanoparticles and platelets, as described in[202,215]. The morphology of the synthesized powders may be influenced by many factors of the synthesis such as solvent properties, precursor concentrations, nucleation kinetics and mainly by surface energetics. Jaśkaniec et al.[219] recently suggested that solvent polarity on the synthesis method is strongly related with this 2D morphology changes as well as the surface energetics, as the crystalline material will adopt the shape that embodies the minimum overall surface energy, as stated by Gibbs-Wulff theorem. Different morphologies from SnO has been reported such as platelets,[20,215] rose-like particles[19,220,226] and other hierarchical architectures[216,217]. In our case, both platelets and nanoparticles are formed via hydrolysis, which may indicate that, with the conditions used in this work, the optimal geometry consist of large platelets of $\sim 1\mu$m and small nanoparticles agglomerates with average sizes of 11 nm. Fig.5.3 shows also the presence of thicker square-like microstructures. The origin of the different structures has been disused on the bibliography. In particular, a possible explanation of the formation of square-like particles which may be produced by hydroxide-to-oxide transformations[219].

The fact of obtaining platelets is no surprising as Zhang et al.[20] reported a complete set of conditions with different pH, precursors and temperatures an their subsequent obtained geometries. They observed that by using $SnCl_2$ as a precursor on an hydrothermal synthesis, in combination with water and ammonia, lead to the formation of such platelets. Low reaction time in this case of 2 hours also led the formation of undesired $Sn_2O_2(OH)_2$. The pH of the reaction is also a key factor to obtain SnO, as at pH lower than 2 (which is the strong acidic nature of $SnCl_2$) only forms SnO_2. Zhang et al.[20] marked as optimal pH=5, but in reality

increasing the pH only diminished the reaction yield. Other structures such as roses were obtained in highly basic pH and using different precursors such as SnF_2 or $Sn_6O_4(OH)_4$, mediated with alcohols[219]. Those results are comparable to our results. However, it must be pointed out that our synthesis procedure is via hydrolysis presents novelty against those synthesis procedures and several advantages, such as the high reaction yield obtained and its simplicity.

For the doped samples with either Li or Ni, dopant presence has been already demonstrated for SnO_2 samples, which are obtained from a thermal treatment of the SnO powders, which *de facto* shows the presence of the dopant on the SnO nanopowders. In this case EDS spectra for Ni doped is shown in Fig.5.7 which resembles the observed results for Ni-doped SnO_2 samples, leading to assure that Li is also present on the sample SnO:$Li_{0.2}$ as it is present on the SnO_2:$Li_{0.2}$ nanoparticles in approximately 0.06% at.

One of the main ideas on this chapter is the study of the stability of the SnO phase under temperature, for which Thermo XRD were acquired on a variable range of temperatures. Undoped and doped SnO XRD patterns were acquired between 25 and 900°C (Fig.5.8). At 900°C, all diffractograms look alike and resemble of pure SnO_2 with very narrow peaks indicating high crystal domain induced by long time and temperature treatment. It should be pointed out that SnO and SnO:$Li_{0.2}$ present still a weak peak around 29.9° attributed to SnO (101) and other peak at 24.3° which origin is discussed below, whereas for SnO:$Ni_{0.2}$ is completely absent pointing that the stable structure after Ni doping might be pure rutile.

Diverse authors reported the oxidation from SnO to SnO_2 at temperatures in the range 400-700 °C as a function of the annealing parameters and the characteristic of the initial SnO nanopowder[220,221]. The transition starts at around 400 °C as observed in Fig.5.9. This oxidation process is nearly completed at temperatures above 800 °C. In general, annealing at temperatures higher than 600°C fully transforms the SnO nanoparticles into the rutile SnO_2 phase[227]. In our case we observe that this transition starts at similar temperatures for both doped or undoped SnO nanoparticles. In some cases an oxidation process involving the formation of intermediate oxides such as Sn_2O_3 and Sn_3O_4 is reported[222]. In our study, SnO (101) and SnO_2 (110) become equally relevant at around 400 °C and at 500 °C a weak maxima near 24.3° start to appear which could be attributed to (101) Sn_3O_4 (ICSD n°:00-016-0737) or even (001) from Sn_2O_3 (ICSD n°:00-025-1259) but it is notably displaced. On top of that, due to the absence of other maxima characteristic of this oxide we cannot unequivocally attribute this peak to this compound but it is most likely produced by some SnO_x compound. However, the oxidation appears to not be mediated by the formation of these oxides as SnO_2 is already substantially present. As pointed out by the thermodynamic phase diagram of the Sn-O system[212,225,228] and the allowed valence changes of Sn a small amount of this intermediate oxides must be present, but seems not to play a major role, in difference to other works[222].

Regarding the undoped sample, the (101) maximum from SnO observed at

29.9°, which dominates the XRD pattern at room temperature, suffers a shift to lower angles as the temperature increases. At 480 °C this peak is placed at 29.40° and then it shifts again towards higher angles, finally reaching 29.89° at 800 °C, although at this high temperature the relative intensity of this peak is drastically decreased (Fig.5.10). The shift to lower angles could be related to a thermal lattice expansion up to 480 °C, where the SnO_2 phase dominates the XRD pattern. During the annealing and oxidation process, an arrangement of the ions in the SnO lattice may take place, leading to small variations in the lattice constants along to the formation of SnO_2. In this regard, the XRD maximum which exhibits more variation in its position and intensity corresponds to the (101) planes in romarchite. F. Wang et al[229] reported a process in which the chemical coordination of the interstitials Sn cations becomes more similar to that of cassiterite SnO_2 during the oxidation process, which can be related to the SnO (101) shift during annealing. This shift is present on the Li-doped samples with a very similar behavior, while Ni-doped presents the same shift towards lower angle, after reaching 480°C, peak disappears, which could indicate SnO is fully transformed to SnO_2 .

Li-doping shows very similar results to the undoped sample as the minimum angle of the SnO (101) is observed at $\sim$ 470°C. Ni doped SnO presents the highest differences. The presence of precursors or other compounds such as $Sn_6O_4(OH)_4$ and possible nickel chloride is further proved due to the disappearance of those peaks at near 200°C due to the inherent volatile nature of those compounds as observed in Fig.5.9(c) as well as the transition to more stable oxides. Also, the transition to SnO_2 is enhanced as it starts at $\sim$ 300°C.
As well as for SnO_2, SnO powders were obtained for both concentrations, 20% and 30% Li or Ni doped. Results of 30% are not presented in this work due to its thermo-XRD patterns showing that they are mostly composed of SnO_2. Two reasons are proposed for that behavior, on one hand, for high Ni or Li doping could be more stable the SnO_2 rather than SnO cell. High dopant concentrations trespassing a debatable low solubility limit could also favor the rutile structure. Previous reports show that the SnO_2 is stable with high Ni doping[54]. On the other hand it could be more easily oxidized to SnO_2, enhanced due to the formation of defects on the structure which serve as potential bonds for Sn-O on rutile structure. Remarkably, Raman results which are measured locally in spots > 1 μm show that there are micro-clusters of SnO as the observed modes can be attributed to SnO. Nevertheless, the study of high Li or Ni doping has been left out of this thesis.

Raman spectroscopy was studied with two different lasers as aforementioned, with the VIS and the UV lasers. Regarding the VIS laser results, SnO Raman modes were observed at $B_{1g}$$\sim$110 cm^{-1} and $A_{1g}$$\sim$208 cm^{-1} (Fig.5.11) but is worth mentioning that, there is still some controversy in the assignment of the Raman modes, as some authors assign the first peak to E_g based on frozen-phonon DFT calculations[32,205]. In our regard, peaks are most likely due to E_g and A_{1g} which vibrations are represented on Fig.5.21.

As observed, Raman signal is strongly affected by the laser intensity. When increased over $0.1 \cdot I_0$ up to I_0 different Raman modes can be distinguished which

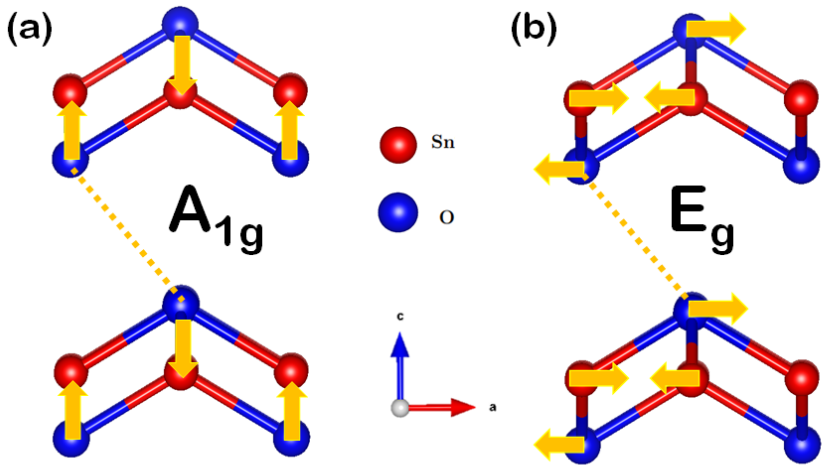

Fig. 5.21: Graphic representation of SnO vibrational modes (a) A_{1g} and (b) E_g.

were carefully depicted on Table 5.3. Guillén et al.[204]attribute these peaks to intermediate SnO_x oxides, mainly to monoclinic Sn_3O_4, as also confirmed by other authors[205]. It can be observed that some peaks such as $\sim$ 204 cm^{-1} is shifted in comparison with most of the reported in the literature. If we look at Fig.5.11 we can observe differences between the doped and undoped samples were this B_{1g}/E_g peak is clearly sensitive to small distortions of the lattice. These results point out to an intermediate oxidation from SnO to SnO_2 by the formation of intermediate Sn_3O_4 when the red laser power density is not high enough.

In addition, when the red laser power is maximum (I_0) formation of SnO_2 is promoted as wide modes appear in the region between 450-700 cm^{-1} (inset in Fig.5.12), which could be attributed to the E_{1g} and A_{1g} modes from SnO_2, also observed by UV irradiation (Fig.5.13), although with much lower intensity in this case. Raman modes at higher wavenumber can be almost certainly attributed to SnO_2 as well to disordered modes related with this structure. It should be noted that, contrary to the almost direct formation of SnO_2 from SnO by thermal annealing, confirmed by XRD analysis, in this case either complete transition to SnO_2 or formation of intermediate SnO_x phases can be also promoted as a function of the laser irradiation conditions.

Concerning doped SnO, Li doped-SnO possesses similar Raman modes than for undoped SnO. On the case of Ni-doping new modes appear in the low wavenumber region. As mentioned, B_{1g} (E_g) and A_{1g} are wider and also they are shifted $\sim$20 cm^{-1} as well as new modes are observed at the following positions 180.1, 259.1 and 408.7 cm^{-1}. $NiCl_2$ has an E_g mode at $\sim$ 175 cm^{-1} and A_{1g} at $\sim$270 cm^{-1}

which might be the origin of those two peaks[206] as aforementioned, while the weak latter contribution might be related to any possible compound formed by the nickel chloride and tin oxides. Furthermore, we see differences between each sample, most notably on its behavior with different laser irradiation. For each sample using the higher irradiation (I_0) the intensity of each mode is very different which is an indicator on different oxidation and presence of multiple valence with laser irradiation (Fig.5.12).

It is worth mentioning that any of the observed modes apart from SnO A_{1g} or E_g could not been observed with lower irradiation energy as $0.1 \cdot I_0$ using the VIS laser, even for longer exposure time. This was observed firstly measuring the Raman spectra with $0.1 \cdot I_0$ over longer periods of time, which did not rise any other contribution. Secondly after measuring an specific point with $0.1 \cdot I_0$ it was continuously irradiated with $0.5 \cdot I_0$ during 600s and finally measured again with $0.1 \cdot I_0$. Clearly, after the irradiation with $0.5 \cdot I_0$ it has been shown that there is a wide variety of new Raman modes, as it has been observed in Fig.5.12. Returning to $0.1 \cdot I_0$ leads to only the observation of the original SnO-related modes, but its signal is strongly quenched which further confirms the oxidation to SnO_2 (Fig.5.22(a)). This peak quenching was followed during a short period of time and tends to decrease exponentially, as observed in Fig.5.22(b) which is reasonable due to the laser propagation through the sample and the nature of the irradiation process.

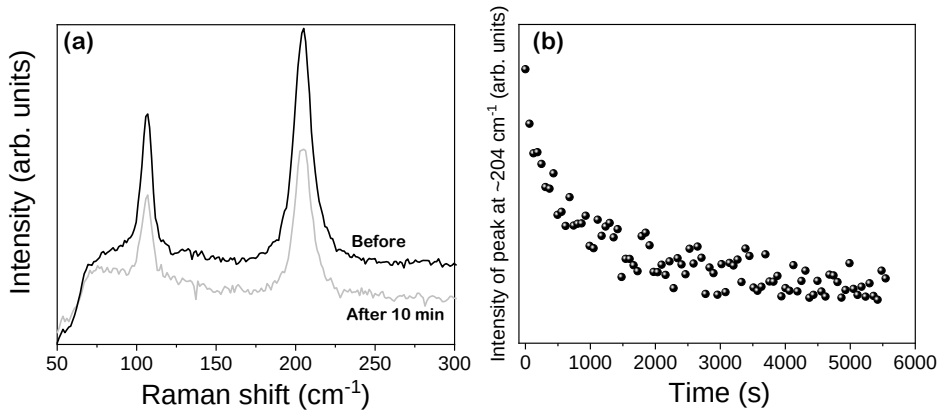

Fig. 5.22: (a) Raman spectra of SnO nanoparticles before irradiation (acquired with a $0.1 \cdot I_0$ neutral filter) and after irradiation with with $0.5 \cdot I_0$ for 600 s (acquired with a $0.1 \cdot I_0$ neutral filter). (b) Decrease of the peak at $\sim$204 cm^{-1} measured with $0.5 \cdot I_0$ over a longer period of time.

As previously mentioned, SnO presents p-type conductivity whereas SnO_2 is a well known n-type semiconductor. The fabrication of n-type SnO_2 and p-type SnO heterojunctions is also gaining increasing attention in recent years, especially in optoelectronics, Li storage[230]and as chemiresistive sensor with enhanced sensibil-

ity for a variety of gases such as of NO_2[231] , H_2[34] , acetone[35]or formaldehyde gas[232]. In those cases, the variability of SnO geometries and hierarchical structures are fundamental for the optimal performance of the devices, while the achievement of a controlled local oxidation from SnO to SnO_2 can also lead to the fabrication of p-n heterojunctions at the micro- and nanoscale with improved performance.

The creation of such SnO_2/SnO structures can be complex as SnO is not stable which may cause oxidation and diffusion processes between SnO and SnO_2. Laser-based processing has arisen as an alternative method to thermal treatment for tailoring Metal Oxide semiconductors (MOs) which had been used in gas sensors, photocatalyst, solar cells or thermistors[233]. Several parameters such the laser intensity, pulse or scanning rate act as optimizing parameters to obtain desired and controlled oxidation. In this work, those parameters were described on chapter 2 but it is worth to mention that the working mode of the laser was continous-wave, the laser was not polarized and the beam profile is Gaussian. The focusing on the sample was performed using the objective described on the experimental section.

Firstly, it is important to mention that the UV-laser radiation exhibits lower energy than the VIS laser but also lower optical depth penetration in the oxides, which strongly changes the observed results between both lasers, being the most notable for the UV laser with the use of neutral filters. Raman UV results show that as the irradiation exposure or energy density increases the modes corresponding to SnO_2 (E_g and A_{1g}) appear, but the former is slightly displaced to lower wavenumbers around 468 cm^{-1}, as it can be observed on Fig.5.13 probably due to the initial lower crystallinity of the formed SnO_2 or even due to temperature shift of the phonon modes. As the irradiation density and duration increases, not only the relative intensity of the Raman modes increases but also their positions are closer to the expected for SnO_2. This formation of SnO_2 from SnO by laser irradiation is irreversible, as expected due to the higher stability of the former oxide. Other studies[157] have been carried out for UV laser irradiation as the irreversible anatase-to-rutile transition discussed in the previous chapter .

Other parameter, which as the irradiation energy should be also considered is exposure (irradiation) time. In Fig.5.14 we observe main differences between the use of different irradiation times (60 or 600s) and laser energy density. For $0.1 \cdot I_0$ and $0.25 \cdot I_0$ new modes appear at 209 and 340-350 cm^{-1}. The mode in 350 could now be assigned to a B_{1g} mode, whereas the previously-observed mode at $\sim$ 109 cm^{-1}, attributed to B_{1g} could be an E_g mode, as some authors have pointed out the controversy between the association of this modes origin[205]. The main difference between those irradiation energies is that for $0.1 \cdot I_0$ a mode appears at 480 cm^{-1} which could be associated to different origin but most likely to SnO or Sn_3O_4 as summarized on Table 5.3. This mode is quenched for $0.25 \cdot I_0$ and arise as a shoulder for $0.5 \cdot I_0$ which suggest that could be associated with the E_g mode from SnO_2. By using $0.5 \cdot I_0$ the A_{1g} mode from SnO_2 arises at $\sim$621 cm^{-1} and the spectra resembles Raman spectra from SnO_2 presented on subsection 3.1.4. This is similar to what we have observed via XRD, much of the Raman modes corresponding to Sn_3O_4 or Sn_2O_3 possess similar Raman shift than SnO_2 modes. Moreover, most of those modes have only been studied theoretically. Hence, contribution at $\sim$340, 480 or

even 620 cm^{-1} could be also attributed to Sn_2O_3, yet the work in which this result is claimed has a dubious stoichiometry of the compounds[229]. Undoubtedly, VIS Raman spectra is more defined and single modes attributed to different phases are easily indexed.

Based on the controlled SnO_2 formation as a function of the irradiation condition, the idea of a SnO/SnO_2 micropatterning was explored. The controlled UV laser irradiation can tailor the oxidation process leading to either n-type SnO_2 and/or p-type SnO spatial distribution following a micrometric patterning. The availability of both n- and p-type conductivity in Sn oxides allows the potential development of bipolar devices based on p-n heterojunctions controlled at the microscale. Moreover, intermediate of SnO_x oxides can be also formed if needed as a function of the irradiation conditions. A simple line on the X axis was presented on Fig.5.15 and a larger cross-like pattern was presented in Fig.5.16. This could be exploited further to create complex patterns, especially interesting to create arrays of p/n type junctions, for sensing purposes, for example, in which the formed p-n junction could led to higher sensitivities.

The exact mechanism which promotes the transition could not be attributed to a single effect[233]. Competing mechanism such as thermalization or photon absorption by the sample as well as carrier diffusion and thermal diffusion could be considered, as well the interaction with adsorbed oxygen on the surface. The combination of such effects enhances the oxidation of SnO, which interacts with adsorbed oxygen and creates SnO_2.

Photoluminescence study was carried out for the undoped and doped SnO powders. The PL spectra with low irradiation energy was presented at Fig.5.18. Even using the lower energy density in which photoluminescence can be observed, these results had to be carefully interpreted. SnO bandgap is between 2.4-3.5 eV, therefore, the high energy emission represented as violet band in Fig.5.18(b) which will be increased with irradiation, is probably related with SnO_2. Differences can be observed between doped and undoped samples, similarly what we have observed for SnO_2 luminescence; Li doped sample presents the main contribution slightly red-shifted as well as there is an absence of the band close to 3 eV. Before the irradiation, PL spectrum acquired with $0.1 \cdot I_0$ is characterized by two main emissions centered at around 2 and 2.3 eV. These emissions could be due to high defective SnO_2 although the presence of SnO, not detected by Raman analysis, cannot be completely disregarded as some authors reported emissions from SnO around 2 to 2.3 eV due to defects such as Sn vacancies and O vacancies and at ∼3 eV related to band-edge emissions[215,223]

For the PL spectrum acquired with the highest laser intensity (I_0), the dominant emission is centered at around 2.25 eV as shown in Fig.5.19. Additionally, a shoulder at about 3 eV up to 3.5 eV, can be observed. This spectrum can be attributed to SnO_2, as this material normally shows characteristic emissions at 1.94 eV and 2.25 eV associated with oxygen vacancies-related defects, ∼2.50 eV due to surface defect states[99] and ∼3 eV due to transitions involving $V_O^{\bullet\bullet}$ levels as

explained in subsection 3.2.1.

Li-doped SnO Fig.5.19(c) presents the highest intensity on the PL signal and Ni-doped samples present a contribution $\sim$ 3 eV. These results are in agreement with the photoluminescene spectra shown on subsection 3.2.1, where we observed that Li doped samples presented a high concentration of oxygen vacancies, with a symmetric-band centered around 2.25 eV. Meanwhile, Ni-doped samples presented not only weaker luminescence, as well as to a contribution related to STE towards higher energy. A main difference is observed on the after irradiation spectrum which should resemble the PL spectra of doped SnO_2. This locally-induced transition is similar to some extent to the thermally-driven transition to SnO_2 but when it is induced with the laser locally it seems that the PL resembles pure SnO_2. Luminescence of both undoped and Li doped SnO present a substantially increase after laser irradiation as opposed to Ni doping which is increased, but less. Note that spectra are normalized.

Fig.5.19(b),(d),(f) present the CIE diagrams of undoped and doped samples with the different filters. Substantial differences are observed between the samples. Luminescence in any case is a wide band that covers the visible range and tends to shift from red-yellow-ish towards yellow-green-ish but differs on the coordinates position for each irradiation energy, both on the position for the maximum energy (I_0) and the path followed by the previous irradiation energies. This is clearly observed for Li doped which up to the maximum irradiation energy presents a green luminescence greatly shifted compared with the other emissions. In any case this shows a wide variability on the emission wavelength of these doped samples which is probably related with the formation of intra-gap levels induced by Li doping.

SnO electrical properties had not been notably studied neither as pressed particles or monocrystalline SnO. Some researchers have measured 2D SnO layers, obtaining conductivity values of stoichiometric SnO_x ranging from of $10^{-1} - 10^3$ S·cm^{-1}[213]. Very few works such as Krishnkumar et al.[234] have obtained SnO nanoplatelets conductivity of $\sim 10^{-3}$ S·cm^{-1} which is similar to our observations. Stannous oxide has intrinsic p-type conductivity due to the presence of both tin vacancies (V_{Sn}) and oxygen interstitials (O_i), being the former the most abundant due to low formation energy which creates acceptor defects near the VBM. However, first principle calculations attribute the p-type behavior to other defects such as intended impurities of V_{Sn}-H complexes or the introduction of dopants which act as shallow donors[235]. However, SnO could posses an ambipolar nature which can be understood in term of its electronic configuration. SnO posses an ionization potential of approximately 5.8 eV which is similar to other p-type materials but with an electron affinity comparable to n-type semiconductors[213]. This shows the complex behavior to understand changes on this oxide conductivity.

It must be pointed out that as far as our concern, there are almost no research literature on the topic of doped SnO nanoparticles or other hierarchical structures, especially regarding electrical or optical characterization, as on section 1.4 it were mentioned a few works dealing with doped SnO and its magnetic properties. Higher conductivity was obtained for the Li those samples which could be attributed to

the effect of the dopant. Li doping has been studied for other p-type oxides such as NiO[236], in which increasing Li content lead to higher conductivity mainly due to two different effects. Firstly, the incorporation of lithium on the lattice created oxygen vacancies which may result in the absorption of oxygen by the lattice from the surroundings, which increases the hole concentration and therefore, the conductivity. Secondly, the incorporation of Li^+ ions by substitution of the Ni^{2+} in the case of NiO (and Sn^{2+} in our case), increases the hole density, which also increases the overall conductivity.

5.5. Conclusions

In this chapter, undoped and Li or Ni doped SnO nanoparticles (and other nanostructures) have been synthesized via a co-precipitation method based on hydrolysis. A characterization of morphological, structural, compositional, electrical, and optical properties has been carried out. Particularly, their stability under temperature, storage and UV irradiation has been analyzed, focusing on the possible oxidation from SnO to SnO_2.

- Crystalline SnO nanoparticles and platelets have been synthesized via a hydrolysis method which allows to achieve large amount of SnO powders avoiding an atmosphere-control during the synthesis. The nanoparticles dimensions range from 4 to 22 nm as confirmed by TEM observations. XRD measurements confirm the minor oxidation and stability of the as-synthesized SnO stored at room conditions during up to 24 months. Other geometries such as platelets appear altogether with nanoparticles. The reaction yield allows to obtain a significant amount of SnO nanostructures.

- The oxidation from SnO to SnO_2 have been promoted by thermal annealing or by controlled laser irradiation. Temperatures at least above 300°C are required to initiate the oxidation from SnO to SnO_2 which is completed at temperatures near 800°C following a nucleation and growth process with minimum formation of intermediate SnO_x, as confirmed by thermodiffraction measurements.

- By UV or red laser irradiation the transition from SnO to SnO_2 can be controlled, assisted by formation of intermediate Sn_3O_4, as confirmed by Raman spectroscopy. Careful attention should be paid during the PL and Raman analysis, as the use of the laser as excitation source can induce formation of SnO_2 during measuring, thus leading to possible misleading results. Hence, the evolution from SnO to SnO_2 has been studied as a function of the laser excitation source (UV and red laser), the laser power density (controlled by using neutral filters) and the irradiation exposure time, in order to achieve deeper knowledge and control of the oxidation process. The evolution of the oxidation of the SnO_2 towards higher crystallinity promoted by UV laser irradiation obeys Avrami behavior.

- Controlled SnO oxidation and a tailored spatial SnO/SnO_2 micropatterning has been developed based on a controlled laser irradiation with the UV laser, without the use of any mask. This laser-induced micropatterning can be of potential interest for the fabrication of p-n devices based in all Sn-oxides with applicability in electronic, optoelectronic and sensing devices.
- Among the undoped and doped nanoparticles, some differences are observed. Ni-doped SnO presents the most notable differences, as a high presence of the precursors can be observed in XRD and Raman, and as observed by SEM micrograph, samples are mostly composed by nanoparticles. Li-doped SnO nanopowders possesses higher conductivity and similar properties than undoped SnO powders (regarding morphology and temperature stability). A slight shift in the luminescence towards higher energies is promoted by Li doping.

Chapter 6.
PEDOT:PSS composites based on SnO, SnO_2 or TiO_2 nanoparticles for hybrid Si-solar cells

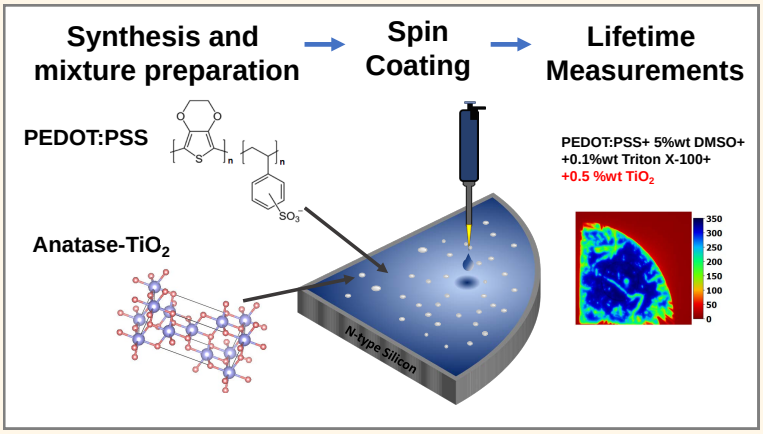

Abstract: Hybrid p-n junctions based on PEDOT:PSS and n-type silicon wafers have been fabricated. Different mixtures of PEDOT:PSS have been analyzed and different spin coating procedures have been used to obtain the optimal coverage of the silicon surface. SnO, SnO_2 and TiO_2 were added to PEDOT:PSS and improvements in the PEDOT:PSS films were achieved leading for enhanced silicon surface passivation.

This chapter includes adapted material from:

- A. Vázquez-López et al., Hybrid Materials and Nanoparticles for Hybrid Silicon Solar Cells and Li-Ion Batteries, *Journal of Energy Power Technology*, **2021**, 3, 2.[155]

- A. Vázquez-López et al., Improved Silicon surface passivation by hybrid composites formed by PEDOT:PSS with anatase TiO_2 nanoparticles, *Materials Letters*, **2020**, 271, 127802.[237]

- A. Vázquez-López et al., Synergetic Improvement of Stability and Conductivity of Hybrid Composites formed by PEDOT:PSS and SnO Nanoparticles, *Molecules*, **2020**, 25, 695.[215]

In this chapter some of the results obtained during a 3-month internship at IFE (Institute for Energy Technology) at Kjeller, Oslo, Norway are presented.

N-type silicon wafers, which properties have been summarized in Table 2.4 on subsection 2.1.3 were coated with PEDOT:PSS to obtain hybrid p-n junctions with enhanced silicon surface passivation. This chapter is divided in two sections. In the first section, we will describe and analyze the main parameters to obtain these thin PEDOT:PSS layers over silicon. In the second section we will evaluate the use of the nanoparticles synthesized in the previous chapters to form hybrid composites, studying their effect on passivation and stability.
Therefore, in the first section, we will compare different candidates mixtures of PEDOT:PSS with organic additives such as DMSO or EG and evaluate also the use surfactant Triton X-100. Besides, we will analyze the effect of the removal of the native silicon oxide layer of the silicon wafer and its effect on the recombination processes. Secondly, the coating procedure for obtaining thin layers based on spin-coating is described. Finally, the degradation over time of the different composites is measured. After this first section we will have obtained an improved method for passivating silicon surfaces.

On the second part, the results of PEDOT:PSS with the addition of the nanoparticles, which were synthesized and characterized in Chapter 3, Chapter 4 and Chapter 5 are described and evaluated. The main focus on the effect of these nanoparticles is aimed to improve electrical or optical response, enhanced silicon passivation as well as obtaining higher stability over degradation with time.

6.1. Obtaining PEDOT:PSS thin layers

The first step to obtain thin layers of PEDOT:PSS over a silicon substrate is to prepare a mixture with the selected compounds. The flow diagram of the steps to obtain the desired composites has been described on the experimental part, in subsection 2.1.3 in Fig.2.4.

6.1.1. Mixture preparation

PEDOT:PSS was described in the chapter 1 as a conductive p-type polymer conformed by two ionomers PEDOT (poly(3,4-ethylenedi-oxythiophene)) and PSS (polystyrenesulfonate). Nominally, PEDOT:PSS possesses low conductivity which limits its applicability. Moreover, its stability with respect to high temperatures, UV irradiation or humidity is questionable. In this thesis, PEDOT:PSS (Clevios, PH1000, 1.0%–1.3% wt. in water) was combined, in order to enhance conductivity with additives such as dimethyl sulfoxide (DMSO, Sigma-Aldrich), Etylene Glycol (EG, Sigma-Aldrich) or Triton X-100.

Different mixtures were evaluated in this part of the thesis. Based on previous reports, adding 5% wt of DMSO is suggested as the optimal ratio for enhancing conductivity and preventing degradation[238,239]. In our research, adding this weight percentage did improve the silicon surface coverage, which was also other main factor to accomplish. To maximize this surface coverage Triton X-100 was also added in 0.1% wt. This compound is a surfactant which is known to enhance wettability as well as slightly increase conductivity[240]. Both the order and mixing procedures were evaluated, finding the best results after magnetic stirring for 2 h, an then filtrated with a PolyEtherSulfone (PES) Millex® membrane (pore size = 0.45 μm) to achieve higher homogeneity via segregating bigger particles out of the mixture. Steps are schematically shown in Fig.2.4.

From this time on, any sample that is referred as PEDOT:PSS is refereed to this mixture, as bare PEDOT:PSS was not considered due poor electrical results as it showed mostly high sheet resistance.

6.1.2. Spin coating

This technique has been described in section 2.1.3. The main idea to assemble hybrid composites consists in covering a silicon wafer (or a glass substrate) with a mixture of PEDOT:PSS which is commercially distributed already diluted in water. Deposition steps to obtain high quality coverage have been described on Table 2.5. The main parameters to control the quality of the deposition are: spin speed, spin acceleration (with their respective duration) as well as the deposition time (which corresponds to the effective time where the liquid is poured over the sample). Although the step process could be pretty complicated as we could add the desired number of steps, the main idea was to keep it as simple as possible. Following manufacturer (Clevios^{TM}) recommendations, spin coating speeds around 6000 rpm allows to achieve thin layers of around 100 nm. To estimate the thickness of the PEDOT:PSS layers deposited over silicon, samples were introduced into a SEM chamber an placed at grazing incidence respective to the electron beam, so the interlayer of PEDOT:PSS/nSi and the electron beam are perpendicular to each other. To assure that there is no bending of the PEDOT:PSS over the edge of the silicon wafer or that the thickness is not clear due to an increasing thickness towards the center of the sample, the sample was cut forming a 1.5×1.5 cm^2 square. Fig.6.1(a) shows a SEM micrograph where we can observe the PEDOT:PSS layer over silicon which thickness was measured in different parts of the sample. Averaged

thickness of 154 nm was obtained, as shown in Fig.6.1(b) and marked by the red dot on the box diagram, where each of the measurements is represented by a blue dot with a blue line which indicates the data dispersion values. It should be noted that the sample might be ±1-2° degrees tilted, so the thickness results have an inherent uncertainty.

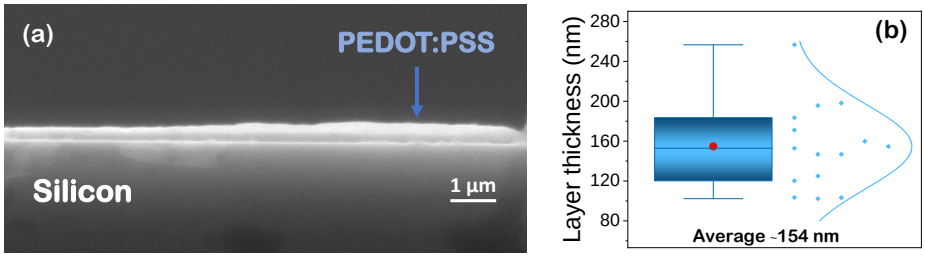

Fig. 6.1: (a) SEM micrograph acquired at grazing incidence on the silicon substrate (b) estimated thickness of the PEDOT:PSS layer measured by averaging the thicknesses observed in different zones. Red dot shows average thickness.

Therefore, AFM was performed to further estimate the layer thickness by placing the tip near a region where a step was created by removing the PEDOT:PSS with 2-propanol. As observed in Fig.6.2(a), the cantilever was placed above the step and an image was obtained where the contrast evidences the strong change in height (Fig.6.2(b)). The profile image (Fig.6.2(c)) shows that between point A (over PEDOT:PSS layer) and B (over Silicon substrate) there is a height change of around 150 nm, which agrees with the SEM observations. Profilometry results (not shown here) performed on some of the samples show a step size between 100-200 nm, agreeing with these results.

The designed spin-coating process consisted on primarily two steps, in which initially the substrate started spinning at 2000 rpm during 20 s. After the first seconds of spinning, a pipettor which contained 70-150 μL of the PEDOT:PSS mixture, depending on the coating substrate, was placed ∼2 cm over the substrate and was manually poured through the spinning substrate. This is often referred as delay/solution dispense time, being the delay time the time period before deposition while solution dispense time consisted on the time when the deposition takes place. The substrate then was left spinning at 6000 rpm during 50 s, which creates a thin homogeneous layer to finally decrease its speed until stoppage.

The substrates where the mixture was deposited by spin coating were silicon n-type float-zone (FZ) substrates (TOPSIL) as described in[215,237], either without any treatment or with the oxide layer removed with HF as explained in the next subsection. Glass substrates were also used when necessary, mainly for optical measurements. The selected glass substrates were previously treated with isopropanol and boiling water and dried with N_2, while some other substrate post-

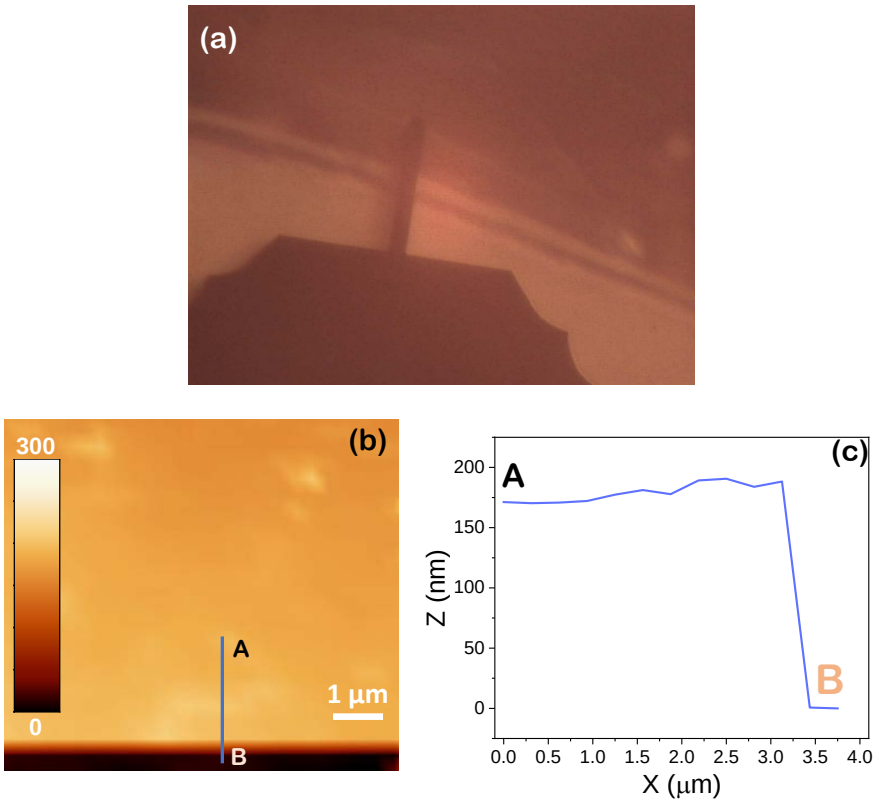

Fig. 6.2: (a) Optical image of the cantilever over the step conformed by the PEDOT:PSS (b) AFM image of the profile and (c) the AFM profile.

treatments (such as thermal treatment to evaporate remaining moisture) were also performed. Hence, samples were heated in a hot plate for 120°C during 15 min for each face if the sample was coated by its two faces, or only by one side if only one face of the sample was coated, with the coating side preferably looking upwards. The use of higher temperatures could be counterproductive as near this temperature PEDOT:PSS is expected to posses maximum conductivity, which tends to decrease for higher temperatures[71].

It is important to note that, in this chapter, three different coatings geometries have been followed, which are considered in Fig.2.4. Their differences are as follows:

- To analyze I-V, Si substrates were coated only from one side. Over this side, a mask is placed and Ag is evaporated as described in section 2.2.15 and a full-back silver contact is made on the other side, over the uncovered silicon. Sides are carefully protected to avoid shortcuts of the sample due to Ag on the sides of the sample. Substrate size was 1/4 of the circular commercial

substrate, which was ∼78.5 cm^2 as described in Table 2.4.

- To measure PL-QSSPC, Si substrates were coated from both sides. If coated only for one side, the effect of the non-passivated back side could interfere with the obtained lifetimes measured for the front-side. The substrate used is the same silicon substrate as for measuring I-V. The other main difference is that in this case there is no contacts evaporated over the sample.
- To analyze other properties such as optical absorption or Hall effect, deposition was performed over glass substrates of 2.2×2.2 cm^2 to minimize substrate contribution as the glass substrate is transparent to VIS light as well as being highly resistive. For measuring Hall effect, front contacts with either Au or silver paint were used to obtain Ohmic contacts.

Particularly, the two silicon substrates-coating geometries are described on Table 6.1, in which an average of the thickness of each layer is presented. The thickness of the oxide layer (SiO_x) was measured with ellipsometry (not shown here). Clearly, if the oxide layer is removed with the processes that will be described on the following sections, this layer will be absent.

Table 6.1: Different configurations of the composites.

For I-V measurements

Layer	Thickness (nm)
Ag front-contacts	250-290
PEDOT:PSS	120-140
SiO_x	1.5-1.9
Silicon wafer	(280-300)·10^3
Ag back-contacts	250-290

For PL-QSSPc

Layer	Thickness (nm)
PEDOT:PSS	120-140
SiO_x	1.5-1.9
Silicon wafer	(280-300)·10^3
Composite	120-140

6.1.3. DMSO vs EG

The first decision was whether to use DMSO or EG and observe if Triton X-100 modified the PEDOT:PSS properties. As a first step, mixtures with DMSO and EG adding Triton X-100 were prepared and deposited over silicon and glass to analyze their differences. It was observed that adding Triton X-100 improved the surface coverage. Absorbance spectra of the different layers coated onto glass substrates are shown in Fig.6.3(a), which was obtained from measurements of transmittance as the ones of Fig.6.3(b) and reflectance (not shown here). High transparency (around 90%) is observed in the visible spectral range, as an inset in Fig.6.3 for the three samples. As observed in Fig.6.3(b), the transmittance of the films were 86.23%, 87.58% and 85.14% for DMSO+Triton X-100, EG and EG+Triton X-100 at 550 nm, respectively. No major differences were observed using either EG or DMSO in the same weight percentage of 5% and Triton X-100 in 0.1% wt. We observe that

the use of Triton X-100 increases the absorption on the NIR range (DMSO) or VIS range (EG) Fig.6.3(b). The glass substrate spectrum did not show any absorbance on the visible range, see Fig.6.3(a). However, it shows a very similar spectrum on the NUV range. In this thesis and concerning solar cell applications, we will focus only on the VIS range.

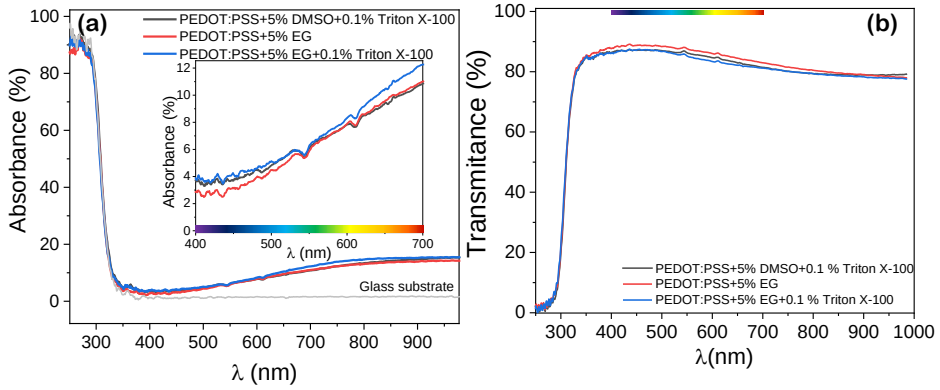

Fig. 6.3: (a) Absorption spectra of PEDOT:PSS with either DMSO+Triton X-100, EG or EG+Triton X-100, where inset shows detailed region on the visible range and (b) transmittance spectra of the same samples.

The optical bandgap of the three samples was calculated from the absorbance measurements shown in Fig.6.3(a) and represented on Fig.6.4(a) using the Tauc relation:

$$\alpha h\nu = A(h\nu - E_g)^n \tag{6.1}$$

where α is the absorption coefficient; ν is the frequency; h is the Plank's constant, A is a constant; E_g is the energy band gap and n is a parameter which can be $\frac{1}{2}$ if the transition is direct and allowed and 2 if the transition is indirect and allowed[241,242]. α can be calculated from $\alpha = \frac{2.303 \cdot A}{t}$ [243] where A is the absorbance of the film and t is the thickness. This allows to determine the optical band gap of the samples. Again, similar results around 3.6 eV are obtained for the three samples and summarized on Table 6.2, showing the lowest value for EG+Triton X-100 and DMSO+Triton X-100. This, alongside with the good coverage of the surfaces pushed the decision of using DMSO and Triton X-100.

To estimate the value of the refraction index $n(\lambda)$, equation 6.2 was used following the process used in different works[243,244]:

$$n(\lambda) = \left[\frac{4r}{(r-1)^2} - k^2\right]^{\frac{1}{2}} - \frac{r+1}{r-1} \quad \text{where} \quad k = \frac{\alpha\lambda}{4\pi} \tag{6.2}$$

Table 6.2: Calculated optical band gaps from PEDOT:PSS layers.

PEDOT:PSS samples	
Sample	**E_g (eV)**
DMSO+TRITON	3.59 ± 0.05
EG	3.60 ± 0.05
EG+TRITON	3.59 ± 0.05

where r and t are obtained from the dependent equations:

$$r = \frac{2R}{1 + t^2 + \sqrt{(1+t^2)^2 - 4t^2R(2-R)}} \quad \text{and} \quad t = \frac{2T}{(1-r)^2 + \sqrt{(1-r)^4 + 4T^2r^2}} \tag{6.3}$$

where n refers to the refraction index, R, and T are the values of reflectance and transmittance for each wavelength. The iterative method to solve these equations was implemented using Matlab R2019b.

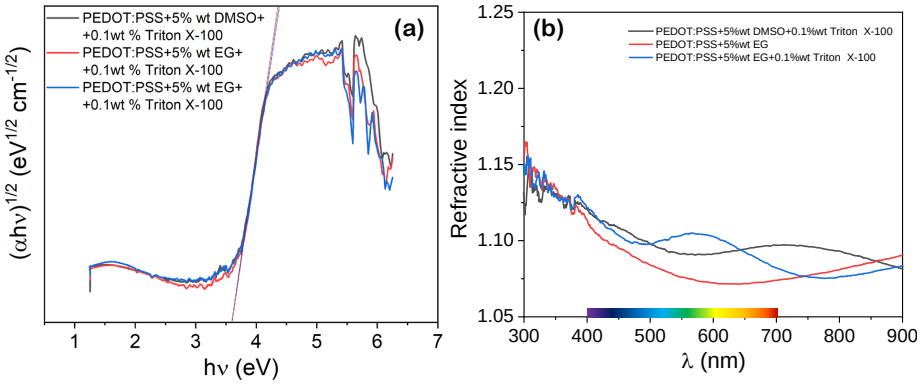

Fig. 6.4: (a) Tauc-plot obtained from the absorbance spectra and (b) simulated refractive index n(λ).

Fig.6.4(b) shows the simulated refractive index n(λ) of the different samples. PH1000 PEDOT:PSS refraction index has been reported between 1-1.6 depending on the characteristics of the PEDOT:PSS, the use of additives and the PEDOT:PSS ratio[245] (chapter 1).

From this time on, as pristine PEDOT:PSS is not considered for high efficiency solar cells, the mixture and process chosen is PEDOT:PSS+ 5% DMSO +0.1% Triton X-100, and these samples will be hereinafter referred to simply as PEDOT:PSS.

6.1.4. Etching vs no etching

The interface between Si/PEDOT:PSS is a matter of study for Si-passivation[22,62] as it plays a major role on its performance. To assess its influence on the passivation effects, the native oxide layer was etched and compared with the substrate without any etching. First, the silicon wafer was introduced into a mixture of HF and distilled water (1:8) during 30 s. Right after it was rinsed with water. A second step consists on the use of a solution of sulfuric acid (H_2SO_4) and hydrogen peroxide (H_2O_2) mixed into a beaker, commonly refereed as Piranha solution, with a ratio of 4:1 (1L of sulfuric acid per 250 mL of hydrogen peroxide). The reaction is strongly exothermic and abruptly rises to boiling temperature, a hot plate was used to maintain the temperature constant at 100°C. Each silicon wafer was introduced on the beaker for 30 min. Finally, it was rinsed with water and carefully dried with a flow of nitrogen gas.

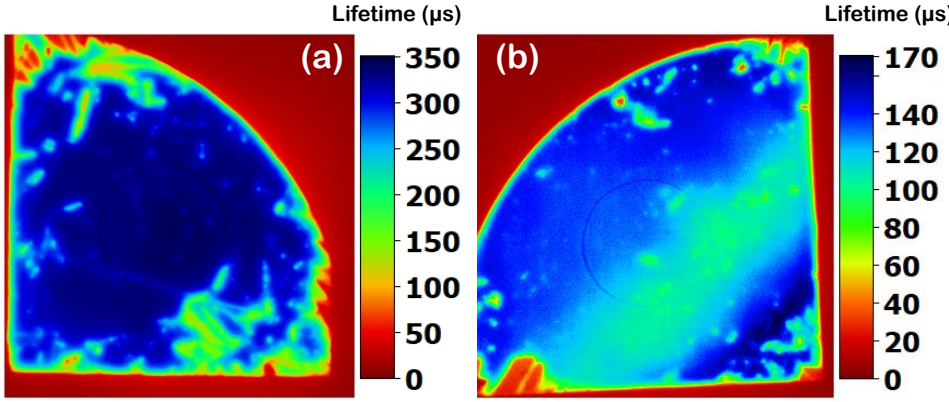

Fig. 6.5: PEDOT:PSS over FZ wafers PL-QSSPC of (a) untreated FZ-substrate and (b) Piranha-treated substrate. Note that the scale is different between the two images.

PL-QSSPC results for both PEDOT:PSS/nSi over FZ substrates without piranha treatment and with piranha treatment are shown on Fig.6.5(a) and (b) respectively. Color bars besides the PL images indicate the charge carrier lifetime values, which were calculated from the corresponding QSS-PC curves as a function of the injection level. It is important to point out that for measuring correct PL-QSSPC imaging, reflectance of each sample was measured at $\lambda = 808$ nm and used as a correction factor. As seen in Fig.6.5, lifetime strongly decreases from ∼300 μs to ∼150 μs with the removal of the native silicon oxide with Piranha treatment of the surface. This is an indicator that removing the oxide layer is not the best approach to obtain better silicon passivation as the native oxide appears to be more stable on the passivation effects leading to higher lifetime. It is important to mention that the position of the sample to be measured over the QSSPC coil may vary between each measurement. Other parameters such the ambient light or humidity could af-

fect the measurement. To avoid misunderstanding results, each measurement was repeated and the results presented are the best within the uncertainty inherent to these measurements.

6.1.5. Degradation over time

One of the main issues of the organic compounds is their stability over time and under certain conditions of humidity, temperature or irradiation among others. PEDOT:PSS is known to degrade in presence of humidity, temperature or oxidizing atmospheres[246,247]. This degradation is accompanied with a decrease of the conductivity and the charge carriers lifetime values.

Some of the samples which were spin-coated on FZ- Silicon substrates either with or without piranha treatment were stored at room temperature and laboratory conditions of humidity during the period of three months. During that time, PL-QSSPC measurements were performed.

As seen in Fig.6.6 lifetime values of both samples decrease during the period of three months. Fig.6.6(a) shows both the images of PL-QSSPC acquired during the day of the synthesis and up to 60 days for the sample without piranha pretreatment and 70 days for the sample with piranha treatment. On the right the pixels with the corresponding carrier lifetime values are presented as an histogram. Similarly, the results from the substrate treated with piranha are presented on Fig.6.6(b). Fig.6.6(c) shows a comparison between both samples as well as other similar sample of PEDOT:PSS/FZ without treatment over a longer period of time of 400 days, which has been also shown in our work[155]. Over this longer period it can be observed that lifetime values reach a steady value of ~ 75 μs, within the uncertainty of the measurement. Both samples (with or without treatment) show similar degradation over time following an exponential decrease over time.

In sight of these results, it was decided to not perform any etching of the silicon oxide. Not only it decreased the lifetime values of the charge carrier recombination, it is an additional hazardous step for obtaining these hybrid p-n junctions. Therefore, PEDOT:PSS/nSi from this time on refers to the previously higher-quality mixture of PEDOT:PSS+5% DMSO+0.1%Triton X-100 deposited over n-type FZ silicon without treatment of the surface previous to the deposition.

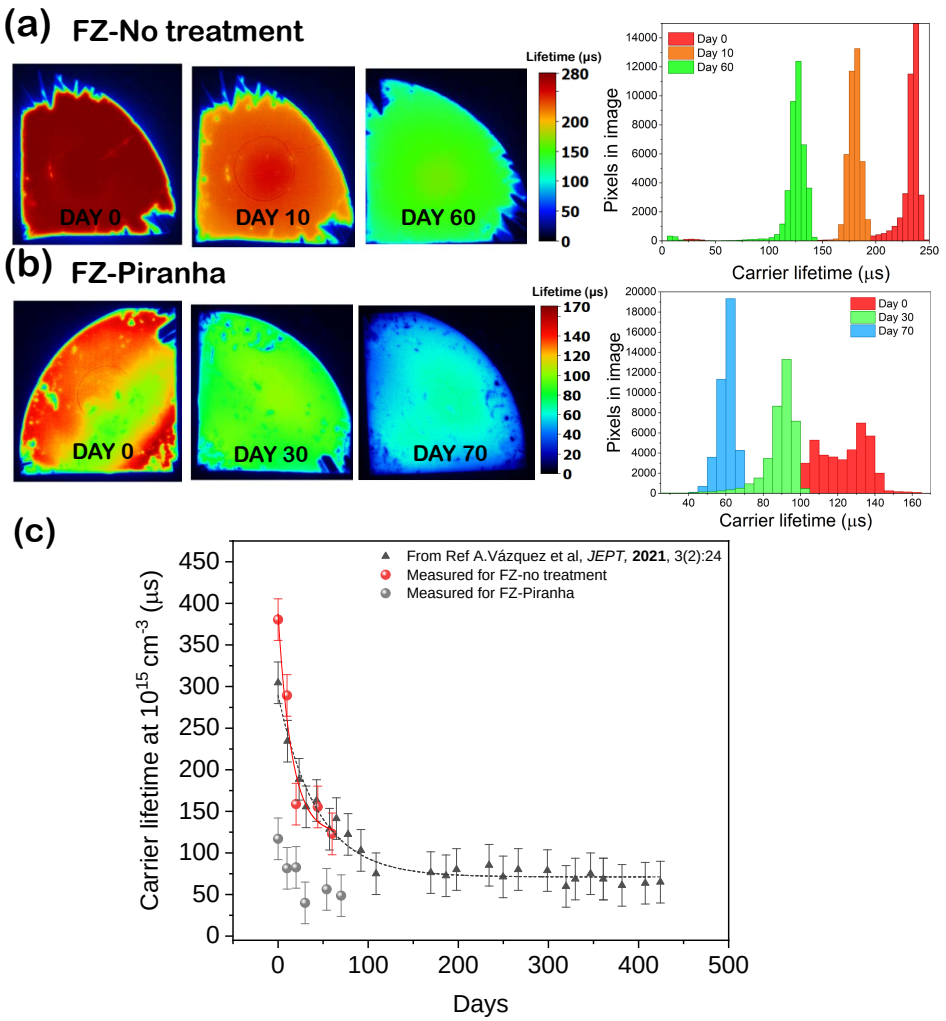

Fig. 6.6: PL-lifetimes degradation over time measured for an injection level of $\Delta n=10^{15}$ cm^{-3} corresponding to the samples deposited over FZ n-type Si (a) without treatment and (b) with Piranha treatment. On the right of both images an histogram corresponding to the distribution of pixels near the center of the sample. Figure (c) shows detailed lifetimes for each samples on different periods of time and as compared with[155] where lifetime of PEDOT:PSS/FZ-without treatment is measured over a time period of over 400 days.

6.2. Characterizing PEDOT:PSS thin layers

At this point, we have obtained PEDOT:PSS/nSi junctions with the highest lifetime values. For a more in-depth study of the PEDOT:PSS thin layers, morphology

and composition of these were also analyzed through the use of various techniques.

To assure compositional homogeneity of the spin coated PEDOT:PSS samples, EDS was performed. Low electron beam intensity and voltage were used (500pA-1nA, 10-12 kV) as PEDOT:PSS could be easily damaged under the electron beam irradiation.

There is clearly an homogeneous distribution of the different elements comprising PEDOT:PSS throughout the sample which indicates that the use of DMSO or Triton X-100 avoids the agglomeration of the different atomic species Fig.6.7. Table 6.3 shows the elemental quantitative analysis from EDS. Carbon is clearly overestimated as H is not measured with this technique. Normally PEDOT presents around 2% at H[248].

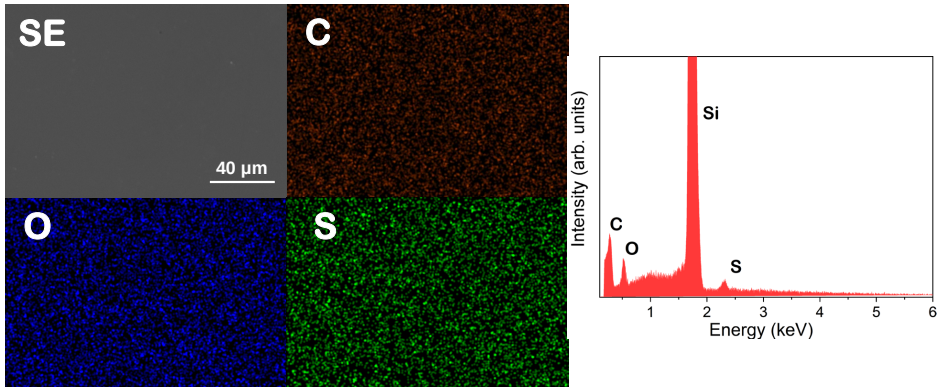

Fig. 6.7: EDS mapping of PEDOT:PSS/nSi with its corresponding element mappings labeled on each image (Secondary Electrons, Carbon, Oxygen and Sulfur). On the right the EDS spectrum of the sample is presented.

Table 6.3: Elemental quantification from EDS.

Element	% at
Sulfur	1.34 ±0.1
Carbon	69.99± 1.5
Oxygen	26.66 ± 0.9

An optical image corresponding to a PEDOT:PSS/nSi layer can be observed in Fig.6.8(a). The morphology observed is in agreement with previous works in which they attribute the observed topography to the conformation of PEDOT domains surrounded by insulating PSS chains. Fig.6.8(b) shows an AFM image showing surface homogeneity as well as a profile in Fig.6.8(c) corresponding to the line marked in Fig.6.8(b). Based on AFM profiles, a reduced average height of 2.3 nm is measured as a clear indicator of local sample homogeneity.

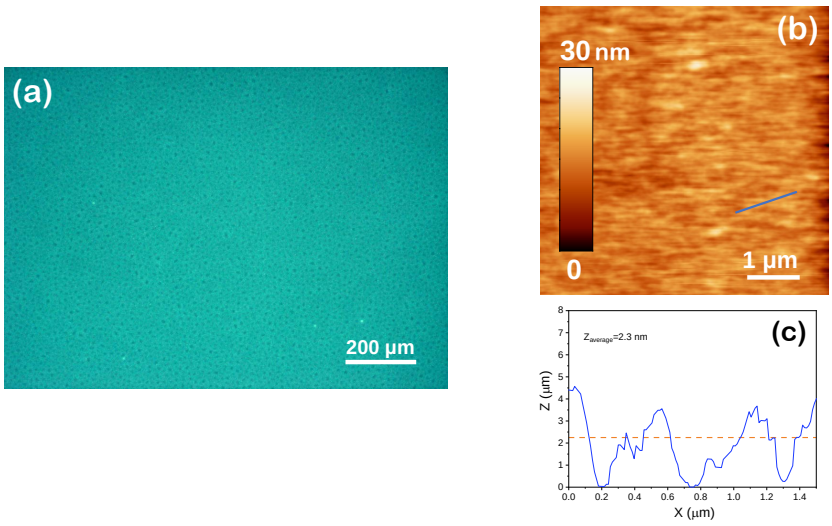

Fig. 6.8: (a) Image from PEDOT:PSS sample deposited over a glass substrate obtained with an optical microscope (b) AFM image of the same sample and (c) height profile image on the line marked in blue on image (b).

Electric measurements were also performed on these samples and are summarized on Table 6.4. PEDOT:PSS (with the additives) presents high carrier concentration and a high value of conductivity $\sim$ 189 S·cm^{-1} due to solvents addition.

Table 6.4: PEDOT:PSS Hall effect measurements performed with I = 0.1 mA.

Sample	Charge Carrier Concentration (cm^{-3})	Resistivity (Ω·cm)	Conductivity ($S \cdot cm^{-1}$)
PEDOT:PSS	$(7.37 \pm 1.38) \cdot 10^{21}$	$(5.30 \pm 0.03) \cdot 10^{-3}$	$(1.89 \pm 0.01) \cdot 10^{2}$

Raman spectra were acquired from PEDOT:PSS mixture deposited on Si, using as excitation source a red laser (λ = 633 nm), and different pinhole sizes of 200-900μm and a D_1 filter ($0.1 \cdot I_0$). The reason behind using different pinhole size, as well different filters, has been taken in order to obtain variable irradiation densities and collection of light to observe differences on the modes upon laser irradiation, besides to determine any possible the degradation induced by the laser as a function of time.

As shown in Fig.6.9(a) the complete set of Raman modes can be attributed to to PEDOT or PSS ionomers or to the Silicon substrate, as a Raman spectrum from bare Si is also shown in Fig.6.9 as a reference. Silicon Raman spectrum shows an intense peak peak at 520 cm^{-1} which corresponds to the transverse optical(TO)[249] mode, a broad peak which can be attributed to the longitudinal acoustic (LA) mode at 300 cm^{-1} and other broad peak at 920-1000 cm^{-1} attributed to Si-O bonds[249]

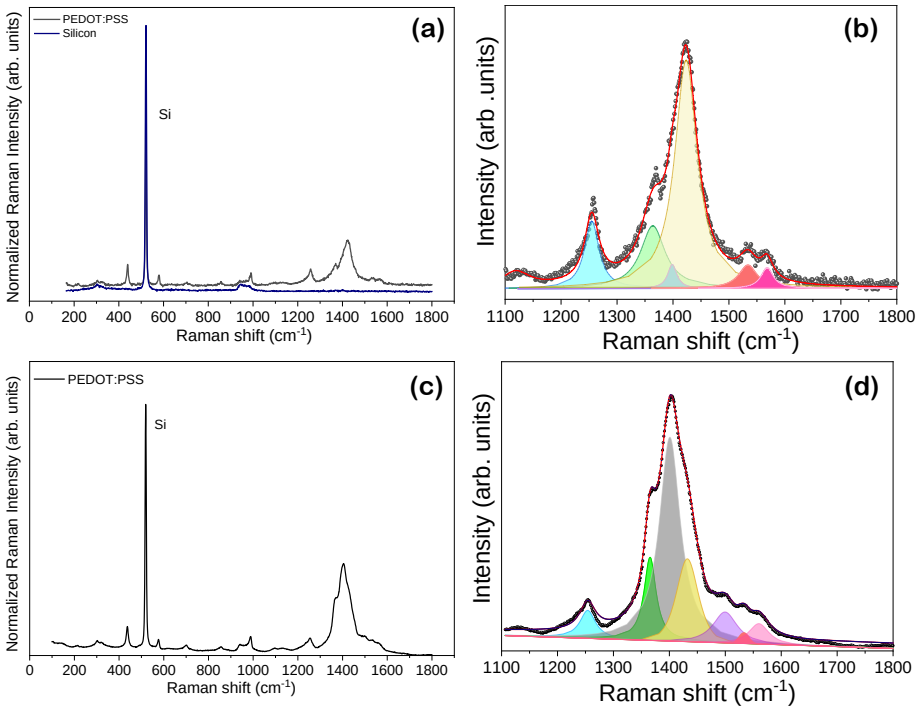

Fig. 6.9: Raman spectra of the PEDOT:PSS mixture and bare silicon substrate (n-type FZ) acquired with a red laser (λ =633 nm) and pinhole of (a) 200 μm or (c) 900 μm. Images (b) and (d) show deconvolutions to Gaussian-Lorentz functions of the region between 1200 cm^{-1} and 1800 cm^{-1} which correspond to images (a) or (c), respectively.

or to the second transverse optical phonon model (2TO)[250]. Remaining Raman modes, mostly attributed to PEDOT:PSS are listed on Table 6.5. Note that for most of the literature, the laser used for measuring PEDOT:PSS may vary, which explain shifts on the measured and literature values.

Fig.6.9(a) shows that the main modes of PEDOT:PSS measured with the red laser (λ=633 nm) and pinhole of 200 μm, are concentrated on the region between 1000 cm^{-1} and 1800 (shown in Fig.6.9(b). Outside of this region modes are observed $\sim$ 439 cm^{-1}, $\sim$ 578 cm^{-1}, $\sim$ 706 cm^{-1}, $\sim$ 855 cm^{-1}, $\sim$ 988 cm^{-1} which are at the same positions using pinhole size of 900 μm, which is shown on Fig.6.9(c). The positions of the observed modes using the pinhole of 200 μm or 900 μm are summarized on Table 6.5. Modes on the region of 1000-1800 cm^{-1} are sensitive to pinhole size as it can be clearly observed on inset on Fig.6.9(b)-(d), as they vary in position up to $\sim$ 9 cm^{-1}. The most notable difference among both spectra is that the main contribution using pinhole 200 μm was peaked at 1420 cm^{-1} (yellow) with a subtle contribution at 1400 cm^{-1} (grey) and for 900 μm the main contribution is

placed at 1400 cm^{-1} whereas the other maxima appears as a shoulder appears at ∼1430 cm^{-1} and, most notably, a new contribution is observed at 1500 cm^{-1}.

Table 6.5: Raman modes of PEDOT:PSS mixture between 1200 and 1800 cm^{-1} observed with the VIS red laser ($\lambda = 633$) nm where (†) represents measurements obtained with a pinhole and 200 μm and (‡) represents pinhole of 900 μm. Position of the vibrational modes reprinted from the scientific literature are shown for comparison, which were acquired with wavelengths of ($\lambda = 632$ nm, He-Ne laser)[251,252], 532 nm[253], 785 nm[254] or unspecified[68].

Wavenumber cm^{-1}		
This work	**Literature**	**Attributed origin**
578	578[254]	PEDOT Oxyethylene ring deformation
706	699[254]	PEDOT Symmetric C–S–C deformation
988	988[254]	PEDOT Oxyethylene ring deformation
1120†,1111‡	1097[254],1100[68]	PEDOT C–O–C deformation or PSS
1257†, 1254‡	1269[253],1253[68], 1270[251]	C_α-$C_{\alpha'}$ interring stretching,C_β-H bending
1363†,1365‡	1368,1369,1366, 1370[68,238,251,253]	single C_β-C_β stretching
1400†,‡	-	associated with C_α=C_β
1424†, 1429‡	1424[253],1431[254],1435[68]	C_α=C_β symmetric stretching vibrations
1499‡	1508[238],1504[252], 1490[68]	C_α=C_β symmetric stretching vibration
1534†, 1530‡	1530[251],1532[68],1540[238]	arises from the splitting of the C_α=C_β asymmetric vibrations
1568†, 1561‡	1568[238,252],14576[253]	C_α=C_β asymmetric stretching vibration

PEDOT:PSS/nSi samples were also measured using the UV laser ($\lambda = 325$ nm). It was observed a rapid degradation of the samples due to the irradiation which is shown in Fig.6.10(a). This rapid decrease on the Raman relative intensity was monitored by measuring the decrease of the Raman modes most notably for the mode ∼ 1608 cm^{-1} for each of the available laser energy densities as shown in Fig.6.10(b). Note that the Raman spectra observed in Fig.6.10(a) due to the UV irradiation is very different from the Raman spectra shown until this moment, due to the use of the different excitation source. With this irradiation source, main Raman modes are observed at ∼1370, 1452 and 1608 cm^{-1}.

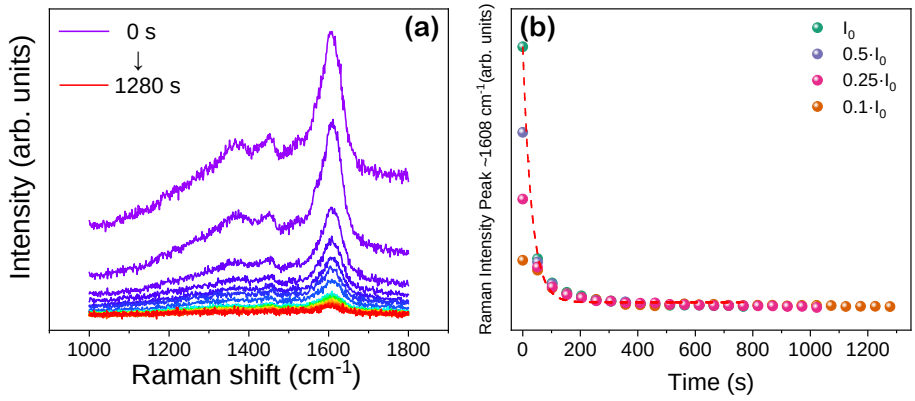

Fig. 6.10: (a) Quenching of the Raman spectra acquired with the UV laser (λ=325 nm) with pinhole of 200 μm using different laser irradiation energies (0.1, 0.25, 0.5 and I_0) over exposure time, (b) Decrease of the relative intensity of the peak at ~1608 cm^{-1} using different laser irradiation energies (0.1, 0.25, 0.5 and I_0) over exposure time.

Similarly, Raman was acquired after the irradiation but this time with the VIS laser as it possesses more well-defined Raman modes for PEDOT:PSS. In this case, as shown on the inset on Fig.6.11(b), different spots were irradiated using the UV laser with each energy density (from upper row left to right 0.1, 0.25, 0.5 and I_0 and viceversa for the second row) during 8 s and acquired with the VIS laser and pinhole of 900 μm, which Raman spectra is depicted in Fig.6.11(a). As observed with short UV irradiation some of the modes (mainly those situated at ~1499, 1530 cm^{-1}) increase their relative intensity.

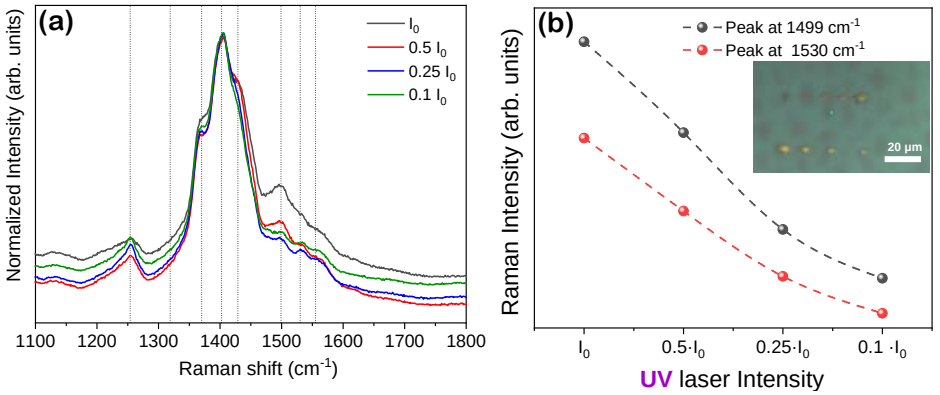

Fig. 6.11: (a) Raman spectra acquired with the VIS laser (λ=633 nm) after short time UV laser (λ=325 nm) irradiation with the different UV laser intensities. (b) Increase upon laser irradiation intensity on the relative intensity of the peaks at ∼1499, 1530 cm^{-1} due to UV irradiation with variable irradiation energies acquired with the VIS red laser and pinhole of 900 μm. Inset shows optical image from the irradiated spots.

6.3. PEDOT:PSS composites with SnO, SnO_2 or TiO_2 nanoparticles.

After the previous study of the bare PEDOT:PSS films, the optimal composition was selected. Thus, in this section nanoparticles were added to the organic mixture in order to fabricate hybrid composites as shown in Fig.2.4. From the previous section, we have concluded that the best results were obtained using non-treated FZ n-type silicon wafers with a thermal treatment at 120°C for 15 min.

The procedure to add the nanoparticles and conform the composite consisted on adding the desired quantity of the nanoparticles (mostly in 1% wt, while for some of the composites 0.5% wt or 2% wt were also used) respect to the mixture of the PEDOT:PSS and organic solvents described for the bare PEDOT:PSS. Different approaches were considered obtaining the best results by introducing the vessel with the PEDOT:PSS mixture and the nanoparticles into an ultrasonic bath for 15-20 min and subsequently, using an ultrasonic probe during ∼1 min with ultrasonic pulses dispersing the nanoparticles (10% power to avoid PEDOT:PSS damage).

6.3.1. PEDOT:PSS and SnO composites

The SnO nanoparticles used were described previously in chapter 1 and chapter 5. Fig.6.12 represents the composites with the nanoparticles. Firstly, the effect of incorporating SnO nanoparticles was studied, as this material has not been studied embedded into PEDOT:PSS polymer for these applications.

Composition of the composite was observed via EDS as shown in Fig.6.13. According to the chemical mapping acquired with the Sn signal, SnO nanopowders

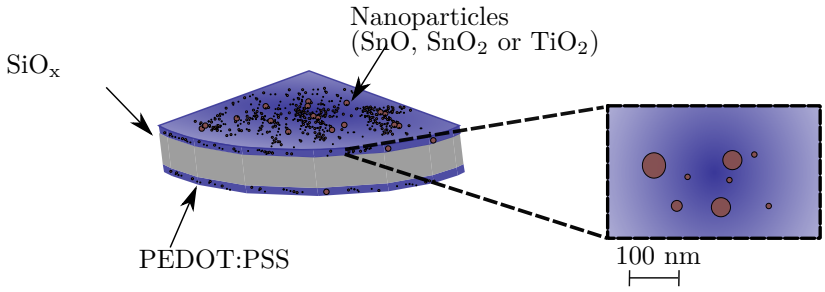

Fig. 6.12: Representation of the composites with nanoparticles. As observed, there is a certain size dispersion of nanoparticles in the sample.

were spin-coated homogeneously over the substrate. Variable agglomerate sizes can be observed from μm to dozens of nm.

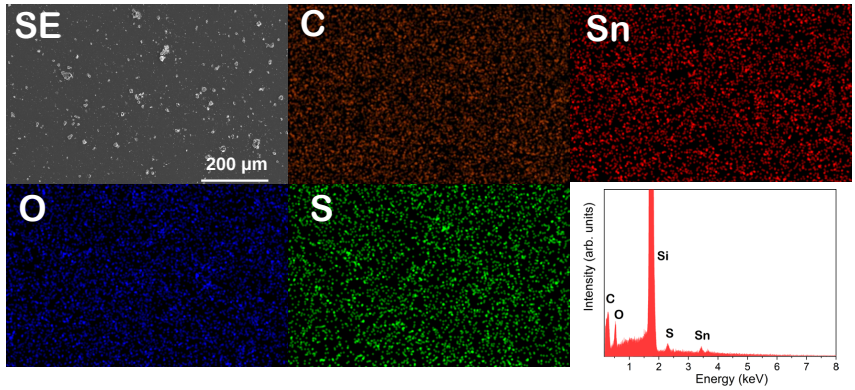

Fig. 6.13: EDS mapping of PEDOT:PSS+SnO with the corresponding element mappings labeled on each image (SE: Secondary Electrons, C: Carbon, Sn: Tin, O: Oxygen and S: Sulfur). A representative EDS spectrum of the sample is also shown.

Raman spectra from the hybrid composite acquired with the VIS laser and variable laser intensity are shown in Fig.6.14(a). The characteristic peaks in the region between 1100-1800 cm^{-1} are observed at the same positions that for PEDOT:PSS layers, with higher relative intensity which may be related to the deposition of a thicker layer. Inset shows detailed region with higher acquisition time (20 times) in which we can observe the characteristic modes corresponding to SnO, B_{1g} (or E_g) and A_{1g}, showing the presence of the SnO nanopowders in the sample.

Contrary to the results from PEDOT:PSS, the Raman spectra of PEDOT:PSS+ 1% wt SnO nanoparticles shown in Fig.6.14(b) exhibit no remarkable variations on the Raman signal as a function of the UV laser irradiation intensity, contrary to the changes described for bare PEDOT:PSS as show in the inset of Fig.6.14(b), which demonstrates the improved stability of the polymer under UV illumination

by adding SnO nanoparticles. It should be considered that UV irradiation could promote SnO oxidation to SnO_2. However, peaks from SnO_2 were not observed after UV illumination, which can be related to the fact that the PEDOT:PSS matrix prevents SnO oxidation to SnO_2. The addition of SnO nanoparticles, even in a low concentration (1% wt.), induces slight variations in the Raman signal from the hybrid composite in comparison with bare PEDOT:PSS, as shown in the inset of Fig.6.14(b). Some other authors also reported changes in the properties of the polymer by adding low amounts of nanoparticles[255].

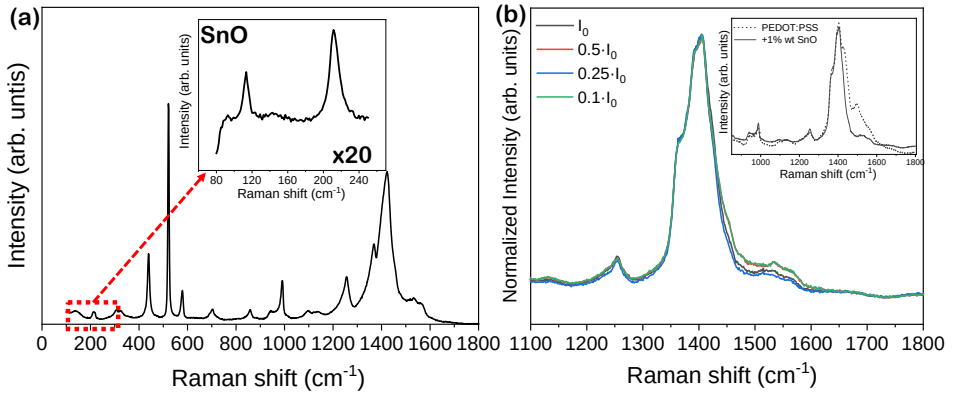

Fig. 6.14: (a) Raman spectrum acquired with the VIS laser corresponding to SnO composites. Inset shows detailed region between 80-240 cm^{-1} acquired during a longer period of time (b) Raman spectra acquired with the VIS laser after irradiation with the UV laser with the different irradiation energies (0.1, 0.25, 0.5 or I_0). Inset shows Raman spectra from bare PEDOT:PSS and SnO composite after UV irradiation with I_0.

A clear decrease in the relative intensity of the vibrational modes at 1430 cm^{-1}, 1500 cm^{-1}, and 1540 cm^{-1} that after UV irradiation for the PEDOT:PSS composite were enhanced, can be distinguished in the SnO composite, which can be due to structural changes in the polymer related to interactions between the polymer and the SnO nanoparticles. Actually, some authors propose conformational changes in the polymer coils due to electrostatic interactions with embedded nanoparticles showing charged surfaces[26]. These changes can affect the vibrations of specific functional groups, which leads to variations in the Raman signal.

Electrical characterization of the samples was performed by Hall effect measurements. Averaged values of charge carrier concentration, resistivity, and conductivity are shown in Table 6.6. Bare PEDOT:PSS shows good p-type conductivity with averaged values of 1.9 $\cdot 10^2$ $S \cdot cm^{-1}$, similar to Data Sheet results provided by the manufacturer taking into account a 5% addition of DMSO, in our case due to the addition of DMSO and Triton-X-100. Hybrid SnO composite exhibits improved conductivity as compared with the bare polymer, reaching averaged values of about 6.3 $\cdot 10^2$ $S \cdot cm^{-1}$ and high charge carrier concentration values around 1.4

$\cdot 10^{22}$ cm^{-3}.

Table 6.6: SnO, PEDOT:PSS and PEDOT:PSS+SnO Hall effect measurements performed with I=0.1 mA.

Sample	Charge Carrier Concentration (cm^{-3})	Resistivity (Ωcm)	Conductivity ($S \cdot cm^{-1}$)
SnO	$(2.98 \pm 0.66) \cdot 10^{15}$	$(5.49 \pm 0.12) \cdot 10^{1}$	$(1.82 \pm 0.21) \cdot 10^{-2}$
PEDOT:PSS	$(7.37 \pm 1.38) \cdot 10^{21}$	$(5.30 \pm 0.03) \cdot 10^{-3}$	$(1.89 \pm 0.01) \cdot 10^{2}$
PEDOT:PSS+1% wt SnO	$(1.41 \pm 0.27) \cdot 10^{22}$	$(1.58 \pm 0.02) \cdot 10^{-3}$	$(6.33 \pm 0.01) \cdot 10^{2}$

PL imaging and QSS-PC values of charge photocarrier lifetimes were also analyzed. Fig.6.16(a) shows PL images from the tested samples, where color bars indicate charge carrier lifetime values (τ) in μs. The corresponding QSS-PC curves under an injection level of $10^{15}cm^{-3}$ are included on Fig.6.16(b). Averaged carrier lifetime value around 410 μs was estimated for bare PEDOT:PSS, while the hybrid composite shows slightly lower, but still good, lifetime value around 297 μs. The hybrid composite shows good transparency in the visible range and a slight improvement of the absorption in the range 350–450 nm, as compared with bare PEDOT:PSS, due to the addition of SnO nanoparticles, see Fig.6.16(c). The wide optical band gap from SnO can explain the slightly improved absorption in the hybrid composite.

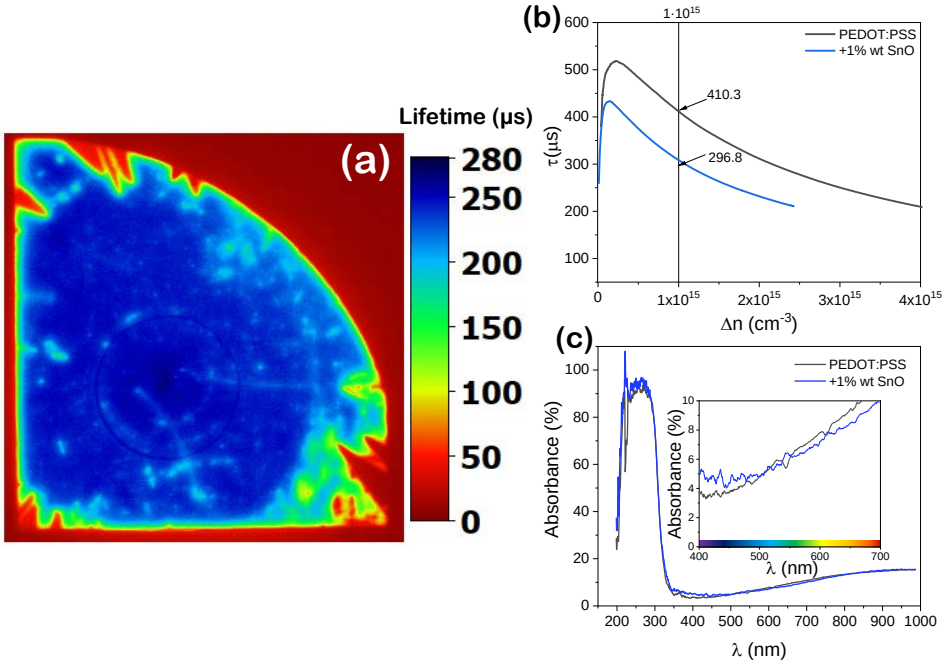

Fig. 6.15: (a) PL-QSSPC imaging of SnO composite and (b) the corresponding QSSPC curve and (c) absorption spectra of the samples. Inset shows detailed region on the visible range. QSSPC and absorption data include spectra from PEDOT:PSS for comparison.

6.3.2. PEDOT:PSS and SnO_2 composites

SnO_2 composites were as well fabricated following the same procedure described for the SnO composites, by adding the SnO_2 nanoparticles, in this case with variable weight percentages: 0.5, 1 or 2% wt, to observe changes due to nanoparticles percentages.

PL-QSSPC images show a decrease of the carrier lifetime Fig.6.16(a)-(c). This behavior is clearly observed in the QSSPC curves in Fig.6.16(d). When SnO_2 nanoparticles were added to the composites actually lower passivation behavior was observed as the concentration of SnO_2 increases. Despite this drawback, UV-VIS shows good transparency to visible light Fig.6.16(e) where the addition of 2% presents lower absorption in the high VIS range and higher on the NIR which differs with 0.5% as it presents the opposite behavior. Adding 1% wt of SnO_2 shows similar absorbance compared with PEDOT:PSS.

Hall effect measurements of the composites with SnO_2 shows that both conductivity and charge carrier concentration are increased with the addition of SnO_2 (Table 6.7). Precisely, the charge carrier concentration is slightly decreased with 0.5%wt but it within the high uncertainty values from bare PEDOT:PSS composites. Addition of SnO_2 in 1 or 2% wt percent increases the carrier concentration

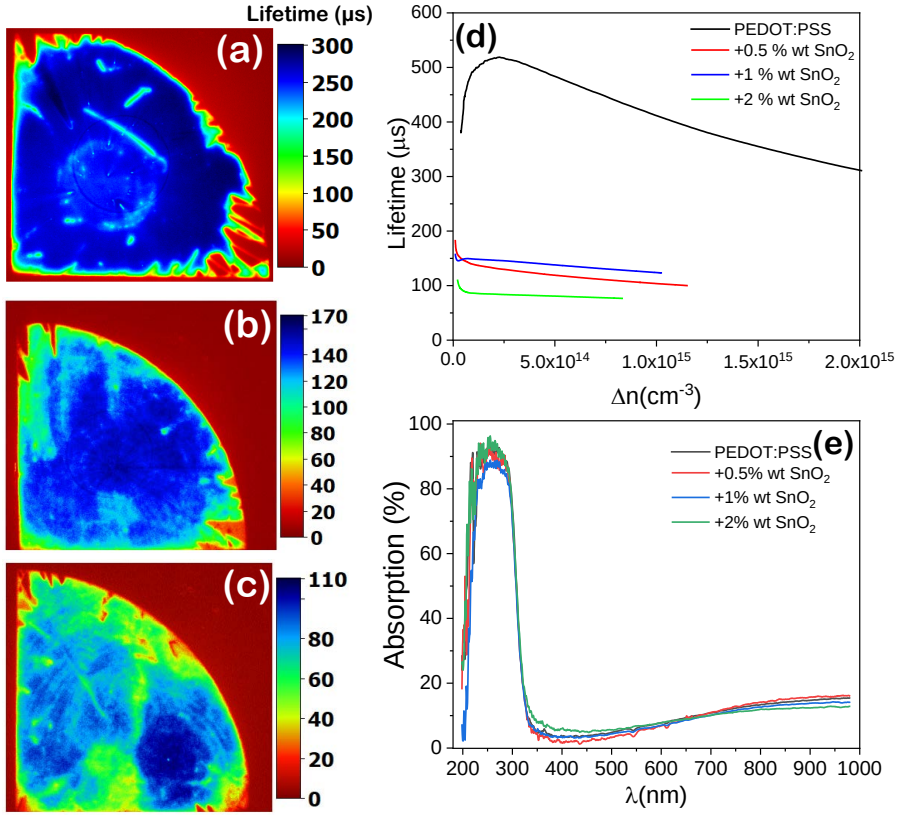

Fig. 6.16: PL-QSSPC images of the SnO_2 with (a) 0.5%wt (b) 1%wt (c) 2%wt composites (d) its corresponding QSSPC curve (e) UV-VIS spectra.

up to 10^{22} cm^{-3}. Conductivity values increases with the addition of SnO_2. The highest conductivity value was achieved for 0.5% wt which is almost 5 times higher than without the addition of nanoparticles.

Table 6.7: PEDOT:PSS+SnO_2 nanoparticles in different concentrations Hall effect measurements performed with I=0.1 mA.

Sample	Charge Carrier Concentration (cm^{-3})	Conductivity ($S \cdot cm^{-1}$)
PEDOT:PSS	$(7.37 \pm 1.38) \cdot 10^{21}$	$(1.89 \pm 0.01) \cdot 10^{2}$
PEDOT:PSS + 0.5 %wt SnO_2	$(5.79 \pm 0.78) \cdot 10^{21}$	$(8.47 \pm 0.01) \cdot 10^{2}$
PEDOT:PSS + 1 %wt SnO_2	$(1.41 \pm 0.27) \cdot 10^{22}$	$(6.33 \pm 0.01) \cdot 10^{2}$
PEDOT:PSS + 2 %wt SnO_2	$(3.22 \pm 0.56) \cdot 10^{22}$	$(7.84 \pm 0.01) \cdot 10^{2}$

6.3.3. PEDOT:PSS and TiO_2 composites

The addition of anatase TiO_2 nanoparticles was carried out following the same procedure than previously reported in this thesis. The percentage of nanoparticles (0.5, 1 or 2 %wt) was added to the vessel of the mixture and introduced to an ultrasonic bath 20 min (slightly more time than SnO nanoparticles) as these nanoparticles were more difficult to disperse. Then it was placed on an ultrasonic probe 1 min with less than 10% power. Finally it deposited over FZ silicon on both sides (for PL-QSSPC measurements) and over glass (For Hall effect and absorption measurements).

EDS mappings shows that TiO_2 is homogeneously distributed throughout the sample. In this case the size of different particle agglomerates are similar and about a dozen of nm. The presence of Ti on the sample is further confirmed with the EDS spectrum shown in Fig.6.17.

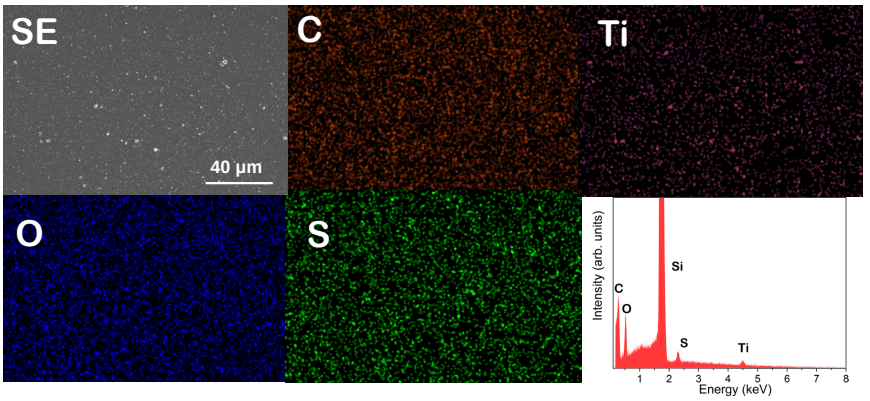

Fig. 6.17: EDS mapping of PEDOT:PSS+TiO_2 with its corresponding element mappings labeled on each image (SE: Secondary Electrons, C: Carbon, Ti: Titanium, O:Oxygen and S: Sulfur). On the right a representative EDS spectrum of the sample is shown.

Table 6.8 shows Hall effect results acquired with I=0.1 mA. Higher concentration of nanoparticles increases the carrier density up to 10^{22} cm^{-3} as well as the composite conductivity, with the highest value observed for 2% wt however this composite shows the lowest charge carrier concentration as compared to the composites including Sn based compounds.

PL-QSSPC images and QSSPC injection curve are observed on Fig.6.18(a)-(d). High carrier lifetimes around 0.5 ms were obtained with the addition of DMSO and Triton X-100 to the PEDOT:PSS for an injection level of $0.5{\cdot}10^{15}$ cm^{-3}. This lifetime value can be slightly increased (τ ~520 μs) for the composites with TiO_2 nanoparticles in 0.5 wt%, which also improves the conductivity of the composite (Table 6.8). However even higher concentrations of nanoparticles decreases the averaged lifetime values (τ ~400 μs).

Table 6.8: PEDOT:PSS+TiO_2 nanoparticles in different concentrations Hall effect measurements performed with I=0.1 mA.

Sample	Charge Carrier Concentration (cm^{-3})	Conductivity ($S \cdot cm^{-1}$)
PEDOT:PSS	$(7.37 \pm 1.38) \cdot 10^{21}$	$(1.89 \pm 0.01) \cdot 10^{2}$
PEDOT:PSS + 0.5 %wt TiO_2	$(2.99 \pm 0.71) \cdot 10^{21}$	$(2.33 \pm 0.03) \cdot 10^{2}$
PEDOT:PSS + 1 %wt TiO_2	$(1.24 \pm 0.38) \cdot 10^{21}$	$(1.92 \pm 0.05) \cdot 10^{2}$
PEDOT:PSS + 2 %wt TiO_2	$(1.30 \pm 0.49) \cdot 10^{22}$	$(4.39 \pm 0.03) \cdot 10^{2}$

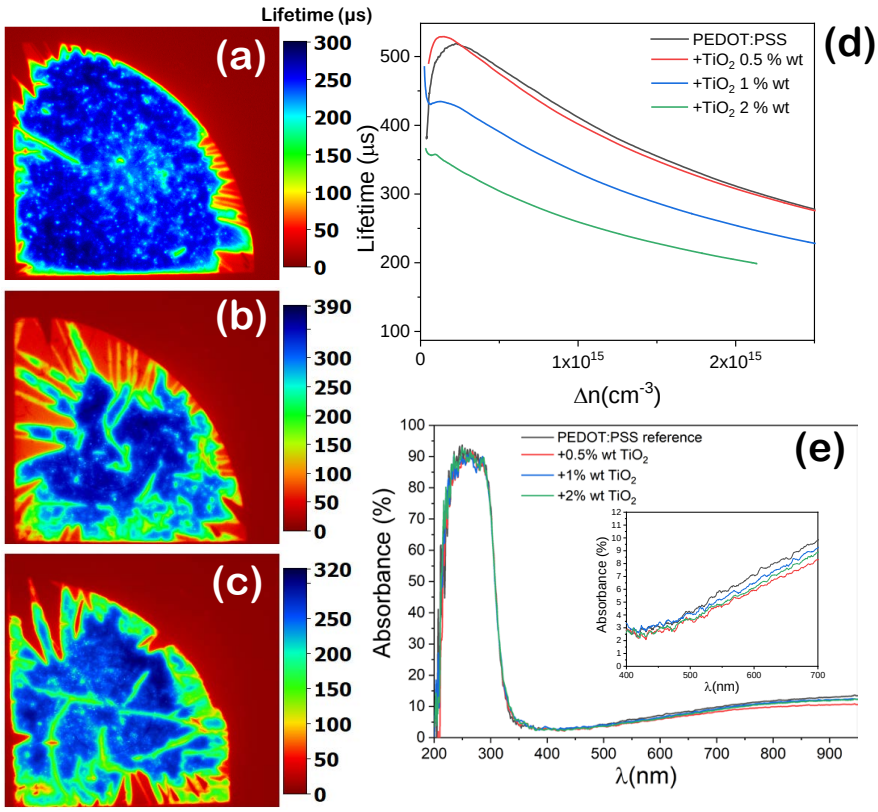

Fig. 6.18: PLQSSPC images of TiO_2 composites with different weight percentages (a) 0.5% wt, (b) 1% and (c) 2% and (d) its corresponding QSSPC curves and (e) shows absorption spectra of the TiO_2 composites where inset shows detailed region of the visible range.

6.3.4. IV- curves

Current-voltage (I-V) measurements are a relevant tool for solar cell characterization. Dark IV examines the diode-like properties without any light contribution

to determine the rectification behavior expected on a solar cell p-n junction. I–V curves were obtained with a Keithley 4200 Semiconductor characterization system.

Illumination results were obtained under standard test conditions, i.e irradiance on the solar cell is 1000W/m^2 with a spectrum resembling AM1.5 and the solar cell kept at a constant temperature of 25°C.

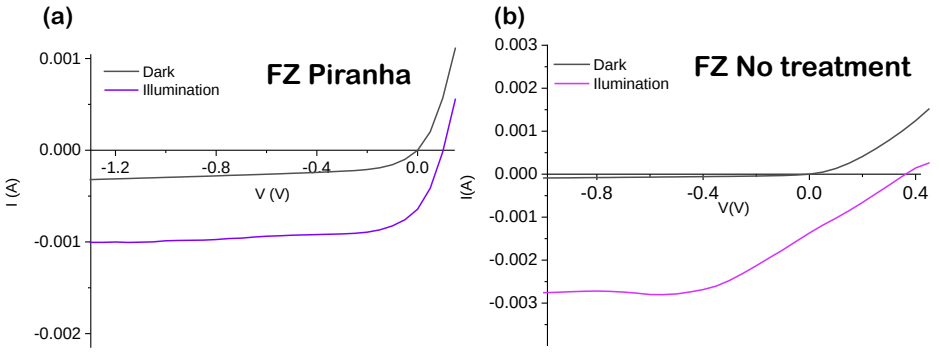

Fig. 6.19: I-V Curves corresponding to PEDOT:PSS samples (a) treated with Piranha (b) non-treated.

Fig.6.19 shows the comparison of the I-V curves between Piranha treated and untreated FZ substrates. Si substrates without etching posses V_{oc}=0.365 V and I_{sc}=1.35 mA whereas piranha treated substrates leads to values of I_{sc}= 0.652 mA V_{oc}=0.104 V with similar FF of 33%.

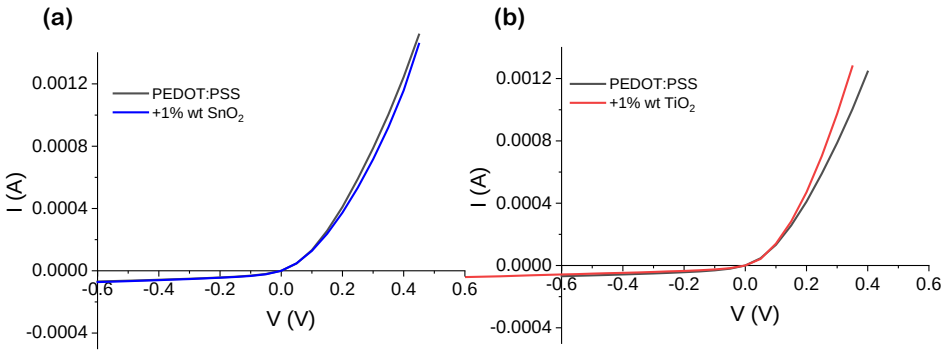

Fig. 6.20: I-V Curves corresponding to PEDOT:PSS with 1% wt of (a) SnO_2 or (b) TiO_2.

Dark IV curves of some representative samples are observed in Fig.6.20. The use

of undoped TiO_2 or SnO_2 samples preserves the diode behavior of the composites.

6.4. Discussion

Photovoltaic material technologies have grown non-stop over the last 50 years. Actually, solar cell technologies currently at the 4th generation, are also known as inorganics in organics, which combines the low cost/flexibility of polymer thin films with the stability of novel inorganic nanostructures[21]. Among this generation, hybrid silicon solar cells, which combine silicon and organic material, stand out as remarkable technology. Silicon technologies have been dominating PV market (1st and 2nd generation) since the past second half century, so it is a reasonable idea aiming to combine organic materials with silicon, which can bring properties inherent to organics (flexibility, light weight, low cost, transparency). The use of organic polymers could overcome some of the issues of traditional P-V technologies[28]. This is because the combination of inorganic materials such as Si with organic materials, involves advantages of large-area process ability, leads to low-assembly temperatures and competitive prices.

This chapter deals with the ideas of fabricating organic/inorganic composites and the search for enhancement of silicon passivation to obtain hybrid-Si improved solar cells. The main idea behind passivation is that in solar cells and especially for silicon-based technologies, one on the main factors which limits the efficiency is the carrier recombination, where the generated electrons and holes by the photoelectric effect may recombine before they can be collected and contribute to the photogenerated current. There are mostly three types of recombination on a bulk semiconductor: radiative recombination, Auger recombinations and Shockley–Read–Hall (SRH) through defect recombination. However, when reducing the cell thickness surface passivation arises as a main contributor to the loss of photogenerated current. This is due to the abrupt end of the atomic lattice at the surface, which introduces band gap defect levels. Those surface states may enhance the electron hole recombination affecting the other mentioned recombination transitions. The total recombination is given by the sum of the different transitions $U_b = U_{rad} + U_{Aug} + U_{SRH}$, which correspond to a life time values as seen in 6.4:

$$\frac{1}{\tau_{bulk}} = \frac{1}{\tau_{rad}} + \frac{1}{\tau_{Aug}} + \frac{1}{\tau_{SRH}} \rightarrow \frac{1}{\tau_{eff}} = \frac{1}{\tau_{bulk}} + \frac{1}{\tau_{surf}} \tag{6.4}$$

In the case of silicon, τ_{rad} is often neglected and Auger recombination is only considered when there is a strong dependence of doping and defects.

The recombination process could happen on bulk and on the two surfaces, therefore we can rewrite Equation 6.4, for a thin cell:

$$\frac{1}{\tau_{eff}} = \frac{1}{\tau_{bulk}} + \frac{2S}{W} \tag{6.5}$$

Where W is the sample thickness and S is Surface recombination Velocity (SRV), which equals the surface recombination rate (U_s) divided by the excess carrier concentration at the surface (Δn_s), $\sim 1/\tau_{surf}$. Hence, what is going to be referred as

passivation consists on different methods to reduce the presence of surface states. There are two main strategies to pursuit this objective: chemical passivation and field-effect passivation. As the recombination rate is proportional to the interface defect density one can reduce the number of defects at the interface to enhance passivation. This is achieved by chemistry methods such the growth/removal of a native oxide layer by chemical etching, which reduce the number of states i.e the number of unsaturated Si bonds with atomic O or H of the material. In this work, we have seen that removing the oxide layer with HF has a clear impact on the passivation. In our recent work,[155] we have reported that the best approach is not only, as considered in this thesis, to maintain the native oxide layer, instead it has been observed that growing a thicker oxide layer after the removal is more effective, which has been supported by other authors with controlled growth of SiO_x[256], Al_2O_3 or the addition of different compound such as sorbitol[257]. The most common materials for surface passivation of silicon, especially c-Si, are not only SiO_x or Al_2O_3 which are indeed the most recent materials to get attention as passivation layers, as the most well known are a-SiN_x:H or a-Si:H. Silicon nitride is the most important film passivator as it presents a tunable refractive index, good chemical stability and a large charge density suitable for passivation. However, its main drawback is not only a low effective SRV of 4 cm/s, but also its synthesis by expensive methods such as Plasma-Enhanced Chemical Vapor Deposition (PECVD), similarly to amorphous silicon which is deposited using rather low temperatures 200-300°C but by the same PECVD method[86]. Field-effect passivation consists on the reduction of the concentration of the charge carrier at the interface by applying an internal field. This field is often obtained by doping or by the presence of a dielectric layer. A review on the different mechanisms of passivation on bulk defect in silicon can be found in[258].

In the literature it has been pointed out that PEDOT:PSS is a good pasivation layer for Si[28,62,258–260]. Chen at al.[259] demonstrated that the passivation of the Si surface is mostly due to the oxidation at the PSS/Si interface which can be controlled by electron transfer. This effect is further impulsed by light, where electron-hole pairs are created and separated by the internal electric field which transport the holes to the PEDOT:PSS/nSi interface reducing defect states and increasing minority carrier lifetime. Oxygen and humidity could also diffuse throughout the material and led to an oxidize Si surface. PEDOT:PSS/nSi form a p-n junction dominated by the diffusion of minority charge carriers[22,62]. Jäckle et al.[62] reported that using a passitavion layer based on silicon (a-Si) for PEDOT:PSS mono-crystalline n-type silicon (c-Si) solar cells, increased power conversion efficiencies up to 14.8% with high open-circuit voltages exceeding 660 mV. But not only the results of PEDOT:PSS as a passivation layer of silicon are remarkable, also PEDOT:PSS possesses p-type electrical conductivity and good procesability which can establish a good anti-reflectant VIS transparet coating. These properties and its chemical stability can be improved with the addition of dopants.

PEDOT:PSS, as discussed on section 1.5, has been used as HTL in PeSC or transparent electrode in PSC. In particular, recent studies show remarkable results

on the field of hybrid silicon solar cells[28,261], reaching efficiencies up to 14.8%[62]. PEDOT:PSS has reached even higher efficiencies used as back contact in Si-solar cells what is called Back-PEDOT concept surpassing the limit of 20%[260] and showing V_{oc} values up to 663 mV. One of the main advantages is that PEDOT:PSS can be dispersed in water what allows low-expensive methods to deposit cheaply over large area surfaces such as spin coating, which differs with of other methods such as Plasma Vapor Deposition (PVD) or CVD.

Still, even reaching efficiencies close to 18%, there are mechanism which can push the boundaries of high efficiency such as different devices structures, surface texturing, interlayer engineering, secondary doping and composite formation[28]. However, PEDOT:PSS exhibits low electrical conductivity, besides its degradation under certain conditions of temperature or irradiation, which limits its applicability. To enhance its conductivity, many efforts have been made so far. In this thesis we have studied both the secondary doping and the composite formation, via the addition of organic solvents such as DMSO[68,238,239] and EG[243], which are the most commonly employed, among many others[26,252]. These compounds improved the quality of the deposited layer as well as enhanced its electrical properties. It is fair to say that this has been established as a primary method to improve PEDOT:PSS conductivity. Nonetheless, many other compounds have been used such as DiEthylene Glycol (DEG), sorbitol as well as different approaches based on the treatment of the film via immersion on the aforementioned solvents rather than the addition of the compound on the mixture,[26] and treatments with different acids[262]. Some reports also use a two-step process of addition of the solvent and a post-treatment afterwards[263]. The effect of DMSO on the PEDOT:PSS is attributed to the removal of excess PSS which facilitates a phase separation leaving conductive PEDOT:PSS grains behind, reducing the layer thickness[22]. Also these solvents are believed to reduce the ionic interaction between PEDOT and PSS, which facilitates phase separation as well as a conformational change of PEDOT from benzoid to quinoid and increasing crystalline packing.

Our findings over the particular FZ-100 Silicon and PH1000-PEDOT:PSS type used, initally demonstrated a poor wettability. To overcome this issue the idea of using one surfactant additive has been also found to enhance electrical conductivity due to its amphiphilic nature weakening ionic bonds on PEDOT:PSS, which plays a similar role than solvent additives[25,240]. Different surfactants are used, such as Zonyls, Dynols, and Triton X-100. Adding Triton X-100 has discussed on the scientific literature,[24,69,240] which has been found to improve surface wettabillity. In our case, our approach was conservative with the use of surfactant to preserve the chemical composition of PEDOT:PSS and its possible chain composition controlled, 0.1% wt of Triton X-100 was used at it has been reported a reduction of film thickness of about ∼8%[240].

After the mixture of PEDOT:PSS, DMSO and Triton X-100 different procedure were tested as well as the process for mixing these compounds. The best results were obtained after magnetically stirring during 2h and after filtering the PEDOT:PSS mixture through a PES(polyethersulfone) membrane with 0.45 μm

pore size to discard any possible PEDOT:PSS agglomerates (Fig.2.4). Two different substrates were tested in this work, FZ-n type silicon and glass (cover glass substrates). Regarding the spin coating process, the steps were tested and optimized taking into consideration the manufacturer recommendations. In our case a three-step process was selected, firstly a low speed of 2000 rpm when the 70-150μL of the samples were manually deposited over the spinning substrate at a constant rate and with the help of a pipettor, which was placed $\sim$ 2 cm over the sample, as discussed on section 2.1.3. Following, a second step of 6000 rpm was used to assure an homogeneous distribution and a final thickness of near 120$\pm$20 nm, as observed with profilometry, SEM and AFM to finally decrease its speed until stop on a final step. Similar steps and spin speeds (between 2000-6000) rpm can be found through the references mentioned in this text[22,259], but mostly low speed are used[238,264]. In our case increasing the speed demonstrated to improve surface covering. It should be mentioned that in this work substrate size of the silicon was substantially large, as the complete covered area was 78.5 cm^2. Normally, substrates used on the literature are around 1.5x1.5 cm^2 which are insufficient to test large scale manufacturing. After deposition, substrates were submitted to a thermal post treatment to homogenize the surface and evaporate remaining water or other undesired volatile solvents, while the organic solvents remain unharmed as their boiling point is higher (Table1.4). Annealing temperatures between 120-130°C for 15 min have been widely used on the literature[22] whereas other authors suggest even higher temperatures close to 160°C[24] which also are expected to increase conductivity. The stability under temperature was assured during Raman measurements, where the PEDOT:PSS substrates were heated over 20 min at different temperatures up to 160°C and no changes were observed on the Raman spectra.

The first characterization step was aimed to decide the use of either DMSO or EG and asses the effect of Triton X-100 on the VIS spectra via UV-VIS spectroscopy. Fig.6.3 shows minor changes with the DMSO or EG respective to the use of Triton X-100 which was necessary for the deposition on the Si substrates and also used for the glass substrates. The absorption spectra show slightly improved absorption with the use of EG respective to DMSO but as shown in the estimated optical bandgap values the change was slight, see Fig.6.4(a) and Table 6.2. The UV-vis spectra resembled what was expected for PEDOT:PSS. There is a high absorption on the UV range which drastically decreases near 400 nm as it is transparent on the visible range (Fig.6.3(b)). One fingerprint of doping PEDOT chains may induce the formation of polarons which effects could be observed on the absorption spectra at different wavelengths: the neutral polymer chains show absorption around 600 nm; chains in the polaron state show absorption around 900 nm and chains in the bipolaron state show broad absorption in the near infrared region[263]. In our case, not much can be said about the transition for PEDOT:PSS to either polaron or bipolaron state as those absorption range are out of the range of our equipment.

The refraction index of a thin layer can be determined via different approaches,

such as ellipsometry[62], Swanapoel method from UV-VIS modulations or photoluminescence optical resonances. In our case, we decided to estimate its value with UV-VIS performing an iterative calculation based on the single oscillator model developed by Wemple and DiDomenico. This method has been used for different organic compounds such as poly(vinyl alcohol)[244], ethylene[265] and also for PEDOT:PSS[241]. In particular we only focused on the calculation of the refraction index but with this method many optical parameters can be calculated such as the plasma resonance frecuency or the dispersion energy.

The observed $n(\lambda)$ value close to 1.15 (see Fig.6.4(b)) is in accordance with previous reports using ellipsometry PH1000 PEDOT:PSS[245], although minor changes were obtained with the use of EG or DMSO in this work. Other works have shown an slight increase of the refractive index by adding EG[241] which is clearly attributed to their observed changes on the absorbance. In our case, as well as in other reports, the addition of DMSO increases the absorption in the NIR and increase in the visible region[245]. We also observe that the use of Triton X-100 also enhances the absorption on the VIS-IR of PEDOT:PSS, most likely due to a better coverage of the substrate.

Returning to silicon substrates, we have discussed that other factors may interfere on the passivation behavior. The control of the native SiO_x layer has been also tested as a possible method to improve lifetime values. The interface between n-Si/PEDOT:PSS has an impact on the final solar cell product. When fabricated, normally silicon substrates posses numerous chemical free bonds with different species such as -H or -OH that generates native oxide growth. This oxide layer has been also measured on the scientific literature with the employ of Hard X-Ray, and it was observed that its thickness increase even after the synthesis and during *in operando* measurements[22]. Our approach was testing the lifetime values of PEDOT:PSS deposited over commercial silicon substrates with a native oxide layer of few nm and to remove that layer with an acidic bath of HF and Piranha solution. As observed by PL-QSSPC images on Fig.6.5, lifetime values with the removal of the oxide lead to lower lifetime of $\sim$ 170 μs which was almost half of the values obtained without removing the oxide layer. Recombination lifetime values of $\sim$ 350 μs obtained without the removal of the Si oxide are competitive values[27]. Other recent works of our collaborators have shown that removing the oxide layer and regrowing the same layer which ends on a thicker oxide layer may increase lifetime values[87,155]. To obtain a more environmental friendly and easy fabrication, the oxide layer was not removed in this work.

To create an efficient solar cell it has to be stable over time, as it is intended to be used over variable conditions (temperature, humidity and under UV light). As commercially water diluted, it is clear the attraction between water and PEDOT:PSS. PEDOT:PSS possesses an hygroscopic nature, so it is expected to humidify if not adequately stored. In this work, lifetime measurements were performed on PEDOT:PSS/nSi using both piranha treated and non-treated substrates. Initially the non-treated substrate shows homogeneity as well as high

lifetimes of ∼280 μm. Note that the substrate of PEDOT:PSS used as reference showed higher values as it was obtained after optimizing the process. During the period of 90 days (see Fig.6.6) both samples degrade following a similar behavior. The observed lifetime values lay very close to the observed in our of latest works, in which it was measured over 400 days, and as observed the degradation tends to stabilize after 150 days[87,155]. In those works,[87,155] degradation was also tested by placing the wafers at low temperatures or inside a desiccator with a N_2 atmosphere. The wafers inside the desiccator show lower degradation but still carrier lifetime decreases. It is clear that degradation over time is an unsolved issue and is commonly ignored on the research literature. There are works which deal with studies of the changes over time of sheet resistance or conductivity values[71] but none regarding the recombination lifetimes, to the best of our knowledge. It has been reported the use of TiO_2 as a solution for long-term stability[44], which also spiked interest for this research.

Electronic, optical and morphological characterization of the PEDOT:PSS/nSi and composites with nanoparticles were also tested in this work.

Both optical microscope and AFM images are observed in Fig.6.8. Optical microscopy (Fig.6.8(a)) shows apparently the presence of small grain-like domains on the sample. This could be due to the PSS encapsulating PEDOT as a result of the use of both Triton X-100 or either a topography effect on the sample. AFM, Fig.6.8(b)-(c), further asses the idea of the topography of the sample being presenting small steps as expected. The sample presents a mean roughness near 2 nm which is in good agreement with values from literature. It is widely accepted that DMSO-treated PEDOT:PSS exhibit a grain-like structure of ∼20-30 nm large conductive PEDOT:PSS grains surrounded by PSS[22,266].

In this work we have performed an in depth-study of PEDOT:PSS composites. Raman spectra of PEDOT:PSS presents multiple modes on the region between 1200-1800 cm^{-1}, and were summarized on Table 6.5. Main Raman vibrational modes from PEDOT:PSS, observed with the 900 μm pinhole, are placed at around 1254 cm^{-1} related to C-C interring stretching,[253] 1366 cm^{-1} due to single C_β-C_β stretching,[238,254] 1400 cm^{-1} associated with C_α=C_β, 1429 cm^{-1} due to C_α=C_β symmetric stretching vibrations, and 1500 and 1561 cm^{-1} due to C_α=C_β asymmetric stretching vibrations related to the carbons on the thiophone ring in PEDOT in the middle and the end of the chains, respectively[252] The peak around 1530 cm^{-1} arises from the splitting of the C_α=C_β asymmetric vibrations and it is normally unseen, depending on the conditions.
Peaks at 1400-1500 cm^{-1} were clearly enhanced when the pinhole of 900 μm was used. Usually, contribution ∼1430 cm^{-1} can be divided into two regions originating from benzoid and quinoidic structures. The benzenodic form appears at ∼ 1440 cm^{-1} and quinoidic appears at ∼ 1410 cm^{-1} which increases with increasing DMSO content[68] and are associated, respectively, with coil-like conformation or linear conformation of the PEDOT:PSS chains. Considering this, it is possible that the Raman signal from PEDOT:PSS acquired with higher pinhole size is more sensitive

and thus, small changes can be detected. Other option could be that the C_α=C_β are more sensitive to a higher volume of laser irradiation, as well. Notice that in the reprinted scientific literature in some cases there is no specification on the laser conditions used to acquire some of these measurements as well as the DMSO content, which might differ from 5%.

Few works can be found in which they use an UV laser for the Raman acquisition as PEDOT:PSS is clearly photo-affected by UV light, as seen in Fig.6.10. Raman spectra intensity decreases upon laser irradiation (Fig.6.10(a)-(b)), in which initially three main modes are observed, 1370, 1452 and 1608 cm^{-1} being the latter the most intense. Lin et al[267] used a 532 nm laser and the reported Raman spectra of PEDOT:PSS +(1, 3 or 5%) EG resembles the spectra presented in Fig.6.6(a). Between 1200 and 1400 cm^{-1}, peaks are assigned to C–C stretch vibrations, and between 1400 and 1600 $cm^{-1}$to C=C stretch vibrations. As shown in Table 6.5, Du. et al[253] also used the same laser but in this case they observe peaks at 1356, 1431 and 1583 cm^{-1}. However, their origin is not correctly explained as they use rGO, GO or graphene quantum dots, which presents modes very close to the C-C modes attributed to PEDOT:PSS. Toto et al.[70] showed that PEDOT:PSS is specially sensitive to UV-C damage and that after prolonged irradiation a shift of the main peak of PEDOT:PSS toward higher wavenumber was detected and attributed to the shortening of the conjugation length of the neutral parts due to the UV irradiation. They did not comment that there is a shift of the set formed by all the Raman modes as well of an increase of the Raman mode near 1500 and 1530 cm^{-1}, very similar to our findings (see Fig.6.11(a)). As observed, modes ∼1499, 1530 cm^{-1} tend to increase upon laser UV irradiation (Fig.6.11(b)) and a clear change on the structure was observed on the inset, which shows an optical image after the controlled irradiation. This rather counter-intuitive behavior shows higher stability to UV light than expected as the energy density used in our equipment is rather high. Nonetheless, prolonging the exposure time will quench the intensity of the Raman signal.

Nominal conductivity for PH1000 PEDOT:PSS is expected at around 0.2-1 $S{\cdot}cm^{-1}$, and with the addition of 5%wt DMSO > 800 $S{\cdot}cm^{-1}$ as explained in chapter 1 which is close to our results. In this work, we have also added 0.1 %wt Triton X-100. In previous reports[69] it has been shown that it also improves the conductivity but mostly for 2.0% wt or higher values. With 0.1% wt, film conductivity was reported around 1 $S{\cdot}cm^{-1}$ without addition of DMSO or EG. Thus probably our enhancement of conductivity is mostly due to the addition of DMSO. Best results were obtained by adding 5% wt of DMSO as some previous results suggest 5% is the perfect ratio for enhancing conductivity and preventing degradation reaching > 10 $S{\cdot}cm^{-1}$[238] but multiple results varying from 1-1000 $S{\cdot}cm^{-1}$ have been reported[24,26]. Observed values of carrier concentration are in agreement with the literature as PH1000 usually increases carrier concentration from 10^{17} up to 10^{21} cm^{-3} after film treatment[262]. The increment on the conductivity is mostly related to the change on the chain like structure of PEDOT:PSS. In the case of the addition of the nanoparticles, based on ouir results, there could be a coulombic

interaction between the PEDOT chain and the charged particles.

Secondary doping has been mainly focused on the use of organic solvents or surfactants. However, nanoparticle addition has shown some preliminary results preventing PEDOT:PSS degradation as it has been recently studied that the addition of inorganic materials can enhance its performance. In addition to the use of metallic nanostructures such as Ag or Au in the hybrid composites[268], the use of semiconductor nanomaterials as counterparts is gaining increased attention[253]. Previous research has been made on the use of either TiO_2 or SnO_2 nanoparticles for different purposes such as gas sensing[242], organic photovoltaics[76] but only a few can be found which aim to solar cell passivation[27]. In 2015, Liu et al.[264] achieved 15.5% efficiency through the use of titanium dioxide (TiO_2) as a reflective layer. SnO has not been studied yet most probably due to its inherent instability.

Herein we have tested the use of SnO, SnO_2 and anatase TiO_2 nanoparticles with PEDOT:PSS to produce hybrid composites deposited over n-type silicon. Firstly, p-type SnO composites composed with 1% wt of SnO show a higher stability under laser irradiation as observed in Fig.6.14. After UV irradiation almost no changes were observed on the Raman spectra, contrary with the bare PEDOT:PSS composites for which we have observed an increase on the modes at 1499 and 1535 cm^{-1} upon laser irradiation. Besides, these composites presented an increase of the bulk concentration up to 1.4 $\cdot 10^{22}$ cm^{-3}, even when the conductivity of SnO nanoparticles shows low values around 1.8 $\cdot 10^{-2}$ $S \cdot cm^{-1}$ as discussed on the previous chapter. Some authors reported that, when the surface of the nanoparticles embedded in the polymer is positively charged, the negatively charged PSS chains can be electrostatically attracted, leading to changes in the PEDOT:PSS chains' configuration, which can enhance the electrical conductivity[74]. Rearrangement of the PEDOT:PSS can lead to better pathways for charge transport. Actually, an expanded-coil configuration is usually associated with improved conductivity. It should be noted that both PEDOT:PSS and SnO presents p-type conductivity. Despite those promising results, the use of SnO decreases the lifetime values observed by PL-QSSPC in Fig.6.15. At the injection level of $10^{15} cm^{-3}$ lifetime of the carrier levels of this composite is 296.8 μs which is 1.4 times lower than for bare PEDOT:PSS. Hence, in this case, synergy between the counterparts in the composite leads only to improved electrical performance. It should be mentioned that the particles of SnO embedded on the polymer matrix presented a higher stability under laser irradiation, as its transition to SnO_2 was hindered. The synergetic effect between SnO and PEDOT:PSS was observed by measuring Raman spectra with the UV laser with $0.1 \cdot I_0$ and monitor its decay over time, as observed on Fig.6.21. It can be observed that, as compared with PEDOT:PSS, the decay is less pronounced.

Secondly, n-type SnO_2 composites were tested, in this case in different weight concentrations to assess the effect of the nanoparticle concentration. Lifetime values decrease by increasing the concentration of SnO_2. In this case, the injection level is lower than 10^{15} cm^{-3} (Fig.6.16). Despite this, electrical measurement shows

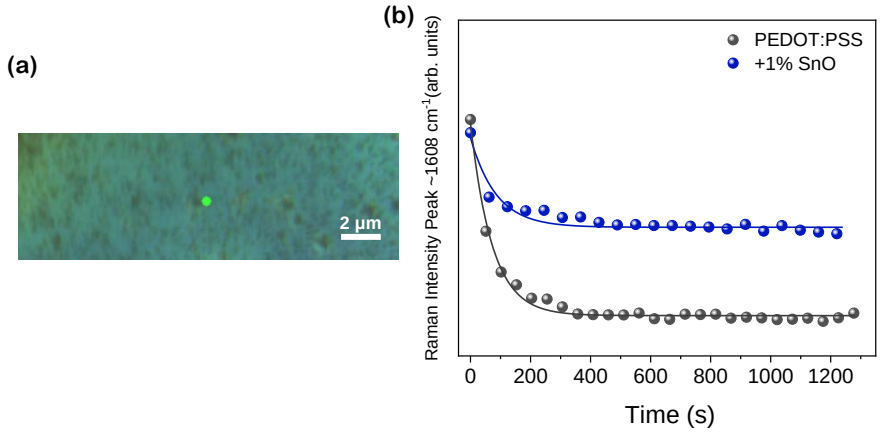

Fig. 6.21: (a) Irradiated zone corresponding to the composite of PEDOT:PSS+ 1% SnO with the UV laser with $0.1 \cdot I_0$ (b) Decrease of the relative intensity of the peak at ∼1608 cm^{-1} comparison for PEDOT:PSS and PEDOT:PSS+ 1% SnO composite.

improved electrical conductivity with increasing SnO_2 content.

Finally, n-type anatase TiO_2 composites were fabricated with the same weight percentages as for SnO_2. PL-QSSPC results show the best results for the use of 0.5% TiO_2 as observed in Fig.6.18, which is close to the values obtained without the use of nanoparticles, but it is increased with low injection levels close to 10^{14} cm^{-3}. A charge-assisted passivation mechanism due to the presence of nanoparticles with positively charged surfaces, mainly due to hydroxyl groups, can be considered in the understanding of the observed passivation behavior of some of the composites[27]. The lifetime values obtained in this work are competitive as compared with classical lifetime values reported for SiN_x:H or a-Si deposited which involve high temperature and expensive techniques.

As well as the recombination rates and the surface passivation, to obtain a high-efficiency solar cell is necessary to obtain a rectification behavior when measuring I-V. For that purpose, both dark and light photocurrent were measured. As observed in Fig.6.19, the results were analyzed and compared to the values obtained for FZ n-type Si without and with piranha treatment. Low values of V_{OC} could be affected due to the lack of a back surface passivation. To obtain the value of the current density, J, it is tentative to apply a correction factor mainly due to the fact that the silver contacts over the samples, in which different patterning were tested to see the most suitable geometry, bring a disadvantage as most of the surface is shaded by the presence of Ag and does not work as effective surface which may

interact with light, as suggested in[87]. Our fill factor of 33% is below the most recent advances, but this is mostly due to the non-optimized grid, contacts and high coverage surface, hence still there is room for improvement. The FF could reach values close to 70% without the removal of the SiO_x layer and via the correction of the J-V curves considering the shading due to the silver grid[87].

Finally, the focus on this chapter has been the study of PEDOT:PSS as a candidate for hybrid silicon solar cells. However, we have mentioned during the introduction that PEDOT:PSS is commonly used as a transparent conductive electrode. Having obtained composites based on nanoparticles and PEDOT:PSS it is worth to quantify its possible use as electrodes. Transparent conductive electrodes are often evaluated by the Figure of Merit (FoM). The value of FoM is influenced by film transmittance and sheet resistance[239,262,269]:

$$T = \left(1 + \frac{Z_0 \sigma_{op}}{2 R_S \sigma_{dc}}\right)^{-2} \tag{6.6}$$

where T is the transmittance, R_S is the sheet resistance, $Z_0 = 377\ \Omega$ is the impedance of free space, and σ_{op} and σ_{dc} are the optical and dc conductivities, respectively.

For transparent electrodes, transmittance higher than 90% and sheet resistance less than 100 $\Omega/\square$[262] with a combined FoM of $\sigma_{dc} \cdot \sigma_{op}^{-1} > 35$ is considered the minimum commercial standard. In our case we have tested PEDOT:PSS in combination with organic solvents and nanoparticles as a proof of concept and we do not fulfill this criteria. However, closer inspection on Table 6.9 shows that SnO composites increase the FoM as well as diminishes the sheet resistance to almost 100 $\Omega/\square$. Notice that the size of the cells as well of the procedure performed in this work could be easily improved and if the tendency when using SnO nanoparticles is preserved, this composite could be used not only for hybrid silicon solar cells but also it would be useful as a cell electrode. TiO_2 does also decrease sheet resistance of the composite, with the lowest value of 226.33 $\Omega/\square$ for 2% wt. This effect could be mostly due to film quality. Previous reports obtained increasing sheet resistance with increasing nanoparticle content[242], which is a possible approach to consider.

Table 6.9: Sheet resistance, Transmittance and $\sigma_{dc} \cdot \sigma_{op}^{-1}$ variations of PEDOT:PSS films from the different composites of this work.

Sample	R_s ($\Omega/\square$)	Transmittance @550 nm	$\sigma_{dc} \cdot \sigma_{op}^{-1}$
PEDOT:PSS	644.40	0.859	3.69
PEDOT:PSS+1% wt SnO	159.67	0.858	14.89
PEDOT:PSS+ 0.5%wt TiO_2	487.31	0.879	5.79
PEDOT:PSS+ 1%wt TiO_2	620.66	0.873	4.32
PEDOT:PSS+ 2%wt TiO_2	226.33	0.873	11.86

6.5. Conclusion

In this chapter it has been successfully designed a method for coating n-type silicon substrates via spin coating, taking into consideration all the steps in the process: blending different additives to improve wettability and the electrical and optical properties of the formed composite, the spin coating parameters and other pre- and post-treatments of the substrate. In particular, composites have been successfully obtained by combining the nanoparticles synthesized in the previous chapters with the PEDOT:PSS. Through the use of the spin coating technique, it is not necessary to use expensive highly complex methods, which greatly reduces the cost of production that could be extended to medium-large scale, since homogeneity has been obtained for substrates of $\sim$100 cm^2.

- In this chapter composites based on PEDOT:PSS and nanoparticles have been assembled. Silicon surface passivation has been successfully achieved by the deposition of PEDOT:PSS over the silicon surface. The chosen method was low cost effective as it has been demonstrated that expensive and environmental unfriendly procedures such as silicon oxide removal with chemical etching decreases passivation performance.

- Stability over time has been also analyzed and its dependence with the surface interface between PEDOT:PSS and silicon. It can be concluded that removing the silicon oxide layer and immediately depositing the mixture containing PEDOT:PSS provides worse silicon passivation but retains a similar degradation tendency (percentage wise) over time, which after 400 days seems to stabilize at $\sim$ 75 μs.

- Raman spectra has been analyzed with different irradiation energies and lasers as well as variable pinhole size and variations were observed in the vibrational modes.

- Following a similar procedure, SnO, SnO_2 and TiO_2 have been incorporated to the PEDOT:PSS blend mixture prior deposition, obtaining in the end hybrid composites formed by the inorganic MOs and PEDOT:PSS.

- SnO/PEDOT:PSS composites presented more than twice the conductivity and lower sheet resistance of bare PEDOT:PSS as well as improved stability under laser irradiation. These factors are improved as compared with bare PEDOT:PSS which, although involving low lifetime recombination, make this material as a good candidate for both hybrid silicon solar cell as well as transparent flexible electrode. Similarly, it has been observed an synergy effect between PEDOT:PSS/SnO, as SnO prevented changes with UV irradiation, observation by the stability of the mode at $\sim$1530 cm^{-1}.

- TiO_2 in low concentrations such as 0.5% wt improves lifetime of the charge carriers, retaining UV-VIS transparency and silicon passivation. Lifetime improvement is slightly better with this content, however increasing TiO_2

decreases passivation. P-n junctions of the silicon surface and PEDOT:PSS have shown rectification I-V behavior but with low FF, probably due grid shading.

Chapter 7.
PEDOT:PSS composites based on SnO, SnO_2 or TiO_2: thermoelectric and gas sensing properties

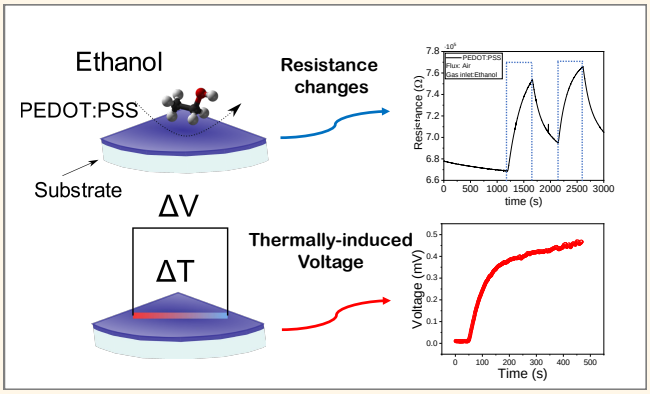

Abstract: In this chapter, bare PEDOT:PSS and composites conformed by PEDOT:PSS and SnO, SnO_2 or TiO_2 nanoparticles were assembled by spin-coating. Their optical electrical and morphological properties were analyzed by different techniques such as UV-VIS, AFM, Hall effect or XPS. The possible uses of these composites in two main applications have been tested: as gas sensors and as thermoelectric materials. For that purpose, chemiresistive response of the obtained composites was tested via the injection of different test gases under variable atmosphere and other conditions such as temperature. Gas sensing properties showed a sensitive response to a gas analyte, especially enhanced with the use of SnO. Finally, to measure the thermoelectric properties of the samples under study, an experimental set-up and data acquisition system was designed based on the use of two Peltier heating modules and both a voltage and temperature acquisition system. With this device, it was observed that the thermoelectric Power Factor could be enhanced with the use of the nanoparticles in the composite.

In this chapter, PEDOT:PSS thin layers were fabricated via spin coating. Silicon or glass substrates were coated with PEDOT:PSS and with mixtures prepared with the addition of ethylene glycol (EG) and/or the synthesized nanoparticles described in the previous chapters.

The process to obtain the composites was described carefully on Fig.2.4. In this chapter, we are using PEDOT:PSS from Sigma-Aldrich which main properties are described on chapter 1. Pristine PEDOT:PSS is used to coat substrates for comparison. Herein, we are going to assess the differences on the electronic and morphological properties of PEDOT:PSS when EG is used and also when the nanoparticles (SnO, SnO_2 or TiO_2) are added and the combined effect of both, focusing on the potential applicability of such composites. Therefore, as seen in the upper right corner in Fig.2.4 either we use pristine PEDOT:PSS or we add EG, in two different weight concentrations, 1 or 5%. If added, the mixture was immersed on an ultrasonic bath for 30 min to assure homogeneity. Secondly, following a similar procedure than in the previous chapter, if we want to use nanoparticles we will add their percentage in weight (in this case, 1%). However, in contrast with the previous chapter, the mixture will only undergo through ultrasonication bath for other 15-30 min. The reason why the ultrasonic probe is omitted is due to the fact that the homogeneity of the dispersion without this step was adequate. The next steps are equal to the previously described: we select the desired substrate (either silicon or glass) which properties are described in chapter 2 and then spin coated onto the substrates. The obtained composites present an average thickness of ∼100 nm.

To summarize, the samples studied in this chapter are the following:

- Pristine PEDOT:PSS, labeled as PEDOT:PSS.
- PEDOT:PSS with the addition of ethylene glycol in two weight percentages, 1% and 5%, labeled as PEDOT:PSS +x% wt EG where x=1 or 5.
- PEDOT:PSS with the addition of the nanoparticles (SnO, SnO_2 or TiO_2) in 1% wt, labeled as PEDOT:PSS+1% wt Y where Y=SnO, SnO_2 or TiO_2.
- PEDOT:PSS with both the addition of Ethylene glycol(1% wt) and the nanoparticles (SnO, SnO_2 or TiO_2) also 1% wt, labeled as PEDOT:PSS+1% EG +1% wt Y where Y=SnO, SnO_2 or TiO_2.

7.1. Morphological and optical characterization

7.1.1. Optical microscopy

The first characterization step of these composites was to observe them under the optical microscope. Fig.7.1(a)-(b) show composites using SnO without and with the addition of ethylene glycol, while Fig.7.1(c)-(d) show composites with SnO_2 without and with the addition of ethylene glycol. It is clear that the addition of EG enhanced the dispersion of the nanoparticles observed in the optical images. In the case of SnO_2 composites, agglomerates are avoided and for SnO composites

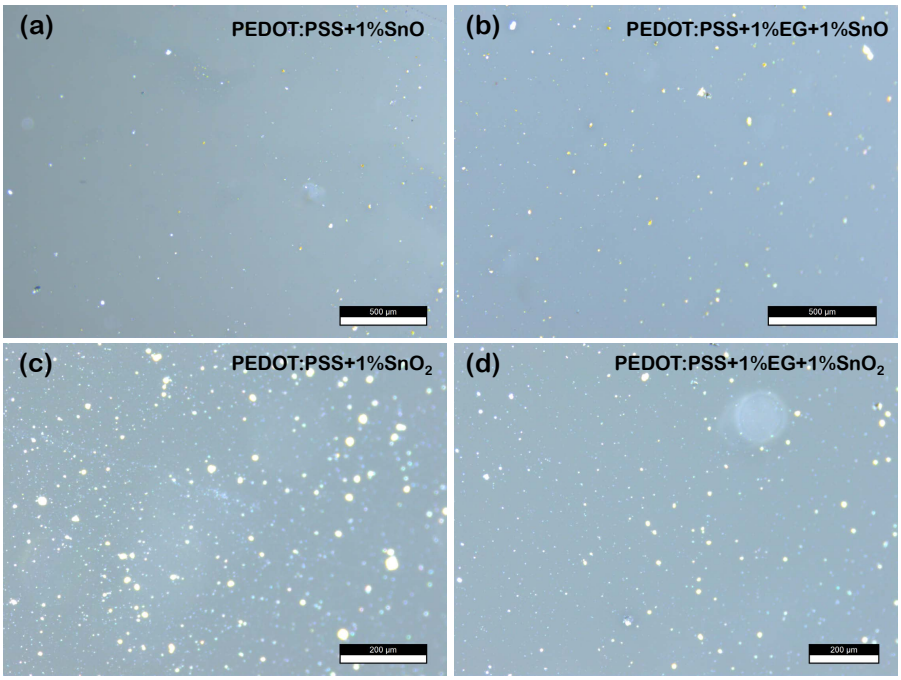

Fig. 7.1: Optical images corresponding to the PEDOT:PSS composites (a) with 1% SnO (b) with 1% EG + 1% SnO (c) 1% SnO_2 and (d) 1% EG +1% SnO_2, obtained with an optical microscope Leica DFC295.

there is an homogeneous dispersion. This influence is attributed to EG acting as a surfactant lowering the surface tension between the surface-charged nanoparticles and the polymer matrix, decreasing the aggregation phenomena.

7.1.2. AFM

The surface topography of the different samples was recorded on a spot size of 1×1 μm^2 in different parts of the samples near the center.

Fig.7.2 shows the AFM images of the different samples. The pristine PEDOT:PSS film shows a typical phase image in which the bright (positive) regions refer to conducting rigid PEDOT-rich domains, while the dark (negative) regions refer to soft PSS-rich areas[269]. The polymer layers are slightly rough and posses a mean roughness of 1.76 nm, in agreement with values reported on the scientific literature[22]. The presence of EG eases the PEDOT:PSS structure which tends to form a grain-like the structure, which can be observed on Fig.7.2(b)-(c) for 1% or 5% EG, respectively. This small plateaus difficult the AFM measurements, which

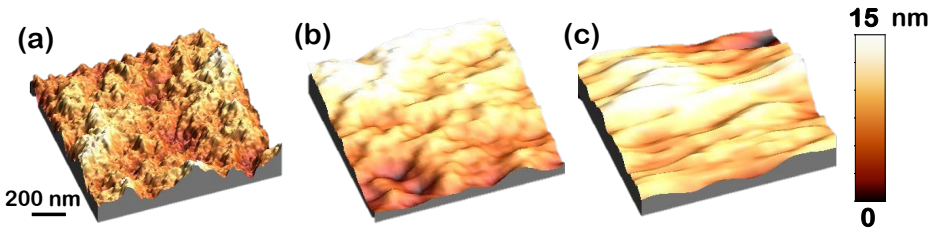

Fig. 7.2: AFM images of (a) PEDOT:PSS, (b) PEDOT:PSS+1%wt EG (c) PEDOT:PSS+5%wt EG. All images correspond to an area of 1×1 μm^2 and were obtained in contact mode.

creates images of less quality. Moreover, the mean roughness is slightly large as some areas of the polymer are difficult to measure, being the average roughness 2.77 and 2.15 nm, respectively.

7.1.3. UV-VIS

All films, both doped and undoped present a high transmittance in the visible range between 400-600 nm, as depicted in Fig.7.3(a)-(c). Fig.7.3(a) shows the comparative spectra of PEDOT:PSS and with 1% or 5% EG. It has been reported that transmittance decrease with EG content[269–271], similarly to our observations, where the transmittance decrease at 550 nm from 87.84% to 86.56 % with 1% EG content and further to 86.01 % with 5% wt content.

Fig.7.3(b) shows the transmittance from composites containing the nanoparticles, which also decreases upon nanoparticle addition, most notably for TiO_2 and SnO_2 where transmittance at 550 nm reaches values of 86.10% and 86.07%. Transmittance shape also changes, most notably in the NIR range. For both TiO_2 and SnO_2 addition, a slight improvement of the transmittance in the NIR region is observed. Conversely, adding SnO nanoparticles does not increase transmittance, the shape of the transmittance signal is almost identical to pristine PEDOT:PSS. Composites containing both EG and nanoparticles are presented in Fig.7.3(c). The contribution of the nanoparticles in all cases improves the transmittance as compared with adding solely EG. This could indicate that the transmission changes due the presence of EG are compensated with the nanoparticles presence. The highest transmittance at 550 nm is observed for the composites containing 1 wt% EG and SnO_2 reaching 90.59%.

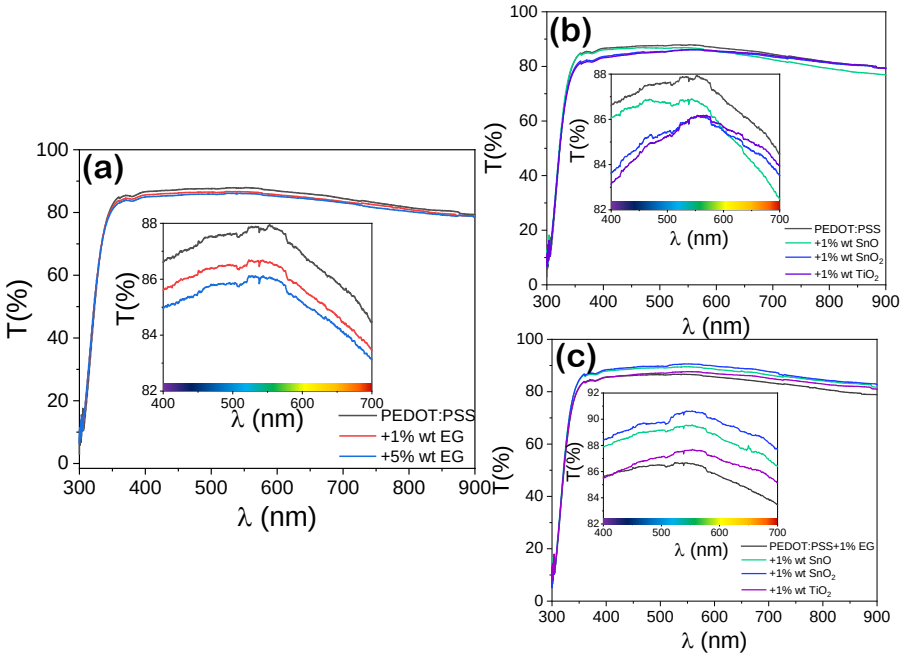

Fig. 7.3: Transmittance spectra of PEDOT:PSS composites (a) with variable EG content, (b) with different nanoparticles and (c) with both EG and nanoparticles. Pristine PEDOT:PSS transmitance spectrum has been included as a reference.

7.2. Electronic characterization by XPS

Synchrotron radiation X-ray photoelectron spectroscopy (XPS) measurements have been performed at the CNR Beamline for Advanced diCHroism (BACH) of the Elettra synchrotron facility in Trieste, Italy. The photoelectron spectra were acquired using a Scienta R3000 electron energy analyzer. Core levels were centered at corrected positions using the Au($4f$) core level. Under these conditions, PEDOT:PSS remained stable under the beam continuous irradiation. To obtain these measurements, PEDOT:PSS mixtures were spin-coated over Si substrates. After Shirley background correction peaks were fitted to Voigt functions. Three main core levels have been studied: S($2p$), C($1s$) and O($1s$).

The S($2p$) core level presents two main regions, one between 162.0-166.5 eV and another in the range between in 166.5-172.0 eV attributed to sulfur atoms in PEDOT and sulfur atoms in PSS, respectively. Both regions posses a clear spin-orbit doublet splitting into $2p_{3/2}$ and $2p_{1/2}$. The S($2p$) contributions of bare PEDOT:PSS are observed on 168.79, 167.64, 164.79 and 163.66 eV, as observed in Fig.7.4(a). The separation between doublet peaks of 1.1 eV is the expected value for S($2p$)[89,247]. The deconvolution of each of the contributions has been attributed to only one band, however other works usually add other contribution in the peak

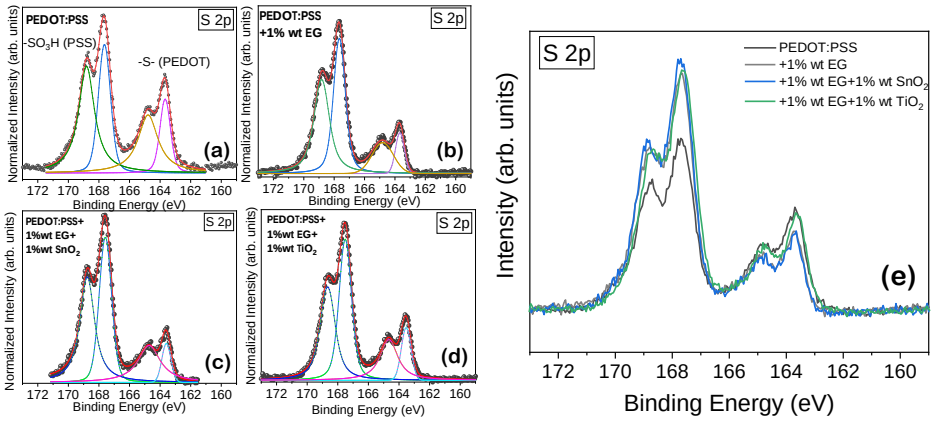

Fig. 7.4: S(2p) core level normalized spectra corresponding to the samples (a) PEDOT:PSS, (b) PEDOT:PSS+1% EG, (c) PEDOT:PSS+1% EG+1% SnO_2 and (d) PEDOT:PSS+1% EG+1% TiO_2. All combined spectra without normalization are shown in figure (e).

of 164.79 eV[269]. Minor changes are observed in both shape and position except for the S(2p) of pristine PEDOT:PSS for which the ratio of the 2p contributions is clearly different.

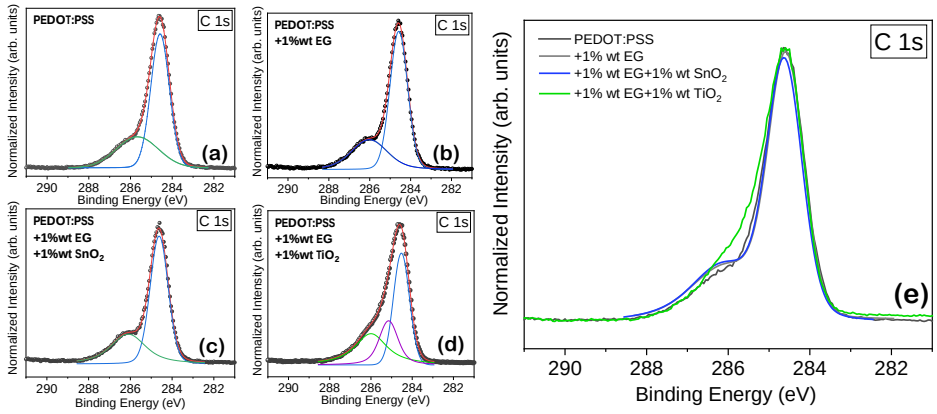

Fig. 7.5: C(1s) core level normalized spectra corresponding to the samples (a) PEDOT:PSS, (b) PEDOT:PSS+1% EG, (c) PEDOT:PSS+1% EG+1% SnO_2 and (d) PEDOT:PSS+1% EG+1% TiO_2. All combined spectra without normalization are shown on figure (e).

The C(1s) core level spectra are depicted in Fig.7.5(a)-(e). Two main contributions are observed, a main contribution centered at 284.58 eV which is attributed to the aromatic C=C of PEDOT bonds and other contribution at 286.6 eV which

is attributed to C-O bonds. As observed, the addition of EG does not change the spectra substantially but with the addition of also TiO_2 another contribution at ∼285.1 eV appears which could be attributed to C-C bonds of the PEDOT:PSS chains[253].

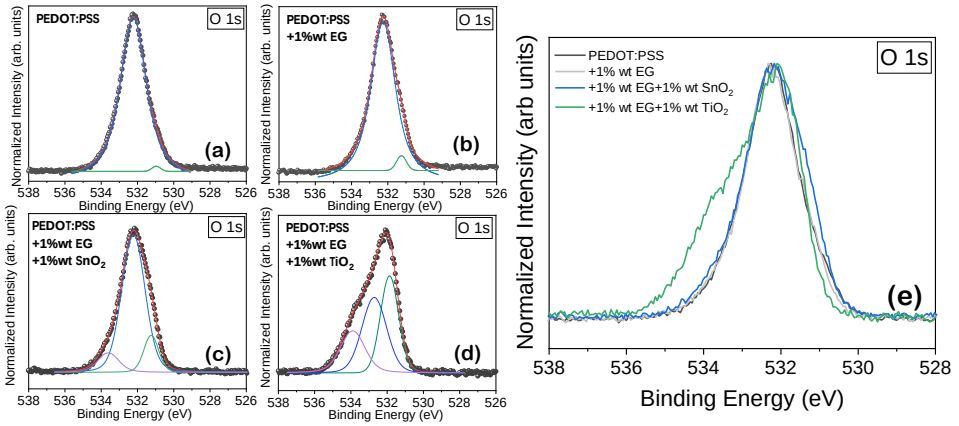

Fig. 7.6: O(1*s*) core level normalized spectra corresponding to the samples (a) PEDOT:PSS, (b) PEDOT:PSS+1% EG, (c) PEDOT:PSS+1% EG+1% SnO_2 and (d) PEDOT:PSS+1% EG+1% TiO_2. All combined spectra without normalization are shown on figure (e).

O(1*s*) core level spectra are presented in Fig.7.6, with the presence of a main contribution at ∼532.2 eV and a small contribution at 530.9 eV for pristine PEDOT:PSS. Some authors have attributed the contribution at lower binding energy to PSS and the higher binding energy to PEDOT[266]. With EG addition an increase of the peak at higher binding energy is also reported. In our case, we observe that a shoulder appears at ∼531.3 eV which is increased with EG addition. With the nanoparticle addition, the core level shape changes the most. When using SnO_2, a contribution at higher binding energy appears at 533.9 eV with low relative intensity. The sample containing TiO_2 not only presents these contributions, but their relative intensity is substantially increased. These peaks clearly show the presence of C-O or -OH bonds as well as Sn-O, Ti-O bonds present due to nanoparticle addition.

7.3. Electrical characterization by Hall effect

As explained in chapter 1, PEDOT:PSS was purchased in this case from Sigma-Aldrich (1.1% water, Ω/□). This product possesses lower conductivity than Ossila PH1000. Therefore in this chapter, although we are not aiming for the highest value reported, our analysis will be focused on the study of the relative variation on the conductivity upon nanoparticle or solvent addition.

Table 7.1: Hall effect measurements performed with I=0.1 mA for the different PEDOT:PSS composites.

Sample	Conductivity ($S \cdot cm^{-1}$)	Charge Carrier Concentration (cm^{-3})
PEDOT:PSS	$(1.41 \pm 0.29) \cdot 10^{-1}$	$(5.83 \pm 0.67) \cdot 10^{18}$
PEDOT:PSS+1% wt SnO	$(5.48 \pm 0.20) \cdot 10^{-2}$	$(1.38 \pm 0.11) \cdot 10^{19}$
PEDOT:PSS+1% wt SnO_2	$(8.35 \pm 0.72) \cdot 10^{-2}$	$(6.26 \pm 0.17) \cdot 10^{18}$
PEDOT:PSS+1% wt TiO_2	$(8.42 \pm 0.37) \cdot 10^{-2}$	$(1.08 \pm 0.55) \cdot 10^{19}$
PEDOT:PSS+1% wt EG	(6.75 ± 0.03)	$(3.29 \pm 0.69) \cdot 10^{20}$
PEDOT:PSS+1% wt EG+1% wt SnO	$(1.65 \pm 0.45) \cdot 10^{1}$	$(1.00 \pm 0.59) \cdot 10^{21}$
PEDOT:PSS+1% wt EG+1% wt SnO_2	$(1.42 \pm 0.26) \cdot 10^{1}$	$(3.20 \pm 0.26) \cdot 10^{21}$
PEDOT:PSS+1% wt EG+1% wt TiO_2	(3.44 ± 0.27)	$(1.61 \pm 0.36) \cdot 10^{20}$
PEDOT:PSS+5% wt EG	$(4.03 \pm 0.26) \cdot 10^{1}$	$(3.34 \pm 0.59) \cdot 10^{20}$

Table 7.1 shows the conductivity results for the complete set of samples carried out at room temperature with a current of I=0.1 mA. As observed, for bare PEDOT:PSS the obtained conductivity is low, 0.141 $S \cdot cm^{-1}$. This is in agreement with previous reports in which without the addition of any solvents PEDOT:PSS exhibits low conductivity around 0.2-1 $S \cdot cm^{-1}$ [26]. By mixing PEDOT:PSS with the nanoparticles the conductivity is not improved, in fact it diminishes down to 0.0548 $S \cdot cm^{-1}$ for SnO_2.

By combining PEDOT:PSS with EG the conductivity is enhanced as the EG content is increased. With 5% EG the conductivity has increased two orders of magnitude, reaching 40.3 $S \cdot cm^{-1}$. With the lowest content of 1% EG conductivity increases up to 6.75 $S \cdot cm^{-1}$. With the addition of nanoparticles, there is a notable increasing of the conductivity when not only 1% EG but also SnO nanoparticles (1% wt) are added to the composite, reaching 16.5 $S \cdot cm^{-1}$.

7.4. Applications

7.4.1. Gas Sensing

To measure the resistance change with the presence of a gas inlet, over each layer a thin deposition of approximately 40 nm of Au was evaporated, leaving one strip of around 0.5 cm uncovered as shown in chapter 1 in Fig.2.4. In this work, different parameters have been tested as the use of N_2 or synthetic air (composed by 79% N_2 + 21% O_2) as carrier gases, different analytes as ethanol (Ethanol 96%v/v pure pharma grade PanReac AppliChem) or water vapor (from distilled water), working temperatures such as 28°C (RT) or 50°C, different gas concentrations parts-per million (ppm) and different cycle times (300, 480 and 600s). The system has a delay time of 10 s which is considered throughout this section calculations.

One of the main parameters considered to analyze the gas sensing properties of

a material is the sensitivity, (S)[i], which is defined for this case as[5,23]:

$$S = \frac{R_g - R_0}{R_0}[\%] \tag{7.1}$$

where R_g and R_0 are the resistances of the sensor when exposed to the testing gas (ethanol, water vapor) and without gas (only exposed to the gas used to push the bubbler which is the carrier gas, in our case dry air or N_2), respectively. Both parameters have a significant relationship with the surface reactions. This formula is often reformulated and only considered as sensitivity the ratio between the sensor output signal and the amount of analyte bound to the sensor surface[242,273]. Other parameters to determine the working properties of a gas sensor are response time and recovery time, being respectively the time required for a sensor to reach 90% of the total response of the signal and the time required for a sensor to return to 90% of the original baseline.

Fig.7.7 shows the behavior of PEDOT:PSS samples under the ethanol exposure. In this case, during 900 seconds the sample was left with a constant flow of N_2 gas of 3.5 l/min and 1 bar of pressure, controlled with a Mass Flow Controller (MFC) which equals to an estimate gas of 200 ppm. At 900 s the valve configuration was changed so that the nitrogen flow passes through a bubbler filled with ethanol. This ethanol (g) passes through the chamber containing the PEDOT:PSS samples. The resistance is heavily increased when the flow containing ethanol is allowed. After that 600 s, the flow of ethanol is closed and the resistance decreased as observed in Fig.7.7. It can be observed that the resistance change occurs a few seconds after the valve is opened.

To study the dependence of different parameters on the sensing properties of PEDOT:PSS towards ethanol, firstly two working device temperatures were tested at RT (28°C) and 50°C, as observed in Fig.7.8(a). This is because, commonly, gas sensors work more efficiently at high temperatures, especially for MOs gas sensors[5]. Very similar results are observed, with sensitivities of 1.93% and 2.10%. In the first cycle, it appears that the response is faster when measured at 50°C. It should be pointed out that in these graphics there is no background subtraction, as removing background for gas sensing measurements is a controversial topic, which does not allows to easily calculate response or recovery time. The original relative resistance is recovered after the up/down cycle only for a few of the samples tested, which allows to determine the value of the response and recovery times but not for all the samples tested in order to assess the effect of moisture on the surface. Besides, the study of the effect of different sensing temperatures, the use of previous thermal treatments was also tested (Fig.7.8(b)). A PEDOT:PSS sample deposited over a substrate was immediately used for sensing while other two samples were prepared by the same method and treated during 20 min at 130°C or 160°C, before

[i]The definition of sensitivity (S) is ambiguous, clearly is an indicator which is related to the ratio between the sensor output signal and the analyte effect on this material: some authors as Wang. et al define Sensitivity as R_0/R_g for reducing gases and R_g/R_0 for oxidizing gases. Other authors consider on the numerator the change of resistance, ΔR[242,272].

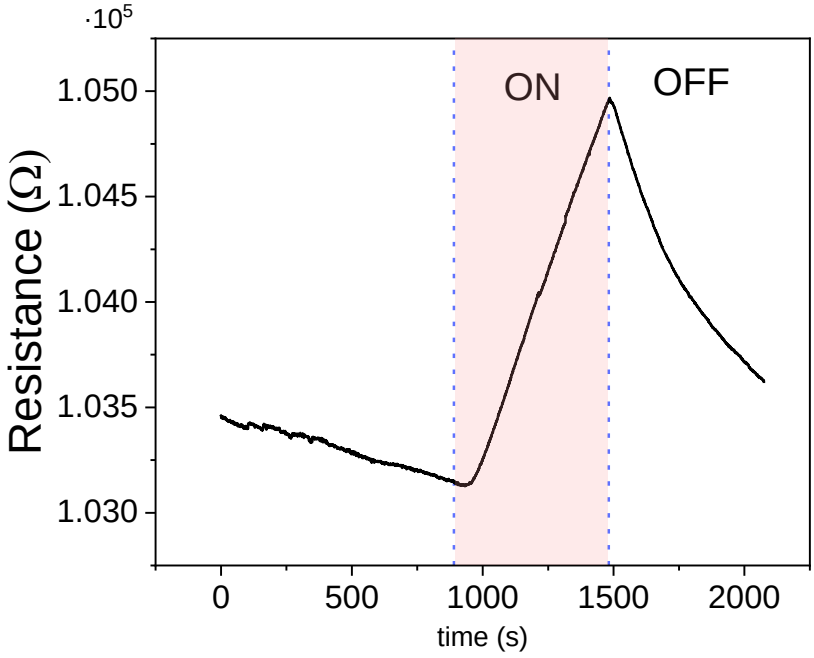

Fig. 7.7: Resistance change vs time using N_2 as gas carrier and ethanol as analyte. Blue line marks the moment when ethanol valve is opened and closed.

recording the measurements. As expected, resistance decreases as the layers were more conductive after removing moisture, during the thermal treatments.

The gas analyte was changed to water vapor as observed in Fig.7.9(a) to check the effect over PEDOT:PSS. In order to compare both analytes under the same conditions, the same sample was used (note that in this case the concentration was higher than 200 ppm as the N_2 was increased up to 4 l/min, therefore the results of ethanol in Fig.7.8 differ from Fig.7.9). PEDOT:PSS possesses a slightly higher sensitivity of 5.56% vs 5.43%, for H_2O as compared with ethanol, respectively. PEDOT:PSS hygroscopic behavior could justify this results, as under water vapor exposure, H_2O will be absorbed by PEDOT:PSS while the PSS layer would decrease its relative thickness. Similarly, in Fig.7.9(b), air was tested as carrier gas and compared with nitrogen. A faster response also was observed but with very similar profile than for the use of N_2 at any working temperature. However, all results were presented at room temperature and using N_2, for simplicity.

Samples with the addition of EG (1% and 5%) were also tested as observed in Fig.7.10, where broad changes were observed. When the EG content was high (5%) the gas sensing response showed and anomalous behavior. On one hand, for both pristine PEDOT:PSS samples and 1% EG, an increase of the resistance with the

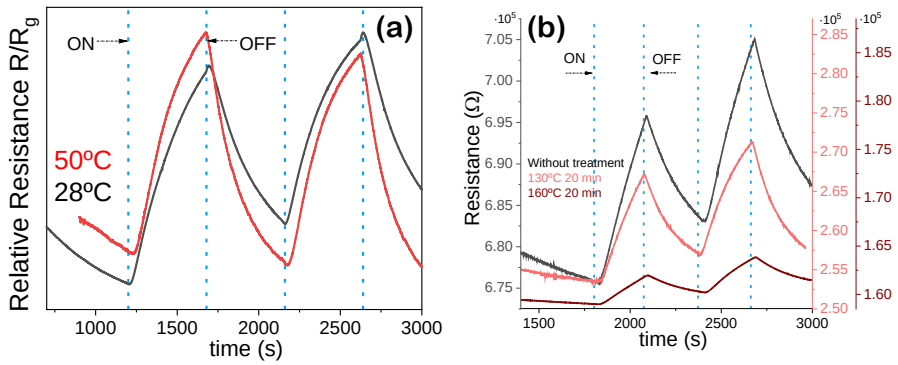

Fig. 7.8: Resistance change vs time due to ethanol interactions with a PEDOT:PSS sample. N_2 carrier gas was introduced at room temperature. In (a) different device working temperatures were used, while in (b) measurements on samples with previous thermal treatments have been studied, at RT.

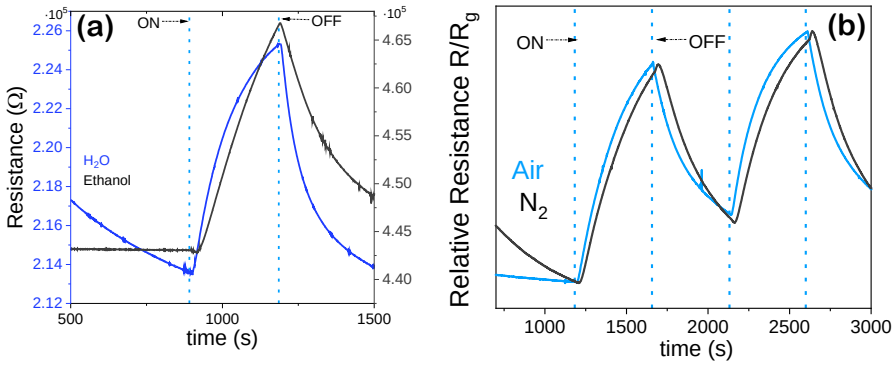

Fig. 7.9: (a) Resistance change vs time due to the ethanol or water vapor entering the chamber, using N_2 as carrier gas and measured at RT and (b) room temperature measurements using ethanol as analyte and either N_2 or air as carrier gas.

ethanol flow is observed. On the other hand, for the sample with 5% EG resistance decreases with the ethanol flow, which is not the expected behavior for a p-type material. Sensitivity also decreases upon EG content, from 0.20% to 0.12%.

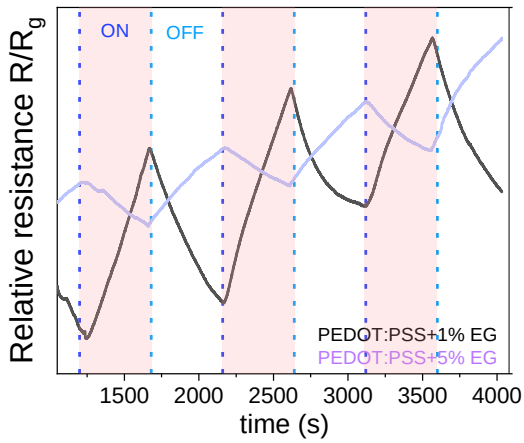

Fig. 7.10: Resistance change vs time for PEDOT:PSS samples with the addition of 1% or 5% EG. The carrier gas is N_2, the gas analyte is ethanol and the measurements were recorded at room temperature.

To asses the effect of the addition of nanoparticles on the sensing mechanism, the same conditions were used for each of the composites. Fig.7.11(a) shows composites with PEDOT:PSS +1%wt of each type of nanoparticle and Fig.7.11(b) shows composites conformed by PEDOT:PSS +1%wt EG as well as +1%wt of each nanoparticle type. To summarize these results, the same cycles were repeated and the sensitivity for each cycle has been calculated and shown Fig.7.12 as a box diagram, in which each point represents one measurement and the central line on the box represent the median which goes from the first quartile to the third quartile of data. Each whisker goes from the maximum to the minimum value recorded.

Without the use of EG very similar results were observed, as shown in Fig.7.12(b), where the best result observed correspond to SnO composites. However, Fig.7.12(b) clearly shows that the best sensitivity was observed when using both EG and SnO nanoparticles.

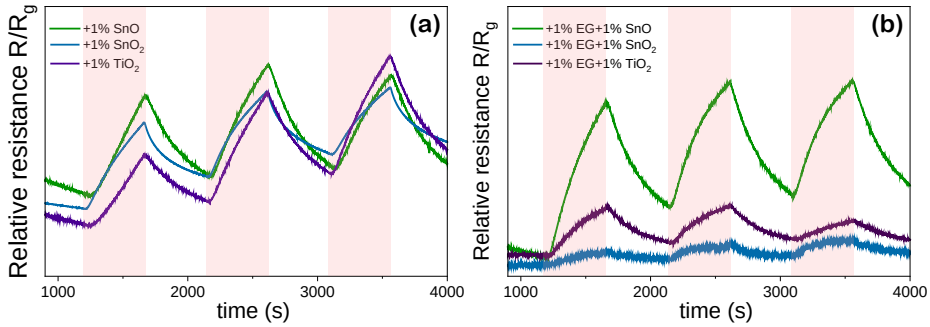

Fig. 7.11: Resistance change vs time for the samples containing (a) PEDOT:PSS +1% wt of either SnO, SnO_2 or TiO_2 and (b) PEDOT:PSS +1% EG+1% wt of either SnO, SnO_2 or TiO_2. For all measurements, the carrier gas is N_2 while the gas analyte is ethanol. Measurements were recorded at room temperature.

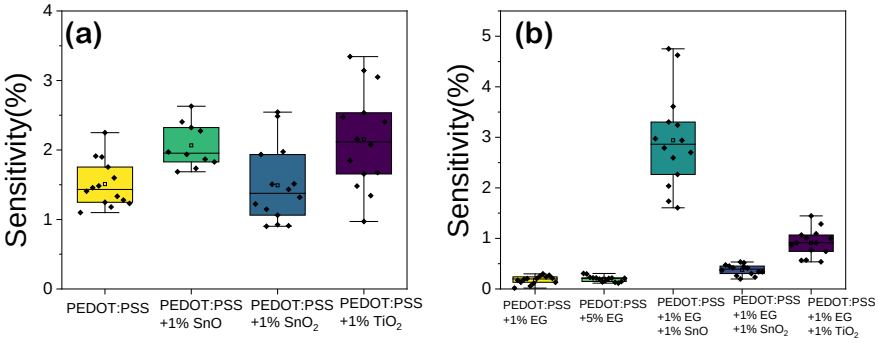

Fig. 7.12: Box diagram showing sensitivity values obtained from PEDOT:PSS composites (a) Containing nanoparticles (b) containing EG+nanoparticles.

7.4.2. Seebeck effect

7.4.2.1. Measuring and data acquisition device: design and testing

The Seebeck coefficient (S), was measured with a homemade setup in a room with relative humidity ranging from 35-38%, which is schematized in Fig.7.13(a). The designed setup consists of two Peltier modules (TEC1-12706, 12V) with a maximum ΔT of 65°C, one of them placed with the hot face facing up and the other facing down. Both Peltier modules were connected to a variable voltage source with two channels to apply different temperature to a single or both Peltier modules, establishing a temperature gradient between them. To dissipate the heat which might be generated on the cold side, both peltier modules were placed over two aluminum heat-sinks (thermal conductivity coefficient, κ ~1.5 W(mK)$^{-1}$). Over

both Peltier modules, a small piece of very thin copper (d <1 mm) was glued with thermal paste (Boron nitride, Akasa AK-456, κ ~1729 W(mK)$^{-1}$). Both Cu thin layers were placed separated by 0.5 cm and over them the sample was placed, in such a way that physical contact was assured between the sample and Cu layer. The layers were deposited over glass substrates. Two K-type thermocouples were placed on the surface sample and connected to a temperature acquisition card (Adaptative Junior Controller ADJ-48-450-UR) to measure the temperature difference (ΔT) and two thin Cu cables were welded with two drops of a Sn/In (95%/5%) alloy (see chapter 1, Fig.2.4) connected to a Keithley 2000 multimeter to measure the voltage difference (ΔV). If the thermocouples were apparently not making physical contact with the sample, both were gently pressed over with a cover glass, fastened with two pressure clamps.

To increase/decrease the Peltier module temperature, a power supply working between 0.0-5.0 V was used. Through the use of only one of the Peltier cells, a temperature difference of ~ 30°C between the cold and hot junction was induced, as observed in the thermal image of the equipment, shown in Fig.7.13(b). This temperature difference was clearly smaller when measured over the sample due to heat losses attributed to heating of both the copper thin metal plate and most notably, the glass substrate, which thermal conductivity were estimated around κ ~400 W(mK)$^{-1}$ and κ ~0.8 W(mK)$^{-1}$, respectively. The maximum difference of temperature over the sample was always less than 40°C. If we inspect Fig.7.13(b) we can see how the heat is transferred to the substrate and how the right side of the sample is heated.

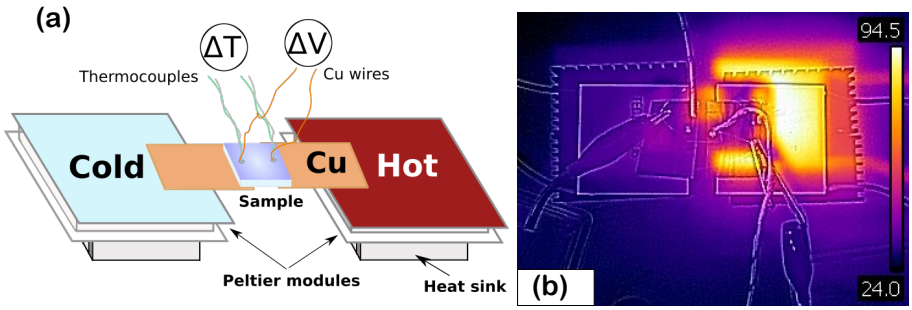

Fig. 7.13: (a) Design of the equipment to obtain the Seebeck coefficient and (b) Top view-thermal image of the equipment when the right Peltier module is heated to the maximum temperature difference.

The measured thermovoltage due to Seebeck effect is shown in Fig.7.14(a). Peltier module was heated until reaching a constant temperature (represented by the plateaus on the graph). As observed, the heating occurs fast (60s) and the

temperature was left unchanged during 200s. Some fluctuations were measured on the voltage during this plateau constant temperatures, of around 7 μV which is less than a 10% error. This error is non-negligible but in average the error is much smaller when the temperature is more stable. This will be considered during the analysis.

The S value was estimated from the slope of the linear relationship between thermoelectric voltage and the temperature difference of the two probes (i.e. $S = -\Delta V/\Delta T$). In practice, the sign of the Seebeck coefficient was not taken into consideration. First, to test the validity of the setup, the same measurement was made by using as cold side the left Peltier module and hot side the right hot Peltier module and switched after. This is possible as in a Peltier module one of the face increases its temperature while the other face decrease it (due to Peltier effect). The approach of this setup was to use one module facing up and the other down, so the cold junction could be decreased at temperatures under room temperature. Still, to test the validity of the setup, both of the modules were placed with the heating side up. These results are shown on Fig.7.14(b) where it is clear that switching the setup brings the same results. The left side of the image was acquired using the left Peltier module as hot junction (i.e increasing its temperature while the right Peltier module was left at room temperature) and vice-versa. It was observed clearly that the slope of the line is the same using either the left or right module as hot junction. So, for the rest of the measurements, the right module was heated and the left module was left at room temperature (cold junction).

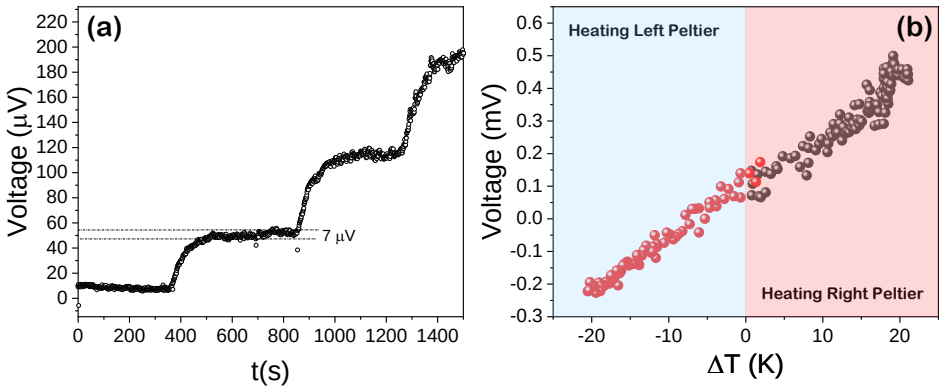

Fig. 7.14: (a) Example of the voltage measured for a sample containing PEDOT:PSS+EG when the temperature was increased and maintained constant represented by the plateau on the graph and (b) voltage measured respective to the temperature difference on the cold and hot junction, where cold and hot junction were reversed.

7.4.2.2. Seebeck effect results

Seebeck coefficient values of PEDOT:PSS whitout and with the addition of EG are shown in Fig.7.15. Seebeck coefficient decreases upon EG addition, decreasing from the pristine value of 22±2 μVK^{-1} until 14.5±2 μVK^{-1}. This value is reasonable compared with the literature which for pristine PEDOT:PSS ranges between 12-25±2 μVK^{-1}[63,182]. For the pristine PEDOT:PSS sample, the corresponding Power Factor (PF), which is defined as $PF = S^2 \cdot \sigma[\mu\text{Wm}^{-1}\text{K}^{-2}]$, and it is an important parameter to determine the thermoelectric properties, are represented in red in Fig.7.15(b). Low value of of $7.07{\cdot}10^{-3}$ μWm^{-1}K^{-2} was estimated for the PEDOT:PSS sample, close to the common value of 0.01 μWm^{-1}K^{-2} for organic polymers[182]. Upon ethylene glycol addition, its conductivity increases as previously discussed, which however, decreases the Seebeck coefficient. In terms of power factor, the best result of 0.84 μWm^{-1}K^{-2} is obtained for 5% EG addition.

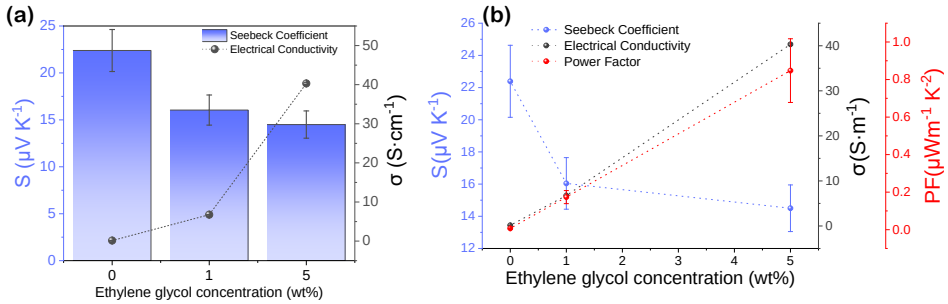

Fig. 7.15: (a) Seebeck and electrical conductivity of the pristine PEDOT:PSS and with 1% wt or 5%wt EG and (b) comparison of the corresponding Power Factor, Seebeck coefficient and electrical conductivity of the samples.

Results on composites without the addition of EG and only composed by PEDOT:PSS and the nanoparticles are summarized in Fig.7.16. Seebeck coefficients are very similar in this case, showing a slight improvement with the use of either SnO or TiO_2 with S values of $\sim$ 27 and 31 μVK^{-1}, respectively. Recalling conductivity from these samples, when nanoparticles are added the conductivity decreases down to $\sigma \sim 10^{-2}$ S·cm^{-1} being the lowest for SnO. Therefore, very similar values within the uncertainty range are observed for each sample.

Finally, composites composed by PEDOT:PSS without and with the addition of 1%wt EG and the nanoparticles in 1% were analyzed. In this case there are substantial changes. For each of the composites, Seebeck coefficient decreases. However, conductivity suffers major changes, reaching the highest value of 16.5 S·cm^{-1} for 1% wt SnO, which corresponds to a PF of 0.23 μWm^{-1}K^{-2} which, compared with PEDOT:PSS+1%wt EG value of 0.17 μWm^{-1}K^{-2}, is clearly higher even for the high uncertainty of the measurement. This improvement can be attributed to the presence of SnO in the composite.

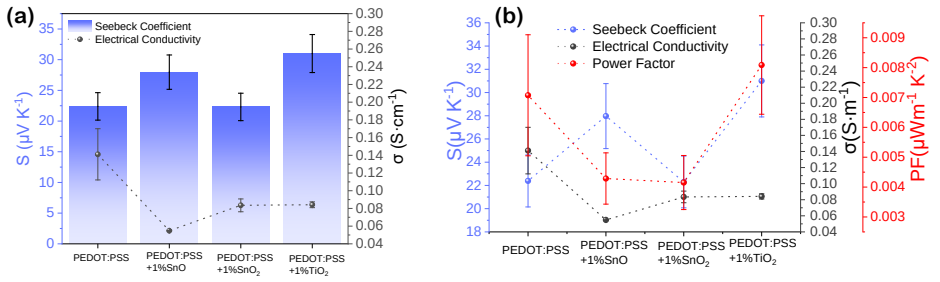

Fig. 7.16: (a) Seebeck and Electrical conductivity of the pristine PEDOT:PSS and with the addition of 1%wt of either SnO, SnO_2 or TiO_2 (b) comparison of the corresponding Power Factor, Seebeck coefficient and electrical conductivity of the samples.

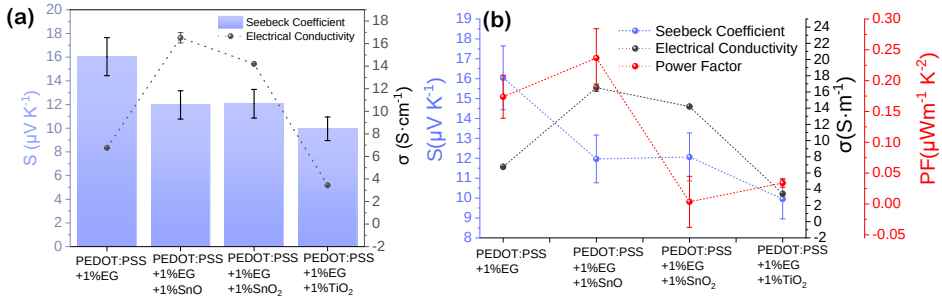

Fig. 7.17: (a) Seebeck and Electrical conductivity of PEDOT:PSS with 1% EG and with the addition of 1%wt of either SnO, SnO_2 or TiO_2 (b) comparison of the corresponding Power Factor, Seebeck coefficient and electrical conductivity of the samples.

7.4.3. Miscellaneous applications: Multi-layers

Finally, in this thesis other structures have been studied. Multilayers are thin films deposited subsequently over the previous layer creating heterojunctions. In this case, PEDOT:PSS layers were coated over previous deposited PEDOT:PSS. For that purpose, the spin coating program was readjusted and before each spin coating the layer or layers were thermally annealed. The thickness of each layer is expected to be around 100 nm. As a proof of concept also TiO_2 thin layers deposited via spin coating were also spin coated over PEDOT:PSS and vice-versa.

As a first approach, stacks were formed by the deposition of PEDOT:PSS layer one over another. A single layer was compared with multi layers formed by either 2 or 3 layers. As shown in Fig.7.18(a), as the PEDOT:PSS thickness increases the layers become more opaque, which is attributed to a higher absorbance on the visible spectra, which is in fact observed in Fig.7.18(b). This is also clear in the Raman modes (Fig.7.18(c)), as due to the thicker layer the signal corresponding to

the PEDOT stretching modes become more intense. The electrical measurements of the layers are shown in Table 7.2 and Fig.7.18(d). Increasing the layer number and therefore, the final thickness, the sheet resistance decreases meanwhile the electrical conductivity increases.

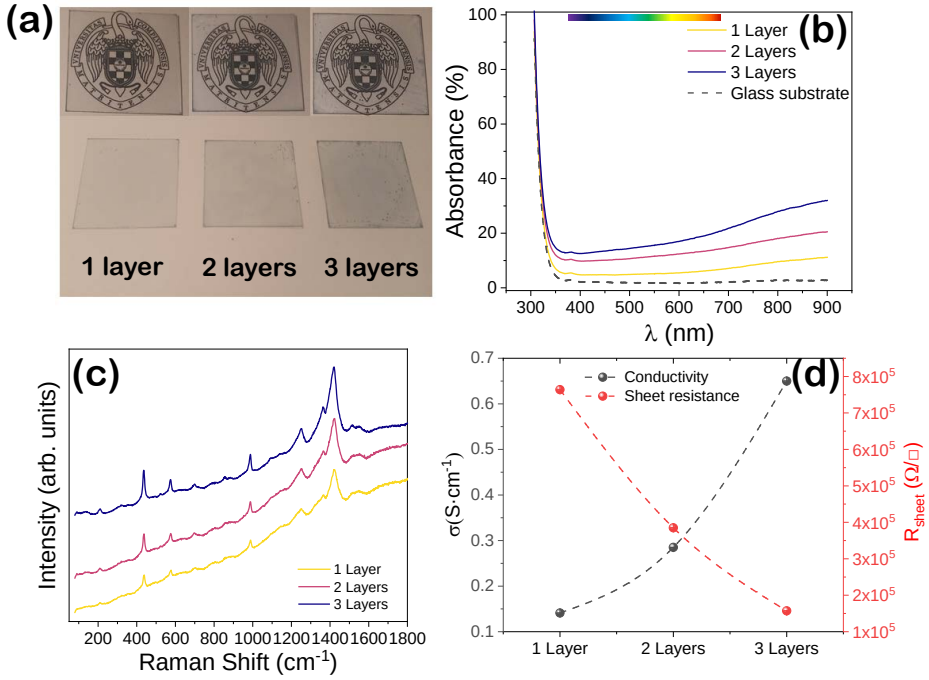

Fig. 7.18: (a) Optical image, (b) absorption spectra, (c) Raman spectra and (d) Hall effect results of PEDOT:PSS samples formed by either 1, 2 or 3 layers.

Table 7.2: Hall effect measurements performed with I=0.1 mA corresponding to the PEDOT:PSS multilayers.

Sample	Conductivity ($S \cdot cm^{-1}$)	Charge Carrier Concentration (cm^{-3})	R_{sheet} ($\Omega/\square$)
1 layer	$(1.41 \pm 0.20)10^{-1}$	$(4.89 \pm 0.11)10^{18}$	$(7.63 \pm 0.11)10^{5}$
2 layers	$(2.85 \pm 0.12)10^{-1}$	$(2.05 \pm 0.11)10^{18}$	$(3.85 \pm 0.21)10^{5}$
3 layers	$(6.52 \pm 0.33)10^{-1}$	$(1.83 \pm 0.29)10^{18}$	$(1.57 \pm 0.07)10^{5}$

Thermoelectric properties of these layers have also been tested, as shown in Fig.7.19(a). As the electrical conductivity increases, there is a decrease on the Seebeck coefficient. However, the decrease on the Seebeck coefficient does not

affect the Power Factor, which is increased upon layer stacking (Fig.7.19(b)).

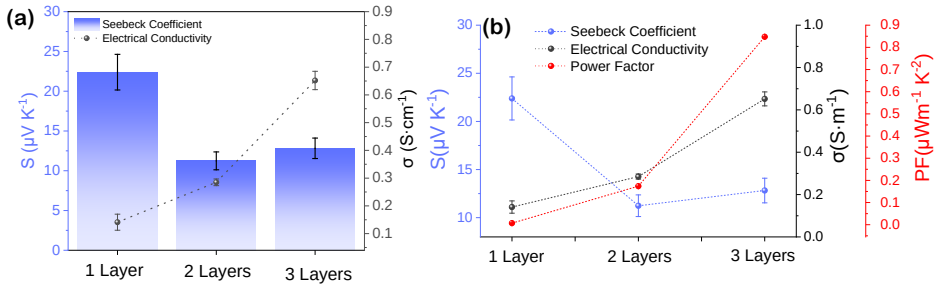

Fig. 7.19: (a) Seebeck and Electrical conductivity of samples formed by 1, 2 o 3 layers of PEDOT:PSS and (b) comparison of the corresponding Power Factor, Seebeck coefficient and electrical conductivity of the samples.

The process of enhancing layer conductivity can be complex and depends of many factors, either the proper morphology of the layers as well as the secondary doping. Decrease upon high secondary doping has been reported[239] which is accompanied by a decrease on the sheet resistance. Electrical conductivity has been reported to increase with thicker PEDOT:PSS layers while the Seebeck coefficient increased with decreasing thickness. Obtaining the balance of the thickness with improved electrical conductivity, while mantaining the Seebeck coefficient as high as possible, which is regarded as the most limitant factor for high PF thermoelectric, should be taken into account.

Similarly, the possibility of obtaining thin layers of the nanoparticles synthesized on the previous chapters was explored. To obtain layers using TiO_2 nanoparticles the first step was to grind them manually until a fine powder was obtained. Different solvents were tested (distilled water, 2-propanol, acetone and ethanol). The best results on terms of dispersion homogeneity were obtained by using 2-propanol (PanReach, AppliChem).

The mixture of the desired nanoparticle concentration was introduced on an ultrasonic bath for at least 30 min. These layers were successfully obtained over both silicon and glass substrates, as observed in Fig.7.20(a)-(c), following the spin-coating steps explained in Table 7.3. It is worth mentioning that, instead of methods for obtaining thin layers such as sputtering or CVD, spin-coating has been also proposed but only for sol-gel techniques. In this case, the product is deposited over the selected substrate rather than, after a synthesis procedure to obtain nanoparticles, dispersing them into a liquid mixture. Either way, the spin-speed reported on the bibliography ranges from 1500-4500 rpm, while the substrates should be heated at temperatures ranging from 250-900°C[274–277], to assure homogeneity. Fig.7.20(d)-(e) shows the absorption and Raman spectrum of the obtained layers, which correspond to anatase TiO_2 which absorbance reach ∼17% at 550 nm.

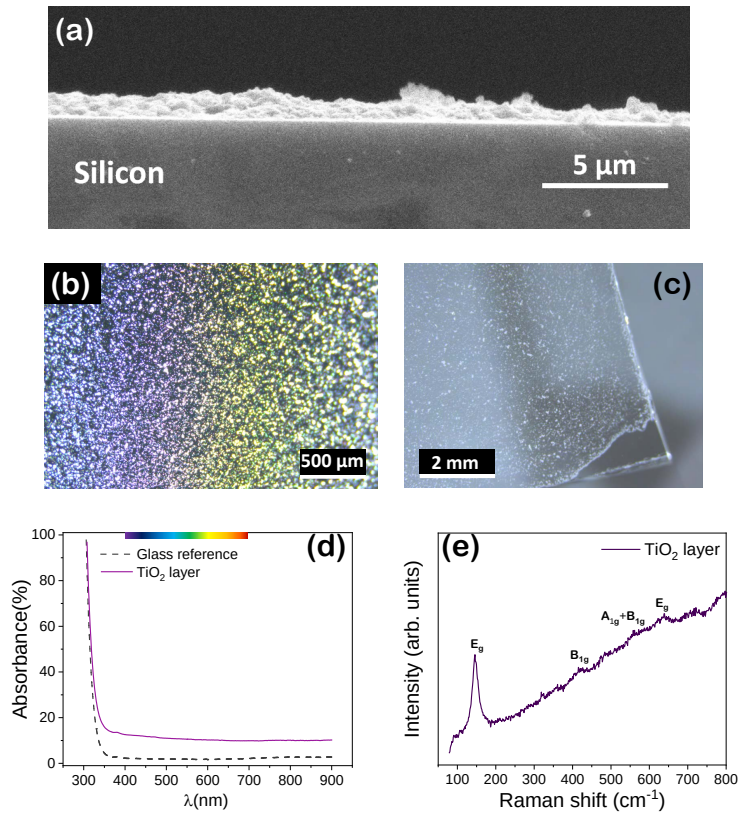

Fig. 7.20: (a) SEM image and (b) optical image of TiO_2 layers deposited over silicon and (c) deposited over glass substrates, (d) absorption spectra and (e) Raman spectra of the TiO_2 film. Optical images were obtained on a Leica DFC295 microscope.

Table 7.3: Thin layer deposition steps and parameters for TiO_2.

$p = 0.08$ bar

Speed (rpm)	Acceleration (rpm/s)	Time (s)	Deposition time(s)	Delay time(s)	Display time(s)
3000	1000	5	5	2	3
3000	1000	30			
4000	1000	20			

7.5. Discussion

In the previous chapter we have discussed the conductivity mechanism of PEDOT:PSS as well as the motivation for its improvement and reduction of the sheet resistance aiming for high performance solar cells. In this chapter, we have focused our attention on two very different PEDOT:PSS applications.

As we have mentioned in Chapter1, PEDOT:PSS (and its based composites), has not been limited to been used in solar cell technologies, two other main applications stand out over the last years: as thermoelectric materials and gas sensors. On one hand, TE are materials, which allow the conversion of heat to energy, are considered as a potential energy source for the near future. To do so, they make use either of the Seebeck or Peltier effect to transform heat in electricity or viceversa. They posses multiple advantages as they do not have moving parts as other devices, which allows to longer operation times and easily scalability[63]. The performance of TE materials is often evaluated with by the dimensionless parameter figure-of-merit ZT. This is because the limit on the energy conversion efficiency is determined by the Carnot cycles, which is related to the figure of merit. This parameter is given by $ZT = S^2\sigma T/\kappa$, where S, T, σ, and κ stand for the Seebeck coefficient, absolute temperature, electrical conductivity, and thermal conductivity, respectively. For simplicity, much works deal with the calculation only of the product of the square of S and σ which is known as Power Factor,PF. This assumption is reasonable for certain materials such as polymers, including PEDOT:PSS, as their value of κ is poor and it also does not change significantly with inorganic additives or dopants ($0.1 - 0.3$ $W{\cdot}m^{-1}K^{-1}$)[63], which is a key factor for high ZT-thermoelectrics. Within this low variation of κ, PF is studied rather than ZT. A higher PF is the fingerprint of better thermoelectric behavior, which increase is not trivial, since sigma and S are related. Taking a look into the Mott formula[278]:

$$S = \frac{8\pi^2 k_B^2}{3eh^2} \cdot m^* \cdot T \cdot \left(\frac{\pi}{3n}\right)^{\frac{2}{3}} \tag{7.2}$$

where n, e, μ, k_B, h, m^* are the carrier concentration, electron charge, carrier mobility, Boltzmann constant, Planck constant, and effective mass of the carrier, respectively. And comparing with the following expression:

$$\sigma = n \cdot e \cdot \mu \tag{7.3}$$

Is clear that S is inversely related to σ.

The most known TE materials have been inorganic fillers, most notably Te, Bi or Sb-based semiconductors (e.g Bi_2Te_3) and oxides (e.g. $SrTiO_3$) with some of them exhibiting outstanding ZT$\sim$1[64,278] which have several limiting factors most notably, toxicity or poor mechanical flexibility. These materials can be considered as critical materials from the point of view of sustainability, as not only their inherent toxicity, but also their synthesis method, generates a high amount of waste. Their scarcity creates the necessity of replacing these materials in their present applications. Instead, PEDOT:PSS-based thermoelectrics can be easily synthesized by low cost effective methods such as electrochemical polymerization[67,279]

and easily assembled in form of thin layers employing different techniques such as inkjet printing, screen printing, doctor blade, spray deposition or spin-coating[60], which are regarded as sustainable processing methods. The main objective for polymer TE is the difficulty to achieve a large Seebeck coefficient in combination with a large electrical conductivity. S is almost constant or increases steadily for different PEDOT:PSS based materials, while σ can increase strongly, up to 4 orders of magnitude. Engineering the electronic structure of polymers to have a favorable density of states and Fermi level is the key to solving the problem[280]. In this sense, the use of dopants could affect the density of states and allow to develop high efficient thermoelectrics.

On the other hand, the detection of harmful gases on low concentrations has become crucial due to security reasons. There are several types of sensors such as electrochemical sensors, biosensors or chemiresistive sensors. Chemiresistive sensors are probably the most used ones due to their simplicity, fast response, scalability and low cost. Their working principle is based on the change of two-point resistance due to chemical reactions induced by the analyte at the surface of the sensor. For the case of polymers such as PEDOT:PSS, the resistance is measured in two points of the sample while a target gas (analyte) passes through the material. This may induce changes due to the caption of electrons via reduction processes or other chemical reactions at the sensor surface, which translates into a resistance change which can be monitored. Resistance change is the primary measurement for calculating the sensor response[281]. MOs are regarded as the main chemiresistive sensors[5], due to their stability and good chemical response, but high operating temperature is their main limitation in gas sensing application. High working temperatures not only raises the power consumption, it also reduces the effective sensor lifetime. Organic materials bring novel properties and balance the energy-efficiency ratio. Not only it is possible to create flexible and scalable sensors, they also are fabricated by low cost methods. Thus, it is necessary to find the balance between energy-efficiency and performance. These chemosensors can be easily deposited over substrates and contacted to measure the changes on the resistance. Polymers such as PEDOT:PSS possess a resistive response to a wide variety of gases. PEDOT:PSS can be blended with different functional materials such as metal oxide semiconductors through solution processes and the obtained composites could improve their performance[279].

In this chapter the assembly of PEDOT:PSS composites and its possible implementation as thermoelectric materials or gas sensors has been presented. The samples used in this chapter have been therefore, pristine PEDOT:PSS, PEDOT:PSS with the addition of the nanoparticles (SnO, SnO_2 and TiO_2) as well as PEDOT:PSS with Ethylene glycol and with the addition of the same nanoparticles in the same concentration (1% wt). The intention is to observe the changes obtained with the addition of nanoparticles and EG all together as well as separately.

Unlike in the previous chapter, where our study was limited to PEDOT:PSS

containing DMSO, herein we will study both pristine and EG-doped PEDOT:PSS. Understanding the possible topography changes due to the addition of different concentrations of EG is important to recognize its effect on the final thin layer electric behavior. It is well known that the structure of PEDOT:PSS, especially after secondary doping, posses a granular-like structure, at is has been widely reported for EG[243,266,269,282] and for DMSO[22,68,272] by AFM results. This morphology is generally described as being composed of a PEDOT-enriched core and a polyanion (PSS^-) shell[64]. Pristine PEDOT:PSS presents an amorphous-like structure, as observed in Fig. 7.2, generally exhibiting a small surface roughness which is increased upon EG content, mainly to the creation of the grains, creating topography-height steps. Cui et al.[269] attribute to EG the favorable phase separation of PEDOT:PSS films, which creates a continuous conductive pathway in the film. This is similar to observations. The use of certain techniques such as Polarized Optical Microscopy (POM) by Bubnova et al.[283], confirms the amorphous structure of PEDOT:PSS thin layers. Concerning PEDOT:PSS structure, Grazing Incidence Wide-Angle X-ray Scattering (GIWAXS) is particularly suited to probe the crystal structure of thin films on molecular length scales and has been proven highly successful in characterizing PEDOT:PSS[283,284], which shows that PEDOT:PSS may be formed by separated PSS domains, with preferably orientation of the π-stacking out-of-plane.

These composites present similar transmittance spectra. The addition of EG decreases the transmittance by 1%. This change is not a relevant drawback as it still preserves nearly $\sim$ 90% transmittance, which we have discussed it is mandatory for high performance optical devices. It should be noted that from AFM measurements, thin thickness has been always considered $\sim$ 100 nm. This is for the most part true as with the selected coating procedure, thin films should be close to this expected thickness ($\pm$40 nm), also induced by the small size of the coating covered glasses (1.5×1.5)cm^2. Although this is true with the use of pristine PEDOT:PSS, the use of 6% EG has shown an improved transmittance at 550 nm near 93%[271], but also this layer shows different thickness. The changes on the thickness due to the addition of EG, which allows a better dispersion on the substrate, could affect the transmittance. This thickness plausible error interval has been considered when calculated some thickness related quantities, such as sheet resistance.

Composites were deposited over silicon substrates and to asses differences with EG addition, XPS measurements had been performed. The S($2p$) core spectra was observed in Fig.7.4. As previously mentioned, the spectra are divided in two main regions, one between 162-166 eV and a higher energy contribution at 166-172 eV. The contribution at lower binding energy is often attributed to sulfur atoms in the PEDOT and the contribution at higher binding energy is attributed to the doping ions PSS^-H^+ or the S atoms in PSS[262,266,285]. Different authors[262,266,285,286] have indicated that the evolution of the corresponding S-peak of PEDOT with increasing EG content, is an indicator of changes on the PEDOT:PSS conformation and removal of PSS, which enhances conductivity. In our case this increment is

observed relative to the PSS -S- peak. The addition of EG has been reported to remove PSS from PEDOT:PSS[26,262] as the addition of EG or DMSO[284] modifies the intensity ratio of the S($2p$) relative to PEDOT, which increases with content. In our observations, PEDOT/PSS ratio changes from 1:1.83 to 1:2.93 with EG addition. Nanoparticle addition of respectively, SnO_2 or TiO_2, changes the ratio to 1:3.16 and 1:2.47. TiO_2 appears to affect PEDOT:PSS the most, which is in agreement with both C($1s$) and O($1s$) observations.

O($1s$) core level shows major changes with the nanoparticle addition. Initially for PEDOT:PSS a major contribution at ∼532.2 eV is observed and upon EG addition a shoulder at ∼531.3 eV increases. Some authors,[286] attribute the first peak to C=O bonds and the peak at higher energy to C-O bonds. With the addition of nanoparticles other contribution appears at ∼533.9 eV, which is strongly increased for the TiO_2 samples, which can be attributed to the formation of bonds within the Ti-O and the polymer.

Hall effect measurements have shown the electrical conductivity and the charge carrier concentration of the different samples summarized in Table 7.1. EG addition has shown an increase of the conductivity, as it has been reported up to 10^3 $S{\cdot}cm^{-1}$ [26,269,287] depending on the EG concentration as well as on the properties of the initial PEDOT:PSS, with 5% wt EG being expected to give an increase of 3 orders of magnitude[282]. PEDOT:PSS posses p-type conductivity which is preserved and enhanced upon EG doping, given by the sign on the carrier concentration which is also enhanced upon doping.

EG-doped films conductivity enhancement is mainly attributed to the creation of a large number of charge carriers in the polymer backbone with the addition of EG. Additionally, the elongation of polymer chain length and the ease with which charge carriers (polarons/bipolarons)[ii] hop between the conducting PEDOT and insulating PSS chain could result in improved conductivity[272]. Moreover, it has been proposed that the EG favors the formation of monolayers of either PEDOT or PSS which also enhances conductivity, due to an screening effect[272]. UV-vis results also give a hint about the presence of bipolarons, as it has been reported that the disappearance of a contribution near 850 nm is related with the formation of bipolarons (enhanced with doping)[288]. On the previous chapter we have discussed that some authors[263] pointed out that the neutral polymer chains show absorption around 600 nm. In that region we observed differences with the addition of nanoparticles, which may interact with the polymer and enhance the number of charge carriers. Morphology of the layers is directly related with their electric properties. Lin et al.[267] reported that increasing EG content increased root-mean-square (R_{rms}) which means that the total number of particle boundaries (for a given volume) increases, and, therefore there are an increase number of energy barriers for charge conduction, which increases the inter-chain hopping resulting in inferior charge transfer between PEDOT chains

In this dissertation, the addition of 1% EG enhances the conductivity by a

[ii] A polaron corresponds to a positive charge on a unit and a bipolaron corresponds to two positive charges that are delocalized over several units.

factor of 40 being $6.75 \cdot 10^1$ S·cm^{-1}, and the use of 5% wt by a factor of 285, reaching $4.03 \cdot 10^1$ S·cm^{-1}. The use of MOs nanoparticles has been gaining interest, despite that some reports have pointed out that the use of TiO_2 increased sheet resistance[76]. Lin et al.[289] have introduced ZnO, which improved conductivity and was attributed mainly to the enhancement of carrier mobility. The temperature dependence showed that the mobility was dominated by tunneling at low temperatures and hopping at high temperatures for bare PEDOT:PSS but with the introduction of ZnO the temperature dependence is increased, dominated by tunneling which was attributed to weak electron-phonon coupling and changes on the chemical structure of PEDOT:PSS. Their observed improvement was by adding only 0.09% wt or 0.18% wt of ZnO, which are low dopant concentrations, as followed in this work. However, the mixture containing ZnO also contains a well-known secondary dopant, methanol, which could be the responsible for the conductivity enhancement. This would agree with our observations when 1% of nanoparticles (a concentration 10 times higher) does not increase conductivity, on the contrary it is decreased up to 10^{-2}S·cm^{-1}. This was avoided with the use of EG which also acts as a surfactant for the nanoparticle dispersion. SnO nanoparticles with EG provide the maximum increase in conductivity which is 117 higher than the observed for pristine PEDOT:PSS, $1.65 \cdot 10^1$ S·cm^{-1}, which is also superior than the obtained when only EG is used, which was $6.75 \cdot 10^1$ S·cm^{-1}. Therefore the addition of the nanoparticles increases the conductivity related with the use of EG by a factor of 2.5.

PEDOT:PSS has been regarded as a high sensitivity sensor with appropriate selectivity[23]. The most important parameters in a chemiresistive sensor are sensibility, selectivity[242], response and recovery time to characterize any gas sensor. In our setup the gas flow was maintained to a constant concentration of 200 ppm on the chamber with a mass flow controller at the exit. Most of the literature dealing with gas sensors based on PEDOT:PSS combine this material with carbon allotropes such as graphene to detect NH_3[290] or reduced graphene to detect nitrogen, NO_2, CO or ammonia[291]. Pristine PEDOT:PSS doped with EG has been used to detect methane, butane[272] and fewer works detail the detection of ethanol or water vapor[279]. To our knowledge, SnO_2 or SnO had not been tested in combination with PEDOT:PSS for gas sensing applications. However, PEDOT:PSS has been tested in combination with TiO_2 for different gases such as NO_2[273] or NH_3[242]. Nonetheless, in those cases TiO_2 is used in form of nanofibers or other hierarchical structures. Our approach using nanoparticles shows also novelty. The idea behind this approach is that the used nanoparticles are well known gas sensor devices, as well as the polymer matrix.

Although the main focus was the effect of the nanoparticle addition on the sensing properties, firstly a study of the different sensing conditions for pristine PEDOT:PSS were tested. It has been reported that for certain gas concentration sensitivity increases linearly with EG content. Firstly we have observed the chemirresistive behavior of PEDOT:PSS with the ethanol gas. As PEDOT:PSS

possesses p-type conductivity, exposed to a reducing analyte such as ethanol, its resistance is expected to increase[281]. In fact, the resistance increases in presence of the gas showing a reduction behavior between the ethanol and PEDOT:PSS. The resistance does not reach a maximum due to the low gas concentration of 200 ppm and short time of the gas passing through the chamber.

Four main parameters were tested: time, carrier gas, analyte and temperature. Increasing sensor temperature increases its sensitivity reaching 2.10% at 50°C. Fig.7.8(a) compares this particular cycle with the measured at room temperature for which a sensitivity of 1.93% is obtained. Other temperature-related sensitivity factor was the initial PEDOT:PSS thermal treatment, which results are reported in Fig.7.8(b). Recalling, in this thesis all PEDOT:PSS substrates were treated at 120-130°C to remove moisture. The presence of clusters of H_2O could affect resistance measurements. The same sample was tested: first, without treatment and then after 20 min at 130 or 160°C, respectively. It has been mentioned on this manuscript that those temperatures have not been regarded as harmful for PEDOT:PSS, for short periods of time[22,24]. Each sensitivity observed was 3.01, 5.45 and 1.88 % peaking at 130°C: this temperature removes the maximum moisture which could cover the polymer-conductivity zones which interact with the test gas. Increasing the temperature, either during the cycle or previously, clearly affects the resistance measurements. The presence of water (moisture) causes additional interference to the sensor signal, which has been reported by Gao et al.[279] as a key factor to take into account, particularly for certain analytes such as NH_3 where the interaction with moisture at high humidity ranges could create other undesired chemical compounds such as NH_4OH, leading to large great fluctuations on the resistance. The best results are obtained at RT for a sample previously treated at 130°C, which contribute to the advantages of PEDOT showing a good performance at RT.

Water or ethanol responses are similar, slightly better for water (5.56% vs 5.43%), as observed in Fig.7.9 and almost identical when used Air or N_2 as carrier gas, showing a faster response for air. When N_2 is used, after cutting the gas flow, resistance peaks and then decreases, which can be attributed to the surface of the sample being poisoned by trapped gas on the chamber, which takes a few seconds to dissipate. This effect is not observed by using air, as the chamber is not sealed at vacuum, and when the air flow is closed, there is still air on the chamber.

Nanoparticles effects were summarized in Fig.7.11 and Fig.7.12. SnO with or without EG showed the best values on sensitivity. Considering different cycles obtained in similar conditions (300, 480 or 600 s), for these composites the sensitivity reached ∼5% which is considerably higher as compared with the rest of composites. The reaction mechanisms to understand PEDOT:PSS sensing behavior are complex. Commonly, on a p-type material, before the analyte arrival to the chamber, the oxygen molecules of either the test gas or atmospheric oxygen as the chamber is not at vacuum, could be initially chemisorbed on the surface, which causes the electrons to be removed from the conduction band. These oxygen are converted to single or double oxygen ions (O_2^-), which are ionsorbed on the

surface ($O_{2,ads} + e^- \longrightarrow O^-_{2,ads}$). The electron loss increases the number of holes (h^+) which are the major carrier on p-type materials. This behavior leads to a reduction of the resistance. However, when a reducing gas (such as ethanol) reacts with this ionosorbed ($O_{2,ads}^-$), electrons are donated to the conduction band of the p-type material, which reduces the hole concentration due to electron-hole recombination resulting on a resistance increase[281]. The chemical decomposition of ethanol, which is a reducing agent, and therefore donate electrons produced after the chemical decomposition over the sensor surface follows the following reaction:

$$CH_3CH_2OH_{(g)} + O^-_{ad} \longrightarrow CH_3CHO_{(g)} + H_2O_{(g)} + e^- \tag{7.5.4}$$

It should be noted that other chemical species could be created such as CO_2, which could donate more electrons to the sensor surface.

However, the behavior of a polymer matrix (and particularly with embedded particles) can be more complicated and several mechanism has been proposed to understand the reduction reaction between the analyte and the polymer[272,290], which are mostly redox-reactions or charge transfer between polymer-analyte and polymer swelling.

- The reaction between analyte and polymer could be a reduction reaction where the oxygen is chemisorbed over the exterior surface on the PEDOT:PSS or PEDOT:PSS EG region, which have shown p-type behavior. This could be a primarily mechanism as at low-temperatures such as room conditions and under 100°C, $O_{2,ads}^-$ is the predominant chemisorbed specie and it also could be trapped on the surface between PEDOT:PSS and for example, the nanoparticles. This oxygen blocks charge carrier hopping which, could be the major reason for increasing the resistance.

- The resistance changes could be related also with indirect or direct charge transfer mechanism where the molecules gas (e.g ethanol) are adsorbed onto the surface of PEDOT:PSS via physisorption, which generates delocalizated π electrons. Dopants enhance the surface area and improves its $\pi - \pi$ links, improving sensing performance.

- Swelling process of the polymer, in which the interaction with the analyte causes that the interchain of the short PEDOT chains increases. This PEDOT chains tends to have a shorter interchain distance than PSS and hopping processes between PEDOT chains are the main electron conduction mechanism of this material. Therefore, swelling may induce an increase on the resistance, which returns to its original value as soon as the analyte exits the chamber, which reduces the polymer swelling.

Remarkable is the anomalous behavior, which is in fact opposite to the expected for a p-type semiconductor, observed for the sample containing 5% EG. This could be attributed to the presence of competitive mechanism, in which one mechanism decreases the resistance and the other increases, as expected, the resistance. The mechanism which could decrease the resistance could be the physisorption of the

ethanol molecule over the PEDOT:PSS surface, which could trap electrons on the surface and therefore, will decrease the resistance. This effect should be considered for energy bonds of low energy in the order of 0.01-0.1 eV and caused by forces of electrostatic nature. It should not be neglected that under water or ethanol exposure the PEDOT:PSS film thickness could decrease, which can also alter its conductivity. We can assume that the most likely configuration of PEDOT:PSS is composed by grains of PEDOT wrapped inside PSS chains, as it has been widely notable under EG or DMSO influence,[22,68,243,266,269,272,282] in agreement with our AFM measurements. It is likely that the water-soluble PSS gets removed first from the surface, thus inducing a posible thickness reduction. This effect is competitive with the overall thickness decrease (lower thickness equals lower resistance). However, the insulator nature of PSS will increase conductivity and, therefore, lowers the resistance.

The proposed mechanisms which could lead to an increase or a decrease on the resistance of the p-type sensor are depicted on Fig.7.21.

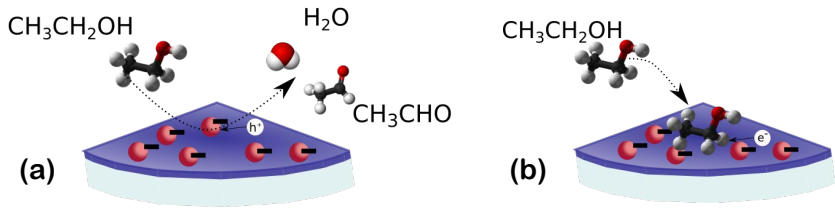

Fig. 7.21: (a) Sensing mechanism of p-type PEDOT:PSS due to ethanol reaction by decomposing the ethanol molecule into acetaldehyde and water (b) physisorption of an ethanol molecule over the surface, which catches an electron.

The differences on the sensing mechanism of composites containing nanoparticles respond to two different effects: polymer-behavior changes due to nanoparticle addition, related to conformational changes on the PEDOT backbone (i.e increase of conductivity due to SnO addition or EG easiness of the chain stiffness) and proper MOs sensing mechanism.

MOs sensing principles have been studied in the last 50 years. In this case, an n-type MOs such as TiO_2 or SnO_2 will posses surface states which behave as electron donors or acceptors at the surface. These states cause an exchange of electrons within the bulk of the semiconductor forming a space layer close to the surface. The target gas will interact, with higher success if the surface presents porosity, and if the gas is reductor the MO will get oxidized resulting on electrons returning to the conduction band, which reduces the space charge width proportionally to the analyte concentration. This results on a conductivity increase (resistance decrease) for a reducing gas for n-type semiconductors. On the case of p-type semiconductors such as SnO, the behavior is the opposite and the resistance increases upon the presence of a reducing gas, which gives electrons to the conduction band, reducing

the number of holes. This behavior could explain the reason of higher sensitivity in SnO doped PEDOT:PSS where there is no competing mechanism in presence of the reducing gas.

Similarly, changes on the PEDOT:PSS structure can be due to the interaction with the nano-size nanoparticles, which via Couloumb interaction will react with the polymer chain (as well as for EG addition) strongly changing the chain conductivity. This interaction could shorten PEDOT paths which would enhance hopping, therefore lowering the resistance. The region between nps/PEDOT:PSS is expected to be complex and mostly conformed by Schottky barriers, which does not differ much with the similar contact between grains on MOs semiconductors. The improvement of SnO upon the rest of MOs studied could be attributed to the enhancement of the charge carrier upon SnO doping.

Regarding the sensitivities, competitive values have been obtained in this work. For most of PEDOT-based devices, at 100-200 ppm sensitivity ranges around $\sim$1%,[281] which is close to our observations. It should be considered that the overall performance of chemiresistive sensors is a consequence of several factors such as the sensing material or the device geometry. Particularly, electronic chemosensors are often based not only on conductive sensing materials directly deposited onto the substrates, rather on simple Interdigital Trasducer (IDT) which due to its low size and cost are commonly used for monitoring humidity and gas chemicals[279]. Optimizing the uncovered surface to interact with the sensor may led to higher sensitivity.

The second application that has been evaluated in this chapter are the thermoelectric properties of the PEDOT:PSS based composites. TE properties of PEDOT:PSS have been widely discussed on the literature[287,292] in recent years. Pristine PEDOT:PSS presents low TE properties mainly due to its poor conductivity ($\sigma \sim 0.1 - 1$ S·cm^{-1}) and limited Seebeck coefficient ($S \sim 15$ μV K^{-1})[293] which leads to poor PF. Low S coefficient for PEDOT:PSS is attributed to the fact that, by recalling Mott's formula, S is proportional to $[d(ln(N(E))/dE)]_{E=E_F}$ where the DOS (represented by $N(E)$) at the E_F does not vary much, as confirmed by UPS results[283,294], which explains the low Seebeck coefficient. However, doping could change the behavior of the PEDOT:PSS chain, which could be at bipolaron state. In this state, the E_F is in a slowly varying region of the DOS, which could indicate a better thermoelectric properties.

In the literature, many different methods to improve the conductivity have been reported so far, as mentioned on the previous chapter, chapter 6. Some of the methods involve acidic treatment or organic solvent dipping[295]. These post treatments enlarge the charge carrier concentration, and bipolaron are the main charge carriers. However, this high doping level results in a small Seebeck coefficient (S) of PEDOT:PSS because of the extra charge carriers[296] and a shift on the Fermi level to the edge of the conductor[278]. Particularly, EG is used to improve the conductivity up to 10^3 S· cm^{-1}[26,269,287]. However, the Seebeck coefficient has been reported to not to change saliently reaching PFs of 25-30 μWm^{-1}K^{-2}.

Before discussing Seebeck coefficient values, it was necessary to design a system to measure it experimentally. Seebeck coefficient measurements are most commonly realized in homemade setups due to simplicity[285,296–298]. Frequently, the designed setups for measuring Seebeck effect can be divided in two-probe or four probe schemes, with thermocouples clamped to the material to determine the temperature gradient. Other methods to more precisely estimate the value of the Seebeck coefficient could be quasi-steady-state differential methods[297]. Our approach to measure PEDOT:PSS Seebeck coefficient was described in Fig.7.13(a). The main objective was to design a simple, low-cost and reliable equipment, based on two Peltier modules with only one of them used as hot junction whereas the other has been left at room temperature. The temperature from the left Peltier module used as cold junction could be decreased up to 3-5°C under room temperature. Reaching lower temperatures (which nominally are possible with attending to the Peltier module specifications) was not possible, as the heat produced from both its other face (hot side) as well the other Peltier module, as they are connected through the sample. The hot junction could reach temperatures as hot as 94.5°C, as observed in the thermal image presented in Fig.7.13(b). The validity of this setup was measured with different samples, times and approaches. As proof-testing step, the same temperature until the steady state was reached, was placed and the values obtained over time were compared. It was observed that the uncertainty was always below 10%, as shown in Fig.7.14(b). This was reasonable with the setup itself. To diminish this error, the measurements were repeated and averaged, and the stage was also isolated with a glass container from vibrations and room humidity. It was also observed that current could flow through the thermocouples so the measurements were repeated and measured over the same conditions. Fig.7.13(b) shows the same thermovoltage obtained over pristine PEDOT:PSS samples when the cold-hot junctions were reversed under the same conditions. Therefore the V/T line could be extended to pursuit a better fitting. Determining the exact uncertainty derived from this equipment was not trivial, as there are oscillations of the measured voltage as well as other uncertainty factors, which mostly are nullified by repetition and averaging. A conservative approximation was rounded to a 10% error. This equipment does not measure *in-situ* conductivity which is obtained via Hall effect. To estimate Power Factor, the conductivity can be more simply obtained from 4-point probe measurements[296] from *ex-situ* measurements, either by Hall effect or even from sheet resistance measurements.

Regarding our results the use of EG improves PF mainly because there is a small decrease of the Seebeck coefficient from ∼22.4 to 16.0 and 14.5 μVK^{-1} accompanied by the previously discussed increase on conductivity, upon EG doping. Composites combining nanoparticles and PEDOT:PSS did not improve conductivity, similar to what has been reported with the use of Au nanoparticles[299]. This behavior contradicts what was observed in the previous chapter when the use of nanoparticles improved conductivity. However, in the present case no secondary dopant is used which properties also increments wettability and might act as surfactants. Optical images clearly showed poor dispersion of the nanoparticles.

Despite that, Seebeck coefficient remains similar and is increased with the use of TiO_2 nanoparticles reaching a value of ~ 31.6 μVK^{-1}. Composites which comprise EG and nanoparticles exhibit upgraded properties. With the addition of SnO conductivity reaches the maximum value observed (with 1% EG) of 16.5 $S{\cdot}cm^{-1}$ with a Seebeck coefficient of $\sim 12.0 \mu VK^{-1}$, causing a PF of 0.23 $\mu Wm^{-1}K^{-2}$. This is $\sim$1.4 times higher rather than using only EG and $\sim$34 higher than pristine PEDOT:PSS. These results are less appealing than discovering a PF$>$ 20, yet it should not be forgotten that conductivity of the pristine PEDOT:PSS used is 10^4 lower than PH1000 PEDOT:PSS which most likely will replicate the same PF improvement up to SnO+EG doping. Relative improvement of 34 times is competitive with the best results obtained upon nanoparticle doping. As an example, during the redaction of this thesis, a first work has been published on the use of SnO_x[284] to create PEDOT:PSS/SnO_x, which increased PF between 7 and 28 times depending if they used DMSO or not. In our case, this enhanced performance of TE is mostly attributed to the enhancement of conductivity as the Seebeck effect tends to decrease. For reader's perusal, PF is not the definitive indicator than the TE properties are enhanced. ZT is much more reliable which are also related with the thermal conductivity coefficient. We are not neglecting that κ could change upon nanoparticle addition as previous reports have indicated an increment within 0.16-0.5 of different Bi, Se nanoparticles compounds[63] and within 0.2-0.4 with carbonaceous fillers. Relative small changes are observed as compared with the wide range of orders of magnitude of the Seebeck coefficient and mainly electrical conductivity, so it could be expected that PEDOT:PSS thermal conductivity is not the limiting factor for thermoelectric applications. The specific effect of the SnO nanopowders over PEDOT:PSS could be also understood with a modification on the crystal structure of PEDOT. This has been recently suggested by GIWAXS measurements by Dong et al.[284] where the overlapping on the PEDOT packing modes can suggest that the driving force is conformed by a dedoping process of the SnO_x-nps and the PSS^-. In our case, we have observed that the addition of nanoparticles such as TiO_2 appears to affect the surface ratio of PSS, as observed via XPS.

To put our results in perspective, it is illustrative to compare our results with the literature. From different reviews on the topic[63,292], we observe a variety of reported PF ranging from 0.1 to $\sim$320 $\mu Wm^{-1}K^{-2}$. To obtain high PF, it is not enough to increase conductivity, as the Seebeck coefficient ideally should be also improved or at least remain constant from the value of pristine PEDOT:PSS, which is low due to the p-type nature of the polymer. The main approaches to increase the thermoelectric abilities could be divided in two groups: modifying PEDOT:PSS by secondary doping, chemical de-doping and post treatments or create composites, most commonly: with inorganic, carbonaceous or other fillers. Some of the most notable results are presented on Table 7.4. In this table not only the enhanced PF values are given, as also the value given by the authors of the pristine material before their treatment is indicated, and so the relative improvement of the PF is calculated. Therefore, as some values are not explicitly given by the authors, they have been obtained from the figures, which may be ± 2 $\mu W\ m^{-1}K^{-2}$ off.

Table 7.4: Improvement factor of the PF before and after different approaches followed on the references presented. Note that PF is given in its common unities,($\mu Wm^{-1}K^{-2}$). Marked in red are our results, which are among the highest relative increments.

Treatment/ Material	PEDOT:PSS	Compounds	PF before	PF after	Increase factor	Ref.
PEDOT:PSS						
Secondary doping	PH100	DMSO and PEO	0.25	156.45	631.87	[294]
	Sigma-Aldrich	EG	0.01	0.85	119.83	This work
Dedoping	Synthesized	hydrazine/ DMSO	54.9	115.5	2.10	[300]
Post-treatments	PH1000	TMF acid/ MeOH	0.02	133.48	6244.92	[298]
	PH1000	Hydrazine	39.63	93.72	2.36	[296]
	PH100	DMSO	0.001	44.97	38932.48	[301]
Composites						
Carbonaceous fillers	PH500	SWNT	9.80	78.40	8.00	[302]
	PEDOT	rGO	1.44	5.14	3.57	[303]
	Sigma-Aldrich	GO	0.25	0.44	1.73	[253]
		GQDs		1.62	6.40	
		rGO		0.68	2.68	
TE inorganic fillers	PH1000	Bi_2Te_3	46.57	131.00	2.81	[280]
	PH1000	Ag_2Se NW	12.22	327.15	26.77	[278]
	PH1000	Au	37.34	51.26	1.37	[299]
Oxide fillers	PEDOT	TiO_2/ZnO	0.44	1.29	2.95	[304]
	PH1000	SnO_x	0.03	0.43	14.34	[284]
		DMSO/SnO_x	6.00	122.20	20.37	
	Sigma-Aldrich	EG/SnO	0.01	0.24	33.45	This work
		TiO_2	0.01	0.01	1.19	

On one hand, creation of composites can enhance the TE properties of PEDOT:PSS. A reasonable idea is using materials with high Seebeck coefficient, as Zhang et al.[280] who used Bi_2Te_3 powder composites with PEDOT:PSS, obtaining power factors ~40 μW m^{-1}K^{-2}. In this approach they create a layer of PEDOT:PSS over Bi_2Te_3 as well as analyze the use of DMSO in different concentrations and the use of p-or n-type Bi_2Te_3. However, neither the relative improvement is outstanding and, most notably, the approach of combining a high-ZT toxic material with PEDOT:PSS misses one of the main reasons of using polymers: low toxicity. In this regard, even that the use of Ag_2Se-NanoWire (NW) led to great relative improvement[278], the low toxicity premise is still broken. Similarly as observed with their applications in solar cell technologies, the first approach was the use of Ag nanoparticles which nonetheless did not improve notably the electrical conductivity[299], which led to a poor increment on the final PF. The family of

carbonaceous materials led to various results. Moriarty et al.[302] et al. added 95% of Single-Walled Carbon Nanotubes (SWNT) on a different approach of embedding materials into a PEDOT:PSS thin layer TE, focusing their study on the thermal conductivity and Seebeck coefficient of the SWNT. Other carbonaceous allotropes (GO,rGO,Graphene Quantum Dot(s) (GQDs))[253] give a modest increase on the PF, most notably for the use of GQDs. Oxides had led to great results. The use of combined TiO_2/ZnO composites with PEDOT increased PF from 0.44 to 1.29 $\mu Wm^{-1}K^{-2}$[304]. Aa aforementioned, recently, a first work has been published on the use of SnO_x[284] to create PEDOT:PSS/SnO_x but in this case the formation of composites were deposited through a diffusion mode and focused on the improvement on S and σ during exposure time, which is different to our approach with SnO nanoparticles/nanostructures. The relative improvement from the power factor was ∼15 respective from the initial value. However, our results lead to some of the highest relative increased, as marked in red (Table 7.4). The use of both EG and SnO leads to an increase of by a factor of ∼34, which is among the highest relative improvement on Table 7.4.

On the other hand, treatments on PEDOT:PSS have been discussed widely in this dissertation, not only the use of DMSO or EG has been studied, other many different materials such as poly(ethylene oxide) (PEO)[294] had led to great results. Dedoping films, which is to some extent similar to the use of acidic treatments, had also shown remarkable results[263,300]. However, the greatest improvement has been observed with the use of acids such as tri-fluoromethanesulfonic acid and methanol (TFMS–MeOH)[298] which gives one of the most notable relative increment one of the PF reported until this date, as for our knowledge. Xiong et al.[301] tested a variety of compounds (water, ethanol, isopropyl alcohol, EG), with remarkable results. Nonetheless, they did not measure the conductivity of pristine PEDOT:PSS and rather use the value given by the manufacturer, which may be the reason of this relative increasing on the PF, which might be not interpreted in this way. A considerable advantage of this method is that is often a complementary approach for increasing TE of PEDOT:PSS, which might be interesting to push the boundaries of high PF on other composites obtained by different approaches.

7.6. Conclusions

In this chapter, PEDOT:PSS composites based on the addition of the nanoparticles and/or EG have been assembled and characterized. However, in this case their possible implementation as gas sensors and thermoelectric materials has been explored.

- Composites based on PEDOT:PSS with SnO, SnO_2 and TiO_2 have been obtained via spin coating, consisting of thin layers of $\sim$ 100 nm of thickness. Composites presented homogeneity especially when EG is used which acts as a surfactant and improves nanoparticle dispersion. This method of obtaining composites is extremely simple and low-cost effective as compared with recent works based on evaporation methods[284]. Composites containing any of the studied nanoparticles (in 1% wt) decrease their electrical conductivity which reaches $\sim 10^{-2}$ S·cm^{-1}, most likely due to the agglomerate formation and poor interaction between the nanoparticles and the polymer matrix. Nonetheless, when 1% EG is added the dispersion of the nanoparticles is enhanced, and so does the electrical conductivity reaching the maximum value of $1.65 \cdot 10^{1}$ S·cm^{-1} for the SnO+EG composites, 2.5 higher than when only EG was used.

- Regarding the composite applications, these materials have been tested as possible gas sensors based on the resistance changes with different target gases, in specific ethanol and water vapor. Pristine PEDOT:PSS responds better when the sensing device temperature is increased to 50°C, but present similarly behaviors when using a carrier gas flow of nitrogen gas or dry air. A mild previous thermal treatment of the composite could increase the sensitivity due to the reduction of moisture in the samples. PEDOT:PSS composites without EG showed similar sensitivity to ethanol, but slightly increased most notably for SnO composites. With the addition of EG the greatest sensitivity is observed for SnO+EG composites, which is close to 5 times higher than the relative to pristine PEDOT:PSS. All these results have been obtained at RT, which assures that PEDOT:PSS-based sensors are comparable to other sensor sensitivities observed on the literature, but are less cost-effective. As effects involved in this enhanced gas sensing performance, the p-type behaviour of SnO, the composite increase of charge carriers, as well as the phase boundaries acting as scattering centers have been considered.

- A simple device for measuring the thermovoltage generated on the PEDOT:PSS composites have been designed, assembled and error proofed. This device, primarily based on two Peltier modules, allows to obtain precise voltage measurements obtained from Seebeck effect (i.e when the substrate is subjected to a temperature gradient). This setup allows to not only establish a voltage difference up to 30°C but also to measure thermovoltage error with an error always below 10%.

- Seebeck measurements shows that composites comprising by PEDOT:PSS+ 1% EG and SnO nanoparticles show the highest Power Factor with an increase

of 34 respective to pristine PEDOT:PSS. This is an outstanding increase as compared to the scarce results reported in the literature. Changes on the PEDOT chain structure due to coulombic interaction could be attributed to this improved behavior.

Chapter 8.
Conclusions

Herein, in the last chapter, the most relevant conclusions obtained during the course of this PhD thesis are summarized, divided into different sections corresponding to each chapter. Along the review of the main results, a critical analysis is made.

SnO_2 nanoparticles doped with Li or Ni

- By means of a hydrolysis method, we have obtained SnO_2 nanoparticles of small size (averaging 10 nm) both doped and Li or Ni doped. XRD, TEM and Raman studies have shown that either doped or undoped SnO_2 nanoparticles, present the characteristic properties expected for rutile SnO_2. However, significant variations in the SnO_2 vibrational modes were observed despite the low doping concentration in some of the probed samples. Substantial differences on the final dopant concentration was obtained, as Ni doped samples presented 0.5 and 3.8 % at and Li doped 0.06 and 0.95 % at, respectively, for the lowest and highest initial dopant concentration. High Ni doping induces an increase in the concentration of defects, while variable Li incorporation induces changes mainly in the A_{1g} and E_g modes, which can involve variable dopant incorporation in substitutional or interstitial sites in the SnO_2 lattice, depending on the Li content.

- PL spectra from the nanoparticles consist of a wide emission centered around 2-2.5 eV. In this case, an increase in the oxygen vacancy concentration can be induced in the SnO_2 nanoparticles with higher Li content, while high Ni doping involves a luminescence quenching due to the formation of a large amount of non-radiative recombination centers.

- XPS measurements confirm the presence of only Sn^{4+} in the Sn($3d$) core levels for all the samples. Contrary to other previous works, bands related to reduced oxidation states (Sn^{2+}) were not observed in this case. Changes in the Li($1s$) signal could be related to the coexistence of interstitial and substitutional Li, being the latter promoted in the SnO_2:$Li_{0.3}$ samples. Mixed Ni^{2+}/Ni^{3+} states can be estimated from the analysis of the Ni($3p$) core levels,

but the information of this core level is insufficient to attribute a possible mixed valence of Ni. The analysis of the valence band regions shows a lower n-type character for the samples with higher doping content, mainly for the SnO_2:$Ni_{0.3}$. Finally, Hall effect measurements were performed, and only for low lithium doping, an increase in the conductivity was observed, whereas for the rest of the samples, a decreasing conductivity and carrier density were measured.

- These nanoparticles were used as anodes in LiBs showing high capacity values and significant cyclability over 150 cycles. In particular, SnO_2 and SnO_2:$Li_{0.3}$- based anodes exhibit promising capacity values over 560 $mAhg^{-1}$ after 100 cycles. Based on these results, the defect structure associated with the Li or Ni doping, variable Li incorporation as interstitial and substitutional sites, mixed Ni oxidation states, and the lack of Sn^{2+} confirmed by XPS could retard some of the intermediate reactions occurred in the LiB, which can be related to the improved cyclability and electrochemical response observed in this work.

TiO_2 nanoparticles doped with Li or Ni

- By means of an hydrolysis method based on co-precipitation, anatase TiO_2 nanoparticles, both undoped or doped with Li or Ni have been obtained presenting high crystallinity and average crystalline size of 6 nm. Doped nanoparticles present a similar dopant concentration despite of different starting dopant precursor weight percentage, which has been confirmed via XRD, TEM, ICP-OES or EDS.

- Raman spectroscopy presents characteristic effects of low dimension nanoparticles as well as differences with commercial nanoparticles. Dopant addition modifies the contribution of the mode at $\sim$ 850 cm^{-1} which, together with the E_g mode presents the most notable changes directly related to the dopant presence, as well as being sensitive to UV laser irradiation.

- CL and PL results show the characteristic emission at the visible range expected for TiO_2. Ni doping enhances the emission at $\sim$ 2.9 eV, which is attributed to self trapped excitons, which are the most notable difference among doped and undoped nanoparticles luminescence. PL results as function of temperature shows that Ni-doped sample can be fitted using only one activation energy, which clearly shows the difference among the undergoing processes on the luminescence of undoped and Ni-doped samples.

- XPS confirms that Ti is present on the sample as Ti^{4+} even after dopant addition. Ni effect on the valence band is evident as it approaches the Fermi level to the valence band, which indicates a higher p-type behavior. The effect of Ni on the band structure was further addressed by DFT, which showed that in fact Ni creates a variety of mid-gap states as well as diminishes the

band gap, in presence of high concentration of oxygen vacancies, which is clearly our case in sight of the previous results. Li($1s$) not only reassures the presence of Li on the samples, the high relative area of the core level as compared with Ti($3s$), which has similar cross section, is a clear indicator that Li is present substantially on the surface, as compared with the ICP-OES results. This may indicate that Li migrates towards the surface, which also could explain the slight higher size of these nanoparticles.

- The absorption edges obtained by XAS corresponding to Ti($2p$) $L_{2,3}$ and O($1s$) K-edge allow the study of the crystal field ($10Dq$) and tetragonal distortion ($\|\delta_1\|$) parameters for the complete set of nanoparticles. It is observed that increasing the dopant concentration led to small variations of those parameters, which are associated with changes on the unit cell structure.

- RPES results show that for Li doped samples a small resonant peak appears at $\sim$ 1 eV which normally is mostly related to the transition Ti($3p$)$\rightarrow$Ti($4s$) or to an effect directly related with lithium core levels. In this case, XPS, PL, Raman aim to speculate that Ti^{3+} is not present in those samples, which could indicate that this small resonance peak, in sight of the CIS plots, is related to Li. Meanwhile, Ni doping enhances a shoulder $\sim$ 2.5 eV which is related to the Ni($3d$) states. This is further confirmed by first principle calculations based on DFT, where Li does not change significantly the DOS while Ni induces the creation of mid-gap states.

- As a proof of concept, undoped anatase TiO_2 and Li-doped based anodes have been prepared with high stability over 200 cycles and higher specific capacity for the anodes based on TiO_2:$Li_{0.3}$, which could be attributed to the higher conductivity of these nanoparticles.

- Via two different approaches, by thermal annealing and UV-laser irradiation, the ART was promoted. By thermal annealing, for undoped TiO_2, this transitions starts at 740 °C while Li or Ni doping accelerates this transition which starts at either 620 or 700°C, mainly due to the high presence of defects (mostly oxygen vacancies) due to the dopant incorporation. The possible break of Ti-O bonds during both the doping and annealing process, could be centers of re-growth of these bonds for rutile. Via laser irradiation with the UV laser, it is observed that some modes are very sensitive to its influence, as the E_g mode. By monitoring this peak as well as the position of the formed A_{1g} of rutile, we can observe the transition from anatase to rutile. This is a fast transition under the conditions used in this work for both undoped and Li-doped samples, however Ni seems to attenuate it. In contrast with the thermal annealing, many different properties should be taken into account to understand this transition, such as the thermal conductivity, morphology and surface of the particles affect the UV-induced transition, which in sight of previous characterization of Ni-doped samples, could explain this different behavior. This is understandable as in this case we are inducing the trans-

ition locally on a small volume of the sample, thus the surface properties of the nanoparticles should not be neglected.

SnO nanoparticles doped with Li or Ni

- Crystalline SnO nanoparticles and platelets were synthesized via a hydrolysis method that allowed the achievement of a large amount of SnO nanopowder, avoiding an atmosphere control during the synthesis, as it has been performed at room conditions. XRD measurements confirmed the minor oxidation and stability of the as-synthesized SnO nanopowder stored at room conditions for up to 24 months, which is fundamental for long-term applicability. The nanoparticles dimensions ranged from 4-22 nm, as confirmed by TEM observations, but as observed by SEM and TEM, most of the structures appear to be platelets, which grow interleaved. XRD results shows that, while the Li-doped sample presents very similar diffraction pattern that undoped SnO contrary with Ni doped sample which presents a high contribution from the precursors.

- Testing the limits of existence of SnO can be monitored by enhancing the oxidation from SnO to SnO_2, either promoted by thermal annealing or by controlled laser irradiation. Temperatures above 300°C are required to initiate the oxidation from SnO to SnO_2 which was completed at 800°C, following a nucleation and growth process with minimum formation of intermediate oxides, as confirmed by thermodiffraction measurements. This can be deduced from the changes on the SnO (101) and the SnO_2 (110) diffraction planes. In particular, for Li-doped samples very close behavior is observed, in which for both undoped and Li-doped, a clear shift on the SnO(101) is observed, which shifts toward lower angle up to $\sim$ 450°C, and then towards higher angle, which is a clear indicator on the accommodation of the lattice to a rutile-like structure. Ni doped samples present a high presence of intermediate oxides and other precursors, which at $\sim$ 200°C tend to disappear, due to the volatile nature of the compounds. This leads to the formation of SnO_2 with the lowest presence of SnO, as apparently Ni-doped SnO structures are not as stable.

- On the contrary, by using UV or red laser irradiation the transition from SnO to SnO_2 could be controlled, assisted by the formation of intermediate Sn_3O_4, as confirmed by Raman spectroscopy. This is clearly observed by using the highest laser intensities for the VIS laser, which allows to observe multiple modes attributed to intermediate oxides, while measuring with the UV laser allows the observation of some of the modes after longer exposure time and lower irradiation intensity, as the highest irradiation intensity leads to the observation of the main Raman modes of SnO_2, the E_g and A_{1g}. Careful attention should be paid during the PL and Raman analysis, as the

use of the laser as excitation source can induce formation of SnO_2 during measurement, thus leading to possibly misleading results and discussion.

- In this work, the evolution from SnO to SnO_2 was studied as a function of the laser excitation source (UV and red laser), the laser power density (controlled by using neutral filters), and the irradiation duration in order to achieve deeper knowledge and control of the oxidation process. The evolution of the oxidation of SnO_2, which posses its Raman modes slightly displaced due to lower crystallinity, is promoted by UV laser irradiation and obeys Avrami equation. The crystallization of SnO_2 obeys a diffusion controlled reaction in two dimensions.

- Finally, advantage can be taken from the controlled SnO oxidation and a tailored spatial SnO/SnO_2 micropatterning can be developed based on a controlled laser irradiation. By using minimum exposure time, different strip/cross-like patternings could be easily produced over the sample, in which the irradiated area correspond unambiguously to SnO_2 and the non-irradiated zone to SnO, establishing a p-n junction. This laser-induced micropatterning can be of potential interest for the fabrication of p-n devices based in all Sn-oxides with applicability in electronic, optoelectronic, and sensing devices.

PEDOT:PSS composites based on SnO, SnO_2 or TiO_2 for hybrid Si-solar cells

- Via spin-coating, composites based on PEDOT:PSS have been assembled in order to test their effect on passivation over FZ n-type silicon, as possible candidates for hybrid silicon solar cells.

- Firstly, a flow diagram of the process was ideated, in which different parts of the assembly were tested: the substrate both pre- and post treatment, spin-coating method, and the materials (solvents, surfactants) which could be used. It was observed that pre-treating the silicon layer with HF+Piranha to remove the native oxide layer decreased the passivation effects of PEDOT:PSS. The use of DMSO (5% wt) and Triton X-100 (0.1% wt) improved the overall wettability of the silicon substrate and film quality, while minimum differences were observed in both the absorption spectra and the simulated-refraction index, via an iterative method. Post-treatment of the assembled layers at 120-130°C removed remaining moisture on the samples. These films showed high transparency to visible light as well as high lifetime carrier recombination values of $\sim$ 350 μs, which are competitive with current values in these technologies.

- An in-depth study using different laser, filters and pinhole diameters has been performed. The use of variable (increased) pinhole size has shown that the contribution $\sim$ 1400 cm^{-1} becomes dominant on the region 1400-1500 cm^{-1},

as well as a new mode appears at 1530 cm^{-1} which is an splitting associated with C_α=C_β vibrations, often neglected on the literature. With the highest pinhole size used of 900 μm, there is a clear shift on the mode at 1420 cm^{-1} towards higher wavenumber (1430 cm^{-1}). This shift with increasing pinhole, difficulties to attribute PEDOT:PSS structure as benzoid or quinoidic structure. Using the UV laser to obtain Raman spectra makes it obvious the fast decrease on the relative intensity with increasing exposure time. However, main modes can be observed which are not extensively disused on the bibliography, such a mode at 1608 cm^{-1}, most likely due to C=C stretch vibrations. This mode is used to monitor the degradation of PEDOT:PSS, whose relative intensity decrease notably under laser irradiation. Nonetheless, low UV irradiation enhances modes at high wavenumber, which has been recently pointed out by Toto et al.[70], therefore showing stability to some extent, under UV irradiation.

- The stability of these composites was tested over time at room conditions of moisture and pressure, and it shows a decrease of the carrier lifetime recombination values to $\sim$ 75 μs after a long period of 400 days, almost independently on the use or not of pre-substrate treatment.

- Following the procedure explained on the process diagram, nanoparticles of SnO, SnO_2 and TiO_2 were successfully added to the PEDOT:PSS blend and spin coated over either silicon or glass substrates.

- By adding SnO nanoparticles to PEDOT:PSS, improved stability under the UV irradiation and electrical conductivity, as well as a weak increase in the absorption was observed. This composite still exhibits good passivation performance. Synergy effects are observed between both organic and inorganic counterparts, as the SnO nanoparticles provide stability and improved optoelectronic response, while the polymer encapsulates SnO nanoparticles, hindering the oxidation into SnO_2.

- Hybrid composites formed by PEDOT:PSS and TiO_2 nanoparticles in a variable ratio (0.5, 1, 2% wt.) were obtained and spin-coated on Si-substrates. Changes in the conductivity and carrier concentration were induced by a variable incorporation of TiO_2 nanoparticles in the polymeric matrix. Enhanced carrier lifetime values were achieved by addition of 0.5% wt of TiO_2 in the composite.

- Finally, the FoM was calculated in order to check if these composites could be employed, alternatively, as transparent conductive electrodes. Despite not reaching the commercial-standard requirement of $\sigma_{dc} \cdot \sigma_{op}^{-1} > 35$, there is a clear tendency of improved FoM with the addition of the nanoparticles, fact that should not be overlooked when forming new transparent electrodes.

PEDOT:PSS composites based on SnO, SnO_2 or TiO_2: thermoelectric and gas sensing properties

- Pristine PEDOT:PSS and composites formed with the addition of EG and/or the nanoparticles synthesized on the previous chapters, were assembled via spin coating. Composites containing nanoparticles (either SnO, SnO_2 or TiO_2, in 1 % wt) presented homogeneity on the nanoparticle dispersion, especially when EG was added as well as high transparency to visible light, which decreased upon EG content but increase with the addition of EG and the nanoparticles. It should be pointed out that in this chapter we have also looked the pristine PEDOT:PSS properties, in specific, of a lower-conductivity grade PEDOT:PSS and the concrete effect of the secondary dopant (EG) on the morphological and electrical properties.

- Hall effect results demonstrate that the addition of the nanoparticles decreased the conductivity contrary to the effect observed with EG addition. The addition of EG incresed the conductivity which was increased even further with the addition of both the nanoparticles and EG, showing the addition of both 1% SnO and 1% EG the best results, increasing by a factor of 2.5 compared with only the use of EG, and by a factor of 117 compared with pristine PEDOT:PSS.

- Regarding applicability, composites were tested as possible gas sensor devices, for which different oxidation atmosphere and conditions were evaluated, such as the use of different carrier gases, different analytes (ethanol and water vapor), different pre-treatments of the PEDOT:PSS composites and sensing temperatures. From this study two main conclusions can be obtained. First, increasing sensing temperature gave an slight improvement on the sensitivity, as well as a clear recovery of the resistance, which would allow us to correctly subtract the background of the measurements and to obtain, for example, the response and recovery times. However, the possibility of having a sensor at room temperature, which is clearly possible with the use of PEDOT:PSS, is too attractive which pushed our study on analyzing PEDOT:PSS gas sensors at RT. Secondly, a thermal treatment of the pre-sensitized samples is important to obtain a better response in terms of sensitivity. This is because getting rid of moisture micro-clusters, which can interfere in the correct electrical conduction between the short PEDOT chains, allows a better resistive response.

- The best results on terms of sensitivity were obtained for the composites containing SnO and EG, reaching near 5% sensitivity, clearly superior to any other composite. Understanding the exact sensing mechanism in these samples can be highly complex due to multiple synchronous effects. The increase in resistance to a p-type material in the presence of a reducing gas is reasonable, a fact that can be accentuated due to known effects such as chain swelling in the presence of the gas. In particular, samples with SnO, a p-type

MOs, showed the best results. This may be due to configurational changes of the chain as well as to the nanostructure's own sensing mechanisms, which also contribute to the increase in resistance by injecting electrons into the polymeric matrix. Improving the contact covering of the samples, the device itself (e.g. by creating an IDT) or the ppm entering the chamber, could increase this sensitivity, resulting in a highly competitive sensor. However, the results at RT are remarkable, which assures the potential of PEDOT:PSS based composites for gas sensing at RT.

- Finally, to test their use as thermoelectric devices both the design of data acquisition setup to measure Seebeck effect was evaluated and assembled. This setup consisted mainly on the use of two Peltier modules with a controlled temperature gradient (max 30°C), which allowed to measure the temperature gradient on the sample as well as of the thermovoltage generated, obtaining small error not exceeding 10%. This setup shows novelty by using Peltier modules as heating junctions instead of commonly cylindrical or circular thermoresistances. Acquiring data is really simple due to the use of a temperature data acquisition card and a Keithley multimeter.

- The best results in terms of PF were obtained for the SnO and EG composites, which was increased up to 34 times as compared with pristine PEDOT:PSS. This results is among one of the most relevant relative improvements by using oxide fillers as a PF enhancer. With the addition of any of the oxide nanostructures, as well of EG, it was observed that the Seebeck coefficient was always within the range of 10-30 μVK^{-1}, while the electrical conductivity could be enhanced a couple of orders of magnitude (with the EG content). The use of higher EG concentrations could be the way forward to continue to increase the PF.

Bibliography

1. Zhuiykov, S. *Nanostructured semiconductor oxides for the next generation of electronics and functional devices: Properties and applications* (Woodhead Publishing, 2014).

2. Hoffmann, M. R., Martin, S. T., Choi, W. & Bahnemann, D. W. Environmental Applications of Semiconductor Photocatalysis. *Chemical Reviews* **95,** 69–96 (1995).

3. Granqvist, C. *Handbook of Inorganic Electrochromic Materials* (Elsevier Science, 1995).

4. Wang, F. *et al. Metal oxides in batteries* 127–167 (Elsevier, Jan. 2018).

5. Wang, C., Yin, L., Zhang, L., Xiang, D. & Gao, R. Metal oxide gas sensors: Sensitivity and influencing factors. *Sensors* **10,** 2088–2106 (Mar. 2010).

6. Zhang, J., Zhou, P., Liu, J. & Yu, J. New understanding of the difference of photocatalytic activity among anatase, rutile and brookite TiO_2. *Physical Chemistry Chemical Physics* **16,** 20382–20386 (Sept. 2014).

7. Liang, Y., Su, K., Cao, L. & Li, Z. Lithium doped TiO_2 as catalysts for the transesterification of bisphenol-A with dimethyl carbonate. *Molecular Catalysis* **465,** 16–23 (2019).

8. Sang, L., Zhao, Y. & Burda, C. TiO_2 Nanoparticles as Functional Building Blocks. *Chemical Reviews* **114,** 9283–9318 (2014).

9. Noman, M. T., Ashraf, M. A. & Ali, A. Synthesis and applications of nano-TiO_2: a review. *Environmental Science and Pollution Research* **26,** 3262–3291 (2019).

10. Liu, Y. & Yang, Y. Recent Progress of TiO_2-Based Anodes for Li Ion Batteries. *Journal of Nanomaterials* **4,** 1–15 (2016).

11. Guler, M. O., Cevher, O., Cetinkaya, T., Tocoglu, U. & Akbulut, H. High capacity TiO_2 anode materials for Li-ion batteries. *Energy Conversion and Management* **72,** 111–116 (Aug. 2013).

12. Ge, M. *et al.* A review of one-dimensional TiO_2 nanostructured materials for environmental and energy applications. *Journal of Materials Chemistry A* **4,** 6772–6801 (2016).

13. Nyamukamba, P., Okoh, O., Mungondori, H., Taziwa, R. & Zinya, S. *Synthetic Methods for Titanium Dioxide Nanoparticles: A Review* (InTech, June 2018).

14. Joshi, N. *et al.* A review on chemiresistive room temperature gas sensors based on metal oxide nanostructures, graphene and 2D transition metal dichalcogenides. *Microchimica Acta,* 185–313 (2018).

15. Mueller, F., Bresser, D., Chakravadhanula, V. S. K. & Passerini, S. Fe-doped SnO_2 nanoparticles as new high capacity anode material for secondary lithium-ion batteries. *Journal of Power Sources* **299,** 398–402 (2015).

16. Chen, J. S. & Lou, X. W. D. SnO_2 - Based Nanomaterials: Synthesis and Application in Lithium-Ion Batteries. *Small* **9,** 1877–1893 (June 2013).

17. Wang, Z., Nayak, P. K., Caraveo-Frescas, J. A. & Alshareef, H. N. Recent Developments in p-Type Oxide Semiconductor Materials and Devices. *Advanced Materials* **28,** 3831–3892 (May 2016).

18. Guzmán-Caballero, D. E., Quevedo-López, M. A. & Ramírez-Bon, R. Optical properties of p-type SnO_x thin films deposited by DC reactive sputtering. *Journal of Materials Science: Materials in Electronics* **30,** 1366–1373 (Jan. 2019).

19. Iqbal, M. Z. *et al.* Structural and electrochemical properties of SnO nanoflowers as an anode material for lithium ion batteries. *Scripta Materialia* **67,** 665–668 (2012).

20. Zhang, F., Zhu, J., Zhang, D., Schwingenschlögl, U. & Alshareef, H. N. Two-Dimensional SnO Anodes with a Tunable Number of Atomic Layers for Sodium Ion Batteries. *Nano Letters* **17,** 1302–1311 (Feb. 2017).

21. Luceño-Sánchez, J., Díez-Pascual, A. & Peña Capilla, R. Materials for Photovoltaics: State of Art and Recent Developments. *International Journal of Molecular Sciences* **20,** 976 (Feb. 2019).

22. Jäckle, S. *et al.* Unveiling the Hybrid n-Si/PEDOT:PSS Interface. *ACS Applied Materials and Interfaces* **8,** 8841–8848 (Apr. 2016).

23. Wang, D. *et al.* Layer by layer assembly of sandwiched graphene/SnO_2 nanorod/carbon nanostructures with ultrahigh lithium ion storage properties. *Energy and Environmental Science* **6,** 2900–2906 (2013).

24. Hu, L., Song, J., Yin, X., Su, Z. & Li, Z. Research Progress on Polymer Solar Cells Based on PEDOT:PSS Electrodes. *Polymers* **12,** 145 (Jan. 2020).

25. Sun, K. *et al.* Review on application of PEDOTs and PEDOT:PSS in energy conversion and storage devices. *J Mater Sci: Mater Electron* **26,** 4438–4462 (2015).

26. Shi, H., Liu, C., Jiang, Q. & Xu, J. Effective Approaches to Improve the Electrical Conductivity of PEDOT:PSS: A Review. *Advanced Electronic Materials* **1,** 1–16 (2015).

27. García-Tecedor, M. *et al.* Silicon surface passivation by PEDOT: PSS functionalized by SnO_2 and TiO_2 nanoparticles. *Nanotechnology* **29,** 035401 (2018).

28. Khang, D. Y. Recent progress in Si-PEDOT:PSS inorganic-organic hybrid solar cells. *Journal of Physics D: Applied Physics* **52,** 503002 (2019).

29. Ben Haj Othmen, W. *et al.* Effect of high Fe doping on Raman modes and optical properties of hydrothermally prepared SnO_2 nanoparticles. *Materials Science in Semiconductor Processing* **77,** 31–39 (Apr. 2018).

30. Jain, A. *et al.* Commentary: The materials project: A materials genome approach to accelerating materials innovation. **1,** 11002 (July 2013).

31. Solola, G. T. *et al.* First principle calculations of structural, electronic, optical and thermoelectric properties of tin (II) oxide. *Materials Research Express* **6,** 125915 (Jan. 2019).

32. Wang, X. *et al.* Structural properties, infrared reflectivity, and Raman modes of SnO at high pressure. *physica status solidi (b)* **241,** 3168–3178 (Nov. 2004).

33. Zhang, Y. *et al.* Titanate and titania nanostructured materials for environmental and energy applications: A review. *RSC Advances* **5,** 79479–79510 (2015).

34. Shanmugasundaram, A., Basak, P., Satyanarayana, L. & Manorama, S. V. Hierarchical SnO/SnO_2 nanocomposites: Formation of in situ p-n junctions and enhanced H_2 sensing. *Sensors and Actuators, B: Chemical* **185,** 265–273 (Aug. 2013).

35. Yin, G. *et al.* Enhanced gas selectivity induced by surface active oxygen in SnO/SnO_2 heterojunction structures at different temperatures. *RSC Advances* **9,** 1903–1908 (2019).

36. Gervillié, C., Boisard, A., Labbé, J., Berthon-Fabry, S. & Guérin, K. Influence upon cycling of oxygen amount in tin-based compound used as negative electrode in lithium-ion battery. *Synthetic Metals* **267,** 116477 (Sept. 2020).

37. Lazzeri, M., Vittadini, A. & Selloni, A. Structure and energetics of stoichiometric TiO_2 anatase surfaces. *Physical Review B - Condensed Matter and Materials Physics* **63,** 1554091–1554099 (2001).

38. Rubio-Ponce, A., Conde-Gallardo, A. & Olguín, D. First-principles study of anatase and rutile TiO_2 doped with Eu ions: A comparison of GGA and LDA+ U calculations. *Physical Review B* **78,** 035107 (2008).

39. Hanaor, D. A. & Sorrell, C. C. Review of the anatase to rutile phase transformation. *Journal of Materials Science* **46,** 855–874 (2011).

40. Ravishankar, T. N., Nagaraju, G. & Dupont, J. Photocatalytic activity of Li-doped TiO_2 nanoparticles: Synthesis via ionic liquid-assisted hydrothermal route. *Materials Research Bulletin* **78,** 103–111 (2016).

41. Schneider, J. *et al.* Understanding TiO_2 Photocatalysis: Mechanisms and Materials. *Chemical Reviews* **114,** 9919–9986 (Oct. 2014).

42. Sharma, A., Varshney, M., Shin, H. J., Chae, K. H. & Won, S. O. X-ray absorption spectroscopy investigations on electronic structure and luminescence properties of $Eu:SnO_2$-SnO nanocomposites. *Current Applied Physics* **16,** 1342–1348 (Oct. 2016).

43. Xiaozhen, L., Jie, C., Wenbin, S. & Beiling, Q. Complexation-Coprecipitation Synthesis and Characterization of Erbium and Antimony Doped SnO_2 Conductive Nanoparticles. *Journal of Rare Earths* **25,** 72–76 (June 2007).

44. Ma, L. J., Li, Y. X., Yu, X. F., Yang, Q. B. & Noh, C. H. Using room temperature ionic liquid to fabricate $PEDOT/TiO_2$ nanocomposite electrode-based electrochromic devices with enhanced long-term stability. *Solar Energy Materials and Solar Cells* **92,** 1253–1259 (Oct. 2008).

45. Skoromets, V. *et al.* Conductivity Mechanisms in Sb-Doped SnO_2 Nanoparticle Assemblies: DC and Terahertz Regime. *Journal of Physical Chemistry C* **119,** 19485–19495 (Aug. 2015).

46. Montero, J., Herrero, J. & Guillén, C. Preparation of reactively sputtered Sb-doped SnO_2thin films: Structural, electrical and optical properties. *Solar Energy Materials and Solar Cells* **94,** 612–616 (Mar. 2010).

47. Cristian Vásquez, G. *et al.* Understanding the effects of Cr doping in rutile TiO_2 by DFT calculations and X-ray spectroscopy. *Scientific Reports* **8,** 8740 (2018).

48. Choudhury, B. & Choudhury, A. Luminescence characteristics of cobalt doped TiO_2 nanoparticles. *Journal of Luminescence* **132,** 178–184 (Jan. 2012).

49. Bapna, K., Phase, D. M. & Choudhary, R. J. Study of valence band structure of Fe doped anatase TiO_2 thin films. *Journal of Applied Physics* **110,** 043910 (Aug. 2011).

50. Srivastava, A. K. *Oxide Nanostructures, Growth, Microstructures, and Properties* 1st Edition, 424 (Jenny Stanford Publishing, Apr. 2013).

51. Prasad, P. D., Reddy, S. P. & Deepthi, A. Synthesis , Characterization of Tin Oxide (SnO) Nanoparticles via Autoclave synthesis protocol for H_2 sensing. *International Journal of Nanotechnology and Applications* **11,** 265–276 (2017).

52. Stashans, A., Lunell, S., Bergström, R., Hagfeldt, A. & Lindquist, S.-E. Theoretical study of lithium intercalation in rutile and anatase. *Physical Review B* **53,** 159 (1996).

53. Amutha, T. *et al.* Studies on structural and optical properties of pure and transition metals (Ni, Fe and co-doped Ni–Fe) doped tin oxide (SnO_2) nanoparticles for anti-microbial activity. *Research on Chemical Intermediates* **45,** 1929–1941 (2019).

54. Ahmed, A. S. *et al.* Band gap narrowing and fluorescence properties of nickel doped SnO_2 nanoparticles. *Journal of Luminescence* **131,** 1–6 (2011).

55. Hyun Kim, D., Sub Lee, K., Kim, Y.-S., Chung, Y.-C. & Kim, S.-J. Photocatalytic Activity of Ni 8 wt%-Doped TiO_2 Photocatalyst Synthesized by Mechanical Alloying Under Visible Light. *Journal of the American Ceramic Society* **89,** 515–518 (Feb. 2006).

56. Punnoose, A. *et al.* Development of high-temperature ferromagnetism in SnO_2 and paramagnetism in SnO by Fe doping. *Physical Review B* **72,** 054402 (2005).

57. Farooq, M. H. *et al.* Fabrication, characterization and magnetic properties of Mn-doped SnO nanostructures via hydrothermal method. *Materials Letters* **131,** 350–353 (Sept. 2014).

58. Shirakawa, H., Louis, E. J., MacDiarmid, A. G., Chiang, C. K. & Heeger, A. J. Synthesis of electrically conducting organic polymers: Halogen derivatives of polyacetylene, $(CH)_x$. *Journal of the Chemical Society, Chemical Communications* **0,** 578–580 (Jan. 1977).

59. Dhar, S., Majumder, T., Chakraborty, P. & Mondal, S. P. DMSO modified PEDOT:PSS polymer/ZnO nanorods Schottky junction ultraviolet photodetector: Photoresponse, external quantum efficiency, detectivity, and responsivity augmentation using N doped graphene quantum dots. *Organic Electronics: physics, materials, applications* **53,** 101–110 (2018).

60. Xia, Y. & Dai, S. Review on applications of PEDOTs and PEDOT:PSS in perovskite solar cells. *Journal of Materials Science: Materials in Electronics* **1,** 3 (May 2020).

61. Jeong, S. *et al.* Hybrid silicon nanocone-polymer solar cells. *Nano Letters* **12,** 2971–2976 (June 2012).

62. Jäckle, S. *et al.* Potential of PEDOT:PSS as a hole selective front contact for silicon heterojunction solar cells. *Scientific Reports* **7,** 1–8 (2017).

63. Fan, Z. & Ouyang, J. Thermoelectric Properties of PEDOT:PSS. *Advanced Electronic Materials* **5,** 1800769 (Nov. 2019).

64. Yang, Y., Deng, H. & Fu, Q. Recent progress on PEDOT:PSS based polymer blends and composites for flexible electronics and thermoelectric devices. *Materials Chemistry Frontiers* **4,** 3130–3152 (Nov. 2020).

65. Amanchukwu, C. V. *et al.* Evaluation and Stability of PEDOT Polymer Electrodes for LiO_2 Batteries. *J. Phys. Chem. Lett* **7,** 12 (2016).

66. Liao, J., Si, H., Zhang, X. & Lin, S. Functional sensing interfaces of PEDOT:PSS organic electrochemical transistors for chemical and biological sensors: A mini review. *Sensors (Basel, Switzerland)* **19,** 218 (2019).

67. Gueye, M. N., Carella, A., Faure-Vincent, J., Demadrille, R. & Simonato, J. P. Progress in understanding structure and transport properties of PEDOT-based materials: A critical review. *Progress in Materials Science* **108,** 100616 (Feb. 2020).

68. Hwang, K. H., Kim, D. I., Nam, S. H., Seo, H. J. & Boo, J. H. Study on the effect of DMSO on the changes in the conductivity of PEDOT:PSS. *Functional Materials Letters* **1,** 1–6 (2015).

69. Tevi, T., Saint Birch, S. W., Thomas, S. W. & Takshi, A. Effect of Triton X-100 on the double layer capacitance and conductivity of poly(3,4-ethylenedioxythiophene) :poly(styrenesulfonate) (PEDOT:PSS) films. *Synthetic Metals* **191,** 59–65 (May 2014).

70. Toto, E., Botti, S., Laurenzi, S. & Santonicola, M. G. UV-induced modification of PEDOT:PSS-based nanocomposite films investigated by Raman microscopy mapping. *Applied Surface Science* **513** (May 2020).

71. Vitoratos, E. Conductivity Degradation Study of PEDOT: PSS Films under Heat Treatment in Helium and Atmospheric Air. *Open Journal of Organic Polymer Materials* **02,** 7–11 (2012).

72. Wang, D. *et al.* Defect-Rich Crystalline SnO_2 Immobilized on Graphene Nanosheets with Enhanced Cycle Performance for Li Ion Batteries. *The Journal of Physical Chemistry C* **116,** 22149–22156 (2012).

73. Deng, Y., Fang, C. & Chen, G. The developments of SnO_2/graphene nanocomposites as anode materials for high performance lithium ion batteries: A review. **304,** 81–101 (2016).

74. Bhowal, A. C., Talukdar, H. & Kundu, S. Preparation, characterization and electrical behaviors of PEDOT:PSS-Au/Ag nanocomposite thin films: an ecofriendly approach. *Polymer Bulletin* **76,** 5233–5251 (2019).

75. Maiaugree, W. *et al.* Optimization of TiO_2 nanoparticle mixed PEDOT–PSS counter electrodes for high efficiency dye sensitized solar cell. *Journal of Non-Crystalline Solids* **358,** 2489–2495 (Sept. 2012).

76. Park, Y., Müller-Meskamp, L., Vandewal, K. & Leo, K. PEDOT:PSS with embedded TiO_2 nanoparticles as light trapping electrode for organic photovoltaics. *Applied Physics Letters* **108** (2016).

77. Elton, L. R. B. & Jackson, D. F. X-Ray Diffraction and the Bragg Law. *American Journal of Physics* **34,** 1036–1038 (1966).

78. Patterson, A. L. The scherrer formula for X-ray particle size determination. *Physical Review* **56,** 978–982 (Nov. 1939).

79. Kriegner, D., Matěj, Z., Kužel, R. & Holý, V. Powder diffraction in bragg-brentano geometry with straight linear detectors. *Journal of Applied Crystallography* **48,** 613–618. arXiv: 1501.04885 (Apr. 2015).

80. Goldstein, J. *et al. Scanning Electron Microscopy and X-Ray Microanalysis* XXIII, 550 (Springer-Verlag New York, 2018).

81. Kanaya, K. & Okayama, S. Penetration and energy-loss theory in solid targets. *J.Phys.D:Appl.Phys.* **5,** 43–58 (1972).

82. Drouin, D. *et al.* CASINO V2.42 - A fast and easy-to-use modeling tool for scanning electron microscopy and microanalysis users. *Scanning* **29,** 92–101 (May 2007).

83. National Institute of Standars and Tec. X-Ray Transition Energies Database — NIST. *NIST Standard Reference Database 128* (2005).

84. Williams, D. B. & Carter, C. B. *Transmission Electron Microscopy: A Textbook for Materials Science* (Springer).

85. Hollas, J. M. *Modern Spectroscopy* (J. Michael Hollas, 2004).

86. Haug, H. *New methods for Investigation of surface passivation layers for crystalline silicon solar cells* PhD thesis (2014), 169.

87. Hall, E. *Synthesis and characterisation of PEDOT:PSS/silicon interfaces for use in low cost, high efficiency solar cells* MA thesis (2020).

88. Vij, D. R. *Handbook of Applied Solid State Spectroscopy* (Springer Science+Business Media, LLC, 2006).

89. NIST Standard Reference Database. NIST X-ray Photoelectron Spectroscopy Database. *National Institute of Standards and Technology* **20** (2000).

90. Moulder, J. F., Stickle, W. F., Sobol, P. E. & Bomben, K. D. *Handbook of X-ray Photoelectron Spectroscopy* (Perkin-Elmer).

91. Zangrando, M. *et al.* Polarized high-brilliance and high-resolution soft x-ray source at ELETTRA: The performance of beamline BACH. *Review of Scientific Instruments* **75,** 31–36 (2004).

92. De Groot, F. & Akio Kotani. *Core Level Spectroscopy of Solids* (CRC Press Taylor & Francis Group, 1964).

93. Horcas, I. *et al.* WSXM: A software for scanning probe microscopy and a tool for nanotechnology. *Review of Scientific Instruments* **78,** 013705 (Jan. 2007).

94. Vázquez-López, A. *et al.* Influence of Doping and Controlled Sn Charge State on the Properties and Performance of SnO_2 Nanoparticles as Anodes in Li-Ion Batteries . *The Journal of Physical Chemistry C* **124,** 18490–18501 (July 2020).

95. Wongsaprom, K., Bornphotsawatkun, R. A. & Swatsitang, E. Synthesis and characterization of tin oxide (SnO_2) nanocrystalline powders by a simple modified sol-gel route. *Applied Physics A: Materials Science and Processing* **114,** 373–379 (2014).

96. Diéguez, A., Romano-Rodríguez, A., Vilà, A. & Morante, J. R. The complete Raman spectrum of nanometric SnO_2 particles. *Journal of Applied Physics* **90,** 1550–1557 (2001).

97. Bhatnagar, M., Kaushik, V., Kaushal, A., Singh, M. & Mehta, B. R. Structural and photoluminescence properties of tin oxide and tin oxide: C core-shell and alloy nanoparticles synthesised using gas phase technique. *AIP Advances* **6,** 95321 (2016).

98. Kar, A., Kundu, S. & Patra, A. Surface defect-related luminescence properties of SnO_2 nanorods and nanoparticles. *Journal of Physical Chemistry C* **115,** 118–124 (2011).

99. Maestre, D., Cremades, A. & Piqueras, J. Cathodoluminescence of defects in sintered tin oxide. *Journal of Applied Physics* **95,** 3027–3030 (Mar. 2004).

100. Peche-Herrero, M. A. *et al.* The controlled transition-metal doping of SnO_2 nanoparticles with tunable luminescence. *CrystEngComm* **16,** 2969–2976 (2014).

101. Gallart, M. *et al.* Temperature dependent photoluminescence of anatase and rutile TiO_2 single crystals: Polaron and self-trapped exciton formation. *Journal of Applied Physics* **124** (2018).

102. Kılıç, Ç. & Zunger, A. Origins of coexistence of conductivity and transparency in SnO_2. *Physical Review Letters* **88,** 955011–955014 (2002).

103. Korusenko, P. M. *et al.* Formation of tin-tin oxide core-shell nanoparticles in the composite SnO_{2-x} nitrogen-doped carbon nanotubes by pulsed ion beam irradiation. *Nuclear Instruments and Methods in Physics Research, Section B: Beam Interactions with Materials and Atoms* **394,** 37–43 (2017).

104. Willemen, H., Van De Vondel, D. F. & Van Der Kelen, G. P. An ESCA study of tin compounds. *Inorganica Chimica Acta* **34,** 175–180 (1979).

105. Stranick, M. A. & Moskwa, A. SnO_2 by XPS. *Surface Science Spectra* **2,** 50–54 (2002).

106. Ullah Awan, S., Hasanain, S. K., Bertino, M. F. & Hassnain Jaffari, G. Ferromagnetism in Li doped ZnO nanoparticles: The role of interstitial Li. *Journal of Applied Physics* **112** (2012).

107. Kumar, P., Yadav, A. K., Bhattacharyya, D., Jha, S. N. & Pandey, P. C. Lithium ion assisted luminescence and ferromagnetism in europium doped zinc oxide. *Materials Chemistry and Physics* **214,** 306–319 (Aug. 2018).

108. Qiao, L. & Bi, X. Direct observation of Ni^{3+} and Ni^{2+} in correlated $LaNiO_{3-\delta}$films. *Epl* **93,** 57002 (2011).

109. Themlin, J. M. *et al.* Resonant-photoemission study of SnO_2: Cationic origin of the defect band-gap states. *Physical Review B* **42,** 11914–11925 (1990).

110. Del Prado, F. *et al.* Effect of lithium doping and precursors on the microstructural, surface electronic and luminescence properties of single crystalline microtubular tin oxide structures. *CrystEngComm* **19,** 4321–4329 (July 2017).

111. Kucheyev, S. O. *et al.* Surface electronic states in three-dimensional SnO_2 nanostructures. *Physical Review B* **72,** 035404 (2005).

112. Gu, W., Wang, H. & Wang, K. Nickel L-edge and K-edge X-ray absorption spectroscopy of non-innocent $Ni[[S_2C_2(CF_3)_2]_2]^n$ series (n = -2, -1, 0): Direct probe of nickel fractional oxidation state change. *Journal of the Chemical Society. Dalton Transactions* **43,** 6406–6413 (2014).

113. Kay, A. *et al.* Multi-atom resonant photoemission: A method for determining near- neighbor atomic identities and bonding. *Science* **281,** 679–683 (July 1998).

114. Shkvarin, A. S. *et al.* Guest-Host Chemical Bonding and Possibility of Ordering of Intercalated Metals in Transition-Metal Dichalcogenides. *Inorganic Chemistry* **57,** 5544–5553 (2018).

115. Zhang, K. H. *et al.* Electronic Structure and Band Alignment at the NiO and SrTiO3 p-n Heterojunctions. *ACS Applied Materials and Interfaces* **9,** 26549–26555 (2017).

116. Böhme, S., Philippe, B., Edström, K. & Nyholm, L. Photoelectron Spectroscopic Evidence for Overlapping Redox Reactions for SnO_2 Electrodes in Lithium-Ion Batteries. *Journal of Physical Chemistry C* **121,** 4924–4936 (2017).

117. Chen, J. Recent Progress in Advanced Materials for Lithium Ion Batteries. *Materials* **6,** 156–183 (Jan. 2013).

118. Meduri, P., Pendyala, C., Kumar, V., Sumanasekera, G. U. & Sunkara, M. K. Hybrid tin oxide nanowires as stable and high capacity anodes for Li-ion batteries. *Nano Letters* **9,** 612–616 (2009).

119. Wan, N., Zhao, T., Sun, S., Wu, Q. & Bai, Y. Nickel and nitrogen co-doped tin dioxide nano-composite as a potential anode material for lithium-ion batteries. *Electrochimica Acta* **143,** 257–264 (2014).

120. Chiu, H. C. & Yeh, C. S. Hydrothermal synthesis of SnO_2 nanoparticles and their gas-sensing of alcohol. *Journal of Physical Chemistry C* **111,** 7256–7259 (2007).

121. Aziz, M., Saber Abbas, S. & Wan Baharom, W. R. Size-controlled synthesis of SnO_2 nanoparticles by sol-gel method. *Materials Letters* **91,** 31–34 (Jan. 2013).

122. Liu, Y., Koep, E. & Liu, M. A highly sensitive and fast-responding SnO_2 sensor fabricated by combustion chemical vapor deposition. *Chemistry of Materials* **17,** 3997–4000 (July 2005).

123. Letsholathebe, D. *et al.* Structural, Optical, Morphological and Microbial Studies on SnO_2 Nanoparticles Prepared by Co-Precipitation Method. *Journal of Nanoscience and Nanotechnology* **18,** 3511–3517 (2017).

124. Aragón, F. H. *et al.* Evidences of the evolution from solid solution to surface segregation in Ni-doped SnO_2 nanoparticles using Raman spectroscopy. *Journal of Raman Spectroscopy* **42,** 1081–1086 (2011).

125. Del Prado, F. *et al.* Controlled synthesis of lithium doped tin dioxide nanoparticles by a polymeric precursor method and analysis of the resulting defect structure. *Journal of Materials Chemistry A* **6,** 6299–6308 (Apr. 2018).

126. Ma, Y. *et al.* Influence of the doping ratio and the carbon coating content on the electrochemical performance of Co-doped SnO_2 for lithium-ion anodes. *Electrochimica Acta* **277,** 100–109 (July 2018).

127. Del Prado, F. *et al.* Comparative study of the implementation of tin and titanium oxide nanoparticles as electrodes materials in Li-ion batteries. *Scientific Reports* **10,** 1–8 (Dec. 2020).

128. Lu, Y. C. *et al.* Electrochemical properties of tin oxide anodes for sodium-ion batteries. *Journal of Power Sources* **284,** 287–295 (June 2015).

129. Lee, S. Y. *et al.* Unveiling origin of additional capacity of SnO_2 anode in lithium-ion batteries by realistic ex situ TEM analysis. *Nano Energy* **19,** 234–245 (2016).

130. Poizot, P., Laruelle, S., Grugeon, S., Dupont, L. & Tarascon, J. M. Nano-sized transition-metal oxides as negative-electrode materials for

lithium-ion batteries. *Nature* **407,** 496–499 (2000).

131. Zhang, L., Wu, H. B., Liu, B. & Lou, X. W. Formation of porous SnO_2 microboxes via selective leaching for highly reversible lithium storage. *Energy and Environmental Science* **7,** 1013–1017 (2014).

132. Priyadharshini, E., Suresh, S., Gunasekaran, S., Srinivasan, S. & Manikandan, A. Investigation on electrochemical performance of SnO_2Carbon nanocomposite as better anode material for lithium ion battery. *Physica B: Condensed Matter* **569,** 8–13 (2019).

133. Scanlon, D. O. & Watson, G. W. On the possibility of p-type SnO_2. *Journal of Materials Chemistry* **22,** 25236–25245 (Dec. 2012).

134. Shannon, R. D. Revised effective ionic radii in halides and chalcogenides. *Acta Crystallogr.,* 751. arXiv: `arXiv:1011.1669v3` (1976).

135. Tabassum, S. *et al.* Band gap narrowing and fluorescence properties of nickel doped SnO_2 nanoparticles. *Journal of Luminescence* **131,** 1–6 (2010).

136. Rahman, G., Din, N. U., García-Suárez, V. M. & Kan, E. Stabilizing intrinsic defects in SnO_2. *Physical Review B* **87,** 205205 (2013).

137. Kallel, W., Bouattour, S., Ferreira, L. F. & Botelho do Rego, A. M. Synthesis, XPS and luminescence (investigations) of Li^+ and/or $Y_3{}^+$ doped nanosized titanium oxide. *Materials Chemistry and Physics* **114,** 304–308 (Mar. 2009).

138. Tabei, M., Shionoya, S. & Ohmatsu, H. Mechanism of the Killer Effect of Iron-Group Ions on the Green Luminescence in ZnS:Cu,Al Phosphors. *Japanese Journal of Applied Physics* **14,** 240–247 (1975).

139. Zhou, G. *et al.* Visible photoluminescence of hydrothermal synthesized $Sn_{1-x}Ni_xO_2$ nanostructures. *Journal of Materials Science: Materials in Electronics* **22,** 174–178 (Feb. 2011).

140. Rajeeva, M. P., Naveen, C. S., Lamani, A. R., Bothla, V. P. & Jayanna, H. S. *Study on low temperature DC electrical conductivity of SnO_2 nanomaterial synthesized by simple gel combustion method* in *AIP Conference Proceedings* **1665** (American Institute of Physics Inc., June 2015), 050091.

141. Wang, M., Zhao, T., Li, M. & Wang, H. Perovskite $La_2(NiCu)O_4$catalyst precursors for dry reforming of methane: Effects of Cu-substitution on carbon resistance. *RSC Advances* **7,** 41847–41854 (2017).

142. Meeporn, K., Chanlek, N. & Thongbai, P. Effects of DC bias on non-ohmic sample-electrode contact and grain boundary responses in giant-permittivity $La_{1.7}Sr_{0.3}N_{1-x}Mg_xO_4$ ceramics. *RSC Advances* **6,** 91377–91385 (2016).

143. San Choi, J., Ahn, C. W., Bae, J. S. & Kim, T. H. Identifying a perovskite phase in rare-earth nickelates using X-ray photoelectron spectroscopy. *Current Applied Physics* **20,** 102–105 (Jan. 2020).

144. Zhou, X. T. *et al.* The effect of the surface of nanoribbons on their luminescence using x-ray absorption and luminescence spectroscopy. *J. Chem. Phys* **128,** 144703 (2008).

145. De Groot, F. Multiplet effects in X-ray spectroscopy. *Coordination Chemistry Reviews* **249,** 31–63 (2005).

146. Ikeno, H., De Groot, F. M., Stavitski, E. & Tanaka, I. Multiplet calculations of $L_{2,3}$ x-ray absorption near-edge structures for 3d transition-

metal compounds. *Journal of Physics Condensed Matter* **21** (2009).

147. Stavitski, E. & de Groot, F. M. The CTM4XAS program for EELS and XAS spectral shape analysis of transition metal L edges. *Micron* **41,** 687–694 (2010).

148. Lin, F. *et al.* Hole doping in al-containing nickel oxide materials to improve electrochromic performance. *ACS Applied Materials and Interfaces* **5,** 301–309 (2013).

149. Ferraresi, G. *et al.* SnO_2 Model Electrode Cycled in Li-Ion Battery Reveals the Formation of Li_2SnO_3 and Li_8SnO_6 Phases through Conversion Reactions. *ACS Applied Materials and Interfaces* **10,** 8712–8720 (2018).

150. Smith, M. R., Johnson, P. L. & Teeters, D. Interfacial storage of lithium in the nanostructure of SnO_2 nanobaskets for capacities exceeding theoretical values. *Solid State Ionics* **225,** 680–684 (2012).

151. Wan, N. *et al.* Improved Li storage performance in SnO_2 nanocrystals by a synergetic doping. *Scientific Reports* **6,** 18978 (2016).

152. Diao, G. Q. *et al.* Comparison of SnO_2 -carbon nanotubes composite and the SnO_2 -carbon black mixture as an anode for Li-ion batteries. *IOP Conference Series: Materials Science and Engineering* **474,** 012022 (Feb. 2019).

153. Narsimulu, D., Vinoth, S., Srinadhu, E. S. & Satyanarayana, N. Surfactant-free microwave hydrothermal synthesis of SnO_2 nanosheets as an anode material for lithium battery applications. *Ceramics International* **44,** 201–207 (Jan. 2018).

154. Wang, J., Zhou, W. & Wu, P. Band gap widening and d_0 ferromagnetism in epitaxial Li-doped SnO_2 films. *Applied Surface Science* **314,** 188–192 (Sept. 2014).

155. Vázquez-López, A. *et al.* Hybrid Materials and Nanoparticles for Hybrid Silicon Solar Cells and Li-Ion Batteries. *Journal of Energy and Power Technology* **3** (May 2021).

156. Ohsaka, T., Izumi, F. & Fujiki, Y. Raman spectrum of anatase, TiO_2. *Journal of Raman Spectroscopy* **7,** 321–324 (Dec. 1978).

157. Vásquez, G. C. *et al.* Laser-induced anatase-to-rutile transition in TiO_2 nanoparticles: Promotion and inhibition effects by Fe and Al doping and achievement of micropatterning. *Journal of Physical Chemistry C* **119,** 11965–11974 (2015).

158. Pallotti, D. K., Passoni, L., Maddalena, P., Fonzo, F. D. & Lettieri, S. Photoluminescence Mechanisms in Anatase and Rutile TiO_2. *Journal of Physical Chemistry C* **121,** 9011–9021 (2017).

159. Oku, M., Wagatsuma, K. & Kohiki, S. Ti 2p and Ti 3p X-ray photoelectron spectra for TiO_2, $SrTiO_3$ and $BaTiO_3$. *Physical Chemistry Chemical Physics* **1,** 5327–5331 (Dec. 1999).

160. Tian, J. *et al.* Influence of transition metal doping on the structural, optical, and magnetic properties of TiO_2 films deposited on Si substrates by a sol-gel process. *Nanoscale Research Letters* **8,** 1–11 (2013).

161. Crocombette, J. P. & Jollet, F. Ti 2p x-ray absorption in titanium dioxides (TiO_2): The influence of the cation site environment. *American Laboratory* **26,** 10811–10821 (1994).

162. De Groot, F. M. *et al.* 2 p X-ray absorption of titanium in minerals. *Physics and Chemistry of Minerals* **19,** 140–147 (1992).

163. Thomas, A. G. *et al.* Comparison of the electronic structure of anatase and rutile TiO_2 single-crystal surfaces using resonant photoemission and x-ray absorption spectroscopy. *Physical Review B - Condensed Matter and Materials Physics* **75,** 1–12 (2007).

164. Kapilashrami, M., Zhang, Y., Liu, Y. S., Hagfeldt, A. & Guo, J. Probing the optical property and electronic structure of TiO_2 nanomaterials for renewable energy applications. *Chemical Reviews* **114,** 9662–9707 (2014).

165. Ruus, R. *et al.* Ti 2p and O 1s x-ray absorption of TiO_2 polymorphs. *Solid State Communications* **104,** 199–203 (Oct. 1997).

166. Wang, H. *et al.* Nickel L-Edge Soft X-ray Spectroscopy of Nickel-Iron Hydrogenases and Model CompoundssEvidence for High-Spin Nickel(II) in the Active Enzyme (2000).

167. Chen, J., Lu, G. H., Cao, H., Wang, T. & Xu, Y. Ferromagnetic mechanism in Ni-doped anatase TiO_2. *Applied Physics Letters* **93,** 172504 (Oct. 2008).

168. Elahifard, M. R., Ahmadvand, S. & Mirzanejad, A. Effects of Ni-doping on the photo-catalytic activity of TiO_2 anatase and rutile: Simulation and experiment. *Materials Science in Semiconductor Processing* **84,** 10–16 (Sept. 2018).

169. Vásquez, G. C. *et al.* Influence of Fe and Al doping on the stabilization of the anatase phase in TiO_2 nanoparticles. *Journal of Materials Chemistry C* **2,** 10377–10385 (2014).

170. Pirsaheb, M., Shahmoradi, B., Khosravi, T., Karimi, K. & Zandsalimi, Y. Solar degradation of malachite green using nickel-doped TiO_2 nanocatalysts. *Desalination and Water Treatment* **57,** 9881–9888 (May 2016).

171. Feng, N. *et al.* Unravelling the Efficient Photocatalytic Activity of Boron-induced Ti^{3+}Species in the Surface Layer of TiO_2. *Scientific Reports* **6,** 34765 (Oct. 2016).

172. Bian, Z., Zhu, J. & Li, H. Solvothermal alcoholysis synthesis of hierarchical TiO_2 with enhanced activity in environmental and energy photocatalysis. *Journal of Photochemistry and Photobiology C: Photochemistry Reviews* **28,** 72–86 (Sept. 2016).

173. Yoshitake, H., Sugihara, T. & Tatsumi, T. Preparation of wormhole-like mesoporous TiO_2 with an extremely large surface area and stabilization of its surface by chemical vapor deposition. *Chemistry of Materials* **14,** 1023–1029 (2002).

174. Gaur, L. K. *et al.* Laser induced phase transformation influenced by Co doping in TiO_2 nanoparticles. *Journal of Alloys and Compounds* **780,** 25–34 (Apr. 2019).

175. Kumaravel, V. *et al.* Mo doped TiO_2: impact on oxygen vacancies, anatase phase stability and photocatalytic activity. *J. Phys.: Mater* **3,** 25008 (2020).

176. Zaleska, A. Doped-TiO_2: A Review. *Recent Patents on Engineering,* 157–164 (2008).

177. Giordano, F. *et al.* Enhanced electronic properties in mesoporous TiO_2 via lithium doping for high-efficiency perovskite solar cells. *Nature Communications* **7,** 10379 (Apr. 2016).

178. Lan, C. *et al.* Enhanced charge extraction of Li-doped TiO_2 for efficient thermal-evaporated Sb_2S_3 thin film solar cells. *Materials* **11,** 8–12 (2018).

179. Yildizhan, M. M., Sturm, S. & Gulgun, M. A. Structural and electronic modifications on TiO_2 anatase by Li, K or Nb doping below and above the solubility limit. *Journal of Materials Science* **51,** 5912–5923 (2016).

180. Wagemaker, M., Borghols, W. J. H. & Mulder, F. M. Large Impact of Particle Size on Insertion Reactions. A Case for Anatase Li_xTiO_2 (2007).

181. Zhang, W. F., He, Y. L., Zhang, M. S., Yin, Z. & Chen, Q. Raman scattering study on anatase TiO_2 nanocrystals. *Journal of Physics D: Applied Physics* **33,** 912–916 (Apr. 2000).

182. Xu, Z., Wang, S., Ma, C., Luo, K. & Fang, F. Effect of Nickel Doping on Phase Transformation of TiO_2 Nanotube Arrays. *physica status solidi (a)* **216,** 1800836 (Mar. 2019).

183. Choudhury, B. & Choudhury, A. Oxygen vacancy and dopant concentration dependent magnetic properties of Mn doped TiO_2 nanoparticle. *Current Applied Physics* **13,** 1025–1031 (Aug. 2013).

184. Zhang, J. *et al.* Synthesis, surface morphology, and photoluminescence properties of anatase iron-doped titanium dioxide nano-crystalline films. *Physical Chemistry Chemical Physics* **13,** 13096–13105 (2011).

185. Jiang, H., Song, H., Zhou, Z., Liu, X. & Meng, G. The roles of Li^+ and F^- ions in Li-F^-codoped TiO_2 system. *Journal of Physics and Chemistry of Solids* **68,** 1830–1835 (Oct. 2007).

186. Zhao, Y. F. *et al.* Effects of oxygen vacancy on 3d transition-metal doped anatase TiO_2: First principles calculations. *Chemical Physics Letters* **647,** 36–41 (Mar. 2016).

187. Battiston, S. *et al.* Cathodoluminescence evaluation of oxygen vacancy population in nanostructured titania thin films for photocatalytic applications. *Journal of Physical Chemistry A* **114,** 5295–5298 (Apr. 2010).

188. Saravanan, P. *et al.* Electrical properties of green synthesized TiO_2 nanoparticles. *Pelagia Research Library Advances in Applied Science Research* **7,** 158–168 (2016).

189. Weibel, A., Bouchet, R. & Knauth, P. Electrical properties and defect chemistry of anatase (TiO_2). *Solid State Ionics* **177,** 229–236 (Jan. 2006).

190. Earle, M. D. The electrical conductivity of titanium dioxide. *Physical Review* **61,** 56–62 (Jan. 1942).

191. Vásquez, G. C. *et al.* Effects of transition metal doping on the growth and properties of rutile TiO_2 nanoparticles. *Journal of Physical Chemistry C* **117,** 1941–1947 (2013).

192. Weidler, N. *et al.* X-ray Photoelectron Spectroscopic Investigation of Plasma-Enhanced Chemical Vapor Deposited NiO_x, $NiO_x(OH)_y$, and $CoNiO_x(OH)_y$: Influence of the Chemical Composition on the Catalytic Activity for the O_x. *Journal of Physical Chemistry C* **121,** 6455–6463 (2017).

193. Zhang, Y. H. & Reller, A. Phase transformation and grain growth of doped nanosized titania. *Materials Science and Engineering C* **19,** 323–326 (Jan. 2002).

194. Nair, J., Nair, P., Mizukami, F., Oosawa, Y. & Okubo, T. Microstructure and phase transformation behavior of doped nanostructured titania. *Materials Research Bulletin* **34,** 1275–1290 (Oct. 1999).

195. Spurr, R. A. & Myers, H. Quantitative Analysis of Anatase-Rutile Mixtures with an X-Ray Diffractometer. *Analitical Chemistry* **29,** 760–762 (1957).

196. Kim, J. Y., Jung, H. S., No, J. H., Kim, J. R. & Hong, K. S. Influence of anatase-rutile phase transformation on dielectric properties of sol-gel derived TiO_2 thin films. **16,** 447–451 (July 2006).

197. Dauksta, E. *et al.* Laser-induced crystalline phase transition from rutile to anatase of niobium doped TiO_2. *Current Applied Physics* **19,** 351–355 (Mar. 2019).

198. Labadini, D. *et al.* Visualization and Quantification of the Laser-Induced ART of TiO_2 by Photoexcitation of Adsorbed Dyes. *Langmuir* **36,** 1651–1661 (Feb. 2020).

199. Medvids, A. *et al.* Anatase or rutile TiO_2 nanolayer formation on Ti substrates by laser radiation: Mechanical, photocatalytic and antibacterial properties. *Optics and Laser Technology* **138,** 106898 (June 2021).

200. Ricci, P. C. *et al.* Anatase-to-rutile phase transition in TiO_2 nanoparticles irradiated by visible light. *Journal of Physical Chemistry C* **117,** 7850–7857 (Apr. 2013).

201. Sushko, M. L., Rosso, K. M. & Liu, J. Mechanism of Li^+ /Electron Conductivity in Rutile and Anatase TiO_2 Nanoparticles. *Journal of Physics and Chemistry C* **114,** 20277–20283 (2010).

202. Vázquez-López, A., Maestre, D., Ramírez-Castellanos, J. & Cremades, A. In Situ Local Oxidation of SnO Induced by Laser Irradiation: A Stability Study. *Nanomaterials* **11,** 976 (Apr. 2021).

203. Chen, X. & Grandbois, M. In situ Raman spectroscopic observation of sequential hydrolysis of stannous chloride to abhurite, hydroromarchite, and romarchite. *Journal of Raman Spectroscopy* **44,** 501–506 (2013).

204. Guillén, C. & Herrero, J. P-type SnO thin films prepared by reactive sputtering at high deposition rates. *Journal of Materials Science & Technology* **35,** 1706–1711 (Aug. 2019).

205. Eifert, B. *et al.* Raman studies of the intermediate tin-oxide phase. *Physical Review Materials* **1,** 14602 (2017).

206. Lockwood, D. J. *et al.* Raman spectrum of $NiCl_2$. *Journal of Physics C: Solid State Physics* **12,** 3615–3620 (Sept. 1979).

207. Shebanova, O. N. & Lazor, P. Raman study of magnetite (Fe_3O_4): laser-induced thermal effects and oxidation. *Journal of Raman Spectroscopy* **34,** 845–852 (Nov. 2003).

208. Díaz-Guerra, C., Almodóvar, P., Camacho-López, M., Camacho-López, S. & Piqueras, J. Formation of β-Bi_2O_3 and δ-Bi_2O_3 during laser irradiation of Bi films studied in-situ by spatially resolved Raman spectroscopy. *Journal of Alloys and Compounds* (2017).

209. Almodóvar, P., Díaz-Guerra, C., Ramírez-Castellanos, J. & González-Calbet, J. M. In situ local assessment of laser irradiation-induced phase transformations in hexagonal MoO_3 microrods. *CrystEngComm* **20,** 4954–4961 (Aug. 2018).

210. Del Prado, F. *et al.* Effect of the synthesis method on the properties of lithium doped graphene oxide composites with tin oxide nanoparticles: Towards white luminescence. *Journal of Physics and Chemistry of Solids* **129,** 133–139 (2019).

211. Schanda, J. *Colorimetry: Understanding the CIE System — Wiley* 408 (2007).

212. Batzill, M. & Diebold, U. The surface and materials science of tin oxide. *Progress in Surface Science* **79,** 47–154 (2005).

213. Suman, P. H. *Electrical properties of tin oxide materials* 41–60 (Elsevier Inc., 2020).

214. Dias, J. S., Batista, F. R., Bacani, R. & Triboni, E. R. Structural characterization of SnO nanoparticles synthesized by the hydrothermal and microwave routes. *Scientific Reports* **10** (Dec. 2020).

215. Vázquez-López, A. *et al.* Synergetic Improvement of Stability and Conductivity of Hybrid Composites formed by PEDOT:PSS and SnO Nanoparticles. *Molecules* **25,** 695 (Feb. 2020).

216. Liu, W. *et al.* One-step synthesis of SnO hierarchical architectures under room temperature and their photocatalytic properties. *Nanotechnology* **29** (May 2018).

217. Zhang, R. *et al.* Morphology modulation of SnO photocatalyst: From microplate to hierarchical architectures self-assembled with thickness controllable nanosheets. *CrystEngComm* **20,** 4651–4665 (Aug. 2018).

218. Miller, S. A. *et al.* SnO as a potential oxide thermoelectric candidate. *Journal of Materials Chemistry C* **5,** 8854–8861 (Aug. 2017).

219. Jaśkaniec, S. *et al.* Solvent engineered synthesis of layered SnO nanoparticles for high-performance anodes. *arXiv* **5,** 1–9 (Nov. 2020).

220. Huda, A., Handoko, C. T., Bustan, M. D., Yudono, B. & Gulo, F. New route in the synthesis of Tin(II) oxide micro-sheets and its thermal transformation. *Materials Letters* **211,** 293–295 (Jan. 2018).

221. Pires, F. I. *et al.* Microwave-assisted hydrothermal synthesis of nanocrystalline SnO powders. *Materials Letters* **62,** 239–242 (2008).

222. Campo, C. M., Rodríguez, J. E. & Ramírez, A. E. Thermal behaviour of romarchite phase SnO in different atmospheres: a hypothesis about the phase transformation. *Heliyon* **2,** 1–13 (2016).

223. Eqbal, E. & Anila, E. I. Properties of transparent conducting tin monoxide (SnO) thin films prepared by chemical spray pyrolysis method. *Physica B: Condensed Matter* **528,** 60–65 (Jan. 2018).

224. Domashevskaya, E. P. *et al.* SnO_x obtaining by thermal oxidation of nanoscale tin films in the air and its characterization. *Thin Solid Films* **515,** 6350–6355 (2007).

225. Leitner, J. & Sedmidubský, D. Thermodynamic Modeling of Oxidation of Tin Nanoparticles. *Journal of Phase Equilibria and Diffusion* **40,** 10–20 (Feb. 2019).

226. Sun, Y. H., Dong, P. P., Lang, X. & Nan, J. M. A novel rose flower-like SnO hierarchical structure synthesized by a hydrothermal method in an ethanol/water system. *Chinese Chemical Letters* **25,** 915–918 (Apr. 2014).

227. Pan, X. Q. & Fu, L. Oxidation and phase transitions of epitaxial tin oxide thin films on (1012) sapphire. *Journal of Applied Physics* **89,** 6048–6055 (June 2001).

228. Cahen, S., David, N., Fiorani, J. M., Maître, A. & Vilasi, M. Thermodynamic modelling of the O-Sn system. *Thermochimica Acta* **403,** 275–285 (July 2003).

229. Wang, F., Zhou, X., Zhou, J., Sham, T. K. & Ding, Z. Observation of single tin dioxide nanoribbons by confocal raman microspectroscopy. *Journal of Physical Chemistry C* **111,** 18839–18843 (Dec. 2007).

230. Kim, J. H., Jeon, K. M., Park, J. S. & Kang, Y. C. Excellent Li-ion storage performances of hierarchical SnO-SnO_2 composite powders and SnO nanoplates prepared by one-pot spray pyrolysis. *Journal of Power Sources* **359,** 363–370 (Aug. 2017).

231. Li, L., Zhang, C. & Chen, W. Fabrication of SnO_2-SnO nanocomposites with p-n heterojunctions for the low-temperature sensing of NO_2 gas. *Nanoscale* **7,** 12133–12142 (July 2015).

232. Li, N. *et al.* A low temperature formaldehyde gas sensor based on hierarchical SnO/SnO_2 nano-flowers assembled from ultrathin nanosheets: Synthesis, sensing performance and mechanism. *Sensors and Actuators, B: Chemical* **294,** 106–115 (Sept. 2019).

233. Palneedi, H. *et al.* Laser Processing of Metal Oxides: Laser Irradiation of Metal Oxide Films and Nanostructures: Applications and Advances. *Advanced Materials* **30,** 1870094 (Apr. 2018).

234. Krishnakumar, T., Pinna, N., Perumal, K. & Jayaprakash, R. Preparation and characterization of SnO nanoplatelets by microwave innovative technique. *AIP Conference Proceedings* **1004,** 122–125 (2008).

235. Varley, J. B., Schleife, A., Janotti, A. & Van De Walle, C. G. Ambipolar doping in SnO. *Applied Physics Letters* **103** (2013).

236. Arunodaya, J. & Sahoo, T. Effect of Li doping on conductivity and band gap of nickel oxide thin film deposited by spin coating technique. *Materials Research Express* **7,** 16405 (Dec. 2019).

237. Vázquez-López, A. *et al.* Improved silicon surface passivation by hybrid composites formed by PEDOT:PSS with anatase TiO_2 nanoparticles. *Materials Letters* **271,** 127802 (July 2020).

238. Pathak, C. S., Singh, J. P. & Singh, R. Effect of dimethyl sulfoxide on the electrical properties of PEDOT:PSS/n-Si heterojunction diodes. *Current Applied Physics* **15,** 528–534 (2015).

239. Nagata, R., Yanagi, Y., Fujii, S., Kataura, H. & Nishioka, Y. Application of highly conductive DMSO-treated PEDOT:PSS electrodes to flexible organic solar cells. *IEICE Transactions on Electronics* **E98.C,** 411–421 (2015).

240. Yoon, S. S. & Khang, D. Y. Roles of Nonionic Surfactant Additives in PEDOT:PSS Thin Films. *Journal of Physical Chemistry C* **120,** 29525–29532 (2016).

241. Singh, V. & Kumar, T. Study of modified PEDOT:PSS for tuning the optical properties of its conductive thin films. *Journal of Science: Advanced Materials and Devices* **4,** 538–543 (2019).

242. Long, L. M. *et al.* Optical and NH_3 Gas Sensing Properties of Hole-Transport Layers Based on PEDOT:PSS Incorporated with Nano-TiO_2. *Materials Sciences and Applications* **08,** 663–672 (Aug. 2017).

243. Rahman, Z. A., Sulaiman, K., Shuhaimi, A. & Rusop, M. PEDOT:PSS Thin Film as Transparent Electrode in ITO-Free Organic Solar Cell. *Advanced Materials Research* **501,** 252–256 (2012).

244. Mahendia, S., Kumar Tomar, A., Goyal, P. K. & Kumar, S. Tuning of refractive index of poly(vinyl alcohol): Effect of embedding Cu and Ag nanoparticles. *J. Appl. Phys* **113,** 73103 (2013).

245. Gasiorowski, J., Menon, R., Hingerl, K., Dachev, M. & Sariciftci, N. S. Surface morphology, optical properties and conductivity changes of poly(3,4-ethylenedioxythiophene) :poly(styrenesulfonate) by using additives. *Thin Solid Films* **536,** 211–215 (June 2013).

246. Drakonakis, V. M., Savva, A., Kokonou, M. & Choulis, S. A. Investigating electrodes degradation in organic photovoltaics through reverse engineering under accelerated humidity lifetime conditions. *Solar Energy Materials and Solar Cells* **130,** 544–550 (2014).

247. Vitoratos, E. *et al.* Thermal degradation mechanisms of PEDOT:PSS. *Organic Electronics* **10,** 61–66 (2009).

248. Chiu, W. W., Travaš-Sejdić, J., Cooney, R. P. & Bowmaker, G. A. Spectroscopic and conductivity studies of doping in chemically synthesized poly(3,4-ethylenedioxythiophene). *Synthetic Metals* **155,** 80–88 (Oct. 2005).

249. Huang, Y. *et al.* UV-Raman scattering of thin film Si with ultrathin silicon oxide tunnel contact for high efficiency crystal silicon solar cells. *Solar Energy Materials and Solar Cells* **192,** 154–160 (Apr. 2019).

250. Liu, J., Niu, J., Yang, D., Yan, M. & Sha, J. Raman spectrum of array-ordered crystalline silicon nanowires. *Physica E: Low-Dimensional Systems and Nanostructures* **23,** 221–225 (June 2004).

251. Lee, H., Kim, Y., Cho, H., Lee, J.-g. & Kim, J. H. Improvement of PEDOT:PSS linearity via controlled addition process. *RSC Advances* **9,** 17318–17324 (May 2019).

252. Xu, B. *et al.* Corrigendum: Functional solid additive modified PEDOT:PSS as an anode buffer layer for enhanced photovoltaic performance and stability in polymer solar cells. *Scientific reports* **7,** 46779 (2017).

253. Du, F.-P. *et al.* PEDOT:PSS/graphene quantum dots films with enhanced thermoelectric properties via strong interfacial interaction and phase separation. *Scientific reports* **8,** 6441 (Apr. 2018).

254. Chiu, W. W., Travaš-Sejdić, J., Cooney, R. P. & Bowmaker, G. A. Studies of dopant effects in poly(3,4-ethylenedioxythiophene) using Raman spectroscopy. *Journal of Raman Spectroscopy* **37,** 1354–1361 (2006).

255. Wang, S. *et al.* Organic/inorganic hybrid sensors: A review. *Sensors and Actuators, B: Chemical* **182,** 467–481 (2013).

256. Sheng, J. *et al.* Improvement of the SiO_x Passivation Layer for High-Efficiency Si/ PEDOT:PSS Heterojunction Solar Cells. *ACS Applied Materials & Interfaces* **6,** 16027–16034 (2014).

257. Halbich, M. U. *et al.* Improved surface passivation and reduced parasitic absorption in PEDOT:PSS/c-Si heterojunction solar cells through the admixture of sorbitol. *Scientific Reports* **9,** 1–8 (Dec. 2019).

258. Grant, N. E. & Murphy, J. D. Temporary Surface Passivation for Characterisation of Bulk Defects in Silicon: A Review. *Physica Status Solidi - Rapid Research Letters* **11,** 1–18 (2017).

259. Chen, J. *et al.* Electrochemical grafting passivation of silicon via electron transfer at polymer/silicon hybrid interface. *Electrochimica Acta* **247,** 826–834 (Sept. 2017).

260. Zielke, D. *et al. Organic-silicon Solar Cells Exceeding 20% Efficiency* in *Energy Procedia* **77** (Elsevier Ltd, Aug. 2015), 331–339.

261. Jiang, X. *et al.* High Performance of PEDOT:PSS/n-Si Solar Cells Based on Textured Surface with AgNWs Electrodes. *Nanoscale Research Letters* **13,** 53 (Dec. 2018).

262. Mengistie, D. A., Ibrahem, M. A., Wang, P. C. & Chu, C. W. Highly conductive PEDOT:PSS treated with formic acid for ITO-free polymer solar cells. *ACS Applied Materials and Interfaces* **6,** 2292–2299 (Feb. 2014).

263. Luo, J. *et al.* Enhancement of the thermoelectric properties of PEDOT:PSS thin films by post-treatment. *Journal of Materials Chemistry A* **1,** 7576–7583 (2013).

264. Liu, Q. *et al.* Highly Efficient Solution-Processed PEDOT:PSS / Crystalline- Silicon Heterojunction Solar Cells with Improved Light-Induced Stability. *Advanced Energy Materials* **5,** 1500744 (Sept. 2015).

265. Oreski, G., Tscharnuter, D. & Wallner, G. M. *Development of methods to determine the infrared-optical properties of polymer films* in *Macromolecular Symposia* **265** (May 2008), 124–133.

266. Yan, H. & Okuzaki, H. Effect of solvent on PEDOT/PSS nanometer-scaled thin films: XPS and STEM/AFM studies. *Synthetic Metals* **159,** 2225–2228 (Nov. 2009).

267. Lin, Y. J., Ni, W. S. & Lee, J. Y. Effect of incorporation of ethylene glycol into PEDOT:PSS on electron phonon coupling and conductivity. *Journal of Applied Physics* **117,** 1–5 (2015).

268. Yang, C. *et al.* Performance-enhancing Approaches for the PEDOT:PSS-Si Hybrid Solar Cells. *Angewandte Chemie* (Dec. 2019).

269. Cui, H. Q. *et al.* Optimization of Ethylene Glycol Doped PEDOT:PSS Transparent Electrodes for Flexible Organic Solar Cells by Drop-coating Method. *Chinese Journal of Polymer Science (English Edition)* **37,** 760–766 (Aug. 2019).

270. Zhang, C. *et al.* Investigate the effects of EG doping PEDOT/PSS on transmission and anti-reflection properties using terahertz pulsed spectroscopy. *Optics Express, Vol. 25, Issue 3, pp. 1723-1731* **25,** 1723–1731 (Feb. 2017).

271. Alemu Mengistie, D., Wang, P. C. & Chu, C. W. Effect of molecular weight of additives on the conductivity of PEDOT:PSS and efficiency for ITO-free organic solar cells. *Journal of Materials Chemistry A* **1,** 9907–9915 (Sept. 2013).

272. Pasha, A., Khasim, S., Al-Hartomy, O. A., Lakshmi, M. & Manjunatha, K. G. Highly sensitive ethylene glycol-doped PEDOT-PSS organic

thin films for LPG sensing. *RSC Advances* **8,** 18074–18083 (May 2018).

273. Zampetti, E. *et al.* A high sensitive NO_2 gas sensor based on PEDOT-PSS/TiO_2 nanofibres. *Sensors and Actuators, B: Chemical* **176,** 390–398 (2013).

274. Seeley, Z. M., Bandyopadhyay, A. & Bose, S. Titanium dioxide thin films for high temperature gas sensors. *Thin Solid Films* **519,** 434–438 (Oct. 2010).

275. Mercado, C., Seeley, Z., Bandyopadhyay, A., Bose, S. & McHale, J. L. Photoluminescence of Dense Nanocrystalline Titanium Dioxide Thin Films: Effect of Doping and Thickness and Relation to Gas Sensing. *ACS Applied Materials and Interfaces* **3,** 2281–2288 (July 2011).

276. Mercado, C., Seeley, Z., Bandyopadhyay, A., Bose, S. & McHale, J. L. Photoluminescence of Dense Nanocrystalline Titanium Dioxide Thin Films: Effect of Doping and Thickness and Relation to Gas Sensing. *ACS Applied Materials & Interfaces* **3,** 2281–2288 (July 2011).

277. Khan, M. I., Bhatti, K. A., Qindeel, R., Althobaiti, H. S. & Alonizan, N. Structural, electrical and optical properties of multilayer TiO_2 thin films deposited by sol–gel spin coating. *Results in Physics* **7,** 1437–1439 (2017).

278. Park, D., Kim, M. & Kim, J. Conductive pedot: Pss-based organic/inorganic flexible thermoelectric films and power generators. *Polymers* **13,** 1–12 (Jan. 2021).

279. Gao, N. *et al.* Application of pedot:Pss and its composites in electrochemical and electronic chemosensors. *Chemosensors* **9,** 79 (Apr. 2021).

280. Zhang, B., Sun, J., Katz, H. E., Fang, F. & Opila, R. L. Promising Thermoelectric Properties of Commercial PEDOT:PSS Materials and Their Bi_2Te_3 Powder Composites. *ACS Applied Materials & Interfaces* **2,** 3170–3178 (2010).

281. Wong, Y. C., Ang, B. C., Haseeb, A. S. M. A., Baharuddin, A. A. & Wong, Y. H. Conducting Polymers as Chemiresistive Gas Sensing Materials: A Review. *Journal of The Electrochemical Society* **167,** 037503 (Sept. 2020).

282. Kim, J. R., Jung, J. H., Shin, W. S., So, W. W. & Moon, S. J. Efficient TCO-free organic solar cells with modified poly(3,4- ethylenedioxythiophene): Poly(styrenesulfonate) anodes. *Journal of Nanoscience and Nanotechnology* **11,** 326–330 (2011).

283. Bubnova, O. *et al.* Semi-metallic polymers. *Nature Materials* **13,** 190–194 (Dec. 2014).

284. Dong, J., Gerlach, D., Koutsogiannis, P., Rudolf, P. & Portale, G. Boosting the Thermoelectric Properties of PEDOT:PSS via Low-Impact Deposition of Tin Oxide Nanoparticles. *Advanced Electronic Materials* **7,** 2001284 (May 2021).

285. Jin Bae, E., Hun Kang, Y., Jang, K. S. & Yun Cho, S. Enhancement of Thermoelectric Properties of PEDOT:PSS and Tellurium-PEDOT:PSS Hybrid Composites by Simple Chemical Treatment. *Scientific Reports* **6** (Jan. 2016).

286. Alhummiany, H., Rafique, S. & Sulaiman, K. XPS Analysis of the Improved Operational Stability of Organic Solar Cells Using a V_2O_5 and PEDOT:PSS Composite Layer: Effect of Varied Atmospheric Conditions. *Journal of Physical Chemistry C* **121,** 7649–7658 (2017).

287. Fan, Z., Ouyang, J., Fan, Z. & Ouyang, J. Review Thermoelectric Properties of PEDOT:PSS. *Advanced Electronic Materials* **5,** 1800769 (2019).

288. Reyes-Reyes, M., Cruz-Cruz, I. & López-Sandoval, R. Enhancement of the electrical conductivity in PEDOT: PSS films by the addition of dimethyl sulfate. *Journal of Physical Chemistry C* **114,** 20220–20224 (2010).

289. Lin, Y. J., Tsai, C. L., Su, Y. C. & Liu, D. S. Carrier transport mechanism of poly(3,4-ethylenedioxythiophene) doped with poly(4-styrenesulfonate) films by incorporating ZnO nanoparticles. *Applied Physics Letters* **100** (2012).

290. Seekaew, Y. *et al.* Low-cost and flexible printed graphene-PEDOT:PSS gas sensor for ammonia detection. *Organic Electronics* **15,** 2971–2981 (2014).

291. Pasha, A., Khasim, S., Khan, F. A. & Dhananjaya, N. Fabrication of gas sensor device using poly (3, 4-ethylenedioxythiophene)-poly (styrenesulfonate)-doped reduced graphene oxide organic thin films for detection of ammonia gas at room temperature. *Iranian Polymer Journal (English Edition)* **28,** 183–192 (Mar. 2019).

292. Zhu, Z., Liu, C., Jiang, F., Xu, J. & Liu, E. *Effective treatment methods on PEDOT:PSS to enhance its thermoelectric performance* Mar. 2017.

293. Xu, S. *et al.* High-Performance PEDOT:PSS Flexible Thermoelectric Materials and Their Devices by Triple Post-Treatments. *Chem. Mater* **31,** 5238–5244 (2019).

294. Yi, C. *et al.* Enhanced thermoelectric properties of poly(3,4-ethylenedioxythiophene): poly(styrenesulfonate) by binary secondary dopants. *ACS Applied Materials and Interfaces* **7,** 8984–8989 (May 2015).

295. Sun, Z. *et al.* Enhanced thermoelectric performance of PEDOT:PSS self-supporting thick films through a binary treatment with polyethylene glycol and water. *Polymer* **192,** 122328 (Mar. 2020).

296. Yemata, T. A. *et al.* Modulation of the doping level of PEDOT:PSS film by treatment with hydrazine to improve the Seebeck coefficient. *RSC Advances* **10,** 1786–1792 (Jan. 2020).

297. Fu, Q., Xiong, Y., Zhang, W. & Xu, D. A setup for measuring the Seebeck coefficient and the electrical resistivity of bulk thermoelectric materials. *Review of Scientific Instruments* **88** (2017).

298. Wang, X. *et al.* Enhancement of thermoelectric performance of PEDOT:PSS films by post-treatment with a superacid. *RSC Advances* **8,** 18334–18340 (May 2018).

299. Toshima, N. & Jiravanichanun, N. Improvement of thermoelectric properties of PEDOT/PSS films by addition of gold nanoparticles: Enhancement of seebeck coefficient. *Journal of Electronic Materials* **42,** 1882–1887 (July 2013).

300. Lee, S. H., Park, H., Son, W., Choi, H. H. & Kim, J. H. Novel solution-processable, dedoped semiconductors for application in thermoelectric devices. *Journal of Materials Chemistry A* **2,** 13380–13387 (Sept. 2014).

301. Xiong, J., Jiang, F., Zhou, W., Liu, C. & Xu, J. Highly electrical and thermoelectric properties of a PEDOT:PSS thin-film via direct dilution-filtration. *RSC Advances* **5,** 60708–60712 (July 2015).

302. Moriarty, G. P. *et al.* Thermoelectric behavior of organic thin film nanocomposites. *Journal of Polymer Science, Part B: Polymer Physics* **51,** 119–123 (Jan. 2013).

303. Xu, K., Chen, G. & Qiu, D. Convenient construction of poly(3,4-ethylenedioxythiophene)-graphene pie-like structure with enhanced thermoelectric performance. *Journal of Materials Chemistry A* **1,** 12395–12399 (Oct. 2013).

304. Ramakrishnan, R. *et al.* Nanostructured Semiconducting PEDOT-TiO_2/ZnO Hybrid Composites for Nanodevice Applications. *Journal of Physical Chemistry C* **120,** 4199–4210 (Mar. 2016).